Analyses of Bluff Body and Swirl-Stabilised Flames Using Large Eddy Simulation

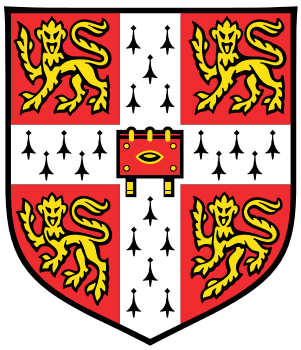

James Charles Massey

Department of Engineering
University of Cambridge

This thesis is submitted for the degree of
Doctor of Philosophy

Selwyn College July 2019

Declaration

This thesis is the result of my own work and includes nothing which is the outcome of work done in collaboration except as declared in the Acknowledgements and specified in the text. It is not substantially the same as any that I have submitted, or, is being concurrently submitted for a degree or diploma or other qualification at the University of Cambridge or any other University or similar institution except as declared in the Acknowledgements and specified in the text. I further state that no substantial part of my thesis has already been submitted, or, is being concurrently submitted for any such degree, diploma or other qualification at the University of Cambridge or any other University or similar institution except as declared in the Acknowledgements and specified in the text. It does not exceed the prescribed work limit for the Engineering Degree Committee. This thesis contains approximately 55000 words, 80 figures and 10 tables.

James Charles Massey
July 2019

Analyses of Bluff Body and Swirl-Stabilised Flames Using Large Eddy Simulation

James Charles Massey

Premixed and partially premixed lean combustion is utilised in modern gas turbine systems, since an improved efficiency and lower flame temperatures can be achieved, thereby offering reductions in pollutant emissions. The stability of these flames in practical combustion systems, where ubiquitous turbulence is present, is enhanced through the use of bluff body flame holders and swirling flow. However, these flames are prone to unstable phenomena that may hinder successful ignition or lead to the occurrence of flashback and other instabilities that may lead to flame blow-off. The stabilisation mechanisms of highly unstable flames are complex and pose as a significant challenge from a modelling perspective.

Large Eddy Simulation (LES) has emerged as an insightful and practical approach for undertaking Computational Fluid Dynamics (CFD) of turbulent lean premixed and partially premixed flames. As the flame front is thinner than the smallest scales of turbulence resolved in a typical LES, the interactions between turbulence and combustion occur within the Sub-Grid Scale (SGS) range of turbulence and these interactions require modelling. Statistical flamelet models are a subgroup of combustion models that are computationally inexpensive, but have proven to be robust in capturing the flame stabilisation mechanisms. In this work, a presumed joint Probability Density Function (PDF) with laminar flamelets is used for modelling the chemical reaction source term. The laminar flamelet concept is employed for decoupling turbulence and combustion chemistry calculations, in order to reduce the computational cost.

This thesis explores the applicability of a flamelet based model for accurately capturing the stabilisation of turbulent flames. The first part of the investigation is focused on premixed flames that are stabilised behind bluff bodies within a chamber or exposed to ambient air. Different operating conditions for the flames are used, which include the supplied turbulence intensity and the fuel–air equivalence ratio of the premixed gas

mixture. Accurately capturing the near-field recirculation zone behind the bluff body is essential for predicting the stabilisation of the flame and experimental measurements are used to validate this. The lengths of the recirculation zones are well captured by the simulations for isothermal and reacting flows of lean to near-stoichiometric flames at different turbulence intensities. The stabilisation of the flames is further explored by observing the evolution of the shear layers and the flame brushes. A scaling expression for the recirculation zone length behind the bluff body is derived to relate the inlet turbulence intensity and the fuel–air equivalence ratio.

Flames close to the lean flammability limit are yet to be explored using the combustion modelling that is used in this work. Hence, the simulation of a swirl-stabilised partially premixed flame in a gas turbine model combustor is undertaken. An extensive experimental data set is used to validate the time-averaged flow field and flame position in the simulation. The velocity components, mixture fraction and temperature fields are all well captured by the LES. Further investigation is undertaken on the stabilisation of the flame by analysing a time series of the flame root properties, such as its position and the local mixture fraction and its dissipation rate. This analysis is undertaken to determine whether the flame root is established or if the flame is experiencing lift-off. Two additional simulations are undertaken of the same flame with the inclusion of heat loss in the modelling framework. One of these two cases uses a non-adiabatic flamelet approach, where its implementation is outlined in this work. Improvements in the near-wall temperature distribution are seen, owing to the inclusion of non-adiabatic wall conditions. The non-adiabatic flamelet simulation over predicts the lift-off height, which is attributed to the presence of heat loss near the flame root region. It is also seen that the flame is more dynamic in the non-adiabatic flamelet simulation in comparison to the adiabatic simulation.

Publications

The studies in this thesis are either published, submitted, or currently under preparation for publication in the following:

Journals:

1. Massey, J. C., Langella, I. & Swaminathan, N. 2018 Large Eddy Simulation of a Bluff Body Stabilised Premixed Flame Using Flamelets. *Flow. Turbul. Combust.* **101** (4), p. 973–992.

2. Massey, J. C., Chen, Z. X. & Swaminathan, N. 2019 Lean Flame Root Dynamics in a Gas Turbine Model Combustor. *Combust. Sci. Technol.* **191** (5–6), p. 1019–1042.

3. Massey, J. C., Langella, I. & Swaminathan, N. 2019 A scaling law for the recirculation zone length behind a bluff body in reacting flows. *J. Fluid Mech.* **875**, p. 699—724.

4. Massey, J. C., Chen, Z. X. & Swaminathan, N. 2019 Modelling Heat Loss Effects in the Large Eddy Simulation of a Lean Swirl-Stabilised Flame. *Flow. Turbul. Combust.* (Submitted).

Conferences:

1. Massey, J. C., Langella, I. & Swaminathan, N. 2016 Influences of Turbulence, Premixed Combustion and Geometry on the Recirculation Zone Behind a Bluff Body. *The Fifth International Education Forum on Environment and Energy Science*, San Diego, CA, USA.

2. Massey, J. C., Langella, I. & Swaminathan, N. 2017 Large Eddy Simulation of a Bluff Body Stabilised Premixed Flame Using Flamelets. *10th Mediterranean Combustion Symposium*, Naples, Italy.

3. Massey, J. C., Langella, I. & Swaminathan, N. 2017 Recirculation Zone Attributes in Bluff Body Stabilised Premixed Flames. *The Sixth International Education Forum on Environment and Energy Science*, Tenerife, Spain (Voted the best presentation on combustion).

4. Massey, J. C., Chen, Z. X. & Swaminathan, N. 2018 Large Eddy Simulation of a Swirl-Stabilised Partially Premixed Flame Close to Blow-off. *37th International Symposium on Combustion*, Dublin, Ireland.

5. Massey, J. C., Chen, Z. X. & Swaminathan, N. 2018 Simulation of a Swirl-Stabilised Partially Premixed Flame Close to Blow-off Using LES. *UKCTRF Annual Meeting*, Cambridge, UK.

6. Massey, J. C., Chen, Z. X. & Swaminathan, N. 2019 Modelling Heat Loss Effects in the LES of a Lean Swirl-Stabilised Flame Close to Blow-Off. *11th Mediterranean Combustion Symposium*, Tenerife, Spain.

Acknowledgements

My PhD journey has been a unique experience and I will remain forever grateful that I have had the opportunity to study at the University of Cambridge. I have experienced many ups (and a few downs), but it has been an experience I will cherish for the rest of my life.

First of all, I would like to sincerely express my gratitude to my supervisor, Prof. Nedunchezhian Swaminathan, for taking me on as his student and for devoting many hours of his time to me throughout my PhD. It has been a privilege to have had him as a teacher for combustion science and a mentor for my development, but being a friend during the times when I experienced difficult periods. His guidance throughout my PhD is extremely appreciated and has influenced my decision in pursuing an academic career.

I would like to thank Prof. Stewart Cant and Prof. Alex Taylor for assessing this thesis and for providing some valuable suggestions to this work. I am extremely grateful to Dr. Zhi Chen for working with me during my PhD. I have enjoyed our discussions with our work and I have learned a lot from him. Thank you also to the past and present members of the Hopkinson Lab that I have been able interact with and, at times, having to endure my Monday morning rants about Manchester United. I would also like to thank the undergraduate students I have been fortunate enough to supervise during my PhD.

I could not have made it through this journey without the love and support from my family. I would like to thank my sister, Elizabeth, for her continuous support and always remaining light-hearted. I would also like to thank my father, Robert, for his continuous support as well. He has always been there for me whenever I have needed to speak to him, which has usually been late at night, due to both of us having to work late on most days. He has also given me a kick up the backside whenever I have needed it, but he frequently reminded me to take breaks as well. Finally, I would to thank my mother, Annette, for always being there for me. Whether it may be for a chat over the phone or making herself available for me to come home for a few days to escape the

Cambridge bubble and make a well needed Sunday roast, she has always supported me with whatever I have needed.

I am grateful to the Department of Engineering for giving me an EPSRC DTP scholarship and to Rolls–Royce plc. for providing top-up funding. I am also grateful to the EPSRC and Selwyn College for providing conference grants. I would like to thank the High Performance Computing Service at the University of Cambridge for maintaining the Darwin and CSD3 facilities. This work used the ARCHER UK National Supercomputing Service (http://www.archer.ac.uk). The UK Consortium on Turbulent Reacting Flows (UKCTRF) led by Prof. Nilanjan Chakraborty is acknowledged for providing resources for ARCHER (e305). The EPSRC is also acknowledged for providing a RAP award for resources on ARCHER (e620). I am grateful to Dr. Wolfgang Meier and Dr. Michael Stöhr from the German Aerospace Centre (DLR) for providing experimental data and for the useful discussions that we have had.

This work is dedicated to my loving parents and to my late Grandad, Ron.

Contents

List of Figures

List of Tables

Nomenclature

Roman symbols

A	Area
a	Strain rate
c	Reaction progress variable
c_p	Specific heat capacity at constant pressure
C_s	Smagorinsky constant
$\mathcal{D}$	Mass diffusion coefficient
E_a	Activation energy
$\boldsymbol{F}$	Force vector
$\mathscr{G}$	LES filter function
h	Total enthalpy (sensible + chemical)
h^*	Normalised enthalpy
Δh^*	Normalised enthalpy deficit
Δh_f^0	Formation enthalpy
$\mathbf{I}$	Identity matrix
k	Turbulent kinetic energy
ℓ	Characteristic eddy length scale
L_R	Recirculation zone length
$\mathcal{M}$	Molecular mass
$\dot{m}$	Mass flow rate
$\hat{\mathbf{n}}$	Normal
P	Probability density function
p	Pressure
$\boldsymbol{q}$	Heat flux vector
$\Re^0$	Universal gas constant
r	Radius
$\boldsymbol{S}$	Symmetric strain rate tensor

S	Swirl number
s	Stoichiometric ratio
s_c	Consumption speed
s_L^0	Laminar flame speed
T	Temperature
t	Time
$\boldsymbol{U}$	Velocity vector
U	Axial velocity
U_r	Radial velocity
U_θ	Azimuthal velocity
u'	Root-mean-square velocity
u'_Δ	Sub-grid velocity scale
$\boldsymbol{x}$	Position vector (x_1, x_2, x_3)
y^+	Dimensionless wall distance
Y_α	Mass fraction of a chemical species α
Z	Passive fluid marker

Dimensionless parameters

Da	Damköhler number
Ka	Karlovitz number
Le	Lewis number
Ma	Mach number
Pr	Prandtl number
Re	Reynolds number
Sc	Schmidt number

Greek symbols

α	Thermal diffusivity
β_c	Flame curvature parameter
Δ	LES filter width
δ_L^0	Laminar flame thickness
ε	Dissipation rate
κ	Heat loss factor
λ	Thermal conductivity
μ	Dynamic viscosity
ν	Kinematic viscosity

ξ	Mixture fraction
ρ	Density
Σ	Flame surface density
σ_φ^2	Variance for a variable φ
$\boldsymbol{\tau}$	Viscous stress tensor
τ	Heat release parameter
τ_c	Chemical time scale
ϕ	Fuel–air equivalence ratio
χ_c	Progress variable scalar dissipation rate
χ_ξ	Mixture fraction scalar dissipation rate
$\dot{\omega}$	Mass based reaction rate

Subscripts

b	Fully burnt conditions
eff	Effective
exp	Experiment
fu	Fuel
L	Laminar
o	Integral length scale
ox	Oxidiser
ref	Reference condition
res	Resolved
sgs	Sub-grid scale
st	Stoichiometric
T	Turbulent/sub-grid
tot	Total
u	Unburnt reactant conditions
η	Kolmogorov scale

Superscripts

R	Residual quantity
r	Anisotropic quantity
0	Reference condition
$+$	Normalised quantity

Operators

$\bar{-}$	Reynolds averaging or LES filtering

$\tilde{}$	Favre averaging or Favre filtering
$\langle\ \rangle$	Time-averaged quantity
T	Transpose

Acronyms

CARS	Coherent Anti-stokes Raman Spectroscopy
CFD	Computational Fluid Dynamics
CFL	Courant–Friedrichs–Lewy
DNS	Direct Numerical Simulation
FGM	Flamelet-Generated Manifold
FPV	Flamelet/Progress Variable
HPC	High Performance Computing
IRZ	Inner Recirculation Zone
LDA	Laser Doppler Anemometry
LDV	Laser Doppler Velocimetry
LES	Large Eddy Simulation
LPP	Lean Premixed Prevaporised
ORZ	Outer Recirculation Zone
PDF	Probability Density Function
PIV	Particle Image Velocimetry
PLIF	Planar Laser-Induced Fluorescence
PVC	Precessing Vortex Core
RANS	Reynolds-Averaged Navier–Stokes
r.m.s.	root-mean-square
RQL	Rich-Quench-Lean
SGS	Sub-Grid Scale
TI	Turbulence Intensity
URANS	Unsteady Reynolds-Averaged Navier–Stokes
WALE	Wall-Adapting Local Eddy

Chapter 1

Introduction

1.1 Combustion in the 21st century

Combustion of fossil fuels has been the focal point of energy production around the world today for thousands of years and it is a means of transforming primary chemical energy into useful secondary mechanical energy. The use of combustion started thousands of years ago with heating for human comfort and the cooking of food (Bilger, 2011). However in the 18th century, the Scottish engineer James Watt proposed one of the first steam engine designs in Glasgow, which produces mechanical power through the use of thermal energy. The working fluid of steam was created by the burning of coal to produce the heat required to boil water. This steam engine was then commercialised around 1775 in Birmingham in collaboration with the English engineer Matthew Boulton and this was one of the most significant advances in technology in the early part of the Industrial Revolution in the United Kingdom. This ubiquitous power source was used during the Industrial Revolution and it allowed factories to be situated anywhere, since previous factories had to be situated by rivers, as they were reliant on water or strong winds to produce power (Allen, 2009; Deane, 1980). The steam engine was later replaced by the gas turbine concept that was invented by Sir Charles Parsons, where the pressurised steam drives an expanding turbine to produce electricity (Richardson, 2014). Furthermore, the first successful internal combustion engine was developed in the early 19th century in Germany during the Industrial Revolution in Europe (Deane, 1980). Before the Second World War, the development of the jet engine was of high interest and Sir Frank Whittle proposed the first jet engine concept during his service in the Royal Air Force (Rolls-Royce, 2015). At present, the internal combustion engine and jet engines on military and commercial aircraft still remain powered by fossil fuels.

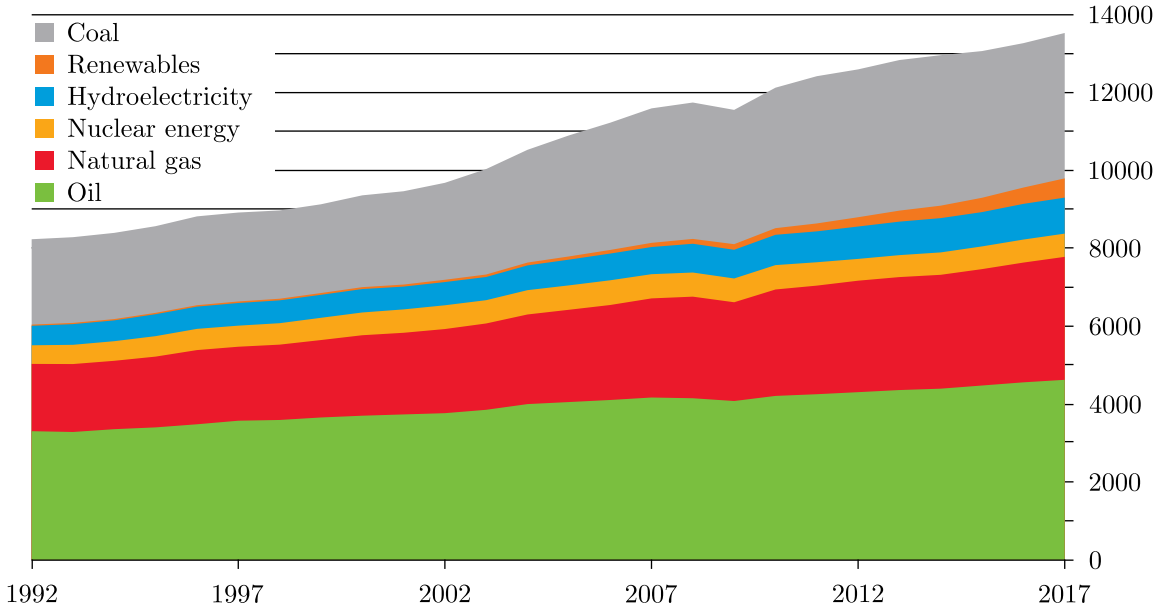

Fig. 1.1 World energy consumption in million tonnes of oil equivalent (BP, 2018).

The burning of fossil fuels today is still primarily used to meet the demand for energy that is required for domestic and industrial use, as well as for transportation purposes. According to the most recent statistical review of energy consumption produced by BP (2018), approximately 85 % of energy consumed was produced by fossil fuels in 2017, as shown in Fig. 1.1. However, the demand for energy is continuously increasing, as also shown in Fig. 1.1. The annual global energy consumption grew by 2.2 % in 2017, which is an increase of 1.2 % from the previous year and 0.5 % higher than the 10 year average. The demand for energy is expected to continually increase, due to the projected increase in the population and GDP. Although renewable energy sources are the fastest growing source of energy, it is expected that energy produced from fossil fuels will also continuously increase up until the projections made towards 2040 (BP, 2019). It is estimated that the reserves of fossil fuels are expected to last for another century and natural gas is also expected to overtake coal as an energy source by 2030 (Bilger, 2011). Therefore, energy that is produced from fossil fuels is expected to remain the dominant source of energy for several decades.

As a consequence of the global increase in burning fossil fuels, this has seen an increase in the amount of pollutants dispersed into the atmosphere in the form of greenhouse gases and other toxic pollutants. Fossil fuels contain carbon and when the fuel is burned with air, the pollutants that are emitted include significant amounts of carbon dioxide (CO_2), as well as nitrogen oxides (NO_x), sulphur oxides (SO_x), unburnt hydrocarbons,

carbon monoxide (CO), particulate matter and soot (Lieuwen & Yang, 2013). Therefore, strict environmental regulations have been introduced to reduce emission levels. For automotive transport, the government in the United Kingdom aims to eliminate the sale of petroleum and diesel vehicles from 2040 (HM Government, 2018). Significant technology advancements have been achieved with reducing emissions with hybrid and electric vehicles. However, such technology is not expected to be available for aviation transport in the near future. Moreover, the service life for an aircraft is expected to be between 20–30 years and therefore, achieving immediate reductions in pollutant emissions is difficult. This poses as a challenge for aircraft manufacturers to produce new technologies, in order to reduce pollutant emissions and comply with the very strict environmental regulations and targets that have been proposed by aviation organisations in Europe and the rest of the world (EASA *et al.*, 2019). The advancement of combustion research must be able to successfully respond to these economic policies and strict environmental restrictions because it is expected that governments will continually tighten these regulations in the future (Bilger, 2011).

Current combustion technologies are unable to simultaneously meet the requirement of reducing emissions while delivering efficiency improvements, but *fuel-lean* combustion has the potential to meet both of these demands. The fuel–air equivalence ratio ϕ is used to describe whether a mixture is lean ($\phi < 1$) or rich ($\phi > 1$). Traditional aero engines operate with Rich-Quench-Lean (RQL) designs. Pressurised air enters the combustion chamber and kerosene is directly injected into the combustion chamber near the air inlet and further downstream, additional air is added to quench the flame and produce a lean mixture at the exit. Swirl vanes are present upstream of the air inlet, as highly swirling flow ensures that fast mixing with the fuel and atomisation of the fuel droplets occurs in the near-field of the air inlet (Lefebvre & Ballal, 2010). Vortex breakdown in the swirling flow occurs further downstream and leads to the formation of a recirculation zone (Syred & Beér, 1974). This recirculation zone contains hot combustion products and radical species, allowing this zone to serve as a constant ignition source for the oncoming fuel–air mixture and improve fuel droplet evaporation times. This is very important when operating under low power conditions, in order to ensure high efficiency combustion. For low power conditions, combustion in the near-field is typically around stoichiometric conditions and the dilution stage of the burner causes the pollutants to include unburnt hydrocarbons and CO, since the temperatures are lower. When operating under high power conditions, the local mixtures in the near-field are more rich and therefore, combustion is closer to stoichiometric conditions in the dilution stage of the

burner (Lefebvre & Ballal, 2010). This leads to the problem of thermal NO_x formation through the Zel'dovich mechanisms, as the rate of NO_x formation increases exponentially with temperature (Williams, 1985*a*). Hence, the residence time in this region should be short to ensure that the thermal NO_x production is minimised. Furthermore, the formation of soot is increased under these high power conditions because the overall equivalence ratio is increased. Therefore, the processes involved in this system are difficult to control, since the rate of mixing governs which pollutants are formed (Lefebvre & Ballal, 2010).

Lean premixed systems on the other hand have the potential of reducing CO_2 and NO_x emissions. Unlike the typical RQL system, the reactants are fully premixed prior to ignition. Premixing the reactants yields shorter flames and allows for the size of the engine to be reduced (Driscoll, 2011). Since the fuel in aero engines is liquid based, the fuel needs to be prevaporised and the degree of premixing is influenced by the degree of prevaporisation. Such combustion systems are referred to as Lean Premixed Prevaporised (LPP) burners. This concept has recently been employed in the GEnx engine on the Boeing 787 aircraft (Jones, 2011). The flames in LPP burners are typically stabilised by inducing swirling flow, as this improves the recirculation of hot combustion products. Bluff body flame holders can also be used in the afterburner region of combustion devices. However, operating under lean premixed conditions leads to the presence of combustion instabilities, which cause close coupling between acoustics, combustion and the swirling flow dynamics (Dowling & Mahmoudi, 2015; Lieuwen, 2012; Matalon, 2009). These instabilities can be detrimental to lean premixed systems and can lead to failed ignition, flashback, autoignition and flame blow-off, where the latter is the complete extinction of the flame. Moreover, it is near impossible to achieve perfect premixing because the mixing time scales are usually larger than the residence time scales for the reactants. Therefore, the combustion is typically in the partially premixed regime (Masri, 2015). These inhomogeneous mixtures can extend the flammability ranges and improve the resistance of the flame to extinction. However, understanding the physical processes that yield partially premixed flames is imperative for the design of such combustion systems (Driscoll, 2011).

1.2 Turbulent combustion modelling

The design of future combustion systems today is reliant on the use of Computational Fluid Dynamics (CFD), which is now on par with experiments as a means for the

research and development of practical combustion systems. The approaches of CFD can be categorised into three topics, which are Direct Numerical Simulation (DNS), Reynolds-Averaged Navier–Stokes (RANS) simulation and Large Eddy Simulation (LES). The use of DNS for practical combustion systems is still not possible, due to the high computational costs that are associated with the approach. The approach is used instead to validate chemistry models and test closure techniques for RANS and LES approaches. Steady RANS and Unsteady RANS (URANS) techniques have been developed as a computationally inexpensive alternative and are advantageous, due to their capability of modelling complex geometries with a significantly lower computational cost. In addition, geometric simplifications, such as axisymmetric analyses, can be used because turbulence is assumed to be isotropic. However, the approach only solves the governing conservation equations for the mean flow variables and the turbulence length and time scales are much larger than the smallest scales of turbulent fluctuations. This means that RANS simulations cannot capture highly unsteady phenomena, such as extinction and flame blow-off. Hence, there has been an emergence of LES approaches for modelling turbulent combustion over the last two decades, since such approaches can capture the transient phenomena exhibited by turbulent flames. These simulations can also satisfy the 20 hr turnaround time that is recommended for CFD to be a successful design tool for industry (Bilger, 2011).

In the LES framework, the large scales of turbulence are obtained by fully resolving the flow field down to a cut-off scale based on a filter width Δ. The remaining scales of turbulence, which are known as being in the Sub-Grid Scale (SGS) region, are modelled by using closure models for the unresolved residual stress and scalar flux terms. It was recommended by Pope (2000) that an acceptable LES should resolve at least 80 % of the turbulent kinetic energy across the flow domain. Since the flame thickness is expected to be smaller than the filter width, this means that a model must be assigned for modelling the flame. Combustion itself is complex, since the chemical kinetics within the flame involves hundreds of species and thousands of elementary reactions. In addition, swirling flows in practical combustion systems are highly turbulent and there are a wide range of length and time scales. Therefore, the interactions between turbulence and combustion cause turbulent combustion to be an extremely complex phenomenon and hence, accurately modelling turbulent combustion is challenging. Partially premixed flames are very complex owing to the presence of compositionally inhomogeneous mixtures and propagating flame fronts. Premixed flames propagate as waves through reactant mixtures, whereas non-premixed regions cannot propagate and hence, the two regions are

governed by different physics. Premixed flames are inherently more difficult to stabilise in high speed flows than non-premixed flames. As previously mentioned, premixed combustion systems employ bluff body flame holders and/or swirling flows to stabilise the flames through the recirculation zones that are formed. Therefore, it is crucial that the development of combustion models are able to accurately capture the stabilisation of flames through these mechanisms. Furthermore, combustion models should also be able to capture the combustion instabilities that arise from acoustic perturbations and other detrimental phenomena to combustion systems, such as failed ignition and flame blow-off.

1.3 Aims and objectives

The last two decades has seen numerous approaches be proposed for the LES of turbulent combustion; these models can be separated into phenomenological, geometric and statistical models (Gicquel *et al.*, 2012). In this work, a presumed joint Probability Density Function (PDF) approach with tabulated chemistry using laminar flamelets is used to model the turbulent reaction rate. The partially premixed reaction rate source term contains premixed and non-premixed contributions and therefore, the joint PDF is parameterised using the progress variable and mixture fraction (Chen, 2017; Langella, 2016; Ruan, 2013). Numerous studies of jet flames (Chen *et al.*, 2017; Langella & Swaminathan, 2016; Langella *et al.*, 2016*b*) and of flames stabilised behind bluff bodies (Langella *et al.*, 2016*a*) with this approach have been undertaken. Studies of flames in gas turbine model combustors with and without acoustic oscillations have also been undertaken (Chen *et al.*, 2019*a*,*b*; Langella *et al.*, 2018*a*). However, studies of flames close to the lean flammability are yet to be explored with the combustion modelling used in the aforementioned studies. Thus, the overall aim of this work is to further assess the ability of the combustion modelling for accurately capturing the stabilisation of lean flames in bluff body and swirling flow configurations. This work is undertaken with a long-term objective of predicting the complete blow-off of flames in bluff body and swirl stabilised burners. The specific aims of this work are as follows:

1. To simulate and validate a bluff body stabilised premixed flame that is exposed to ambient conditions and compare the spatial evolution of the shear layers and the flame brush to confined bluff body stabilised flames of low and high turbulence intensity at a similar equivalence ratio.

2. To analyse a set of premixed flames that are stabilised behind a bluff body and enclosed within a combustion chamber and to elucidate the influence of altering the inlet conditions, i.e., the turbulence intensity and the fuel–air equivalence ratio, on the recirculation zone length. The observations are used to deduce a scaling relation for the recirculation zone length as a function of these inlet conditions.

3. To simulate flames close to blow-off in a gas turbine model combustor and to determine the physical processes influencing the stabilisation of the flame, including the transient phenomena associated with the flame.

4. To investigate the effects of including heat loss within the modelling framework on the flame stabilisation processes. This is important, as the influence of heat loss on the stabilisation of lean flames is unclear. This is achieved by introducing non-adiabatic boundary conditions and implementing non-adiabatic flamelets in the combustion modelling framework.

1.4 Thesis outline

A broad overview of turbulent combustion is presented in Chapter 2. This includes the governing equations for combustion, along with a description of the different types of combustion. A description of turbulence and its influence on combustion follows this.

The relevant modelling approaches for CFD are outlined in Chapter 3 with a focus on LES modelling. The governing equations for the LES framework are presented including closure models for the unresolved residual stress and scalar flux terms. An overview of the state-of-the-art filtered reaction rate closure for premixed and partially premixed flames is provided. This chapter concludes with a description of the CFD solvers that are used in this thesis.

Descriptions of the test cases that are studied in Chapters 5–8 are presented in Chapter 4. The burner configuration and its computational grid are shown with descriptions of the boundary conditions and the LES set-up for all test cases. The isothermal flow LES results are compared against the available experimental data, in order to validate the flow field and ensure that the turbulent kinetic energy fields are well resolved.

The results of a bluff body stabilised premixed flame exposed to ambient conditions are presented in Chapter 5. The general features of these flames are compared with the experimental observations and the time-averaged velocity statistics are also compared with the experimental data. The flame is analysed further by comparing the relative

positioning of the shear layer and flame brush with two flames of low and high turbulence intensity that are enclosed within a combustion chamber.

The next set of results contained in Chapter 6 is for a set of isothermal and reacting flow simulations within a combustion chamber that contains a bluff body flame holder. The recirculation zone is analysed to observe the effect of changing the inlet turbulence intensity and the equivalence ratio. Force balances are undertaken on the recirculation zone to determine which forces influence its structure and to deduce a scaling relation for the recirculation zone length as a function of the inlet conditions. The application of this scaling relation to open flames and backward facing step configurations is also explored.

A more complex burner resembling a main burner in a gas turbine system is studied in Chapter 7. A swirl-stabilised flame in a gas turbine model combustor that is close to the lean blow-off limit is analysed. Detailed comparisons with the measurements are shown. The stabilisation mechanisms of the flame and its unstable phenomena during a lift-off event are analysed on a physical basis.

Chapter 8 contains simulations of the same configuration, which include heat loss within the modelling. These simulations include non-adiabatic wall conditions, where one of these also includes non-adiabatic effects within the combustion modelling. The results obtained are compared with the fully adiabatic simulation contained in Chapter 7.

This thesis concludes with Chapter 9, where the key findings are summarised and some recommendations for future work are proposed.

Chapter 2

Background on Turbulent Combustion

Turbulent combustion is a complex physical phenomenon, due to the presence of strong temperature and density gradients, and turbulence. The full description of the chemistry in a laminar flame involves hundreds of chemical species and thousands of elementary reactions (Peters, 2000). However, the flame in a turbulent environment is influenced by the wide range of the length and time scales associated with the vortical structures in turbulent flows. Turbulent combustion is the result of the two-way interactions between turbulence and combustion and these interactions affect the properties of a flame, such as its rate of propagation and surface area (Poinsot & Veynante, 2012). Therefore, a good understanding of turbulent combustion is required, in order to accurately capture these interactions. This chapter will present the conservation equations for flows with combustion, along with an overview of turbulence and the different turbulent combustion regimes.

2.1 Instantaneous balance equations

The set of equations that describe chemically reacting flows are different to constant density non-reacting flows. The production and consumption rates of the various species in the multi-component gas mixtures require modelling. In addition, a detailed thermodynamic and transport database must be included. The conservation equations required for reacting flows are for mass, momentum, chemical species (using mass fractions) and energy (either in the form of temperature and sensible or total enthalpy). Before these

are presented, the classical assumptions commonly made to simplify these equations are outlined.

For this work, gaseous combustion of low hydrocarbon fuels with air in subsonic flows (Mach numbers of Ma < 1) at atmospheric pressure is considered. The gas mixture is treated as Newtonian, where a linear dependence on the local strain rate is assumed. Gravitational and other body forces (per unit volume) are neglected from the momentum equation. Soret (the molecular species diffusion is dependent upon temperature gradients) and Dufour (the heat flux is dependent upon mass fraction gradients) effects are also neglected (Pope, 1987). Fick's law of diffusion is used to model the diffusive flux of each chemical species; the diffusion velocities can be obtained using a more rigorous approach, as shown by Williams (1985*a*), using multi-component diffusion based on the Hirschfelder and Curtiss approximation (Hirschfelder *et al.*, 1954). Furthermore, the propagation speed of the flame is much smaller than the speed of sound and hence, the pressure across the flame is assumed to be constant (Williams, 1985*a*). Compressibility effects are neglected and the contributions of pressure and viscous effects in the energy equation are neglected; radiation heat transfer effects are also neglected in the energy equation. Finally, the gas is treated as a perfect gas and the equation of state is used.

The instantaneous balance equations can be written in various forms[1] but they are written here as (Kuo, 2005; Peters, 2000; Poinsot & Veynante, 2012; Williams, 1985*a*)

Continuity:

$$\frac{\partial \rho}{\partial t} + \boldsymbol{\nabla} \cdot \Big(\rho \boldsymbol{U}\Big) = 0\,, \tag{2.1}$$

where ρ and $\boldsymbol{U}$ denote the mixture density and the velocity vector respectively.

Momentum:

$$\frac{\partial}{\partial t}\Big(\rho \boldsymbol{U}\Big) + \boldsymbol{\nabla} \cdot \Big(\rho \boldsymbol{U}\boldsymbol{U}\Big) = -\boldsymbol{\nabla} p + \boldsymbol{\nabla} \cdot \boldsymbol{\tau}\,, \tag{2.2}$$

where p represents the pressure. The viscous stress tensor $\boldsymbol{\tau}$ is

$$\boldsymbol{\tau} = \mu \left[\boldsymbol{\nabla}\boldsymbol{U} + \Big(\boldsymbol{\nabla}\boldsymbol{U}\Big)^{\intercal} - \frac{2}{3}\Big(\boldsymbol{\nabla} \cdot \boldsymbol{U}\Big)\mathbf{I}\right], \tag{2.3}$$

[1] The gradient for a scalar or a single component of a vector $\boldsymbol{\nabla}\varphi_1 = (\partial\varphi_1/\partial x_1)\,\mathbf{i} + (\partial\varphi_1/\partial x_2)\,\mathbf{j} + (\partial\varphi_1/\partial x_3)\,\mathbf{k}$ and the divergence for a vector $\boldsymbol{\nabla} \cdot \boldsymbol{\varphi} = \partial\varphi_1/\partial x_1 + \partial\varphi_2/\partial x_2 + \partial\varphi_3/\partial x_3$ are presented in vector notation throughout. Using the Einstein summation notation, these are written as $\boldsymbol{\nabla}\boldsymbol{\varphi} \equiv \partial\varphi_i/\partial x_i$ and $\boldsymbol{\nabla} \cdot \boldsymbol{\varphi} \equiv \partial\varphi_j/\partial x_j$ respectively.

where μ is the molecular dynamic viscosity, the superscript '$\intercal$' is the transpose operator and $\mathbf{I}$ is the identity matrix.

Species transport:

$$\frac{\partial}{\partial t}\left(\rho Y_\alpha\right) + \boldsymbol{\nabla}\cdot\left(\rho \boldsymbol{U} Y_\alpha\right) = \dot{\omega}_\alpha + \boldsymbol{\nabla}\cdot\left(\rho \mathcal{D}_\alpha \boldsymbol{\nabla} Y_\alpha\right), \tag{2.4}$$

where Y_α is the mass fraction for a chemical species α, $\mathcal{D}_\alpha$ is the species mass diffusivity and $\dot{\omega}_\alpha$ is the mass based species production or consumption rate. Three dimensionless parameters are used to characterise molecular transport, namely the *Prandtl*, *Schmidt* and *Lewis* numbers. These are expressed as

$$\mathrm{Pr} = \frac{\mu c_p}{\lambda} = \frac{\nu}{\alpha}, \quad \mathrm{Sc}_\alpha = \frac{\mu}{\rho \mathcal{D}_\alpha} = \frac{\nu}{\mathcal{D}_\alpha} \quad \text{and} \quad \mathrm{Le}_\alpha = \frac{\lambda}{\rho c_p \mathcal{D}_\alpha} = \frac{\mathrm{Sc}_\alpha}{\mathrm{Pr}}, \tag{2.5}$$

where c_p is the specific heat capacity at constant pressure, λ is the thermal conductivity, α is the thermal diffusivity and ν is the kinematic viscosity of the gas mixture. For simplicity, the mass diffusivity is assumed to take a common value for all species in the gas mixture. Therefore, it follows that $\mathrm{Sc} = \mathrm{Sc}_\alpha$ and $\mathrm{Le} = \mathrm{Le}_\alpha$ for all species. Furthermore, the Lewis number is assumed to be unity, which is typical in turbulent combustion analyses (Poinsot & Veynante, 2012), and this implies that $\mathrm{Sc} = \mathrm{Pr}$ for all of the species.

Energy (in terms of enthalpy):

$$\frac{\partial}{\partial t}\left(\rho h\right) + \boldsymbol{\nabla}\cdot\left(\rho \boldsymbol{U} h\right) = -\boldsymbol{\nabla}\cdot\boldsymbol{q}, \tag{2.6}$$

where h is the total enthalpy (the sum of the sensible and chemical enthalpies), otherwise referred to as the thermochemical enthalpy, of the system and this is expressed as

$$\begin{aligned} h &= \underbrace{\int_{T_0}^{T}\left(\sum_{\alpha=1}^{N} Y_\alpha c_{p,\alpha}\right)\mathrm{d}T}_{\text{Sensible}} + \underbrace{\sum_{\alpha=1}^{N} Y_\alpha \Delta h^0_{f,\alpha}}_{\text{Chemical}} \\ &= \int_{T_0}^{T} c_p \,\mathrm{d}T + \Delta h^0_f, \end{aligned} \tag{2.7}$$

where Δh^0_f represents the formation enthalpy of the gas mixture.

The heat flux vector is given as (Swaminathan & Bray, 2011*a*; Turns, 2011)

$$\boldsymbol{q} = -\lambda \boldsymbol{\nabla} T - \rho \mathcal{D} \sum_{\alpha=1}^{N} h_\alpha \boldsymbol{\nabla} Y_\alpha \,, \tag{2.8}$$

where the mass diffusivity again takes a common value for all species. The first and second terms on the right-hand side of Eq. (2.8) are the heat conduction and species diffusion contributions respectively to the heat flux vector. The latter term is decomposed using the chain rule as

$$\begin{aligned} \rho \mathcal{D} \sum_{\alpha=1}^{N} h_\alpha \boldsymbol{\nabla} Y_\alpha &= \rho \mathcal{D} \boldsymbol{\nabla} \left(\sum_{\alpha=1}^{N} h_\alpha Y_\alpha \right) - \rho \mathcal{D} \sum_{\alpha=1}^{N} Y_\alpha \boldsymbol{\nabla} h_\alpha \\ &= \rho \mathcal{D} \boldsymbol{\nabla} h - \rho \mathcal{D} \sum_{\alpha=1}^{N} Y_\alpha c_{p,\alpha} \boldsymbol{\nabla} T \\ &= \rho \mathcal{D} \boldsymbol{\nabla} h - \rho \mathcal{D} c_p \boldsymbol{\nabla} T \,. \end{aligned} \tag{2.9}$$

Substituting Eq. (2.9) into Eq. (2.8) and writing the thermal conductivity as $\lambda = \rho \alpha c_p$ yields the following result (Turns, 2011)

$$\boldsymbol{q} = - \underbrace{\rho \alpha c_p \boldsymbol{\nabla} T}_{\substack{\text{Flux of sensible} \\ \text{enthalpy due to} \\ \text{conduction}}} - \underbrace{\rho \mathcal{D} \boldsymbol{\nabla} h}_{\substack{\text{Flux of absolute} \\ \text{enthalpy due to} \\ \text{species diffusion}}} + \underbrace{\rho \mathcal{D} c_p \boldsymbol{\nabla} T}_{\substack{\text{Flux of sensible} \\ \text{enthalpy due to} \\ \text{species diffusion}}} \,. \tag{2.10}$$

A physical interpretation for the heat flux vector is now shown in Eq. (2.10). However since the Lewis number is assumed to be unity, the first and third terms on the right-hand side of Eq. (2.10) cancel and hence, the heat flux vector is $\boldsymbol{q} = -\rho \mathcal{D} \boldsymbol{\nabla} h$. Therefore, the transport equation for the thermochemical enthalpy in Eq. (2.6) is rewritten as

$$\frac{\partial}{\partial t} \big(\rho h \big) + \boldsymbol{\nabla} \cdot \big(\rho \boldsymbol{U} h \big) = \boldsymbol{\nabla} \cdot \big(\rho \alpha \boldsymbol{\nabla} h \big) \,, \tag{2.11}$$

where $\alpha = \mathcal{D}$ is taken due to the unity Lewis number assumption.

Equation of state:

$$p = \rho \Re^0 T \sum_{\alpha=1}^{N} \frac{Y_\alpha}{\mathcal{M}_\alpha} \,, \tag{2.12}$$

where $\Re^0 = 8.3145\,\mathrm{kJ/kg\,K}$ is the molar universal gas constant and $\mathcal{M}_\alpha$ is the molecular mass for a chemical species.

The solution of the balance equations shown here is sufficient to provide a solution for a reacting flow system. However, these equations must be replaced by a modified form for turbulent combustion. Turbulent combustion is nearly always present in practical combustion systems (Lieuwen, 2012). It is impossible to understand turbulent combustion without a good knowledge of laminar flame theory. The mixing of reactants prior to ignition yields the properties of the laminar flame and this modifies the reacting flow field. Therefore before considering turbulent reacting flows, some important notions of laminar flame theory are presented next.

2.2 Types of flames

A chemical reaction in combustion between a fuel and an oxidiser is accompanied by a flame and the classification of the flame is dependent on how the reactants are mixed prior to ignition. The chemical reaction may be in the form (Law, 2006)

$$\sum_{\alpha=1}^{N} \nu'_{\alpha} \mathcal{M}_{\alpha} \rightleftharpoons \sum_{\alpha=1}^{N} \nu''_{\alpha} \mathcal{M}_{\alpha} \,, \tag{2.13}$$

where ν'_{α} and ν''_{α} are the corresponding molar concentration coefficients for the reactants and products species respectively. Although the chemical reaction equations are consistent for different flames, the initial and boundary conditions set for the combustion system can cause different flames to exist. The flames here are separated into three categories, which are non-premixed, premixed and partially premixed flames (Peters, 2000).

2.2.1 Non-premixed flames

A *non-premixed flame*, or sometimes referred to as a diffusion flame, is present when the fuel and oxidiser enter the combustion chamber through separate inlets (Bilger, 1976*a*). The description of a non-premixed flame was first provided by Burke & Schumann (1928) of a Bunsen flame. The reaction zone of the flame lies between the fuel and oxidiser, which must be transported fast enough to the reaction zone to ensure a flame can be sustained. The molecular diffusion of the species towards the reaction zone controls the burning rate and hence, this influences the rate of heat release out of the reaction zone (Peters, 1984). In addition, non-premixed flames have no propagation mechanism and the thickness of the reaction and mixing zones are controlled by the mixing of the chemical species. The position of the flame is controlled by the local flow field and buoyancy forces.

The flame remains attached to the stoichiometric surface between the fuel and oxidiser and no flame will occur beyond this position, as the mixture will be either too lean or too rich to burn (Veynante & Vervisch, 2002).

Since the rate of mixing influences the heat release of the flame and the chemical time scales are much smaller in comparison to the convection and diffusion time scales, a variable to describe this mixing of the chemical species is introduced. This is a conserved scalar, which represents the mixing between the fuel and oxidiser, and this is known as the *mixture fraction*. This is expressed as (Bilger, 1980; Spalding, 1979)

$$\xi = \frac{sY_{\mathrm{fu}} - Y_{\mathrm{ox}} + Y_{\mathrm{ox},2}}{sY_{\mathrm{fu},1} + Y_{\mathrm{ox},2}}\,, \tag{2.14}$$

where the subscripts 'fu' and 'ox' denote the fuel and oxidiser mass fractions respectively, which are accompanied by subscripts '1' and '2' to represent the reactant streams for pure fuel and oxidiser respectively. The coefficient s is the stoichiometric ratio and is calculated using $s = \nu'_{\mathrm{ox}}\mathcal{M}_{\mathrm{ox}}/\nu'_{\mathrm{fu}}\mathcal{M}_{\mathrm{fu}}$. Bilger (1988) later proposed a more detailed definition for the mixture fraction, which is written as

$$\xi = \frac{\beta - \beta_2}{\beta_1 - \beta_2}\,, \tag{2.15}$$

where $\beta = 2Y_{\mathrm{C}}/\mathcal{M}_{\mathrm{C}} + Y_{\mathrm{H}}/2\mathcal{M}_{\mathrm{H}} - Y_{\mathrm{O}}/\mathcal{M}_{\mathrm{O}}$ and the subscripts 'C', 'H' and 'O' respectively represent carbon, hydrogen and oxygen atoms.

The transport equation for the mixture fraction is the balance between convection and diffusion processes and is expressed as

$$\frac{\partial}{\partial t}\big(\rho\xi\big) + \boldsymbol{\nabla}\cdot\big(\rho\boldsymbol{U}\xi\big) = \boldsymbol{\nabla}\cdot\big(\rho\mathcal{D}\,\boldsymbol{\nabla}\xi\big)\,, \tag{2.16}$$

where the boundary conditions for the fuel and oxidiser are $\xi_{\mathrm{fu}} = 1$ and $\xi_{\mathrm{ox}} = 0$ respectively. It should be noted that this is a simplified form as a single molecular diffusion term $\mathcal{D}$ is taken for all species, as described previously in § 2.1. For laminar non-premixed flames, the time scales for convection and diffusion processes are of the same orders of magnitude, but the chemical time scales are much smaller (Peters, 1984). Hence, it follows that the chemistry is assumed to be fast and Eq. (2.16) is used for a laminar non-premixed flame, whereby such an assumption is known as treating the flame as a *flamelet*. A characteristic diffusion time scale can be determined by introducing an important property known as the *scalar dissipation rate*, which has the dimensions of 1/s. Therefore, the diffusion

time is estimated as the inverse of the scalar dissipation rate of the mixture fraction as $\tau_\xi \approx \chi_\xi^{-1}$. The scalar dissipation rate is given as (Bilger, 1976*a*)

$$\chi_\xi = \mathcal{D}\Big(\boldsymbol{\nabla}\xi \cdot \boldsymbol{\nabla}\xi\Big)\,. \tag{2.17}$$

The scalar dissipation rate is a very important quantity for non-premixed flames, as it represents the molecular mixing rate through the mixture fraction gradient. When the curvature for the iso-contours of ξ is small, the gradients in mixture fraction space along the stoichiometric surface are small in comparison to the gradients in the direction normal to the stoichiometric surface. Bilger (1976*a*) discovered that under fast chemistry assumptions (the reaction takes place within a sheet along the stoichiometric mixture fraction contour), the reaction rate is directly related to the scalar dissipation rate at stoichiometric conditions. The scalar dissipation rate at the stoichiometric mixture fraction χ_{st} describes the departure from chemical equilibrium (Pitsch & Steiner, 2000*b*). Including unsteady effects, the transport equation for a chemical species in mixture fraction space is written as (Peters, 1986)

$$\rho\frac{\partial Y_\alpha}{\partial t} = \rho\chi_{\mathrm{st}}\frac{\partial^2 Y_\alpha}{\partial \xi^2} + \dot{\omega}_\alpha\,. \tag{2.18}$$

The reaction rate source term $\dot{\omega}_\alpha$ in Eq. (2.18) is one of the most fundamental and important properties of the flame, since it represents the rate that a reactant species is consumed, or the rate a product species is produced. The reaction rate is dependent on the chemical system that is being analysed, such as the composition of the fuel and the equivalence ratio of the reactant mixture (Cant & Mastorakos, 2008). Reactions usually proceed through a series of elementary reactions, which is known as a chemical mechanism (Kuo, 2005).

Consider, for illustration purposes, the reaction $\mathrm{M_{fu}} + \mathrm{M_{ox}} \rightarrow \mathrm{M}_P$, where 1 kg of fuel $\mathrm{M_{fu}}$ reacts with s kg of oxidiser $\mathrm{M_{ox}}$ to produce $(1+s)$ kg of products M_P. The reaction rate of the fuel is expressed as (Kuo, 2005)

$$\dot{\omega}_{\mathrm{fu}} = -\rho^2\nu'_{\mathrm{fu}}\mathcal{M}_{\mathrm{ox}}^{-1}Y_{\mathrm{fu}}Y_{\mathrm{ox}}\mathcal{A}\,\exp\left(-\frac{E_a}{\Re^0 T}\right), \tag{2.19}$$

where $\mathcal{A}$ represents the frequency of molecular collisions (Bilger, 1980) and the activation energy is denoted using E_a.

2.2.2 Premixed flames

The reactants for a *premixed flame* are sufficiently mixed to achieve a compositionally homogeneous mixture at a low temperature before ignition and this causes a short and well-defined flame to exist (Peters, 2000). This involves having a characteristic mixing time that must be small in comparison to a time scale representing the rate of chemical reaction under the condition at which mixing occurs, in order to ensure complete mixing is achieved (Bray, 1980). For the non-premixed flame described thus far, the flame lies between the fuel and oxidiser. The convection and molecular diffusion processes, along with the underlying chemical mechanisms, are identical to a premixed flame. Hence, the difference between these two flames are the initial conditions of the reactants prior to ignition.

A typical schematic for a one-dimensional laminar premixed flame is shown in Fig. 2.1. The flame typical consists of three regions, namely the preheat, reaction and equilibrium zones (Law, 2006). The preheat zone contains the unburnt premixed reactant mixture that is gradually heated up through conduction out of the reaction zone. No chemical reaction takes place within the reaction zone and therefore, convection and diffusion processes are dominant and balance one another. When the reactant mixture reaches the ignition temperature, chemical reactions take place and convert the reactant mixture into burnt products. This process is contained within the reaction zone, which is a much thinner region in comparison to the preheat zone. The region beyond the reaction zone is known as the equilibrium zone, as no chemical reaction takes place within the mixture of fully burnt products.

If the steady continuity equation is considered across the flame, then the mass flux is $\rho U = \rho_u s_L^0$, where U is the axial velocity and ρ_u is the unburnt reactant mixture density. The additional term that is denoted as s_L^0 and also marked in Fig. 2.1 is the laminar flame speed. This speed represents the rate of propagation of the flame through a reactant mixture and this yields a crucial difference between premixed and non-premixed flames, as non-premixed flames cannot propagate through a mixture (Law, 2006). Premixed flames propagate in the direction that is normal to the flame front (Pope, 1987). This laminar flame speed is dependent on the thermochemical properties of the reactant mixture. For example, methane–air and propane–air mixtures typically have peak laminar flame speeds of around 0.4 m/s, whereas hydrogen–air mixtures have a much higher flame speed of around 3 m/s (Egolfopoulos & Law, 1990; Vagelopoulos & Egolfopoulos, 1998; Vagelopoulos *et al.*, 1994).

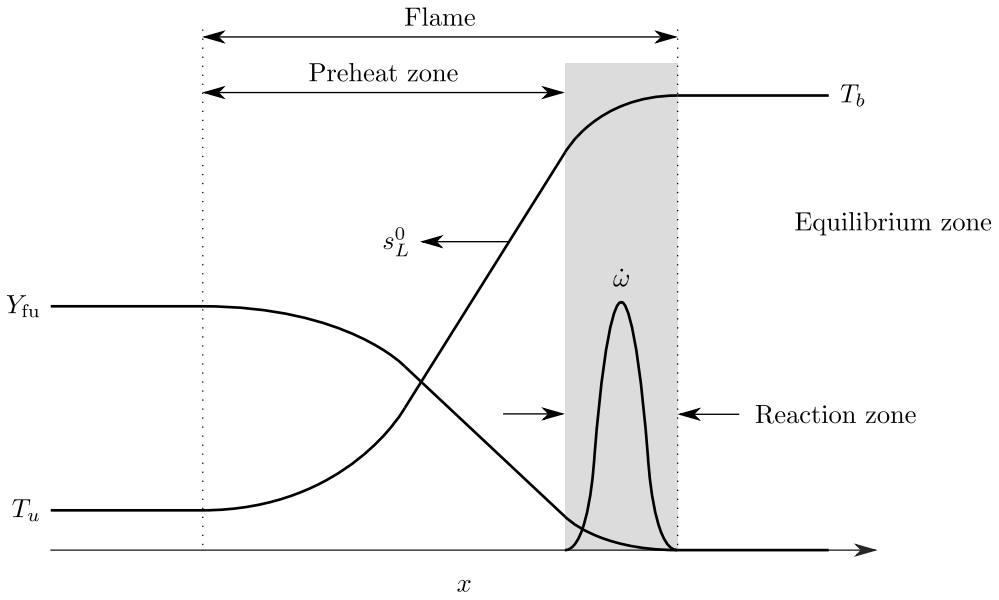

Fig. 2.1 Typical structure of a one-dimensional unstrained laminar premixed flame (Law, 2006).

For unstrained laminar premixed flames, the flame speed can be obtained in numerous ways (Poinsot & Veynante, 2012; Pope, 1988). One approach is based on treating the flame speed as the consumption speed, which is obtained by integrating the fuel reaction rate over a one-dimensional section between the fresh gases and products that is normal to the propagating flame front. Therefore, this is a global value for the laminar flame speed and is written as (Poinsot & Veynante, 2012)

$$s_L^0 = -\frac{1}{\rho_u Y_{\text{fu},u}} \int_{-\infty}^{\infty} \dot{\omega}_{\text{fu}} \, \mathrm{d}\hat{\mathbf{n}} \,. \tag{2.20}$$

Another important property of premixed flames is the flame thickness, as it provides a characteristic length scale for the flame. Multiple definitions have been proposed to estimate the flame thickness (Blint, 1986). The first definition is derived from scaling laws and uses the thermal properties of the flame. This is given as (Bray, 1980)

$$\delta_L^0 = \frac{\lambda}{\rho c_p s_L^0} = \frac{\alpha}{s_L^0} \,. \tag{2.21}$$

This definition is only valid if the Prandtl and Schmidt numbers are close to unity (Cant & Mastorakos, 2008). In general, this expression only serves as an approximation and can significantly underestimate the flame thickness (Poinsot & Veynante, 2012). Alternatively, the flame thickness can be determined by the use of temperature gradients

according to

$$\delta_L^0 = (T_b - T_u) \left| \frac{\mathrm{d}T}{\mathrm{d}x} \right|_{\max}^{-1}, \tag{2.22}$$

where the subscripts 'b' and 'u' representing fully burnt and unburnt conditions respectively. The expression shown in Eq. (2.22) is known as the thermal thickness (Poinsot & Veynante, 2012). The definition is different to Eq. (2.21) because it includes the effects of heat release and heat conduction (Blint, 1986). However, a numerical solution is required to evaluate the flame thickness using Eq. (2.22) because it requires knowledge of the temperature gradient. Blint (1986) proposed a correlation to estimate the flame thickness without a solution and this is given as

$$\delta_L^b = 2\frac{\lambda}{\rho c_p s_L^0}(1+\tau)^{0.7}. \tag{2.23}$$

The heat release parameter is expressed as $\tau = \rho_u/\rho_b - 1$ (Bray *et al.*, 1985), which can also be calculated using the temperature as $\tau = T_b/T_u - 1$, since the pressure is treated as constant across the flame (Williams, 1985*a*). Equation (2.23) assumes that the Prandtl number and the specific heat capacity are constant for the mixture and suggests that the Blint thickness of a flame corresponds to the thermal thickness of the product mixture (Blint, 1986).

A normalised variable can be used to describe how burnt a premixed mixture is. This variable is known as a *reaction progress variable* and takes a value of zero for a fresh reactant mixture and rises monotonically to unity, which represents a fully burnt mixture. When the flame is treated as adiabatic and has a Lewis number close to unity, it is possible to express the reaction progress variable Θ as a normalised function of temperature between the reactant and product temperature. This is expressed as (Cant & Mastorakos, 2008)

$$\Theta = \frac{T - T_u}{T_b - T_u}. \tag{2.24}$$

This definition becomes invalid when the temperature is affected by external factors to the flame, such as heat loss, acoustic perturbations or differential transport of heat and mass. Therefore, using the temperature to define a progress variable is not recommended (Cant, 2011). Using species mass fractions to define the progress variable is preferred, since this offers more flexibility. The reaction progress variable c based on a species mass

fraction Y_α is written in the form

$$c = \frac{Y_\alpha - Y_{\alpha,u}}{Y_{\alpha,b} - Y_{\alpha,u}} \,. \tag{2.25}$$

It is possible to define the progress variable as a single or linear combination of species mass fractions; different definitions are reviewed by Ihme *et al.* (2012) and Fiorina *et al.* (2015). In this work, the progress variable for methane–air combustion is determined using the linear combination of CO and CO_2 mass fractions following previous studies (Chen *et al.*, 2017; Fiorina *et al.*, 2003; Langella *et al.*, 2018*a*; Ruan *et al.*, 2015). This choice of mass fractions allows for a unique mapping of flamelet quantities with the normalised progress variable (Fiorina *et al.*, 2003).

Replacing the species mass fraction in its transport equation, shown in Eq. (2.4), with the progress variable makes it viable to find the thermochemical state of the mixture across the flow domain (Bray *et al.*, 1985). Furthermore, the reaction rate $\dot{\omega}$ is taken as the net production rate of the chosen species for the progress variable and is used as a global value for the flame. The progress variable transport equation is given as (Bray, 1980)

$$\frac{\partial}{\partial t}\big(\rho c\big) + \boldsymbol{\nabla} \cdot \big(\rho \boldsymbol{U} c\big) = \dot{\omega} + \boldsymbol{\nabla} \cdot (\rho \mathcal{D}\, \boldsymbol{\nabla} c) \,. \tag{2.26}$$

Transporting the progress variable was proposed as an alternative approach to solving the transport equations for each of the numerous species in a typical chemical mechanism and modelling each chemical source term (Bray & Libby, 1976; Bray & Moss, 1977; Libby & Bray, 1977). Transporting the progress variable is convenient and widely used for turbulent flame simulations, since the detailed chemical processes are mapped to a reduced system of two scalars. These are the mixture fraction, which tracks the mixing of fuel and oxidiser, and the progress variable, which tracks the global extent of reaction of the local mixture.

2.2.3 Partially premixed flames

There have been two extreme cases described thus far of how the reactants are mixed prior to ignition. This is useful for academic purposes, but in practical combustion systems there is usually a degree of unavoidable mixing between the fuel and oxidiser prior to ignition, which is due to turbulence. This includes applications, such as gas turbine engines and direct injection engines (Peters, 2000), where perfect mixing is restricted, due to the presence of combustion instabilities and size restrictions that prevent perfect mixing

(Masri, 2015). Therefore, compositionally inhomogeneous mixtures are present, which cause different flames to be present and these are referred to as *partially premixed flames* (Bilger, 2000). A mixture that is partially premixed contains pockets of a compositionally inhomogeneous mixture that covers a range of the flammability limits, as well as mixtures that are outside of the flammability range. Introducing high levels of partial premixing can cause new flames to be present, such as triple flames (sometimes referred to as tri-branchial flames), and show different features in comparison to non-premixed and premixed flames (Buckmaster & Matalon, 1988; Domingo & Vervisch, 1996; Peters, 2000; Sohrab *et al.*, 1984). Nonetheless, the premixing of the reactants is compositionally inhomogeneous and far from the degree of mixing in premixed flames (Bilger, 2000).

Partially premixed flames can be separated into two categories, which are distinguished by their mixture fraction range. The first of these is *stratified flames*, which are typically present in premixed configurations (Lipatnikov, 2017). These flames are able to propagate through a compositionally inhomogeneous mixture that is within the flammability limits in mixture fraction space (Bilger *et al.*, 2005). Stratification is also beneficial, since the presence of compositionally inhomogeneous mixtures may extend the flammability limits (Birch *et al.*, 1979; Mastorakos, 2009). These have been investigated experimentally in multi-slot burner configurations at Darmstadt (Kuenne *et al.*, 2012; Seffrin *et al.*, 2010), and the burner developed at Cambridge and Sandia National Laboratories (Anselmo-Filho *et al.*, 2009; Barlow *et al.*, 2009; Sweeney *et al.*, 2011, 2012*a*,*b*). The other case is when the partially premixed flames have compositionally inhomogeneous mixtures that are within and beyond the flammability limits. A typical example of this is a turbulent jet diffusion flame, where fuel enters through a nozzle into a quiescent environment of air. For a low jet exit velocity, the flame is attached to the nozzle and if the velocity is increased, the flame is stretched and eventually the flame lifts off and stabilises further downstream within the jet region (Peters, 2000). However, such flames are more prone to blow-off than anchored flames. These flames have been studied and reviewed in significant detail (Buckmaster, 2002; Kalghatgi, 1984; Lawn, 2009; Lyons, 2007; Mansour, 2003).

Lifted flames are commonly used in gas turbine systems with ubiquitous swirling flows, since the use of swirl increases the robustness of the flame root and extends the flammability limits (Candel *et al.*, 2014; Feikema *et al.*, 1990). As an intermediate step, gas turbine model combustors have been developed as benchmark cases for investigating a wide range of operating conditions. The German Aerospace Centre (DLR) have developed a range of gas turbine model combustors, which include the Siemens SGT–100 (Stopper *et al.*, 2013), a burner with dual co-axial swirlers (Meier *et al.*, 2005, 2006; Weigand

et al., 2006) and the PRECCINSTA burner (Meier *et al.*, 2007; Weigand *et al.*, 2007). Other combustors include the TECFLAM burner (Gregor *et al.*, 2009; Janus *et al.*, 2007, 2005), the CNRS burner in Paris (Galley *et al.*, 2011) and the Michigan Twin Annual Premixed Swirler (TAPS) combustor (Dhanuka *et al.*, 2011, 2009; Temme *et al.*, 2014). The configurations have been tested and analysed under stable conditions and unstable conditions, in order to generate thermo-acoustic instabilities and the occurrence of flame blow-off. Detailed measurements have also been obtained that allow these configurations to serve as benchmark cases for the development of computational models.

The flames in partially premixed configurations are within flows that have high levels of turbulence, which are generated through swirling flows. Therefore, the theory for the flames presented thus far has to be replaced with a modified regime where turbulence and combustion can interact. Turbulence in non-reacting flows is an extremely complex and unsolved problem, due to the presence of a wide range of length and time scales, and its stochastic nature. The presence of combustion exacerbates the difficulty of understanding turbulent combustion and therefore, it is useful to briefly review some of the elementary theory of turbulence before considering turbulent combustion theory.

2.3 Approach to turbulent flows

2.3.1 Reynolds decomposition

Turbulent combustion is a stochastic physical phenomenon, since turbulence is present within and around the flame. Turbulence has been of significant interest for several decades and its fundamental theory has been thoroughly reviewed in numerous classical books (Batchelor, 1953; Hinze, 1959; Tennekes & Lumley, 1972). A quantity φ that varies in space $\boldsymbol{x}$ and time t is known as a stochastic variable (Pope, 2000). This random field can be split into its statistical mean and fluctuating value for a given point in space and time. This is known as Reynolds decomposition and for a stochastic flow variable $\varphi(\boldsymbol{x}, t)$, this decomposition is written as (Tennekes & Lumley, 1972)

$$\varphi(\boldsymbol{x}, t) = \overline{\varphi}(\boldsymbol{x}, t) + \varphi'(\boldsymbol{x}, t)\,, \tag{2.27}$$

where the first and second terms on the right-hand side denote the mean and the random fluctuation. It should be noted that $\overline{\varphi'} = 0$ and $\overline{\varphi'^2} \neq 0$ by definition (Tennekes &

Lumley, 1972). The mean field $\overline{\varphi}(\boldsymbol{x}, t)$ can be determined over a time period $\mathcal{T}$ as

$$\overline{\varphi}(\boldsymbol{x}) = \lim_{\mathcal{T}\to\infty} \frac{1}{\mathcal{T}} \int_0^{\mathcal{T}} \varphi(\boldsymbol{x}, t)\, \mathrm{d}t\,, \tag{2.28}$$

where an upper limit for $\mathcal{T}$ needs to be specified in practice; the time period must be long enough to ensure that the integral converges.

The definition shown in Eq. (2.28) is valid if the measurements taken for the stochastic variable (e.g., $\boldsymbol{U}$) are in a statistically steady and homogeneous flow field (Tennekes & Lumley, 1972). However if the flow field is unsteady, then $\varphi(\boldsymbol{x}, t)$ has to be ensemble averaged. If N realisations are collected and φ_n is the n-th realisation, then the ensemble average is obtained using

$$\overline{\varphi}(\boldsymbol{x}, t) = \frac{1}{N} \sum_{n=1}^{N} \varphi_n(\boldsymbol{x}, t)\,. \tag{2.29}$$

The variance of the field, otherwise referred to as the second central moment, is determined as

$$\sigma_\varphi^2 = \overline{\varphi'^2} = \overline{\varphi^2} - \overline{\varphi}^2\,. \tag{2.30}$$

Stochastic methods are used to describe the fluctuating fields of velocity and other scalar quantities in terms of their statistical distribution (Pope, 2000). For all random variables, it is possible to associate a *Probability Density Function* (PDF) with each variable. The PDF $P(\Phi; \varphi)$ is the probability of finding φ in the range $\Phi \leq \varphi \leq \Phi + \mathrm{d}\Phi$, where Φ is the sample space variable for φ. It follows that should the possible realisations range from $-\infty$ to ∞, then the PDF $P(\Phi; \varphi)$ may be written as $\int_{-\infty}^{\infty} P(\Phi; \varphi)\, \mathrm{d}\Phi = 1$. This is the normalisation condition for a PDF and consequently, the probability of φ occurring between $-\infty$ and ∞ is certain, i.e., unity (Williams, 1985*a*). The sample space of the PDF in practice has a prescribed upper and lower bound. The most common profile of a PDF is Gaussian (normal distribution) and this has a single peak, but bimodal shapes are possible, which have two peak values (Cant & Mastorakos, 2008). Such PDFs describing single variable behaviour are called marginal PDFs. In stationary turbulent flows, the PDF does not depend on t, while for homogenous fields, the PDF does not depend on $\boldsymbol{x}$ (Peters, 2000). It is then possible to find the moments of a stochastic variable once its PDF is known and these are the various powers of φ. The first moment of φ is the mean and this can also be used to find the mean of a function $\mathscr{F}(\varphi)$; these are presented below (Tennekes & Lumley, 1972)

$$\overline{\varphi}\,(\boldsymbol{x}, t) = \int_{-\infty}^{\infty} \Phi P\,(\Phi; \varphi)\ \mathrm{d}\Phi\,, \tag{2.31}$$

$$\overline{\mathscr{F}}\left(\varphi\right) = \int_{-\infty}^{\infty} \mathscr{F}\left(\Phi\right) P\left(\Phi;\varphi\right)\ \mathrm{d}\Phi\,. \tag{2.32}$$

For a given flow, the fluctuations of the stochastic variables (e.g., p, T, $\boldsymbol{U}$, ρ, ...) are different and hence, their PDFs are also different. However, a joint PDF is required for a function that depends on two random variables $\varphi(\boldsymbol{x},t)$ and $\gamma(\boldsymbol{x},t)$, in order to describe the statistical correlations. The mean is therefore written as

$$\overline{\mathscr{F}}\left(\varphi,\gamma\right) = \int_{-\infty}^{\infty}\int_{-\infty}^{\infty} \mathscr{F}\left(\Phi,\Gamma\right) P\left(\Phi,\Gamma;\varphi,\gamma\right)\ \mathrm{d}\Phi\,\mathrm{d}\Gamma\,, \tag{2.33}$$

where Γ is the sample space variable for the second random variable γ. The joint PDF can be determined as the product of the two marginal PDFs $P(\Phi,\Gamma) = P(\Phi)P(\Gamma)$ in the case that the two variables φ and γ are statistically independent. This is typically assumed for combustion problems but may not be valid when there are strong interactions between the two variables.

2.3.2 Favre decomposition

The statistical treatment presented thus far is only suitable for constant density flows. For flows with combustion or high Mach number flows, the variations in density are strong. By applying the Reynolds decomposition to Eq. (2.1), the following result is obtained

$$\frac{\partial\overline{\rho}}{\partial t} + \boldsymbol{\nabla}\cdot\left(\overline{\rho}\,\overline{\boldsymbol{U}}\right) = -\boldsymbol{\nabla}\cdot\left(\overline{\rho'\boldsymbol{u}'}\right), \tag{2.34}$$

where $\overline{\rho\boldsymbol{U}} = \overline{\rho}\,\overline{\boldsymbol{U}}$ and $\boldsymbol{u}'$ is the fluctuation for the velocity vector $\boldsymbol{U}$. This gives rise to a modelling problem, as the density correlation term $\overline{\rho'\boldsymbol{u}'}$ is present and is non-zero in turbulent flows. Instead, it is possible to introduce a density-weighted average, which is known as Favre averaging. For a variable φ, this decomposition is written as

$$\varphi\left(\boldsymbol{x},t\right) = \widetilde{\varphi}\left(\boldsymbol{x},t\right) + \varphi''\left(\boldsymbol{x},t\right)\,, \tag{2.35}$$

where the Favre average is defined as

$$\widetilde{\varphi} = \frac{\overline{\rho\varphi}}{\overline{\rho}}\,. \tag{2.36}$$

Similar to Reynolds decomposition, it should be noted that $\widetilde{\varphi''} = 0$ but $\overline{\varphi''} \neq 0$ by definition. Therefore, applying the Favre decomposition and the Favre definition to

Eq. (2.1) will avoid the presence of a non-zero density flux term in the Favre-averaged continuity equation, i.e., the term on the right-hand side of Eq. (2.34).

For a density-weighted PDF, the Favre definition in Eq. (2.36) can be used for a PDF. This is written as (Bilger, 1975).

$$\overline{\rho\mathscr{F}(\varphi)} = \overline{\rho}\widetilde{\mathscr{F}}(\varphi) = \overline{\rho}\int_{-\infty}^{\infty}\mathscr{F}(\Phi)\,\widetilde{P}(\Phi;\varphi)\;\mathrm{d}\Phi\,, \tag{2.37}$$

which gives $\rho P = \overline{\rho}\widetilde{P}$. The expression in Eq. (2.37) is used in statistical models for combustion, which are covered in § 3.4.3.

2.4 Scales of turbulence and the energy cascade

Nearly a century ago, Richardson (1922) observed whirl-like structures in turbulent flows. These structures, known as *eddies*, are canonical structures that vary in size and are represented by a vortical flow unit riding on the mean flow. It is well known that these structures in turbulent flows consist of a wide range of length and time scales. The average rotational velocity and diameter of these structures yield the relevant velocity and length scales. It was recognised that high Reynolds number flows are turbulent; this dimensionless number can be expressed in terms of characteristic length scales $\mathcal{L}$ and velocity scales $\mathcal{U}$ of the eddies as $\mathrm{Re} = \mathcal{U}\mathcal{L}/\nu$ (Batchelor, 1953). The length scales in a turbulent flow (e.g., a high-velocity jet entering a quiescent environment) can be approximated by using a normalised space correlation based on the axial velocity $U(\boldsymbol{x},t)$ between two points in the flow at a distance $\boldsymbol{r}$ apart. This is written as $R(\boldsymbol{x},\boldsymbol{r},t) = \overline{u'(\boldsymbol{x},t)u'(\boldsymbol{x}+\boldsymbol{r},t)}/\overline{u'^2(\boldsymbol{x},t)}$, where u' is the axial velocity fluctuation. Normalised space correlations would be required for the other components of velocity, but for homogeneous isotropic turbulence, the location $\boldsymbol{x}$ is invariant and the distance between the two points is $r = |\boldsymbol{r}|$. A characteristic length, which is known as the *integral length scale* ℓ_o, can be defined based on this correlation as $\ell_o = \int_0^\infty R(r,t)\;\mathrm{d}r$. Eddies at the integral scale indicate that the largest concentration of turbulent kinetic energy k occurs in the vicinity of such eddies. The turbulent kinetic energy is determined as

$$k = \frac{1}{2}\overline{\boldsymbol{u}'\cdot\boldsymbol{u}'}\,, \tag{2.38}$$

and for the special case of homogeneous isotropic turbulence, the expression is then equal to $k = 3{u'_o}^2/2$, where $u'_o = \left(\overline{u'^2}\right)^{1/2}$ (Hinze, 1959; Tennekes & Lumley, 1972).

It was observed by Richardson (1922) that these large eddies transfer kinetic energy to smaller eddies. A very important property is the *dissipation rate* of kinetic energy per unit mass ε and its rate is dictated by the large eddies. The rate at which kinetic energy cascades from a large eddy of size ℓ_o to a smaller sized eddy is equal to the rate at which kinetic energy is dissipated. Therefore, it is plausible to express the rate of dissipation in terms of the integral length scale and its characteristic velocity scale as $\varepsilon \approx {u'_o}^3/\ell_o \approx k^{3/2}/\ell_o$. Its period of energy cascade, otherwise known as the eddy turn-over time, for these large eddies is $\tau_o \approx \ell_o/u'_o \approx k/\varepsilon$.

Eddies of different sizes consist of different amounts of turbulent kinetic energy. This energy is transferred from large scale eddies to small scale eddies and these small scale eddies consume this energy by viscous dissipation. Kolmogorov (1941) hypothesised that eddies of a size equal to the integral length scale cascade their kinetic energy at the same rate as eddies with a smaller length scale. This hypothesis holds for all eddies in a range extending from the integral scale down to the eddies of the smallest scales, known as the *Kolmogorov scale* ℓ_η. This is known as the *energy cascade*, whereby the rate of energy transfer is independent of the fluid viscosity within this length scale range (Kolmogorov, 1941). The motion of eddies at the Kolmogorov scale is influenced by the viscosity. The Kolmogorov length, time and velocity scales are given respectively as (Batchelor, 1953)

$$\ell_\eta \approx \left(\frac{\nu^3}{\varepsilon}\right)^{1/4}, \quad \tau_\eta \approx \left(\frac{\nu}{\varepsilon}\right)^{1/2} \quad \text{and} \quad u'_\eta \approx (\nu\varepsilon)^{1/4}. \tag{2.39}$$

A third scale does exist between ℓ_o and ℓ_η, which is known as the Taylor microscale and this describes the length a Kolmogorov eddy is convected by a integral scale eddy during the turn-over time τ_η (Taylor, 1935). The Kolmogorov and the integral length and time scales are related through (Tennekes & Lumley, 1972)

$$\frac{\ell_o}{\ell_\eta} \approx \mathrm{Re}_T^{3/4} \quad \text{and} \quad \frac{\tau_o}{\tau_\eta} \approx \mathrm{Re}_T^{1/2}, \tag{2.40}$$

where the turbulent Reynolds number is defined using the scale associated at the integral scale as $\mathrm{Re}_T = u'_o\ell_o/\nu$. This implies that the range of scales becomes larger when the turbulent Reynolds number is increased.

The turbulent kinetic energy spectrum is used to represent the turbulent kinetic energy that an eddy carries and this is denoted as $E(\kappa)$, where κ is a wavenumber that is inversely proportional to the eddy length scale ℓ. A typical turbulent kinetic energy spectrum is illustrated in Fig. 2.2. It is shown that the energy spectrum peaks at the

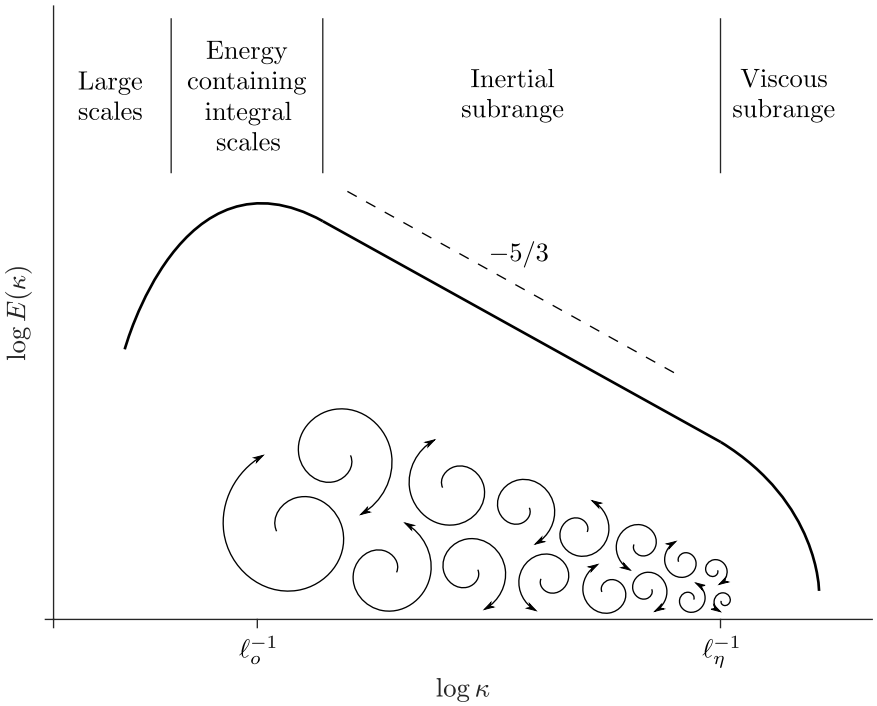

Fig. 2.2 Schematic representation of the turbulent kinetic energy spectrum as a function of the wavenumber κ, which is adapted from the diagram shown by Peters (2000).

integral length scale range and then decreases in the inertial subrange according to the $k^{-5/3}$ law that was proposed by Kolmogorov (1941). This energy dissipation decreases until the cut-off point, which is at the Kolmogorov scale. Beyond this point, the kinetic energy decreases exponentially and this region is known as the *viscous subrange*, where the dissipation of kinetic energy is due to molecular viscosity (Hinze, 1959).

The range of length, time and velocity scales influences the behaviour of a flame within a turbulent flow, as the flame contains reacting species and is continuously releasing heat. Therefore, the physical analysis of a turbulent flame is mainly based on the comparison of these turbulent scales with the corresponding scales associated with the flame. The comparisons yield different flame behaviours and burning modes for all flame configurations, which are summarised next.

2.5 The role of turbulence on combustion

The interactions between turbulence and the chemistry from combustion are very hard to capture because the turbulent and chemical time scales have a strongly nonlinear relationship, due to the rate of mixing being much slower in comparison to the rate

of the chemical kinetics during a chemical reaction (Bilger, 2000). The rates of energy transfer and mixing for turbulent combustion are several orders of magnitude higher than a corresponding laminar flame. This occurs because the rate of mixing is higher than the rates of molecular diffusion and the heat transfer rates in turbulent flames are higher than in laminar flames.

The relevant scales for turbulent eddies presented in § 2.4 are important for turbulent flames, since the turbulent scales can be related to the laminar properties of flames, in order to describe how a flame is affected in a turbulent flow. The *Damköhler number* is used to relate the turbulent and chemical time scales to identify different flame–vortex interactions and it is written in terms of the integral length scale to describe the large scale eddies. Assuming homogeneous and isotropic turbulence, and one-step chemistry, the Damköhler number is written in the form $\mathrm{Da} = \tau_o/\tau_c$, where τ_o is the previously defined integral time scale and τ_c is a chemical time scale. The chemical time scale corresponds to the time required for the flame to propagate over a distance equal to its thickness, which can be determined using s_L^0 and δ_L^0. Therefore, the Damköhler number is given as (Peters, 2000)

$$\mathrm{Da} = \frac{\tau_o}{\tau_c} = \frac{\ell_o}{u'_o}\frac{s_L^0}{\delta_L^0}\,. \tag{2.41}$$

The Damköhler number is used as an indicator to show which combustion regime a flame is operating in. However, these combustion regimes are different for premixed and non-premixed flames.

For turbulent premixed flames, eddies alter the flame structure and distort the flame front, causing the flame to become wrinkled and have a larger surface area (Libby, 1985). Consequently, this causes the propagation speed s_L^0 to increase to a turbulent burning velocity s_T for a turbulent premixed flame. The turbulent flame speed is related to the laminar flame speed as $s_T = s_L^0(A_T/A)$, where A_T/A is area ratio of the turbulent and laminar flame and is referred to as the wrinkling factor. In addition, it has been observed that the turbulent flame speed increases with the root mean square (r.m.s.) of the turbulent velocity fluctuation according to $s_T \approx s_L^0(1 + u'/s_L^0)$. This suggests that for high levels of turbulence, the turbulent flame speed becomes independent of the laminar flame speed (Abdel-Gayed *et al.*, 1984). Turbulent flame speeds have been a topic of high interest and are reviewed in detail by Bradley (1992) and Lipatnikov & Chomiak (2002). On the other hand, eddies can perturb the flame structure and widen the reaction zone, which causes the peak reaction rate to decrease (Bray, 1980). Turbulence does not affect the inner structure of the flame for Damköhler numbers of $\mathrm{Da} \gg 1$, since the

chemistry is treated as fast and the eddies instead wrinkle the flame. Eddies under such conditions have turbulent motions that are too slow to affect the flame's structure and are of the smallest scales of turbulence with turbulent time and length scales of τ_η and ℓ_η respectively. This transition is instead described by using the *Karlovitz number*, which can be interpreted as the reciprocal of a Damköhler number based on the smallest scales of turbulence (Peters, 2000). The Karlovitz number is defined as

$$\mathrm{Ka} = \frac{\tau_c}{\tau_\eta} = \frac{u'_\eta}{\ell_\eta}\frac{\delta^0_L}{s^0_L} = \left(\frac{u'_o}{s^0_L}\right)^{3/2}\left(\frac{\ell_o}{\delta^0_L}\right)^{-1/2}. \tag{2.42}$$

The various combustion regimes for turbulent premixed flames can be shown on a regime diagram by using the Damköhler and Karlovitz numbers as indicators for the regimes of turbulent premixed combustion. Various regime diagrams have been proposed by Abdel-Gayed *et al.* (1988, 1989), Borghi (1988), Peters (1986, 2000), Poinsot *et al.* (1991) and Williams (1985*a*) and such regime diagrams are commonly referred to as the Borghi diagram. The regime diagram shown by Peters (2000) is depicted in Fig. 2.3. The line at $\mathrm{Re}_T = 1$ is a boundary that separates laminar premixed flames from the turbulent premixed flame regimes (Peters, 2000). The turbulent premixed combustion regimes can be classified according to the Klimov–Williams criterion, which corresponds to $\mathrm{Ka} = 1$ (Williams, 1985*a*). This separates the combustion regimes as:

- **Flamelet regime**, where the flame thickness is smaller than any turbulent scale ($\mathrm{Ka} < 1$) and the chemical time scale is smaller than any turbulent time scale ($\mathrm{Da} > 1$). This region is subdivided into the *corrugated flamelet regime* ($u'_o > s^0_L$) and the *wrinkled flamelet regime* ($u'_o < s^0_L$). In the wrinkled flamelet regime, the turbulence intensity is too weak to alter the flame structure, whereas in the corrugated flamelets regime, the smallest eddies alter the flame structure by entering the preheat zone of the premixed flame to form pockets of fresh reactant gases and burnt products. In addition, the flame becomes more wrinkled as the turbulence intensity increases. However, the reaction zone remains unaltered and can be treated as a thin and laminar-like premixed flame.

- **Thickened flame regime**, where in this case the Kolmogorov scales are smaller than the flame thickness and can modify the inner structure of the flame ($\mathrm{Ka} > 1$). This is subdivided at $\mathrm{Ka} = 100$, where Poinsot *et al.* (1991) suggested this bound as an upper limit for when the laminar reaction zones are perturbed by turbulence and the flame thickness is approximately 10 times greater than the reaction zone

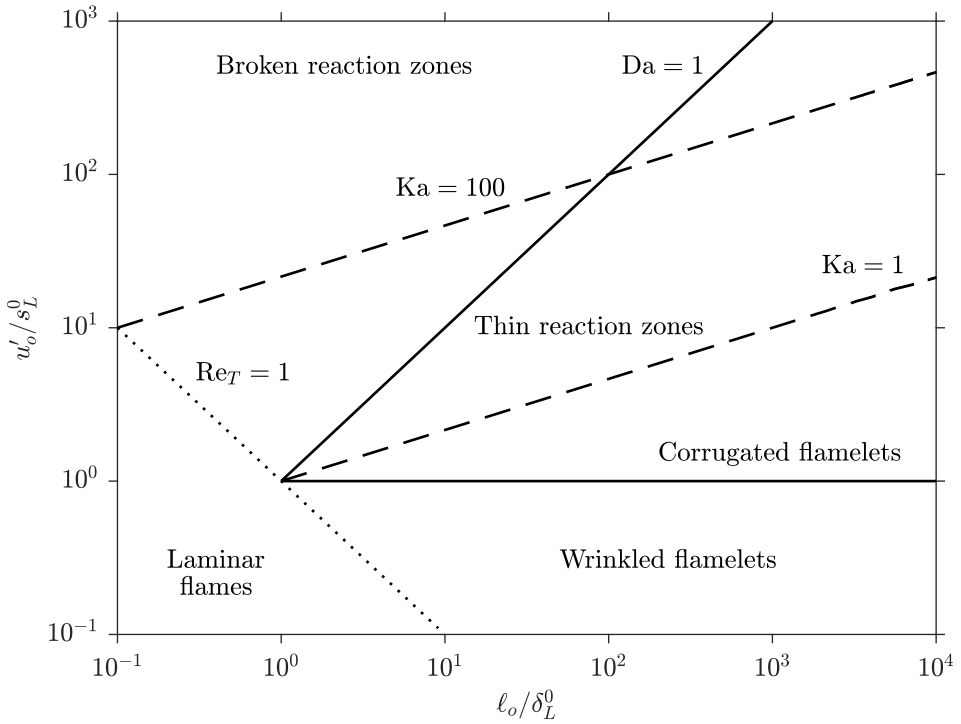

Fig. 2.3 Turbulent premixed combustion regime diagram, which is adapted from the diagram shown by Peters (2000).

thickness. The *thin reaction zones regime* lies in the range $1 < \mathrm{Ka} < 100$, while the *distributed reaction zones regime* is when $\mathrm{Ka} > 100$ and flame quenching may occur in this region, due to significant local extinction.

Identifying the combustion regimes is not straightforward for turbulent non-premixed flames. Choosing a relevant velocity scale for turbulent non-premixed flames is difficult, since there is no propagation velocity. This therefore makes choosing a time scale for the flame ambiguous (Peters, 2000). As shown in § 2.2.1, the preheat zone for a non-premixed flame is determined by the balance between convection and diffusion transport of the mixture fraction. However, the convection–diffusion processes are not the same when a non-premixed flame is in a turbulent flow and the diffusion time scales vary substantially. Moreover, turbulent diffusion will dominate when the Reynolds number is increased and this will lead to smaller turbulent time scales. Therefore, the fast chemistry assumptions are no longer valid. A diffusion length scale based on the mixing length thickness is expressed as $\ell_\xi \approx 1/|\boldsymbol{\nabla}\xi|_{\mathrm{st}} \approx \sqrt{\mathcal{D}_{\mathrm{st}}/\chi_{\mathrm{st}}}$. This can also be expressed in terms of the strain rate a imposed by the flow field, which carries the same units as χ_{st}. High strain rates can lead to extinction at high values of χ_{st}, where the flame will eventually be quenched at a given value χ_q (Peters, 2000). Therefore, the characteristic diffusion time scale

is $\tau_\xi = \ell_\xi^2/\mathcal{D}_{\rm st} = \chi_{\rm st}^{-1}$. The other characteristic time scale is the chemical time scale, which can be used to define a flame Damköhler number $\mathrm{Da}_L = \tau_\xi/\tau_c = (\chi_{\rm st}\tau_c)^{-1}$ (Law, 2006). This is prescribed to indicate the chemical strength of the flame and in contrast to premixed flames, the balance between reaction and diffusion transport does not have to be met under all conditions. Hence, the time scales τ_ξ and τ_c are not required to be the same in mixture fraction space. The regime diagram for turbulent non-premixed flames is shown in Fig. 2.4. It is expected that the Kolmogorov eddies will have the smallest length and time scales and are the most effective in the preheat zone. Therefore, these can be approximately equal to the diffusion length and time scales. The Damköhler number can be written as (Law, 2006).

$$\mathrm{Da} = \frac{\tau_o}{\tau_c} \approx \frac{\tau_o}{\tau_\eta}\frac{\tau_\xi}{\tau_c} = \sqrt{\mathrm{Re}_T}\,\mathrm{Da}_L\,. \tag{2.43}$$

If $\mathrm{Da}_L \approx 1$, then this suggests that the residence time within the reaction zone is not long enough. Hence, the flame may be prone to extinction and the flamelet assumption is no longer valid. The line at $\mathrm{Da} = \sqrt{\mathrm{Re}_T}$ in Fig. 2.4 is used as the bound for the flamelet regime. If $\mathrm{Da}_L < 1$, then some reaction zones may be extinguished through large scalar dissipation rate induced eddies at the Kolmogorov scale. For $\mathrm{Da} < 1$, it is expected that eddies at all scales cause a sufficient amount of scalar dissipation to induce flame quenching. Hence, the thin flame sheet is no longer present and the chemical reactions within the flame are significantly weaker, which is known as the distributed reactions regime (Law, 2006).

These boundaries used to separate the different turbulent flame regimes shown in Figs. 2.3 and 2.4 do not cause abrupt changes in the flame behaviour when moving between regimes. In addition, these regime diagrams serve as guides for the behaviour of the flame and attempt to indicate the combustion regime the flame is operating in. The boundaries can be modified by density changes and other transient effects (Peters, 2000). Nevertheless, these regime diagrams are still useful to allow the general classification of turbulent flames and to draw comparisons between measured and modelled flames in different burner configurations, in order to focus on modelling issues.

The reactants for partially premixed flames may be either premixed or non-premixed prior to ignition, as described in § 2.2.3, and compositionally inhomogeneous mixtures exist. This causes diffusion-like reaction zones and propagating flame fronts to be present. Therefore, constructing a regime diagram for turbulent partially premixed flames is difficult and has not been previously attempted, but the premixed and non-premixed

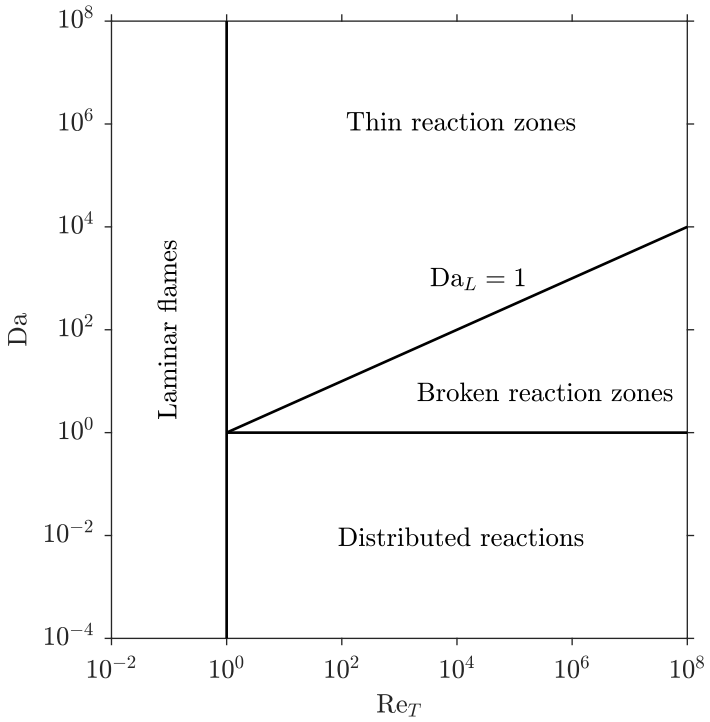

Fig. 2.4 Turbulent non-premixed combustion regime diagram, which is adapted from the diagram shown by Law (2006).

regime diagrams can be used to serve as an approximate guide to indicate which regimes the flame is operating in.

2.6 Summary

This chapter has provided a broad overview of the background for turbulent combustion. The balance equations for reacting flows and the theory for laminar flames has been presented, followed by some of the important notions of turbulence and its role in turbulent combustion. The continuous development of turbulent flame theory has seen the development of computational models for obtaining solutions of turbulent flames. This has been a very active research area for several decades and the design of practical combustion systems is now heavily dependent on the use of accurate numerical models. Therefore, the next chapter provides an overview of different approaches used for simulations of turbulent combustion.

Chapter 3

Computational Approaches for Turbulent Combustion

Computational Fluid Dynamics (CFD) has been used for several decades to model turbulent reacting flows and serves as a design tool for practical combustion systems. Simulations of turbulent reacting flows using CFD can be broadly categorised into three approaches: Direct Numerical Simulation (DNS), Reynolds-Averaged Navier–Stokes (RANS) simulation and Large Eddy Simulation (LES). The selection of which methodology to use is determined by the level of detail required from the results produced. The improvement of computational capabilities has motivated the continuous development of CFD for turbulent combustion, in order to produce more reliable results to compare against experimental data (Poinsot & Veynante, 2012). This chapter will present an overview of the three different modelling approaches for CFD, where a more detailed description of the LES framework is provided, since this approach is used in this work. This is followed by a review of the state-of-the-art combustion models for LES and a description of the closure model used in this work.

3.1 Direct numerical simulation

Obtaining highly accurate simulations of turbulent flames is challenging, due to the strong interactions between the chemistry of combustion and turbulence. The early development of advanced numerical methods with high-order numerical schemes has led to the development and use of DNS for turbulent combustion (Riley *et al.*, 1986; Rutland *et al.*, 1991). This approach has been used since the 1990s as a very useful tool for solving the instantaneous balance equations presented in § 2.1 without the

need of a turbulence model and has offered new ways to investigate the interactions between turbulence and the flame (Jou & Riley, 1989; Poinsot, 1996; Poinsot *et al.*, 1995; Vervisch, 2000; Vervisch & Poinsot, 1998). The aim of DNS approaches is to use high-order spatial discretisation and time marching schemes to inherently resolve all of the relevant turbulent time and length scales. The main challenge is to ensure that these numerical schemes have high accuracy and stability, while also increasing the efficiency from a computational perspective (Moin & Mahesh, 1998).

While DNS has advanced significantly and has proven to be a useful tool for turbulent reacting flow modelling, there are still significant restrictions with using this approach (Poinsot & Veynante, 2012). The variation of the thermochemical properties across a flame front, such as the temperature and species mass fractions, can be captured through the use of DNS exactly like how a high-resolution probe could measure these properties. However for DNS approaches to achieve this, the grid resolution must be very high (usually in the micron range), in order to ensure that the entire range of turbulent scales from the integral scale down to the Kolmogorov scale can be captured (Moin & Mahesh, 1998). As shown in Eq. (2.40), the ratio of the integral and Kolmogorov length scales is approximately equal to $\mathrm{Re}_T^{3/4}$; the ratio of the time scales is approximately equal to $\mathrm{Re}_T^{1/2}$. Hence for high turbulent Reynolds numbers, this means that the number of grid points must be large enough to resolve the full range of length scales, which increases with Re_T, as shown by Eq. (2.40). As shown in detail by Givi (1989), if the Reynolds number is 10^4, then the number of grid points would be approximately 10^9. However, this analysis is based on using only the ratio of the integral and Kolmogorov length and time scales. It is known that the flame thickness may be smaller than the size of the Kolmogorov scale eddies and in order to fully resolve the flame, approximately 10–20 grid cells are required within the flame (Poinsot & Veynante, 2012). This means that the number of grid points must be increased further to ensure that both the flame and the scales of turbulence are inherently resolved by the DNS. This therefore makes DNS a very computationally expensive tool for analysing turbulent flames and the use of DNS is restricted to flows of low turbulent Reynolds numbers.

In addition, complex and large geometries cannot be fully resolved using a DNS from a practical perspective, due to the computational requirements. The continuous advancement of High Performance Computing (HPC) technology has allowed simulations with detailed chemistry to be computed of lifted flames in simple configurations, which use computational grids that contain close to one billion grid cells (Chen *et al.*, 2009). A lean premixed swirl flame in the PRECCINSTA burner (Meier *et al.*, 2007) has been simulated

using DNS by Moureau *et al.* (2011). This simulation used 2.6 billion tetrahedral cells and used a resolution of less than 100 µm, which was deemed to be sufficient in capturing all the turbulent scales and the major species of the flame brush. However, this set-up required further post-processing to obtain the minor species using a tabulated chemistry library. Furthermore, over 16,000 cores and 80 hours of wall clock time were required to obtain 1.9 ms of statistics. Hence, it is not viable to undertake a full simulation with DNS of complex configurations and it is not expected to be feasible for several decades. The use of DNS is still mostly restricted to simple configurations and academic purposes and this has led to the development of RANS and LES modelling, where DNS is often used to aid such model development including their validation (Poinsot & Veynante, 2012).

3.2 Reynolds-averaged Navier–Stokes simulation

Since DNS cannot yet be used to simulate turbulent combustion in practical applications, the development of other methods has been necessary to model turbulent reacting flows. Simulations with the RANS methodology are the most computationally inexpensive and classical approach for modelling turbulent flows (Poinsot & Veynante, 2012). The instantaneous transport equations in § 2.1 are either time or ensemble averaged using the Reynolds and Favre decomposition techniques, as described in § 2.3. The variables are averaged to handle the wide range of length and time scales in high Reynolds number flows. However, the minimum length scales of the Reynolds-averaged variables are much larger than the smallest scales of the turbulent fluctuations. Therefore, all unsteady turbulent motions and their coupling with combustion processes remain unresolved over the entire range of turbulent length and time scales (Williams, 1985*a*).

By applying the Reynolds and Favre decompositions to the momentum equation and to the transport equation for a thermochemical scalar φ, the equations are written respectively as

$$\overline{\rho}\frac{\mathrm{D}\widetilde{\boldsymbol{U}}}{\mathrm{D}t} = -\boldsymbol{\nabla}\overline{p} + \boldsymbol{\nabla}\cdot\overline{\boldsymbol{\tau}} - \boldsymbol{\nabla}\cdot\left(\overline{\rho}\widetilde{\boldsymbol{u}''\boldsymbol{u}''}\right), \tag{3.1}$$

$$\overline{\rho}\frac{\mathrm{D}\widetilde{\varphi}}{\mathrm{D}t} = \overline{S}_{\varphi} + \boldsymbol{\nabla}\cdot\left(\overline{\rho\mathcal{D}_{\varphi}}\boldsymbol{\nabla}\widetilde{\varphi}\right) - \boldsymbol{\nabla}\cdot\left(\overline{\rho}\widetilde{\boldsymbol{u}''\varphi''}\right), \tag{3.2}$$

where $\mathrm{D}/\mathrm{D}t = \partial/\partial t + \widetilde{\boldsymbol{U}}\cdot\nabla$ is the material derivative and $\overline{S}_{\varphi}$ is a source term for the variable φ. The molecular transport terms, which are the second terms on the right-hand side of Eqs. (3.1) and (3.2), are expected to be small for high Reynolds number flows

and may be neglected. However, this is not possible for regions near solid walls, since the effects of local viscosity are significant (Law, 2006). Therefore, these terms are retained in their averaged forms.

As shown in Eqs. (3.1) and (3.2), additional terms arise on the right-hand side of both equations as a result of applying the Reynolds and Favre decompositions. The Reynolds stress term $\overline{\rho}\widetilde{\boldsymbol{u}''\boldsymbol{u}''}$ in Eq. (3.1) and the Reynolds flux term $\overline{\rho}\widetilde{\boldsymbol{u}''\varphi''}$ in Eq. (3.2) are nonlinear terms that describe the exchange between fluctuating quantities, which are generated by the inertial terms. These are higher-order co-variance terms, which lead to the so-called closure problem for turbulence modelling. The Reynolds flux terms for thermochemical scalars are modelled using a turbulent diffusion gradient model with a gradient hypothesis. Modelling of the Reynolds stress term is the main subject of interest for the turbulence closure problem for RANS, with the k–ε model being one of the earliest and well known models (Hanjalić & Launder, 1972; Jones & Launder, 1972; Launder & Spalding, 1974). Details of Reynolds stress closures are covered in review articles (Hanjalić, 1994; Menter, 2009; Nallasamy, 1987; Patel *et al.*, 1984; Speziale, 1998) and numerous books (Hanjalić & Launder, 2011; Pope, 2000).

A final term that requires closure is the source term; an example is the mean reaction rate $\overline{\dot{\omega}}_\alpha$ for a chemical species, which would be present in the species transport equation within the RANS framework. If the Reynolds decomposition is applied to the reaction rate expression in Eq. (2.19), which can be performed in various ways (Bilger, 1976*b*, 1980; Libby & Williams, 1980), then the result is

$$\begin{aligned}\overline{\dot{\omega}}_{\mathrm{fu}} = &-\overline{\rho}^2\nu'_{\mathrm{fu}}\mathcal{M}_{\mathrm{ox}}^{-1}\overline{Y}_{\mathrm{fu}}\overline{Y}_{\mathrm{ox}}\mathcal{A}\,\exp\left(-\frac{E_a}{\Re^0\overline{T}}\right)\\ &\times\left\{1+\frac{\overline{\rho'^2}}{\overline{\rho}^2}+\frac{\overline{Y'_{\mathrm{fu}}Y'_{\mathrm{ox}}}}{\overline{Y}_{\mathrm{fu}}\overline{Y}_{\mathrm{ox}}}+\frac{2\,\overline{\rho'Y'_{\mathrm{fu}}}}{\overline{\rho}\overline{Y}_{\mathrm{fu}}}+\frac{2\,\overline{\rho'Y'_{\mathrm{ox}}}}{\overline{\rho}\overline{Y}_{\mathrm{ox}}}\right.\\ &\left.+\frac{E_a}{\Re^0\overline{T}}\left[\frac{\overline{Y'_{\mathrm{fu}}T'}}{\overline{Y}_{\mathrm{fu}}\overline{T}}+\frac{\overline{Y'_{\mathrm{ox}}T'}}{\overline{Y}_{\mathrm{ox}}\overline{T}}+\left(\frac{E_a}{2\,\Re^0\overline{T}}-1\right)\frac{\overline{T'^2}}{\overline{T}^2}\right]+\ldots\right\}.\end{aligned}\tag{3.3}$$

As shown in Eq. (3.3), there are double correlations present in the expanded expression (e.g., $\overline{\rho'Y'_{\mathrm{fu}}}$) and separate transport equations can be used for each of these terms. However, the continued expansion of Eq. (3.3) will give rise to triple correlation terms and the number of variables will increase. Hence, this leads to the closure problem for turbulent combustion modelling when attempting to directly apply the Reynolds decomposition to the reaction rate expression in Eq. (2.19). Therefore, modelling turbulent combustion is a much greater challenge than modelling laminar combustion because the reaction rate

needs a suitable closure model, as well as the other turbulent flux terms that arise in the conservation equations when applying Reynolds decomposition (Bilger, 1976*b*). Moreover, the exponential term in Eq. (2.19) causes the strongest nonlinearity of the reaction rate mechanism, which exacerbates this closure problem. Hence, various modelling approaches have been developed over the last few decades to accurately model the reaction rate and these have been reviewed in detail by Brewster *et al.* (1999), Veynante & Vervisch (2002), Echekki & Mastorakos (2011), Swaminathan & Bray (2011*b*) and Poinsot & Veynante (2012).

Simulations with RANS or Unsteady RANS (URANS) approaches, where the latter involves time marching the simulation, are advantageous over DNS, since complex full-scale geometries can be modelled. In addition, the computational mesh can contain a smaller number of cells compared to DNS, which makes the RANS calculation more computationally inexpensive. Approaches with RANS also have the potential to reduce computational costs by using geometric simplifications (e.g., asymmetry), since turbulence is assumed to be isotropic. However since the minimum grid cell size can be between 1–5 mm, this means that RANS approaches are only able to capture the average position of the flame front and as previously mentioned, the minimum scales of turbulence are much larger than this minimum cell size (Poinsot & Veynante, 2012). This means that RANS approaches are not able to capture the transient small-scale phenomena, which describe the interactions between turbulence and combustion. It is known that RANS approaches have severe limitations in capturing unsteady phenomena, such as flame quenching, local extinction, ignition and swirling flow dynamics, which are governed by the interactions between turbulence and combustion at the smallest scales. It is essential that simulations are able to capture these phenomena, as these cause the occurrence of failed ignition, thermo-acoustic perturbations and flame blow-off (Echekki & Mastorakos, 2011). Nonetheless, turbulent reacting flow simulations within a RANS framework are still useful because new turbulence–combustion interaction models can be tested before implementing them into more computationally expensive CFD techniques.

3.3 Large eddy simulation

Large eddy simulation is the intermediate level of CFD that lies between RANS and DNS approaches. This is because the whole turbulent kinetic energy spectrum, as illustrated in Fig. 2.2, is neither entirely computed nor modelled, which is the case for DNS and RANS approaches respectively. Since early attempts of undertaking an LES

of turbulent flow (Deardorff, 1970; Lilly, 1967; Smagorinsky, 1963), the development of LES has been significant since the 1990s, due to the improvement of computational efficiency and improved parallel computing (Pope, 2000). For LES, a filtering operation in space and time is applied to the instantaneous quantities within a turbulent flow and decomposes them into filtered and residual components, which are different to the mean and fluctuating components within the RANS approach. This is because the filtered components represent the large scales of turbulence and are computed down to an assigned cut-off scale (Rogallo & Moin, 1984). Hence, the approach has become favourable over the last two decades because the large-scale turbulent motions are explicitly computed by the LES and the small-scale motions below the cut-off scale are modelled. This allows for the grid used to be coarser than one required for DNS, thereby reducing the computational cost. Pope (2000) suggested as a general rule of thumb that around 80 % of the turbulent scales should be directly computed in an LES, whilst the remainder in the region below the cut-off scale and the Kolmogorov scales of turbulence, known as the Sub-Grid Scale (SGS) range, should be modelled. Unclosed residual correlations in the SGS region arise for the turbulent transport and mixing of scalars when applying the filtering decomposition. These SGS residual correlations are analogous to the closure problem of turbulent modelling for RANS and thus, a closure model needs to be used. Many of the notable advances of LES for non-reacting turbulent flow are well covered by Lesieur & Métais (1996), Moin (1997), Piomelli (1999), Meneveau & Katz (2000) and Pope (2004), where attempts had also been made in simulations non-reacting flow within applications of turbulent combustion (Akselvoll & Moin, 1996; Haworth & Jansen, 2000; Moin, 2002). Stable second-order spatial discretisation and time marching schemes, including unsteady pressure-correction schemes, have now been developed (Cant & Mastorakos, 2008). However, these are more computationally expensive because the grid resolution must be smaller than the resolution used in RANS and only full three-dimensional simulations can be undertaken.

To date, using LES for turbulent combustion simulation is becoming standard practice for the simulation of complex geometries and these practices are being applied in industry (Poinsot & Veynante, 2012). Since the late 1990s, significant advances have been made towards the LES of turbulent combustion within complex geometries with initial studies on gas turbine systems (Eggenspieler & Menon, 2004; Kim & Menon, 2000; Kim *et al.*, 1999; di Mare *et al.*, 2004; Selle *et al.*, 2004; Sommerer *et al.*, 2004). It is known that LES is preferred to RANS modelling for turbulent combustion, since the former is superior in capturing the mixing fields and the dissipation rates of scalars. This is because the large-

scale mixing is computed directly within the LES, whereas the mixing is averaged within the RANS framework. It is imperative that the mixing fields are resolved accurately, since this yields the behaviour of the flame and therefore, its accuracy is dependent on a well resolved mesh (Pitsch, 2006). However, in turbulent reacting flows with high Reynolds numbers and fast chemistry, the filtered reaction rate remains unresolved and requires closure, which is similar to the closure problem in the RANS framework, as described in § 3.2. Moreover, the resolved part of the LES can determine the general position of the flame front but is insufficient in capturing the interactions between the chemistry within the flame and the SGSs of turbulence. Therefore, these interactions are entirely modelled within the chosen SGS combustion closure model. Since those early studies mentioned previously, the past 10–20 years has seen significant advances in the development of models for the filtered reaction rate (Gicquel *et al.*, 2012; Pitsch, 2006; Poinsot & Veynante, 2012). As the simulations in this work are undertaken using the LES framework, this will remain the topic of interest in subsequent sections. The filtering operation, governing equations for LES and closure models for the residual Reynolds stress are now outlined, followed by a review of the state-of-the-art filtered reaction rate closure models.

3.3.1 Filtering

Forming the basis of the LES framework involves applying a low-pass filtering operation to the relevant quantities in the instantaneous turbulent flow field. A filter width Δ is chosen, which lies within the inertial subrange of the turbulent kinetic energy spectrum (Pope, 2000). This filter width is the point at which any turbulent motions with length scales smaller than Δ from the domain are removed to allow the larger scale turbulent motions to be fully resolved in both space and time. The filtering operation for a variable $\varphi(\boldsymbol{x}, t)$ is written as (Leonard, 1974)

$$\overline{\varphi}(\boldsymbol{x}, t) = \int \varphi(\boldsymbol{r}, t)\, \mathscr{G}(\boldsymbol{x} - \boldsymbol{r})\, \mathrm{d}\boldsymbol{r}\,. \tag{3.4}$$

Equation (3.4) is written in one-dimensional form for simplicity and it is straightforward to extend the filtering operation in three dimensions (Pope, 2000). The specified filter function $\mathscr{G}$ has a prescribed shape and tends to zero when $\boldsymbol{x} - \boldsymbol{r}$ is large and exceeds the chosen filter size Δ. The integral of $\mathscr{G}$ is across the whole domain and satisfies the normalisation condition $\int_{-\infty}^{\infty} \mathscr{G}(\boldsymbol{x} - \boldsymbol{r})\, \mathrm{d}\boldsymbol{r} = 1$ (Pope, 2000). The filter function can also take different shapes and the most commonly used filters are the box filter, the Gaussian

filter and the sharp spectral filter. The Gaussian filter is typically used and this is given as (Rogallo & Moin, 1984)

$$\mathscr{G}(\boldsymbol{x}) = \mathscr{G}(x_1, x_2, x_3) = \left(\frac{6}{\pi\Delta^2}\right)^{1/2} \exp\left[-\frac{6}{\Delta^2}\left(x_1^2 + x_2^2 + x_3^2\right)\right], \tag{3.5}$$

where the Gaussian filter decreases rapidly outside $\pm\Delta/2$ (Pope, 2000).

The physical variables are decomposed into their filtered and residual components as $\varphi = \overline{\varphi} + \varphi'$, which is analogous to the Reynolds decomposition. The same notation is retained, but it is important to note that the rules of filtering are different to the Reynolds decomposition. These are as follows:

1. The residual contribution φ' cannot be directly computed within the LES and represents the SGS contribution to φ. The criteria $\overline{\varphi'} \neq 0$ and $\overline{\overline{\varphi}} \neq \overline{\varphi}$ also exist for LES filtering.

2. The operation of filtering and differentiating with respect to time do commute, i.e.,

$$\frac{\partial\overline{\varphi}}{\partial t} = \overline{\frac{\partial\varphi}{\partial t}}\,.$$

3. The operation of filtering and differentiation with respect to position do not commute in general, i.e.,

$$\boldsymbol{\nabla}\overline{\varphi} \neq \overline{\boldsymbol{\nabla}\varphi}\,.$$

   It should be noted that filtering and spatial derivatives do commute for homogeneous filters and therefore the left- and right-hand sides in the above expression are equal.

Significant density variations are expected in turbulent flames, due to the presence of strong heat release regions. Applying the filtering operation to the instantaneous balance equations can cause coupling to arise between the residual density and other transported variables, as similarly shown in § 3.2 for the RANS framework. To eliminate this coupling, Favre filtering is introduced and is written as

$$\overline{\rho}\widetilde{\varphi}(\boldsymbol{x}, t) = \int \rho\varphi(\boldsymbol{r}, t)\,\mathscr{G}(\boldsymbol{x} - \boldsymbol{r})\,\mathrm{d}\boldsymbol{r}\,. \tag{3.6}$$

The Favre residual of φ is defined in accordance to the Reynolds residual definition using the Favre decomposition $\varphi = \widetilde{\varphi} + \varphi''$. In addition, the criteria by definition for the LES Favre decomposition are $\widetilde{\varphi''} \neq 0$ and $\widetilde{\widetilde{\varphi}} \neq \widetilde{\varphi}$.

3.3.2 Filtered transport equations

By applying the filtering and Favre filtering decompositions to the instantaneous balance equations in Chapter 2 for mass, momentum, thermochemical enthalpy, mixture fraction and progress variable, it is possible to obtain the filtered balance transport equations for LES that are required for partially premixed combustion. These are given as

Continuity:

$$\frac{\partial \overline{\rho}}{\partial t} + \boldsymbol{\nabla} \cdot \left(\overline{\rho} \widetilde{\boldsymbol{U}} \right) = 0 \,, \tag{3.7}$$

Momentum:

$$\overline{\rho} \frac{\mathrm{D}\widetilde{\boldsymbol{U}}}{\mathrm{D}t} = -\boldsymbol{\nabla} \overline{p} + \boldsymbol{\nabla} \cdot \overline{\boldsymbol{\tau}} - \boldsymbol{\nabla} \cdot \overline{\boldsymbol{\tau}}^{R} \,, \tag{3.8}$$

Enthalpy:

$$\overline{\rho} \frac{\mathrm{D}\widetilde{h}}{\mathrm{D}t} = \boldsymbol{\nabla} \cdot \left(\overline{\rho \alpha \boldsymbol{\nabla} h} \right) - \boldsymbol{\nabla} \cdot \overline{\boldsymbol{\tau}}_{h}^{R} \,, \tag{3.9}$$

Mixture fraction:

$$\overline{\rho} \frac{\mathrm{D}\widetilde{\xi}}{\mathrm{D}t} = \boldsymbol{\nabla} \cdot \left(\overline{\rho \mathcal{D} \boldsymbol{\nabla} \xi} \right) - \boldsymbol{\nabla} \cdot \overline{\boldsymbol{\tau}}_{\xi}^{R} \,, \tag{3.10}$$

Progress variable:

$$\overline{\rho} \frac{\mathrm{D}\widetilde{c}}{\mathrm{D}t} = \overline{\dot{\omega}^{*}} + \boldsymbol{\nabla} \cdot \left(\overline{\rho \mathcal{D} \boldsymbol{\nabla} c} \right) - \boldsymbol{\nabla} \cdot \overline{\boldsymbol{\tau}}_{c}^{R} \,, \tag{3.11}$$

Equation of state:

$$\overline{p} = \frac{\overline{\rho} \Re^{0} \widetilde{T}}{\widetilde{\mathcal{M}}} \,. \tag{3.12}$$

In Eqs. (3.7)–(3.12), there are a number of terms that are unclosed and require modelling. These include the residual stress $\overline{\boldsymbol{\tau}}^{R} \equiv (\overline{\rho} \widetilde{\boldsymbol{U}} \widetilde{\boldsymbol{U}} - \overline{\rho} \widetilde{\boldsymbol{U}} \widetilde{\boldsymbol{U}})$, the residual scalar flux terms $\overline{\boldsymbol{\tau}}_{\varphi}^{R} \equiv (\overline{\rho} \widetilde{\boldsymbol{U}} \varphi - \overline{\rho} \widetilde{\boldsymbol{U}} \widetilde{\varphi})$ in Eqs. (3.9)–(3.11) and the filtered reaction rate $\overline{\dot{\omega}^{*}}$ for partially premixed combustion. These closure problems are similar to the terms that arise through Reynolds averaging the instantaneous balance equations; an example was shown in § 3.2. The molecular diffusion terms in Eqs. (3.9)–(3.11) are approximated as $\boldsymbol{\nabla} \cdot (\overline{\rho \mathcal{D}_{\varphi} \boldsymbol{\nabla} \varphi}) \approx \boldsymbol{\nabla} \cdot (\overline{\rho} \widetilde{\mathcal{D}}_{\varphi} \boldsymbol{\nabla} \widetilde{\varphi})$, where $\mathcal{D}_{\varphi}$ is a characteristic molecular diffusion term representing the diffusion term for a chosen scalar φ.

The residual scalar flux terms are modelled using a gradient hypothesis. This is based on Fick's law of diffusion, where the transport of the scalar flux is in the direction of the scalar gradient $-\boldsymbol{\nabla} \varphi$ (Pope, 2000). Therefore, this is written as

$$\overline{\boldsymbol{\tau}}_{\varphi}^{R} = \overline{\rho} \widetilde{\boldsymbol{U}} \varphi - \overline{\rho} \widetilde{\boldsymbol{U}} \widetilde{\varphi} = -\overline{\rho} \frac{\nu_{T}}{\sigma_{\varphi}} \boldsymbol{\nabla} \widetilde{\varphi} \,, \tag{3.13}$$

where ν_T is the SGS eddy viscosity, which is determined at the SGS level and requires modelling; this is described in further detail in § 3.3.3. In Eq. (3.9), the dimensionless number $\sigma_\varphi \equiv \mathrm{Pr}_T$ and for Eqs. (3.10) and (3.11), the dimensionless number $\sigma_\varphi \equiv \mathrm{Sc}_T$.

Gradient hypothesis models for turbulent premixed flames do not account for the effects of counter-gradient diffusion (Bray *et al.*, 1981; Libby & Bray, 1981; Shepherd *et al.*, 1982). This phenomenon occurs when the flow field in the immediate vicinity of the flame is dominated by thermal dilatation due to chemical reaction. Gradient diffusion on the other hand occurs when the flow field near the flame is dominated by turbulent motions (Veynante *et al.*, 1997). The gradient hypothesis assumption is not an appropriate method for RANS modelling, as the mean of the entire flow field is modelled. However since the large scales of turbulence in LES are directly computed, only the small scales of turbulence are modelled. This means that the assumption is acceptable for LES because only the transport at the small scale needs to be modelled, since the majority of turbulent motions are already computed at the large scale (Lecocq *et al.*, 2010). An example of a model proposed to overcome the counter-gradient transport problem in RANS modelling is given by Veynante *et al.* (1997); models have been reviewed for RANS and LES frameworks by Lecocq *et al.* (2010).

3.3.3 Residual stress closure

The last term in Eq. (3.8) is the residual stress tensor $\overline{\boldsymbol{\tau}}^R \equiv (\overline{\rho}\widetilde{\boldsymbol{U}\boldsymbol{U}} - \overline{\rho}\widetilde{\boldsymbol{U}}\widetilde{\boldsymbol{U}})$. This is decomposed into its isotropic and anisotropic parts respectively as

$$\overline{\boldsymbol{\tau}}^R = \frac{2}{3}\overline{\rho}\widetilde{k}_{\mathrm{sgs}}\,\mathbf{I} + \overline{\boldsymbol{\tau}}^r\,, \tag{3.14}$$

where the SGS kinetic energy $\widetilde{k}_{\mathrm{sgs}}$ is equal to half of the isotropic part of the residual stress tensor and is written as

$$\widetilde{k}_{\mathrm{sgs}} = \frac{1}{2}\left(\widetilde{\boldsymbol{U}\cdot\boldsymbol{U}} - \widetilde{\boldsymbol{U}}\cdot\widetilde{\boldsymbol{U}}\right). \tag{3.15}$$

The SGS kinetic energy is typically absorbed into the filtered pressure term (Pope, 2000). The anisotropic residual stress tensor is modelled using the Boussinesq hypothesis (Hinze, 1959; Pope, 2000; Tennekes & Lumley, 1972)

$$\overline{\boldsymbol{\tau}}^r = -2\,\overline{\rho}\nu_T\left[\widetilde{\boldsymbol{S}} - \frac{1}{3}\left(\boldsymbol{\nabla}\cdot\widetilde{\boldsymbol{U}}\right)\mathbf{I}\right], \tag{3.16}$$

where $\widetilde{\boldsymbol{S}}$ is the symmetric strain rate tensor, which is expressed as

$$\widetilde{\boldsymbol{S}} = \frac{1}{2}\left[\boldsymbol{\nabla}\widetilde{\boldsymbol{U}} + \left(\boldsymbol{\nabla}\widetilde{\boldsymbol{U}}\right)^{\intercal}\right]. \tag{3.17}$$

The eddy viscosity requires modelling in Eq. (3.16) and in the gradient hypothesis expression, as shown in Eq. (3.13). Eddy viscosity based models assume that the anisotropic residual stress tensor and the filtered strain rate are aligned. The study by Meneveau & Katz (2000) concluded that this was not the case and that this assumption leads to overestimating the residual stress. This can make eddy viscosity based models more dissipative than required (Piomelli & Zang, 1991). However, such models are still adequate for turbulent reacting flow, since they contain already filtered quantities and have proven to be robust and widely successful (Gicquel *et al.*, 2012). Three models are used in this work, which are described next and an assessment of their performance is provided in § 4.4.

Smagorinsky based models

The classical Smagorinsky model for the eddy viscosity is given as (Smagorinsky, 1963)

$$\nu_T = (C_s\Delta)^2||\widetilde{\boldsymbol{S}}||\,, \tag{3.18}$$

where $||\widetilde{\boldsymbol{S}}|| = (2\,\widetilde{\boldsymbol{S}} : \widetilde{\boldsymbol{S}})^{1/2}$ is the Frobenius norm of the resolved strain rate tensor and C_s is the Smagorinsky constant, which typically takes the value of $C_s = 0.167$ that was found by Lilly (1967), although the value is dependent on the flow configuration and can vary between 0.1 and 0.2 (Deardorff, 1970; Lesieur & Métais, 1996; Rogallo & Moin, 1984). The model is based on a mixing length hypothesis ($\sim \Delta$) with a velocity difference at that scale ($\sim \Delta||\widetilde{\boldsymbol{S}}||$). The filter width is estimated by taking the cube root of the numerical cell volume. For compressible flow with small density variations, the expression proposed by Yoshizawa (1986) can be used to model $\widetilde{k}_{\text{sgs}}$.

There are some limitations with the constant Smagorinsky model. The value for C_s is dependent on the configuration used, as mentioned previously, and the model does not vanish in laminar flow and is known to be too dissipative in the laminar–turbulent transition region (Moin *et al.*, 1991). This has led to proposed modifications to the classical Smagorinsky model. A dynamic formulation of this model was proposed by Germano *et al.* (1991), in order to calculate C_s dynamically by attempting to estimate the small-scale dissipation of the eddies from knowledge of locally resolved large eddy

motions; this is known as scale-similarity. The dynamic procedure computes values of C_s that vary in space and time. The dynamic procedure also assumes that C_s is filter-invariant. Moin *et al.* (1991) adopted this approach for variable density flows and proposed a method to obtain the local turbulent Prandtl number. Lilly (1992) provided a follow-up study on this procedure by using a least squares analysis to obtain C_s. The test filter for these dynamic procedures is usually taken as $\widehat{\Delta} = 2\Delta$. This procedure is not able to model the backscatter of kinetic energy from the small-scale to large-scale eddies, which leads to the local values of C_s obtained being less than zero (Sarghini *et al.*, 1999). Hence, the spatial averaged procedure should be used to avoid the numerical issues that may arise with backscatter. A thorough overview of Smagorinsky based models is given by Pope (2000).

Wall-adapting local eddy viscosity model

A weakness of this set of Smagorinsky models is accurately capturing the eddy viscosity near solid walls. This is because a non-zero value for ν_T is produced when there is a velocity gradient, as shown by Smagorinsky model in Eq. (3.18). The Van Driest function is commonly used to dampen fluctuations and improve the viscosity in the near-wall regions, as shown by Moin & Kim (1982). However, this is an *ad hoc* modification and incorrectly yields that ν_T scales with the square of the wall distance (Pope, 2000). Moreover, the Smagorinsky constant is limited to $C_s = 0.1$ to ensure that turbulence is sustained, as shown in the channel flow study by Moin & Kim (1982).

The Wall-Adapting Local Eddy (WALE) model is an algebraic model that has been developed by Nicoud & Ducros (1999) to improve modelling the eddy viscosity in the near-wall regions. The model also reproduces the scaling of ν_T with the wall distance cubed (Pope, 2000) and causes ν_T to approach zero near solid walls. As detailed by Nicoud & Ducros (1999), the SGS viscosity model uses the traceless symmetric part of the square of the velocity gradient tensor $\widetilde{\boldsymbol{g}} = \boldsymbol{\nabla}\widetilde{\boldsymbol{U}}$. This is written as

$$\widetilde{\boldsymbol{S}}^* = \frac{1}{2}\left(\widetilde{\boldsymbol{g}}\widetilde{\boldsymbol{g}} + \widetilde{\boldsymbol{g}}^{\intercal}\widetilde{\boldsymbol{g}}^{\intercal}\right) - \frac{1}{3}\operatorname{tr}\left(\widetilde{\boldsymbol{g}}\widetilde{\boldsymbol{g}}\right)\mathbf{I}\,. \tag{3.19}$$

The symmetric strain rate tensor $\widetilde{\boldsymbol{S}} = (\widetilde{\boldsymbol{g}} + \widetilde{\boldsymbol{g}}^{\intercal})/2$ and the asymmetric strain rate tensor $\widetilde{\boldsymbol{\Omega}} = (\widetilde{\boldsymbol{g}} - \widetilde{\boldsymbol{g}}^{\intercal})/2$, which is the rotation rate, can be used to rewrite Eq. (3.19) as

$$\widetilde{\boldsymbol{S}}^* = \widetilde{\boldsymbol{S}}\widetilde{\boldsymbol{S}} + \widetilde{\boldsymbol{\Omega}}\widetilde{\boldsymbol{\Omega}} - \frac{1}{3}\left[\operatorname{tr}\left(\widetilde{\boldsymbol{S}}\widetilde{\boldsymbol{S}}\right) - \operatorname{tr}\left(\widetilde{\boldsymbol{\Omega}}\widetilde{\boldsymbol{\Omega}}\right)\right]\mathbf{I}\,. \tag{3.20}$$

The symmetric strain rate tensor in Eq. (3.17) and the tensor defined by Nicoud & Ducros (1999) in Eq. (3.20) are contained in the algebraic expression for the eddy viscosity, which is written as

$$\nu_T = C_w \Delta^2 \frac{\left(\widetilde{\boldsymbol{S}}^* : \widetilde{\boldsymbol{S}}^*\right)^{3/2}}{\left(\widetilde{\boldsymbol{S}} : \widetilde{\boldsymbol{S}}\right)^{5/2} + \left(\widetilde{\boldsymbol{S}}^* : \widetilde{\boldsymbol{S}}^*\right)^{5/4}}\,, \tag{3.21}$$

where the WALE constant C_w can take a value between 0.3 and 0.6.

k-equation model

An alternative approach modelling the residual stress is to directly obtain $\widetilde{k}_{\text{sgs}}$ through its transport equation (Ghosal *et al.*, 1995; Kim & Menon, 1995; Yoshizawa & Horiuti, 1985). This approach is commonly referred to as a one equation model, since it is assumed that the length scale for $\widetilde{k}_{\text{sgs}}$ is Δ and therefore, no transport equation is required for its dissipation. In addition, the eddy viscosity depends on the SGS kinetic energy rather than the strain rate. The eddy viscosity is modelled using the expression

$$\nu_T = C_v \Delta \widetilde{k}_{\text{sgs}}^{1/2}\,, \tag{3.22}$$

where the model constant C_v can take a constant value of 0.1 or it can be evaluated dynamically (Ghosal *et al.*, 1995).

The transport equation for the SGS kinetic energy is given in form by Chai & Mahesh (2012) and is written as

$$\overline{\rho}\frac{\mathrm{D}\widetilde{k}_{\text{sgs}}}{\mathrm{D}t} = \boldsymbol{\nabla}\cdot\left(\overline{\mu}\boldsymbol{\nabla}\widetilde{k}_{\text{sgs}}\right) + \widetilde{\boldsymbol{U}}\cdot\left(\boldsymbol{\nabla}\cdot\overline{\boldsymbol{\tau}}^R\right) - \boldsymbol{\nabla}\cdot\widetilde{\boldsymbol{f}} - \overline{\rho}\widetilde{\varepsilon}_k + \Pi\,. \tag{3.23}$$

Starting on the right-hand side of Eq. (3.23), the first term represents the molecular diffusion of $\widetilde{k}_{\text{sgs}}$. The second term is the work done through the residual stress tensor, which is determined as written in Eqs. (3.14) and (3.16). The third term is the turbulent transport of $\widetilde{k}_{\text{sgs}}$, where $\overline{\boldsymbol{f}} \equiv (\overline{\rho}\widetilde{\boldsymbol{U}\boldsymbol{U}\boldsymbol{U}} - \overline{\rho}\widetilde{\boldsymbol{U}}\widetilde{\boldsymbol{U}}\widetilde{\boldsymbol{U}})/2$, which is modelled using the gradient hypothesis shown in Eq. (3.13) and is written as $\overline{\boldsymbol{f}} = -\overline{\rho}(\nu_T/\sigma_k)\boldsymbol{\nabla}\widetilde{k}_{\text{sgs}}$. The constant σ_k is assumed to be unity (Pope, 2000). The fourth term is a sink term that represents the dissipation rate of $\widetilde{k}_{\text{sgs}}$. This is modelled using an algebraic expression $\widetilde{\varepsilon}_k \approx C_\varepsilon \widetilde{k}_{\text{sgs}}^{3/2}/\Delta$ with $C_\varepsilon \approx 0.7$ (Pope, 2000). The final term is the pressure work term Π, which is

expressed as

$$\begin{aligned}\Pi &= \widetilde{\boldsymbol{U}} \cdot \boldsymbol{\nabla}\overline{p} - \overline{\boldsymbol{U} \cdot \boldsymbol{\nabla} p} \\ &= \left[\overline{p\big(\boldsymbol{\nabla} \cdot \boldsymbol{U}\big)} - \overline{p}\big(\boldsymbol{\nabla} \cdot \widetilde{\boldsymbol{U}}\big)\right] - \left[\overline{\boldsymbol{\nabla} \cdot \big(p\boldsymbol{U}\big)} - \boldsymbol{\nabla} \cdot \big(\overline{p}\widetilde{\boldsymbol{U}}\big)\right]. \end{aligned} \tag{3.24}$$

This can be modelled using an expression based on the laminar flame properties that is given by Zhang & Rutland (1995), which has been tested in RANS (Kolla & Swaminathan, 2010*a*) and LES (Langella *et al.*, 2017) studies. It was concluded in the LES study by Langella *et al.* (2017) that flame-generated turbulence is negligible and hence, the term Π is neglected from Eq. (3.23).

3.4 Filtered reaction rate closure

The last term that requires closure for the LES framework described thus far is modelling the interactions between turbulence and combustion through the filtered reaction rate. The main challenge with turbulent combustion modelling is accurately capturing the interactions between turbulence and the effects of chemistry in combustion. Various methods have been proposed to model the filtered turbulent reaction rate, where some models contain algebraic expressions and other models require additional transport equations. The development of turbulent reaction rate models within the LES framework are contained in numerous review articles and books (Bilger *et al.*, 2005; Echekki & Mastorakos, 2011; Gicquel *et al.*, 2012; Janicka & Sadiki, 2005; Pitsch, 2006; Poinsot & Veynante, 2012; Swaminathan & Bray, 2011*b*). Most of these models have been extended from earlier models developed for RANS simulations (Brewster *et al.*, 1999; Veynante & Vervisch, 2002). A brief summary of each of these models is given next within the context of premixed and partially premixed combustion, since the simulations undertaken in this work are of such flames. The models are separated into phenomenological, geometric and statistical models, following the review by Gicquel *et al.* (2012).

3.4.1 Phenomenological models

Eddy break-up model

The Eddy Break-Up (EBU) model for RANS modelling is based on the phenomenological analysis of turbulent combustion with high Damköhler ($\mathrm{Da} \gg 1$) and Reynolds ($\mathrm{Re} \gg 1$) numbers (Spalding, 1971). The baseline assumption of the EBU model is that the

chemical time scales are much smaller than the turbulent time scales, i.e., the reaction rate is controlled only by the turbulent mixing rate. Therefore, the reaction zone is viewed as a collection of fresh and burnt fluid parcels. For the context of RANS, the model is taken as inversely proportional to the turbulent time scale $\widetilde{k}/\widetilde{\varepsilon}$. The EBU model for the filtered reaction rate is written as

$$\overline{\dot{\omega}} = C_{\mathrm{EBU}}\overline{\rho}\frac{\widetilde{\varepsilon}}{\widetilde{k}}\sigma_c^2\,. \tag{3.25}$$

The EBU expression shown in Eq. (3.25) contains a model constant C_{EBU} that requires *ad hoc* tuning. The variance of the progress variable σ_c^2 can be assumed to be bimodal $\widetilde{c}(1-\widetilde{c})$ for the limit of an infinitely thin flame (Bray *et al.*, 1985). However, the model contains no chemical reaction mechanisms and the thickness of the flame is also unknown, as the high Damköhler assumption yields a thin flame front. This results in overestimates of the reaction rate. Another disadvantage with the EBU model is that unphysical solutions close to walls are caused by the abnormally high values of $\widetilde{\varepsilon}/\widetilde{k}$.

The model has been extended by Magnussen & Hjertager (1977) for non-premixed combustion with an Arrhenius type expression to include finite rate chemistry and has been adapted by Ertesvåg & Magnussen (2000) for premixed combustion; these models are known as Eddy Dissipation Concept (EDC) models. The EBU models have been adapted for LES by replacing the turbulent time scale with a SGS time scale $\tau_{\mathrm{sgs}} = \widetilde{k}_{\mathrm{sgs}}/\widetilde{\varepsilon}_{\mathrm{sgs}}$ (Fureby & Möller, 1995; Giacomazzi *et al.*, 2004; Möller *et al.*, 1996). In addition, the variance is replaced by the SGS variance and is modelled using an algebraic expression $\sigma^2_{c,\mathrm{sgs}} = \mathscr{A}\Delta^2(\boldsymbol{\nabla}\widetilde{c}\cdot\boldsymbol{\nabla}\widetilde{c})$, where $\mathscr{A}$ can take a constant value or be evaluated dynamically; the constant typically takes a value of 0.5 (Pierce & Moin, 1998). The EBU model is very computationally inexpensive, since it is computed from known quantities and no additional transport equations are used. In addition, the EBU model within LES can capture the effects of wrinkling, unlike the RANS based closure and overestimates are not as severe within the LES approach (Poinsot & Veynante, 2012).

Artificially thickened flame model

The Artificially Thickened Flame (ATF) model was first proposed by Butler & O'Rourke (1977), where the underlying principle of the model is to thicken the laminar flame front by a factor F. This is achieved by multiplying the thermal diffusivity by F to give a flame thickness $F\delta_L^0$, while dividing the Arrhenius constant $\mathcal{A}$ by F, which yields an increased chemical time scale of $F\tau_c$. Hence through a scaling argument, the laminar flame speed

$s_L^0 \sim (F\delta_L^0)/(F\tau_c)$ and remains unchanged when the flame is artificially thickened. This means that the flame front can be resolved on a coarser grid. However, the Damköhler number also decreases by a factor F because the laminar flame speed remains unchanged when the flame is thickened, as shown using the definiton in Eq. (2.41). This causes a reduction in the SGS wrinkling of the flame front. The LES study for turbulent premixed combustion by Colin *et al.* (2000) introduced an efficiency function based on the SGS turbulence properties. Static and dynamic procedures for the efficiency function have been previously proposed (Charlette *et al.*, 2002*a*,*b*; Wang *et al.*, 2011) and a detailed overview of the model validation using numerous benchmark cases is provided by Gicquel *et al.* (2012). While the use of the ATF model can reduce the grid size, the model is still associated with high computational costs, since detailed chemical mechanisms are required to explicitly solve the Arrhenius expression for the reaction rate. The ATF model has been previously combined with other approaches, which include tabulated chemistry approaches (Fiorina *et al.*, 2010; Kuenne *et al.*, 2012; Proch & Kempf, 2014; Wang *et al.*, 2011); tabulated chemistry approaches are elaborated on in § 3.4.3. The one-dimensional laminar flamelets are explicitly filtered using the LES grid size, while the SGS wrinkling effects are considered through the use of a wrinkling factor.

Linear-eddy model

The Linear-Eddy Model (LEM) was introduced to overcome the need for a model to account for changes in the combustion regimes (Kerstein, 1988). The equations for mass and momentum are solved in the typical manner, but the species transport equations are not directly solved. Instead, the molecular diffusion, small-scale and large-scale turbulent convection, and the chemical reaction are all simultaneously modelled at their respective time scales. Decomposing the velocity field into its resolved field from the LES, the resolved SGS fluctuation from $\widetilde{k}_{\text{sgs}}$ and its unresolved SGS fluctuation leads to the LEM model, as viewed by the length and time scales from the LES (McMurtry *et al.*, 1992). This model contains three processes, namely the molecular diffusion at the SGS, the reaction kinetics and sub-grid stirring; there is also a fourth process that represents the phase change for liquid fuel in spray configurations (Menon & Patel, 2006). All of these processes are modelled using a one-dimensional domain within each LES grid cell. The unsteady one-dimensional reaction–diffusion equation for the species mass fraction Y_α is considered, with an additional term to represent the sub-grid stirring. The

reaction–diffusion equation for the LEM model is written as

$$\rho\frac{\partial Y_\alpha^m}{\partial t} = \dot{\omega}_\alpha + \frac{\partial}{\partial s}\left(\rho\mathcal{D}\frac{\partial Y_\alpha^m}{\partial s}\right) + \mathcal{F}_s^m\,, \tag{3.26}$$

where the superscript 'm' indicates that the sub-grid field within each cell is discretised along the co-ordinate s, which represents the local normal specified by the gradient $\partial Y_\alpha^m/\partial s$. The number of cells for the length of each LEM domain within each LES grid cell is chosen to ensure that all scales are resolved within the inertial subrange (McMurtry *et al.*, 1992). The Kolmogorov scale eddies are typically resolved using six LEM cells (Menon & Patel, 2006). Detailed chemical kinetics can be included within this approach using direct integration or *In Situ* Adaptive Tabulation (ISAT) (Pope, 1997). Since the molecular diffusion and chemical reaction kinetics are resolved within the LEM cells, the SGS terms therefore require no modelling. The benefit gained with not requiring an SGS model for the reaction rate is burdened by the significant increase in the computational cost. The term $\mathcal{F}_s^m$ represents the mixing at the SGSs, which is done through a stochastic mapping procedure, known as a *triplet map* (Kerstein, 1988). Further detail on this approach is available in the review by Menon & Kerstein (2011).

3.4.2 Geometric models

Geometric models are based on treating the flame as a flamelet with a high Damköhler number and its surface propagates through the reactant mixture. Two approaches are briefly described here, which are based on tracking the evolution of the flame surface.

Flame surface density approach

The Flame Surface Density (FSD) approach is one of the physical models for the flamelet assumption for reaction rate modelling, where it was recognised by Marble & Broadwell (1977) that the mean reaction rate is proportional to the mean flame surface per unit volume $\overline{\Sigma}$. The general idea is to observe the amount of flame surface area per unit volume $\Sigma = \Sigma(c = \zeta; \boldsymbol{x}, t)$ at a specified location of the reaction progress variable ($c = \zeta$) along an iso-surface within the laminar flame. If the flamelet assumption holds, then the propagation velocity of this surface is close to the unstrained laminar flame speed. Therefore, the reaction rate can be written in the form

$$\overline{\dot{\omega}} = \rho_u s_L^0 I_0 \overline{\Sigma}\,, \tag{3.27}$$

where I_0 is a function accounting for the effect of straining and changes in the local burning velocity (Bray & Cant, 1991). The main challenge of the FSD approach is to find closure for $\overline{\Sigma}$, as this appears in Eq. (3.27) for $\overline{\dot{\omega}}$. Algebraic expressions have been proposed for modelling $\overline{\Sigma}$, which include relating the FSD to the scalar dissipation rate of the progress variable (Borghi, 1990) or using an EBU-type expression, which was deduced using DNS data (Boger *et al.*, 1998) and contains an SGS wrinkling factor $\Xi_\Delta = \overline{|\boldsymbol{\nabla} c|} \,/\, |\boldsymbol{\nabla} \overline{c}|$. This can be obtained by assigning a constant (Boger *et al.*, 1998) or evaluating this factor dynamically (Charlette *et al.*, 2002*a*,*b*).

Another approach for FSD modelling consists of solving an FSD transport equation to obtain $\overline{\Sigma}$. The studies by Pope (1988) and Candel & Poinsot (1990) have rigorously deduced transport equations for the evolution of the flame surface within turbulence. This has been applied within the LES framework by Hawkes & Cant (2001*a*) and it was noted that the net propagation rate of the flame was independent of the filter size and that wrinkling was more prominent at the SGS for higher turbulence levels. The study by Hawkes & Cant (2001*b*) also highlighted that the physically realisable condition $\overline{\Sigma} \geq 0$ may not always be satisfied for algebraic closures or transporting $\overline{\Sigma}$ and care must be taken when using this approach. Further details on FSD approaches are well covered by Cant (2011).

G-equation model

The G-equation model is another example of a physical flamelet model, which was proposed by Williams (1985*a*,*b*) for modelling turbulent premixed flames. This approach is otherwise referred to as a *level-set* approach, since the propagating flame front is captured by defining the front as an iso-surface of a continuous function for a scalar field. The level-set equation used to describe the propagation of the flame front is valid only on this prescribed surface. In addition, the level-set equation does not contain any information on the thickness of the flame and therefore, this approach has been used for thin laminar flamelets within turbulence to study the wrinkling of the flame. In order to use this approach for simulations using RANS or LES methodologies, the level-set function is converted to a distance function (Pitsch, 2006).

The approach uses a non-reactive scalar G, such as a constant temperature or progress variable, and the flame surface is represented by a level set of the scalar at $G(\boldsymbol{x}, t) = G_0$, where G_0 is a fixed constant that represents the flame surface. The field is divided into regions, whereby $G > G_0$ is the product region and $G < G_0$ is the reactant region (Pitsch, 2006). The chosen surface moves with a displacement speed s_d and its normal is

directed into the unburnt reactants; the normal is expressed as $\hat{\mathbf{n}} = -\boldsymbol{\nabla} G \,/\, |\boldsymbol{\nabla} G|$. The displacement speed is closely related to the laminar flame speed and its modelling can consider effects of finite rate chemistry and non-unity Lewis numbers. Since the constant is a non-reactive scalar, it avoids complications associated with counter-gradient diffusion. Furthermore, no source term is required in the corresponding transport equation for G (Peters, 2000). However, the turbulent burning velocity in the transport equation for G needs to be specified as in input function. This marks a key difference between the G-equation model and the FSD approach, as the turbulent burning velocity emerges as a result with the FSD approach (Cant, 2011).

The transport equation for a RANS approach has been derived by Peters (1992, 1999) and its applications are outlined by Chen *et al.* (2007) and Peters (2000). Various approaches has been proposed for LES using the standard filtering operation (Chakravarthy & Menon, 2001; Im *et al.*, 1997; Kim & Menon, 2000). However, these approaches are not valid for both the corrugated flamelets regime and the thin reaction zones regime. The study by Pitsch (2005) provided a revised formulation with a new filter kernel, which averages along the flame surface. However, a main challenge of the formulation is that the flame is only represented by this surface and the broadening of the reaction zone due to turbulence is not resolved and must be modelled. This is a severe issue for $\mathrm{Da} < 1$ and mixing of the scalar field at the resolved scale must be considered in the future (Pitsch, 2006).

3.4.3 Statistical models

The last category of models are known as statistical models, which are based on using a PDF to obtain closure for the filtered reaction rate. As shown in Eq. (3.3), the reaction rate for a chemical species is a function of its composition $\boldsymbol{Y} = (Y_\alpha, \ldots, Y_N)$ and temperature. Therefore, the filtered reaction rate $\overline{\dot{\omega}}_\alpha$ can be obtained from the laminar reaction rate and a multi-dimensional PDF that contains the SGS statistics of the flame. This is expressed using the expression for a joint PDF in Eq. (2.33) as

$$\overline{\dot{\omega}}_\alpha(\boldsymbol{Y}, T) = \int\int \dot{\omega}_\alpha(\boldsymbol{\mathcal{Y}}, \mathcal{T})\, P(\boldsymbol{\mathcal{Y}}, \mathcal{T})\, \mathrm{d}\boldsymbol{\mathcal{Y}}\, \mathrm{d}\mathcal{T}\,, \tag{3.28}$$

where $\boldsymbol{\mathcal{Y}}$ and $\mathcal{T}$ are the sample space variables for $\boldsymbol{Y}$ and T respectively. This sub-grid PDF is determined by either assigning the shape of the PDF, known as the *presumed* PDF approach, or by finding the PDF of the variable by solving a transport equation, which is a *transported* PDF approach. Both approaches do not use geometric assumptions

for the flame front. An overview of PDF based approaches is provided here, which have been reviewed in detail by Pope (2013).

Transported PDF

An early approach for turbulent combustion modelling is to obtain the one-point, one-time PDF for a set of variables that describe the hydrodynamic and thermochemical state of a chemically reacting mixture. This approach was first introduced by Dopazo & O'Brien (1974*a*,*b*) and extended to a Lagrangian particle based approach through the solution of stochastic ordinary differential equations for the particles (Pope, 1985). This has been proposed for RANS modelling (Dopazo, 1994; Pope, 1990) and extended to LES by using a Filtered Density Function (FDF) approach (Gao & O'Brien, 1993; Pope, 1990; Sheikhi *et al.*, 2003); the review by Givi (2006) provides the physical FDF formulation for LES. Transported PDF/FDF approaches are unique compared to other combustion models because the filtered turbulent reaction rate can be obtained from the FDF and therefore, it appears as a closed term. On the other hand, the main challenge for this approach is to accurately capture the molecular mixing, in particular the mixing at the SGS (Haworth, 2010). Celis & Figueira da Silva (2015) have provided a review on modelling the molecular mixing and concluded that no model has been proposed yet that performs well at high Damköhler numbers. Hybrid Lagrangian Particle/Eulerian Mesh (LPEM) algorithms (Rembold & Jenny, 2006) are the current mainstream approach for implementing PDF and FDF methods, but standalone Lagrangian particle methods are still being developed (McDermott & Pope, 2007). However, Lagrangian particle solvers are computationally very expensive, since the number of particles must be one order of magnitude higher than the number of cells in the mesh. An alternative method, known as the stochastic Eulerian fields method, has been proposed to reduce the computational requirements of transported PDF models (Hauke & Valiño, 2004; Mustata *et al.*, 2006; Valiño, 1998). This approach uses standard Eulerian numerical methods with smooth stochastic fields to represent the PDFs instead of solving the stochastic particle differential equations. The approach has proved to be a more practical approach and has been applied in numerous follow-up studies (Jones *et al.*, 2015*a*, 2014, 2015*b*; Jones & Prasad, 2010, 2011). More information on transported PDF/FDF approaches can be found in the reviews by Haworth (2010) and Haworth & Pope (2011).

Conditional moment closure

The Conditional Moment Closure (CMC) model was originally proposed for non-premixed combustion within the RANS framework by Klimenko (1990) and Bilger (1993), where they also derived the CMC transport equation by using a mixture fraction based approach. The general idea is to solve the transport equations for the conditional mean in reactive scalar space, which include the species mass fractions and temperature. This method has since been able to be used for turbulent premixed flames by using the reaction progress variable as the reactive scalar (Mantel & Bilger, 1995). The conditional mean of the species mass fraction can be written based on a conditional chosen scalar. The conditional mean of $Y_\alpha(\boldsymbol{x}, t)$ is expressed as (Klimenko, 1990)

$$Q_\alpha(\zeta; \boldsymbol{x}, t) = \left\langle Y_\alpha(\boldsymbol{x}, t) \,|\, c = \zeta \right\rangle . \tag{3.29}$$

There have been significant advances over the last decade with the CMC model, with a focus on improving the accuracy of closure for the filtered chemical source term (Kronenburg & Mastorakos, 2011). There has also been progress in modelling the different combustion regimes (see Fig. 2.3), as local correlations between scalars can be weakened. This therefore increases fluctuations about the conditional mean and they must be accounted for in the modelling of the unclosed terms, particularly for the chemical source term. The CMC model is beneficial as it can be used with complex geometries and practical applications, such as internal combustion engines and gas turbines (Giusti & Mastorakos, 2017; Kronenburg & Mastorakos, 2011; Zhang & Mastorakos, 2016, 2019). Using CMC within the LES framework was initially achieved for non-premixed flames by Kim & Pitsch (2005) and Navarro-Martinez *et al.* (2005). However for turbulent premixed flames, the amount of progress that has been achieved is less, due to the difficulty with modelling the scalar dissipation rate of c. Amzin *et al.* (2012) were first to test and validate a RANS–CMC approach for premixed flames and the approach was extended to LES by Farrace *et al.* (2018, 2017) by using an algebraic closure for the scalar dissipation rate of c (Dunstan *et al.*, 2013; Kolla *et al.*, 2009); this is elaborated on in § 3.5.1.

Multiple mapping conditioning

The Multiple Mapping Conditioning (MMC) method is a unified approach that combines CMC and PDF methods with a mapping procedure (Klimenko & Pope, 2003; Kronenburg & Mastorakos, 2011; Pope, 1991). The study by Klimenko & Pope (2003) extends CMC, which is used for the evaluation of reactive scalars, and a mapping closure is used for

consistent modelling of the conditional dissipation. This converts the model into a joint PDF method, which enforces mixing between the Lagrangian particles closely located in a reference space. The reference space variables are selected to emulate the properties of a turbulent flow, which have a strong effect on reactive quantities, such as the mixture fraction. The scalars are usually divided into major and minor groups. The fluctuations of the minor scalars are completely restricted or the minor scalars are allowed to fluctuate jointly or relative to the major scalars.

Two formulations of MMC were proposed in the study by Klimenko & Pope (2003), known as deterministic MMC and stochastic MMC. The deterministic formulation is the natural extensions of CMC, where the fluctuations for minor scalars around the conditional means are completely neglected. Several conditioning variables are used to emulate selected Lagrangian properties of turbulence, such as the scalar dissipation and velocities. Klimenko (2005) later extended the deterministic approach by exploiting the neglected minor scalar fluctuations. This approach allows for the reference variables to take other roles in addition to conditioning, such as emulating scalar dissipation fluctuations. The approach also maintains a lower computational cost.

The stochastic formulation is a joint PDF method and MMC is used as the mixing model. The PDF is either assigned *a priori* or simulated typically with Markov processes. In the context of LES, Cleary & Klimenko (2009) introduced sparse Lagrangian particle methods with a generalised MMC closure for the FDF that is used to model the LES sub-grid contributions. The expression 'sparse' refers to the number of stochastic particles, which can be as low as one stochastic particle per 30 LES cells. This concept was originally developed for non-premixed flames by Cleary & Klimenko (2009) and has recently been used to model multi-regime combustion in lifted non-premixed flames (Galindo *et al.*, 2017) and one flame from the Sydney swirl flame series (Huo *et al.*, 2019). The stochastic variant of the model has recently been applied to premixed combustion by Straub *et al.* (2019, 2018). The filtered progress variable is used as the reference variable for the MMC mixing model. In order to resolve the flame, the ATF model (Colin *et al.*, 2000) is used and a two-dimensional flamelet generated manifold approach is used to model the chemical source term. This MMC–ATF approach for premixed combustion was applied to the stratified flame at Darmstadt (Seffrin *et al.*, 2010; Stahler *et al.*, 2017).

Presumed PDF models

The computational cost of including full chemical kinetics in turbulent combustion simulations remains extremely high, which has led to statistical flamelet models being

developed as an approach for chemistry reduction. Statistical flamelet models are based on using a presumed PDF and one of the earliest models proposed for premixed flames is the Bray–Moss–Libby (BML) model (Bray *et al.*, 1981; Libby & Bray, 1981). The presumed PDF approach for turbulent premixed flames can be written in terms of the reaction progress variable and its moments. The progress variable is determined using temperature, as shown in Eq. (2.24), and its sample space variable for the PDF is denoted as ζ. The BML model treats the reaction zone as a statistical laminar flamelet (Bray *et al.*, 1985). The reacting flow field is separated into reactants ($0 \leq \zeta \leq \zeta^*$), reaction zones ($\zeta^* \leq \zeta \leq 1-\zeta^*$) and combustion products ($1-\zeta^* \leq \zeta \leq 1$). Their corresponding probabilities are denoted as $\alpha(\boldsymbol{x})$, $\gamma(\boldsymbol{x})$ and $\beta(\boldsymbol{x})$ respectively, with the condition $\alpha(\boldsymbol{x}) + \beta(\boldsymbol{x}) + \gamma(\boldsymbol{x}) = 1$ (Bray *et al.*, 1985). The PDF that is in the limit $\zeta^* \to 0$ is expressed as

$$P(c, \boldsymbol{x}) = \alpha(\boldsymbol{x})\,\delta(c) + \beta(\boldsymbol{x})\,\delta(1-c) + \gamma[H(0) - H(1)](\boldsymbol{x})\,f(c;\boldsymbol{x})\,, \tag{3.30}$$

where the Dirac delta functions $\delta(c)$ and $\delta(1-c)$ represent the reactants and products respectively and H represents the Heaviside function. The internal part of the PDF $P(c, \boldsymbol{x})$ is represented by the function $f(c;\boldsymbol{x})$, which must satisfy the condition $\int_0^1 f(c;\boldsymbol{x})\,\mathrm{d}c = 1$. Since it is assumed that the Damköhler number is high, the flame is treated as a very thin unstrained interface that separates the reactants and the products ($\gamma \ll 1$) and α and β can be expressed as a first moment of c and the heat release parameter τ.

An underlying principle of the BML model is that the reaction zone thickness is neglected. This means the consumption and production rates for each chemical species cannot be explicitly obtained. An alternative presumed PDF approach is based on using *tabulated chemistry*, which involves using flame data and storing this within a look-up table as a function of the chosen parameterising variables. This was initially proposed by Liew *et al.* (1981) for non-premixed flames and Libby & Bray (1980) for premixed flames. For non-premixed flames, the PDF is based on the mixture fraction while for premixed flames, the PDF is based on the progress variable. Bradley *et al.* (1990) extended this by proposing the use of a joint PDF for the mixture fraction and progress variable; this is known as the *mixedness-reactedness* approach. This approach has been extended to include the strain rate as a third variable in the joint PDF (Bradley *et al.*, 1998). The study by Maas & Pope (1992*a*,*b*) developed the Intrinsic Low-Dimensional Manifold (ILDM) approach, which exploits the fast chemistry assumptions through analysing the chemical time scales associated with the reaction system. An eigenvalue analysis of the

local Jacobian of the chemical source term is used and allows chemical time scales that are smaller than a given time to be neglected. The eigenvectors which represent the slow chemical processes are used to construct a low-dimensional manifold in composition space. A limitation with this approach is that a high number of control variables are required for hydrocarbon–air flames, due to the number of species and this significantly increases the number of dimensions of the look-up table. Furthermore, the assumption of fast chemical time scales leads to issues with predicting the low temperature domains of the flame and more dimensions in the look-up table are required, which leads to a significantly increased computational cost.

Two models have been independently proposed to overcome these limitations of the ILDM approach, namely the well-known Flamelet-Generated Manifold (FGM) (van Oijen & de Goey, 2000) and the Flame Prolongation of ILDM (FPI) models (Gicquel *et al.*, 2000). These approaches involve obtaining the solution of one-dimensional freely propagating laminar premixed flames over a range of equivalence ratios and storing the reaction rates and species mass fractions as functions of defined co-ordinates, which can include the mixture fraction, progress variable, strain rate or enthalpy. It was concluded by Fiorina *et al.* (2003) that the flamelet database can be constructed using either freely propagating or burner-stabilised flames. The progress variable is usually taken as a single or linear combination of species mass fractions (Fiorina *et al.*, 2015; Ihme *et al.*, 2012), as noted in § 2.2.2. The reaction zone is typically described using a beta function PDF. This PDF is parameterised using the filtered progress variable and its SGS variance for premixed flames within the LES framework. This beta PDF P_β for the progress variable is written as (Cook & Riley, 1994)

$$P_\beta(\zeta) = \frac{\zeta^{a-1}(1-\zeta)^{b-1}}{B(a,b)} \quad \text{with} \quad B(a,b) = \int_0^1 \zeta^{a-1}(1-\zeta)^{b-1}\,\mathrm{d}\zeta\,, \tag{3.31}$$

and the constants a and b are related to $\widetilde{c}$ and $\sigma^2_{c,\mathrm{sgs}}$ by

$$a = \widetilde{c}\left[\frac{\widetilde{c}(1-\widetilde{c})}{\sigma^2_{c,\mathrm{sgs}}} - 1\right] \quad \text{with} \quad b = \frac{(1-\widetilde{c})a}{\widetilde{c}}\,. \tag{3.32}$$

This PDF is parameterised using $\widetilde{c}$ and its SGS variance $\sigma^2_{c,\mathrm{sgs}}$, which is either transported or modelled; the issue of whether to model or transport the SGS variance is addressed in § 3.5.1.

Another example of a presumed PDF flamelet approach is the Flamelet/Progress Variable (FPV) model, which was originally proposed by Pierce & Moin (2004). This

approach builds on the previous works on steady (Peters, 1984) and unsteady (Pitsch & Steiner, 2000*a*) flamelet models and views the turbulent diffusion flame as an ensemble of steady laminar flamelets, which are solved using the steady form of the flamelet equation in mixture fraction space, as written in Eq. (2.18). However, the significant difference between these approaches is that the diffusion flamelet solutions in the FPV model are parameterised using the progress variable instead of the mixture fraction scalar dissipation rate. Therefore, this requires the solution of the progress variable transport equation for the LES, which indirectly maps the chemical species. The thermochemical variables are mapped using a presumed joint PDF of two statistically independent PDFs for the mixture fraction and the progress variable. The mixture fraction PDF is parameterised using the filtered mixture fraction and its SGS variance, while the reaction progress variable is parameterised using only the filtered progress variable. Ihme *et al.* (2005) extended the approach by including a transport equation for the SGS variance of the progress variable and included this term as a control variable within the progress variable PDF. The FPV model has been developed to include unsteady flamelets by Pitsch & Ihme (2005). It was also shown by Ihme *et al.* (2005) that using a presumed beta PDF for reaction progress variable PDF instead of a delta distribution provided improvements in the case with strong local extinction and reignition. A Statistically Most Likely Distribution (SMLD) can be employed to increase the moments of the progress variable PDF, but led to only marginal improvements in the model (Ihme & Pitsch, 2008*a*,*b*).

Statistical flamelet models have proven to be beneficial in terms of reducing computational requirements and are able to provide physically meaningful results of turbulent flames within complex configurations. The state-of-the-art FPV and FGM models either opt not to include the SGS progress variable variance within the beta PDF for the progress variable, or choose to model $\sigma^2_{c,\mathrm{sgs}}$ with an algebraic model (Pierce & Moin, 1998) or using its transport equation. If the SGS variance for the progress variable has been transported, e.g., as done in the study by Ihme *et al.* (2005), the scalar dissipation rate $\chi_{c,\mathrm{sgs}}$ in the transport equation for $\sigma^2_{c,\mathrm{sgs}}$ is modelled using an algebraic expression based on turbulent mixing (Pierce & Moin, 1998; Pitsch, 2006). This algebraic expression is suitable for passive scalars, since their gradients are generated through turbulence. However, such models do not account for the effects of chemical reactions, thermal expansion and the multi-scale turbulent–combustion interactions. Hence, the gradients for the progress variable are influenced by combustion and turbulence (Swaminathan & Bray, 2005). The study by Langella & Swaminathan (2016) demonstrated that algebraic models based on passive scalar gradients for $\sigma^2_{c,\mathrm{sgs}}$ and $\chi_{c,\mathrm{sgs}}$ are not sufficient for modelling turbulent

premixed flames. A transport equation for $\sigma^2_{c,\mathrm{sgs}}$ is included, which contains an algebraic closure for $\chi_{c,\mathrm{sgs}}$ that was developed by Kolla *et al.* (2009) for RANS and Dunstan *et al.* (2013) for LES. This has also yielded improvements for modelling partially premixed flames (Ruan *et al.*, 2012, 2014). Hence, the flamelet model that has been developed within the doctoral theses by Ruan (2013), Langella (2016) and Chen (2017) is used in this work and an overview of the model is given next.

3.5 Partially premixed flamelet model

3.5.1 Adiabatic flame model

The combustion modelling framework uses the unstrained flamelets concept and is based on the early *mixedness-reactedness* concept proposed by Bradley *et al.* (1998, 1990), which was also used for the FPV model, as described in § 3.4.3. This closure has been tested for premixed combustion using RANS and URANS methodologies for laboratory-scale flames (Ahmed & Swaminathan, 2013, 2014; Darbyshire & Swaminathan, 2012; Kolla & Swaminathan, 2010*b*; Swaminathan *et al.*, 2011) and for practical burners (Ruan *et al.*, 2015). This model for the LES of premixed combustion has been developed by Langella & Swaminathan (2016) and tested for laboratory-scale flames (Langella *et al.*, 2016*a*,*b*). The use of this model for partially premixed combustion has also been developed by Chen *et al.* (2017) and applied for gas turbine combustor simulations (Chen *et al.*, 2019*a*,*b*; Langella *et al.*, 2018*a*). With this closure, the thermochemical quantities that are required for partially premixed combustion are the first two moments of the mixture fraction and progress variable, and the thermochemical enthalpy, where the latter variable is required to calculate the temperature. The transport equations for the filtered enthalpy, mixture fraction and progress variable are shown in Eqs. (3.9), (3.10) and (3.11) respectively. The filtered transport equation for the SGS mixture fraction variance $\sigma^2_{\xi,\mathrm{sgs}}$ is given as

$$\overline{\rho}\frac{\mathrm{D}\sigma^2_{\xi,\mathrm{sgs}}}{\mathrm{D}t} \simeq \boldsymbol{\nabla}\cdot\left[\left(\overline{\rho\mathcal{D}}+\overline{\rho}\frac{\nu_T}{\mathrm{Sc}_T}\right)\boldsymbol{\nabla}\sigma^2_{\xi,\mathrm{sgs}}\right] - \overline{\rho}\widetilde{\chi}_{\xi,\mathrm{sgs}} + 2\,\overline{\rho}\frac{\nu_T}{\mathrm{Sc}_T}\left(\boldsymbol{\nabla}\widetilde{\xi}\cdot\boldsymbol{\nabla}\widetilde{\xi}\right), \tag{3.33}$$

where the mixture fraction scalar dissipation rate $\widetilde{\chi}_{\xi,\mathrm{sgs}}$ is modelled using a linear relaxation model $\widetilde{\chi}_{\xi,\mathrm{sgs}} = C_\xi\,(\nu_T/\Delta^2)\,\sigma^2_{\xi,\mathrm{sgs}}$ with a model constant $C_\xi = 2$ (Pierce & Moin, 1998).

The filtered transport equation for the SGS progress variable variance $\sigma^2_{c,\mathrm{sgs}}$ is written similarly as

$$\overline{\rho}\frac{\mathrm{D}\sigma^2_{c,\mathrm{sgs}}}{\mathrm{D}t} \simeq \boldsymbol{\nabla}\cdot\left[\left(\overline{\rho\mathcal{D}}+\overline{\rho}\frac{\nu_T}{\mathrm{Sc}_T}\right)\boldsymbol{\nabla}\sigma^2_{c,\mathrm{sgs}}\right] - \overline{\rho}\widetilde{\chi}_{c,\mathrm{sgs}} + 2\,\overline{\rho}\frac{\nu_T}{\mathrm{Sc}_T}\left(\boldsymbol{\nabla}\widetilde{c}\cdot\boldsymbol{\nabla}\widetilde{c}\right) + 2\left(\overline{c\,\dot{\omega}^*}-\widetilde{c}\,\overline{\dot{\omega}^*}\right). \tag{3.34}$$

As mentioned previously, the SGS scalar dissipation rate $\widetilde{\chi}_{c,\mathrm{sgs}}$ is influenced by both combustion and turbulence and thus, its modelling should include those influences. The LES model proposed by Dunstan *et al.* (2013), which has been tested thoroughly in previous studies (Chen *et al.*, 2019*a*,*b*; Gao *et al.*, 2014, 2015; Langella & Swaminathan, 2016; Langella *et al.*, 2015, 2017, 2016*a*), is used here and is written as

$$\widetilde{\chi}_{c,\mathrm{sgs}} = \mathcal{F}\left[2\,K_c(\xi)\frac{s^0_L(\xi)}{\delta^0_L(\xi)} + \left(C_3 - \tau(\xi)C_4\mathrm{Da}_\Delta\right)\left(\frac{2\,u'_\Delta}{3\,\Delta}\right)\right]\frac{\sigma^2_{c,\mathrm{sgs}}}{\beta_c}. \tag{3.35}$$

The function $\mathcal{F} = 1-\exp\left(-0.75\,\Delta^+\right)$ ensures that the SGS dissipation rate approaches zero when the filter width Δ approaches zero and the normalised filter width is $\Delta^+ = \Delta/\delta^0_L$. The variables s^0_L, δ^0_L and τ in Eq. (3.35) depend on the local mixture fraction (Ruan *et al.*, 2014). The heat release parameter is the normalised temperature rise and is defined as $\tau(\xi) = (T_b(\xi)-T_u)/T_u$. These values are obtained from one-dimensional unstrained planar laminar premixed flame calculations over the flammability range in mixture fraction space; this procedure is described in § 3.5.2. The symbol $K_c = 0.79\,\tau$ is a thermochemical parameter for turbulence–combustion interactions. The other parameters are defined as $C_3 = 1.5\sqrt{\mathrm{Ka}_\Delta}/(1+\sqrt{\mathrm{Ka}_\Delta})$ and $C_4 = 1.1/(1+\mathrm{Ka}_\Delta)^{0.4}$ following earlier studies (Dunstan *et al.*, 2013; Langella *et al.*, 2015). The dimensionless parameters Da_Δ and Ka_Δ are defined as $\mathrm{Da}_\Delta = s^0_L\Delta/(u'_\Delta\delta^0_L)$ and $\mathrm{Ka}_\Delta = (u'_\Delta/s^0_L)^{3/2}(\delta^0_L/\Delta)^{1/2}$ respectively. The sub-grid velocity scale u'_Δ is modelled using a scale-similarity approach as $u'_\Delta = C_q\sum|\widetilde{\boldsymbol{U}}-\widehat{\widetilde{\boldsymbol{U}}}|$, where $\widehat{\widetilde{\boldsymbol{U}}}$ is the velocity field obtained using a Gaussian test filter of width $\widehat{\Delta}\simeq 2\,\Delta$ (Pope, 2000). This model for u'_Δ is used to be consistent with the previous studies (Langella *et al.*, 2016*a*; Ruan *et al.*, 2014), but different models are available, as outlined by Langella *et al.* (2018*b*).

It was established in previous studies that the parameters in Eq. (3.35) and their values are closely connected to certain physical aspects of turbulence–combustion interactions and their influences on the scalar dissipation rate (Dunstan *et al.*, 2013; Gao *et al.*, 2014; Kolla *et al.*, 2009). The term $\sigma^2_{c,\mathrm{sgs}}/\beta_c$ in Eq. (3.35) comes from influences of

flame curvature induced by wrinkling, where β_c is a flame curvature parameter. This scale-dependent parameter here will either use a constant value $\beta_c = 7.5$, which is a proposed optimum value for methane–air combustion (Langella *et al.*, 2015), or be obtained dynamically (Gao *et al.*, 2015; Langella *et al.*, 2015).

The last term that requires closure is the filtered reaction rate for partially premixed combustion $\overline{\dot{\omega}^*}$, which also appears as a source term in Eq. (3.34). This is determined by treating it as a combination of the instantaneous burning modes, which is written as (Bray *et al.*, 2005)

$$\overline{\dot{\omega}^*} = \underbrace{\overline{\dot{\omega}}}_{\text{Premixed mode}} + \underbrace{\overline{\rho\chi_\xi \frac{c}{\psi^{\text{eq}}} \frac{\mathrm{d}^2\psi^{\text{eq}}}{\mathrm{d}\xi^2}}}_{\text{Non-premixed mode } \overline{\dot{\omega}}_{\text{np}}} + \underbrace{\overline{2\,\rho\chi_{\xi c} \frac{1}{\psi^{\text{eq}}} \frac{\mathrm{d}\psi^{\text{eq}}}{\mathrm{d}\xi}}}_{\text{Cross term } \overline{\dot{\omega}}_{\text{cdr}}}, \tag{3.36}$$

where the instantaneous mixture fraction dissipation rate is defined using Eq. (2.17) and the cross-dissipation is $\chi_{\xi c} = \mathcal{D}(\boldsymbol{\nabla}\xi \cdot \boldsymbol{\nabla}c)$ (Bray *et al.*, 2005). The third term on the right-hand side of Eq. (3.36) represents the contribution that arises through the cross dissipation rate of ξ and c. Previous studies have shown that this term is at least one order of magnitude smaller than the other two contributions and therefore, this term is neglected in this work (Domingo *et al.*, 2005; Ruan *et al.*, 2012). The reaction progress variable is defined using the sum of the CO and CO_2 mass fractions following previous studies (Fiorina *et al.*, 2003; Ruan *et al.*, 2015). This is written as

$$c = \frac{Y_{\text{CO}} + Y_{\text{CO}_2}}{Y^{\text{eq}}_{\text{CO}}(\xi) + Y^{\text{eq}}_{\text{CO}_2}(\xi)}, \tag{3.37}$$

where the superscript 'eq' denotes the equilibrium condition at a given mixture fraction.

The first term of Eq. (3.36) is the premixed contribution, which is based on a presumed sub-grid joint PDF approach for the mixture fraction and progress variable. This is written as (Ruan *et al.*, 2014)

$$\overline{\dot{\omega}} = \overline{\rho} \int_0^1 \int_0^1 \frac{\dot{\omega}(\eta,\zeta)}{\rho(\eta,\zeta)} \widetilde{P}(\eta,\zeta)\, \mathrm{d}\eta\, \mathrm{d}\zeta\,, \tag{3.38}$$

where $\dot{\omega}(\eta,\zeta)$ and $\rho(\eta,\zeta)$ are the flamelet reaction rate and density respectively, which are obtained through one-dimensional unstrained planar laminar premixed flame calculations over the flammability range in mixture fraction space. The joint PDF contains the sample space variables η and ζ for the first two moments of the mixture fraction and progress variable respectively. This density-weighted PDF is approximated as

$\widetilde{P}(\eta,\zeta) \approx \widetilde{P}_\beta(\eta\,;\,\widetilde{\xi},\sigma^2_{\xi,\mathrm{sgs}}) \times \widetilde{P}_\beta(\zeta\,;\,\widetilde{c},\sigma^2_{c,\mathrm{sgs}})$ and the shape of the two PDFs are assigned using beta functions. This assumes that both beta PDFs are statistically independent. However, there are fluctuations of ξ and c that influence each other and this correlation is significant in RANS modelling, as the fluctuations are entirely modelled. This correlation is included within the joint PDF through the *copula* method (Darbyshire & Swaminathan, 2012; Ruan *et al.*, 2014). The DNS study by Chen *et al.* (2018*b*) demonstrated that the sub-grid correlation is relatively less influential on the time-averaged statistics because the contribution related to the large-scale fluctuations is resolved in LES. Therefore, the sub-grid correlation is not considered and the statistical independence assumption for the two beta PDFs is made for simplicity. It is assumed that reaction source term in Eq. (3.34) is $\overline{c\,\dot{\omega}^*} \approx \overline{c}\,\overline{\dot{\omega}}$ for modelling simplicity and is evaluated in a similar manner to Eq. (3.38). This is written as

$$\overline{c\,\dot{\omega}} = \overline{\rho}\int_0^1\int_0^1 \zeta\,\frac{\dot{\omega}(\eta,\zeta)}{\rho(\eta,\zeta)}\,\widetilde{P}(\eta,\zeta)\,\mathrm{d}\eta\,\mathrm{d}\zeta\,. \tag{3.39}$$

The non-premixed contribution $\overline{\dot{\omega}}_{\mathrm{np}}$ is modelled using the expression (Ruan *et al.*, 2014)

$$\overline{\dot{\omega}}_{\mathrm{np}} = \overline{\rho}\,\widetilde{c}\,\widetilde{\chi}_\xi \int_0^1 \frac{1}{\psi^{\mathrm{eq}}(\eta)}\frac{\mathrm{d}^2\psi^{\mathrm{eq}}(\eta)}{\mathrm{d}\eta^2}\widetilde{P}(\eta)\,\mathrm{d}\eta\,. \tag{3.40}$$

The non-premixed contribution does not come from counterflow diffusion flamelets and is instead a correction term for the premixed contribution term. This term contains the filtered mixture fraction scalar dissipation rate, which is the sum of the resolved and SGS contributions and is expressed as $\widetilde{\chi}_\xi = \widetilde{\mathcal{D}}(\boldsymbol{\nabla}\widetilde{\xi}\cdot\boldsymbol{\nabla}\widetilde{\xi}) + \widetilde{\chi}_{\xi,\mathrm{sgs}}$. The non-premixed contribution is typically significant in the stoichiometric regions, where strong levels turbulent diffusion of the fuel and oxidiser are present.

The premixed and non-premixed reaction rate expressions in Eqs. (3.38) and (3.40) contain the filtered density, which is computed using the filtered equation of state, as shown in (3.12). This requires knowledge of the Favre-filtered temperature and the mixture molecular mass. The filtered temperature is obtained using the filtered enthalpy transport equation and is calculated as $\widetilde{T} = T_0 + (\widetilde{h} - \widetilde{\Delta h_f^0})/\widetilde{c}_p$. This step is required because the temperature is not directly obtained from the energy equation, since the enthalpy is transported instead. The three thermochemical quantities for the mixture $\widetilde{\Delta h_f^0}$, $\widetilde{c}_p$ and $\widetilde{\mathcal{M}}$ are calculated in a similar manner as the premixed reaction rate term in

Eq. (3.38) and are given as

$$\widetilde{c}_p = \int_0^1 \int_0^1 c_p^e(\eta,\zeta)\,\widetilde{P}(\eta,\zeta)\,\mathrm{d}\eta\,\mathrm{d}\zeta\,, \tag{3.41}$$

$$\widetilde{\Delta h}_f^0 = \int_0^1 \int_0^1 \left(\sum_{\alpha=1}^{N} Y_\alpha(\eta,\zeta)\Delta h_f^0\right)\widetilde{P}(\eta,\zeta)\,\mathrm{d}\eta\,\mathrm{d}\zeta\,, \tag{3.42}$$

$$\widetilde{\mathcal{M}} = \int_0^1 \int_0^1 \left(\sum_{\alpha=1}^{N} \frac{Y_\alpha(\eta,\zeta)}{\mathcal{M}_\alpha}\right)^{-1}\widetilde{P}(\eta,\zeta)\,\mathrm{d}\eta\,\mathrm{d}\zeta\,. \tag{3.43}$$

It should be noted that Eq. (3.41) includes its temperature dependence at the flamelet level through the use of an effective specific heat capacity, which is defined as $c_p^e = (T_1 - T_0)^{-1}\int_{T_0}^{T_1} c_p(T)\,\mathrm{d}T$. The aforementioned flamelet thermochemical variables, along with the reaction rate and density, are determined through the solution of one-dimensional unstrained planar laminar premixed flame calculations. This procedure is briefly outlined next.

3.5.2 Flamelet library

The overall procedure of generating the flamelet library is shown by a schematic in Fig. 3.1. In this work, the flamelet calculations are undertaken using the PREMIX code in CHEMKIN–II (Kee *et al.*, 1985) and Cantera (v2.3.0) (Goodwin *et al.*, 2017) using the GRI–Mech 3.0 chemical mechanism (Smith *et al.*, 2000), which involves 53 species and 325 chemical reactions. The flamelet library is obtained through the solution of the steady one-dimensional flame equations for species transport and energy (in the form of temperature), which are written as

One-dimensional species transport:

$$\rho U\frac{\mathrm{d}Y_\alpha}{\mathrm{d}x} = \dot{\omega}_\alpha + \frac{\mathrm{d}}{\mathrm{d}x}\left(\rho\mathcal{D}_\alpha\frac{\mathrm{d}Y_\alpha}{\mathrm{d}x}\right), \tag{3.44}$$

One-dimensional temperature:

$$\rho c_p U\frac{\mathrm{d}T}{\mathrm{d}x} = \frac{\mathrm{d}}{\mathrm{d}x}\left(\lambda\frac{\mathrm{d}T}{\mathrm{d}x}\right) + \rho\frac{\mathrm{d}T}{\mathrm{d}x}\left(\sum_{\alpha=1}^{N} c_{p,\alpha}\mathcal{D}_\alpha\frac{\mathrm{d}Y_\alpha}{\mathrm{d}x}\right) - \sum_{\alpha=1}^{N} h_\alpha\dot{\omega}_\alpha\,, \tag{3.45}$$

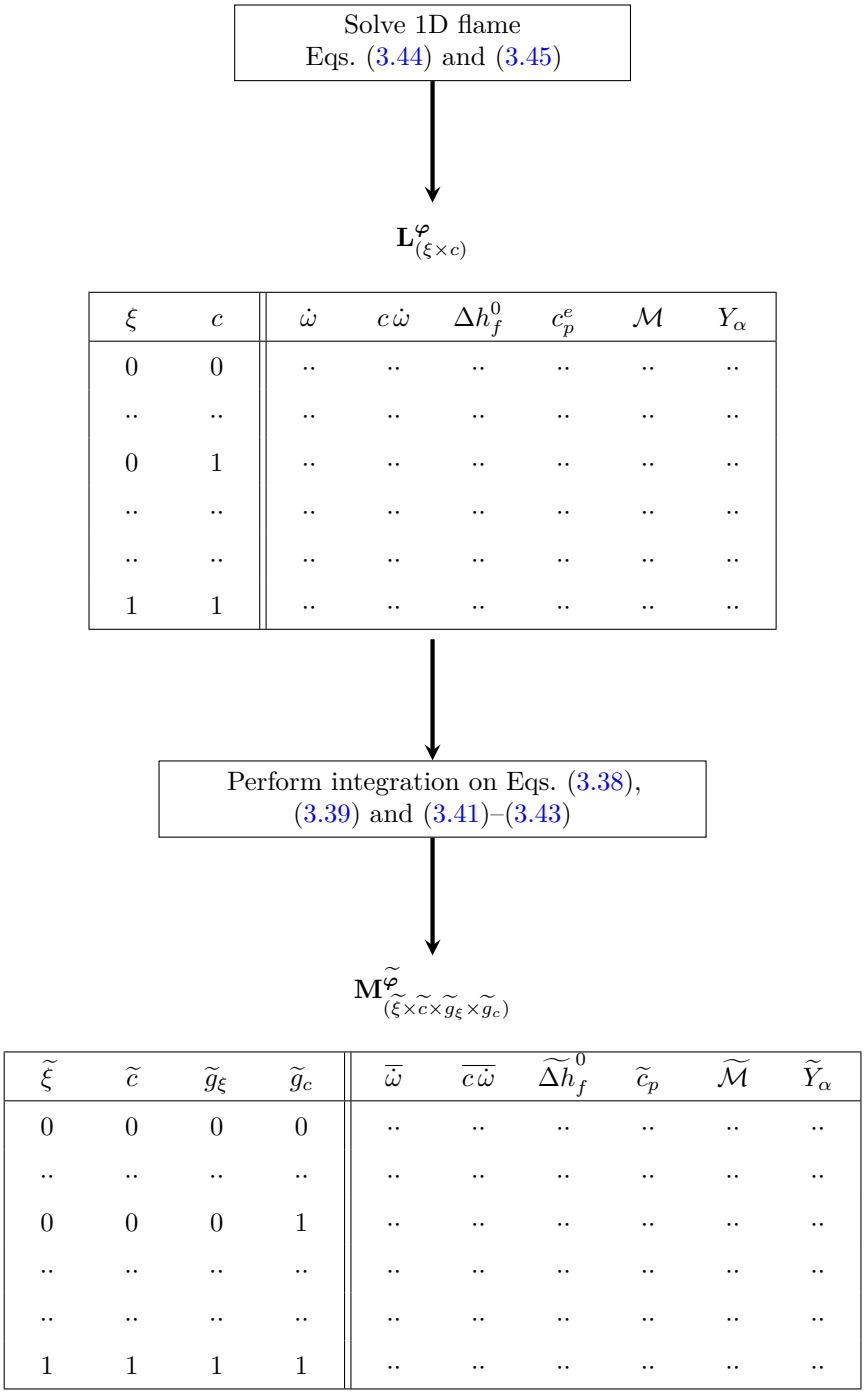

Fig. 3.1 Schematic of generating the flamelet look-up table, adapted from the diagram by Chen (2017).

where mass conservation is achieved through $\rho U = \rho_u s_L^0$.

The thermochemical properties for the one-dimensional flame are mapped through the progress variable, which is discretised with N_c points. The overall flamelet reaction rate is taken as $\dot{\omega} = \dot{\omega}_{\mathrm{CO}} + \dot{\omega}_{\mathrm{CO_2}}$. This is then repeated to obtain the flamelets across the flammability range by varying the equivalence ratio. The set of flamelets are then mapped in mixture fraction space with N_ξ points. This results in a two-dimensional laminar flame matrix $\mathbf{L}^{\varphi}$ of size $\mathrm{N}_\xi \times \mathrm{N}_c$ for each thermochemical variable φ.

The next step is to perform the integration to obtain the look-up table for the filtered quantities. The SGS variances for the mixture fraction and progress variable are normalised respectively as $\widetilde{g}_\xi = \sigma^2_{\xi,\mathrm{sgs}}/\widetilde{\xi}(1-\widetilde{\xi})$ and $\widetilde{g}_c = \sigma^2_{c,\mathrm{sgs}}/\widetilde{c}(1-\widetilde{c})$, where the denominators are the maximum possible variances between the fresh reactants and burnt products across the flammability range (Bray, 1979). Integrating results in a four-dimensional matrix $\mathbf{M}^{\widetilde{\varphi}}$ of size $\mathrm{N}_{\widetilde{\xi}} \times \mathrm{N}_{\widetilde{c}} \times \mathrm{N}_{\widetilde{g}_\xi} \times \mathrm{N}_{\widetilde{g}_c}$. This look-up table is interpolated during the LES using four-dimensional linear interpolation schemes, in order to obtain the thermochemical variable quantities in each grid cell. It was shown by Ruan *et al.* (2014) that this interpolation procedure produced errors of approximately 1 %.

3.5.3 Extension for non-adiabatic flamelets

It is of interest in this work to introduce non-adiabatic effects into turbulent flame simulations. Heat loss effects can be modelled by considering non-adiabatic chemistry in flamelet calculations. Early work employed an enthalpy defect approach in the flamelets, which is achieved by considering the heat loss through radiation (Bray & Peters, 1994; Hossain *et al.*, 2002; Marracino & Lentini, 1997). A burner-stabilised flame method for building the library for FGM and FPI approaches with non-adiabatic flamelets was introduced by van Oijen & de Goey (2000) and Fiorina *et al.* (2003) respectively, where the non-adiabatic effects are included by submitting a heat flux to the wall of the burner, in order to decrease the enthalpy in that region (Donini *et al.*, 2017; Pantangi *et al.*, 2014). This is achieved by including the enthalpy as an additional tabulated variable. Other approaches have more recently been proposed for non-adiabatic flamelet approaches, which include a wall heat transfer model (Ma *et al.*, 2018) and a Perfectly Stirred Reactor (PSR) approach (Chen *et al.*, 2018*a*) that have been applied for Moderate or Intense Low-oxygen Dilution (MILD) combustion.

The original studies by van Oijen & de Goey (2000) and Fiorina *et al.* (2003) for the FGM and FPI approaches respectively suggested that freely propagating premixed flames or burner-stabilised flames can be used to build the flame library for adiabatic conditions.

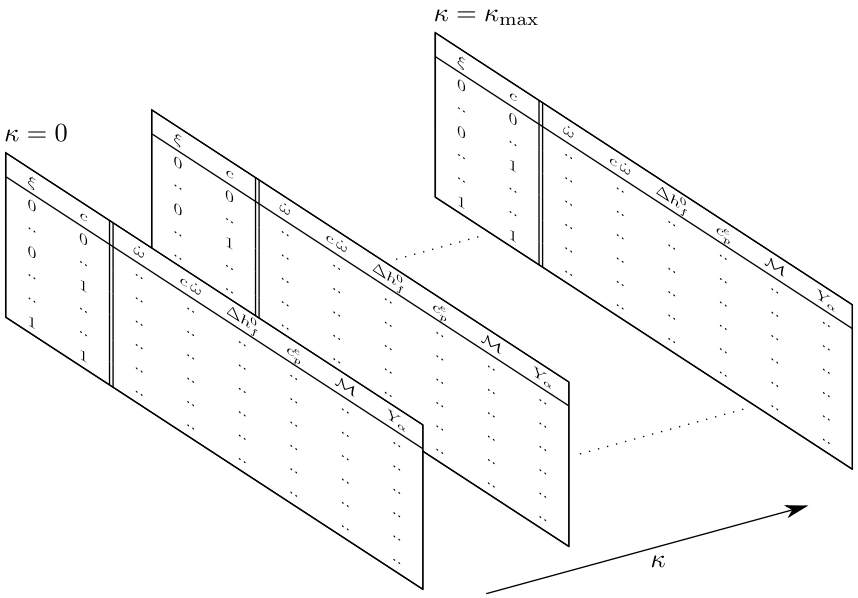

Fig. 3.2 Schematic of generating the flamelet solutions with the heat release damping approach.

However, only the burner-stabilised flame method was used for the non-adiabatic flame calculations. The study by Proch & Kempf (2015) proposed a method for undertaking non-adiabatic calculations of freely propagating premixed flames. The heat loss is introduced by scaling the source term due to chemical reaction in the one-dimensional energy equation. The method is referred to as the heat release damping method. This approach has also been applied to non-premixed flames by introducing the same scaling on to the chemical reaction source term in the counterflow diffusion flame equation, as well as to the energy equation (Wollny *et al.*, 2018).

The heat release damping approach is applied in this work to build a non-adiabatic flamelet library, since the adiabatic library is constructed using one-dimensional freely propagating premixed flames, as described in § 3.5.2. The non-adiabatic effects at the flamelet level are included in the premixed contribution of the filtered reaction rate in Eq. (3.36) by following the approach outlined by Proch & Kempf (2015) that was proposed for premixed flames. This approach is adopted here by undertaking the calculations in mixture fraction space at different heat loss levels. The heat loss is introduced in the one-dimensional freely propagating premixed laminar flame calculations by altering the chemical reaction source term in the energy equation. The one-dimensional energy equation that is shown in Eq. (3.45) is rewritten as

$$\rho c_p U \frac{\mathrm{d}T}{\mathrm{d}x} = \frac{\mathrm{d}}{\mathrm{d}x}\left(\lambda \frac{\mathrm{d}T}{\mathrm{d}x}\right) + \rho \frac{\mathrm{d}T}{\mathrm{d}x}\left(\sum_{\alpha=1}^{N} c_{p,\alpha}\mathcal{D}_\alpha \frac{\mathrm{d}Y_\alpha}{\mathrm{d}x}\right) - (1-\kappa)\sum_{\alpha=1}^{N} h_\alpha \dot{\omega}_\alpha \,, \tag{3.46}$$

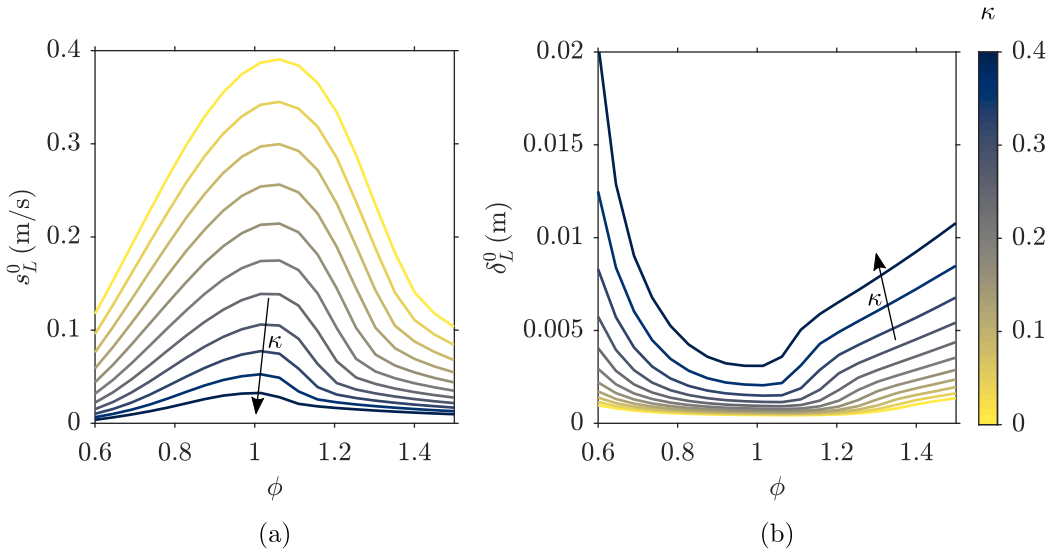

Fig. 3.3 Flamelets generated using the heat release damping approach (Proch & Kempf, 2015; Wollny *et al.*, 2018). The flame speed (a) and flame thickness (b) are plotted against ϕ for different values of κ in the range $0 \leq \kappa \leq 0.4$.

where κ is the introduced heat loss factor. For a given equivalence ratio, laminar flame calculations are performed for a number of heat loss factor values ranging from $\kappa = 0$ (adiabatic conditions) to $\kappa = 0.4$ with increments of 0.04 to give 11 flamelet solutions for each equivalence ratio. These calculations are then repeated for 20 different equivalence ratios covering the flammability range. Beyond $\kappa = 0.4$, no flame solution could be obtained for the case closest to the lean flammability limit. This produces N_{h^*} two-dimensional laminar flame matrices $\mathbf{L}^{\varphi}$ of size $\mathrm{N}_{\xi} \times \mathrm{N}_c$, as shown previously in § 3.5.2. A schematic of the laminar non-adiabatic flamelet calculations procedure is shown in Fig. 3.2. As shown in Fig. 3.3, the flame speed decreases and the flame thickness increases when the heat loss factor is increased. For the highest heat loss case with $\kappa = 0.4$, the value for s_L^0 is less than 8 % of the adiabatic value for all equivalence ratios. Therefore, the flame is considered to be quenched for higher heat losses.

It is possible in the LES that the heat loss (enthalpy defect) is higher than that for $\kappa = 0.4$ at a given local equivalence ratio. To cover this in the flamelet table, four more heat loss levels are included and these solutions are obtained by progressively lowering the gas temperature to 300 K for each solution point in the one-dimensional laminar flame at the last heat loss factor $\kappa = 0.4$. As a result, only the temperature related quantities (T, c_p, ρ and h) are different in these four additional solutions, whereas the mixture composition remains the same as that for the solution produced with $\kappa = 0.4$. In total, there are 15 (heat loss levels) $\times$ 20 (equivalence ratios) computed flamelet solutions

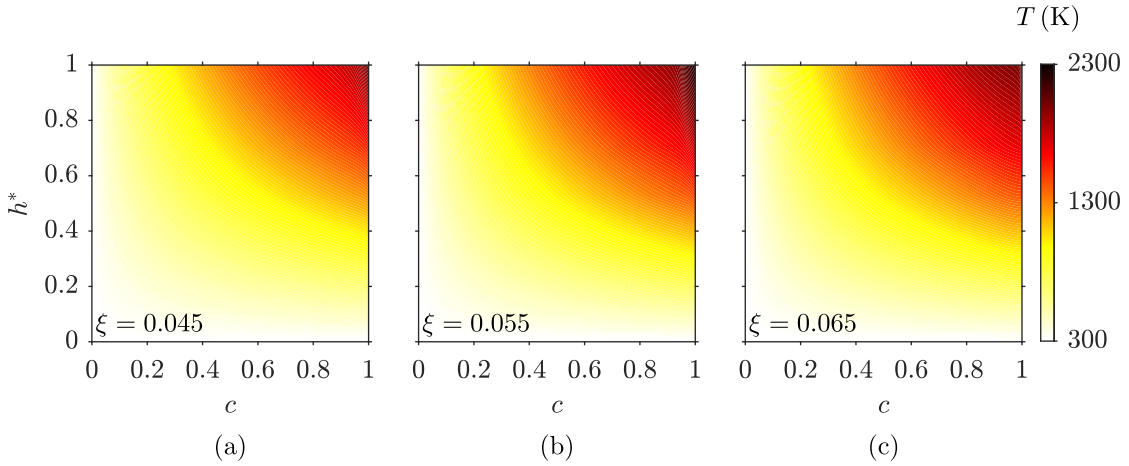

Fig. 3.4 Contour plots of the flamelet temperature over progress variable and normalised enthalpy space.

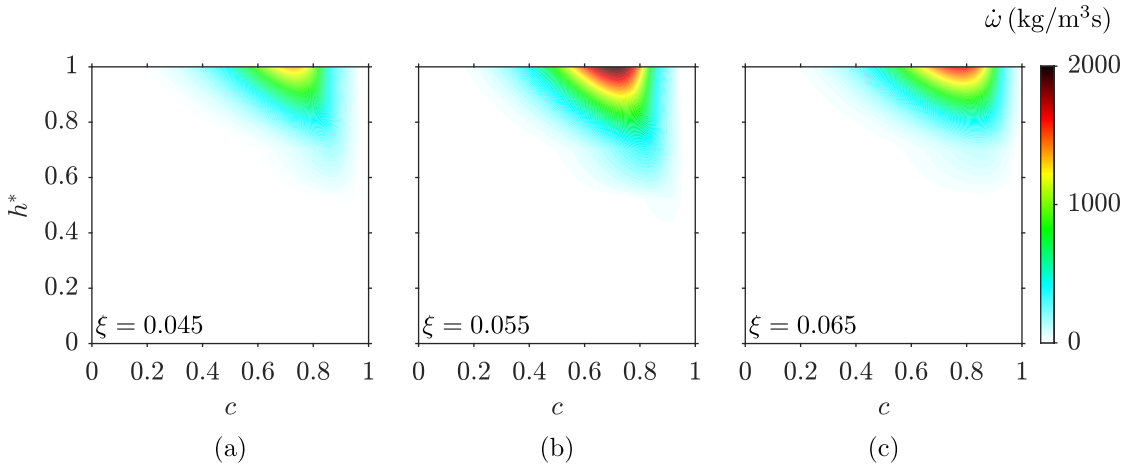

Fig. 3.5 Contour plots of the flamelet reaction rate over progress variable and normalised enthalpy space.

and subsequently, these one-dimensional solutions are interpolated into three-dimensional space and are parameterised by the mixture fraction, progress variable and enthalpy.

For the non-adiabatic flamelets, the progress variable definition is rewritten as

$$c = \frac{Y_{\mathrm{CO}} + Y_{\mathrm{CO_2}}}{Y^{\mathrm{eq}}_{\mathrm{CO}}(\xi, h^*) + Y^{\mathrm{eq}}_{\mathrm{CO_2}}(\xi, h^*)}\,, \tag{3.47}$$

and the normalised enthalpy is given by

$$h^* = \frac{h - h_{\mathrm{min}}(\xi, c)}{h_{\mathrm{ad}}(\xi, c) - h_{\mathrm{min}}(\xi, c)}\,. \tag{3.48}$$

The subscripts ‘min’ and ‘ad’ denote the minimum and adiabatic mixture enthalpies respectively at a given mixture fraction and progress variable. The values of h_{min} and

$h_{\max}$ are tabulated as functions of ξ and c for the normalisation of the filtered enthalpy in the LES. Figures 3.4 and 3.5 respectively show the temperature and reaction rate fields obtained from the flamelet calculations in c and h^* space for three representative ξ values. It can be seen that the reaction rate is zero when $h^* < 0.6$ for all three mixture fractions, whereas the temperature smoothly decreases to 300 K as h^* approaches zero. This is physically consistent with the heat loss process when the flame is quenched by the wall and reaction rate decreases to zero, but the temperature decreases gradually through heat conduction.

These laminar flame solutions are then used for the integration of filtered quantities required in the LES. Following the previous study by Chen *et al.* (2018*a*), the filtered premixed reaction rate source term is modelled as

$$\overline{\dot{\omega}} = \overline{\rho} \int_0^1 \int_0^1 \int_0^1 \frac{\dot{\omega}(\eta, \zeta, \mathcal{H})}{\rho(\eta, \zeta, \mathcal{H})} \widetilde{P}(\eta, \zeta, \mathcal{H}) \, \mathrm{d}\eta \, \mathrm{d}\zeta \, \mathrm{d}\mathcal{H} \,, \tag{3.49}$$

where $\widetilde{P}(\eta, \zeta, \mathcal{H}) \approx \widetilde{P}_\beta(\eta \,;\, \widetilde{\xi}, \sigma^2_{\xi,\mathrm{sgs}}) \times \widetilde{P}_\beta(\zeta \,;\, \widetilde{c}, \sigma^2_{c,\mathrm{sgs}}) \times \delta(\mathcal{H} - \widetilde{h}^*)$ is the joint PDF of the mixture fraction, progress variable and normalised enthalpy and $\mathcal{H}$ denotes the sample space variable for the normalised enthalpy. The presumed beta PDF distribution is again used for ξ and c, while a Dirac delta function is used for h^*. The look-up table for the LES now has five dimensions of size $\mathbf{M}^{\widetilde{\varphi}}$ with dimensions $\mathrm{N}_{\widetilde{\xi}} \times \mathrm{N}_{\widetilde{c}} \times \mathrm{N}_{\widetilde{g}_\xi} \times \mathrm{N}_{\widetilde{g}_c} \times \mathrm{N}_{\widetilde{h}^*}$.

3.6 Numerical solvers

The combustion closure has been implemented into two CFD codes that are used in this work, which are PRECISE–MB and OpenFOAM. Both solvers are based on the finite volume methodology (Ferziger & Perić, 2002). In this work, the former solver is used for modelling turbulent premixed flames, whereas the latter solver is used for modelling turbulent partially premixed flames. Both of these codes are highly parallelised with the open source Message Passage Interface (Open MPI) library. These solvers are briefly described next.

3.6.1 PRECISE–MB

The numerical simulations that are conducted using PRECISE–MB (Anand *et al.*, 1999) use structured hexahedral multi-block computational grids with a Cartesian co-ordinate system. The blocks in the computational grid are manually split across each of the

processors with the aim of achieving an equal distribution of the grid cells across the processors, which optimises parallelisation. The spatial gradients of the filtered transport equations are discretised using second-order accurate central difference schemes and the discretised equations are time marched using an implicit second-order scheme (Ferziger & Perić, 2002). The velocity and pressure coupling is maintained using the Semi-Implicit Method for Pressure-Linked Equations-Consistent (SIMPLEC) algorithm (Van Doormaal & Raithby, 1984). The constant and dynamic Smagorinsky models are implemented for modelling the residual stress.

The cases that use this solver are premixed flames and hence, the filtered transport equations for the mixture fraction and its SGS variance are not included. Non-adiabatic flamelets are not used with this solver. Consequently, the joint PDF is replaced by a single beta PDF for the progress variable that is parameterised with the filtered progress variable and its SGS variance. The second-order central difference schemes used for $\widetilde{c}$ and $\sigma^2_{c,\mathrm{sgs}}$ use a blending factor of 0.1 to control small overshoots, since these numerical schemes are unbounded. A blending factor of 0.1 indicates that the numerical scheme used is 10 % first-order accurate and 90 % second-order accurate. The reaction rate term $\overline{\dot{\omega}^*}$ in Eq. (3.36) is replaced with just the premixed term and is written as

$$\overline{\dot{\omega}} = \overline{\rho} \int_0^1 \frac{\dot{\omega}(\zeta)}{\rho(\zeta)} \widetilde{P}(\zeta)\, \mathrm{d}\zeta\,, \tag{3.50}$$

where the PDF $\widetilde{P}(\zeta) = \widetilde{P}_\beta(\zeta\,;\widetilde{c}, \sigma^2_{c,\mathrm{sgs}})$. The flamelets are computed using the PREMIX code and the final look-up table for the LES is two-dimensional of size $\mathrm{N}_c \times \mathrm{N}_{\widetilde{g}_c}$. This look-up table has $\mathrm{N}_{\widetilde{c}} = 101$ and $\mathrm{N}_{\widetilde{g}_c} = 51$ evenly distributed points for $\widetilde{c}$ and $\sigma^2_{c,\mathrm{sgs}}$ respectively. To capture the effects of the flame being exposed to air at ambient conditions, a filtered fluid marker is used following earlier studies (Langella & Swaminathan, 2016; Langella *et al.*, 2016*b*), which is required to obtain the thermochemical property of the mixtures. This is determined by using a mixing rule $\widetilde{\varphi}_{\mathrm{mix}} = \widetilde{Z}\widetilde{\varphi}_{\mathrm{reac}} + (1-\widetilde{Z})\widetilde{\varphi}_{\mathrm{air}}$, where the subscripts 'reac' and 'air' denote the values of $\widetilde{\varphi}$ for the flamelet and air respectively. This procedure allows for the inclusion of mixing or dilution of the burnt mixture with the entrained air. The dilution is tracked by transporting the filtered fluid marker $\widetilde{Z}$, where its transport equation is given as

$$\overline{\rho}\frac{\mathrm{D}\widetilde{Z}}{\mathrm{D}t} = \boldsymbol{\nabla}\cdot\left(\overline{\rho\mathcal{D}\boldsymbol{\nabla}Z}\right) - \boldsymbol{\nabla}\cdot\overline{\boldsymbol{\tau}}^R_Z\,, \tag{3.51}$$

Flames	$N_{\widetilde{\xi}}$	$N_{\widetilde{c}}$	$N_{\widetilde{g_\xi}}$	$N_{\widetilde{g_c}}$	$N_{\widetilde{h^*}}$
Adiabatic	46	75	15	40	-
Non-adiabatic	44	51	15	31	15

Table 3.1 Look-up table dimensions for adiabatic and non-adiabatic partially premixed flames.

where $\overline{\boldsymbol{\tau}}_Z^R \equiv (\overline{\rho}\widetilde{\boldsymbol{U}Z} - \overline{\rho}\widetilde{\boldsymbol{U}}\widetilde{Z})$ is modelled using a gradient hypothesis, as outlined previously in § 3.3.2. The values of $\widetilde{Z}$ vary between zero and unity, with unity representing the fuel–air mixture and zero representing pure air.

All of the simulations conducted using PRECISE–MB for this study used the Darwin cluster (University of Cambridge High Performance Computing Service). Each node has two 2.6 GHz eight-core Sandy Bridge E5–2670 processors.

3.6.2 OpenFOAM

The CFD toolkit OpenFOAM (v2.3.0) (Weller *et al.*, 1998) is a widely used open source software for commercial and academic purposes. The filtered transport equations for mass and momentum, the residual stress closure models described in § 3.3.3, the pressure-correction algorithms, and the spatial and temporal numerical schemes are already implemented into OpenFOAM. This means a thermo-physical solver can be separately developed that solves the equations required for the combustion modelling described in § 3.5 and call upon the other already implemented libraries directly from the main OpenFOAM source code. Chen (2017) has implemented the partially premixed unstrained flamelet model into OpenFOAM, which include the five transport equations for the mixture fraction, progress variable and their SGS variances, and the thermochemical enthalpy.

A Pressure-based Implicit Splitting of Operators (PISO) method (Issa, 1986) is used as the pressure-correction algorithm. This scheme is iterated for a maximum of five times within each time step on an outer loop with the Semi-Implicit Method for Pressure-Linked Equations (SIMPLE) scheme (Patankar, 1980), in order to ensure close coupling between the pressure and velocity. This iterative scheme on the PISO algorithm is referred to as the PIMPLE algorithm in OpenFOAM. All of the residual stress closure models described in § 3.3.3 are available to use, but the dynamic Smagorinsky model, along with other dynamic procedures, are not used, since the procedure does not work well on unstructured tetrahedral grids (Pope, 2000). The solver process is illustrated in

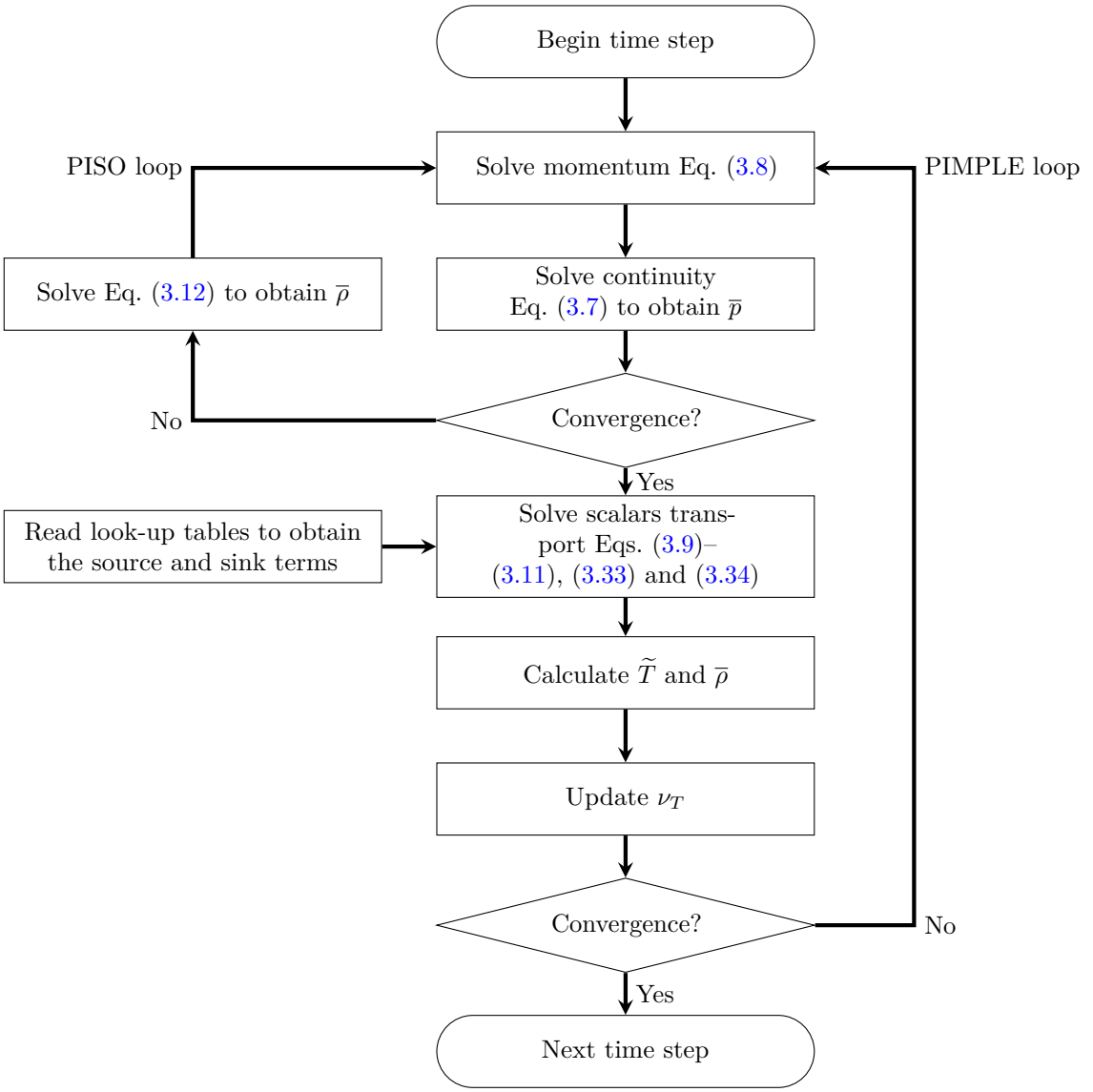

Fig. 3.6 Schematic of the OpenFOAM LES combustion solver, adapted from the diagram by Chen (2017).

Fig. 3.6. The dimensions of the look-up tables that are required for the scalar transport equations for the adiabatic and non-adiabatic flamelet approaches are shown in Table 3.1. Second-order central difference schemes are used to discretise the spatial gradients with no blending factors. A first-order implicit Euler scheme is used for the temporal derivatives and therefore, a small constant time step is used to ensure suitable accuracy for the time derivatives and that the Courant–Friedrichs–Lewy (CFL) number remains below 0.4 across the whole domain. The CFL number is used to monitor the stability of the numerical schemes, which is written as $\mathrm{CFL} = |U|\Delta t/\Delta x$, where Δt is the time step and

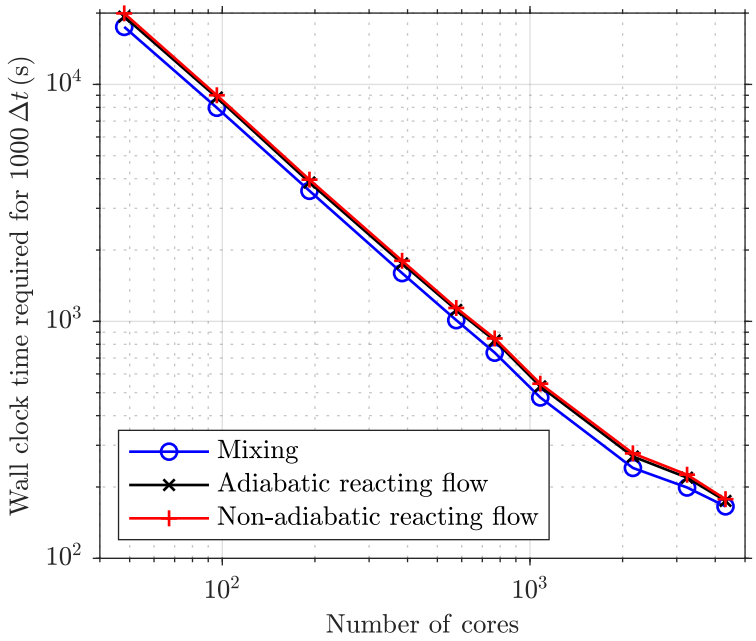

Fig. 3.7 Comparison of the elapsed wall-clock time for the simulation of $1000\Delta t$ in physical time. Three tests are undertaken, which are the flow and mixing fields, reacting flow and non-adiabatic reacting flow for a flame in a gas turbine model combustor, which is described in § 4.4.

Δx is the cell spacing. It is recommended that the CFL number should be less than 1 for isothermal flow simulations and less than 0.4 for reacting flow simulations; see the OpenFOAM v2.3.0 manual (Weller *et al.*, 1998).

The simulations undertaken with OpenFOAM are run using ARCHER, a national high performance computing facility in the United Kingdom. The ARCHER hardware consists of the Cray XC30 MPP supercomputer, external login nodes and post-processing nodes, and the associated file systems; there are a total of 118080 processing cores available across 4920 nodes. A chart is shown in Fig. 3.7, which shows a comparison of the wall-clock time that is required for 1000 time steps Δt for mixing, reacting flow and reacting flow with the non-adiabatic closure of the combustion modelling framework that is detailed in § 3.5. All three simulations use the same time step and the number of subiterations for each time step is the same. The simulations are undertaken of a gas turbine model combustor, which is described in § 4.4 and § 7.2; the grid is unstructured with 20 million tetrahedral cells. It is shown that there is a near-perfect scaling up to 2160 cores for this grid, but the scaling is still satisfactory up to 4320 cores. For all of the cases, the elapsed wall-clock time is increased by approximately 9 % for reacting flow. The wall-clock time required increases by a further 2.5 % for the non-adiabatic closure.

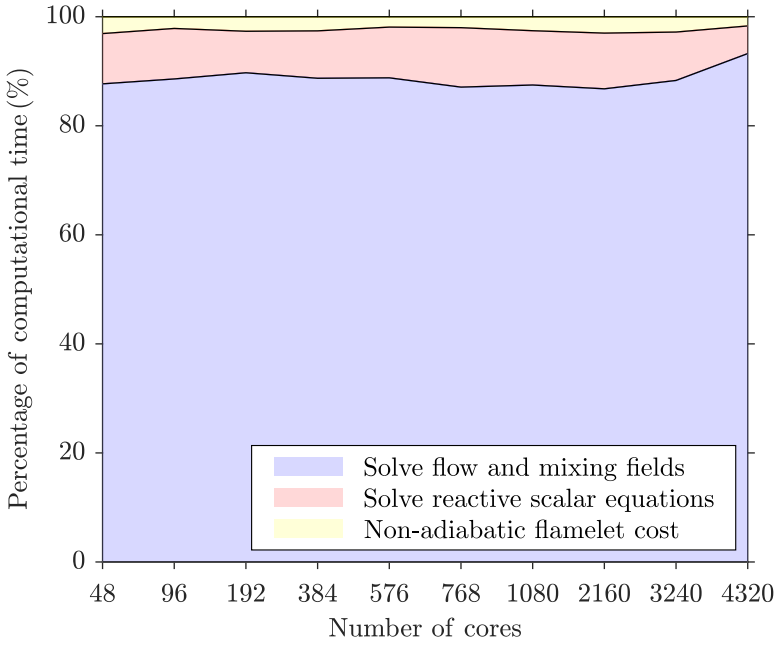

Fig. 3.8 Computational time split of the OpenFOAM LES combustion solver for the cases shown in Fig. 3.7.

The split in the computational cost is shown in Fig. 3.8. In general, the split between solving the flow and mixing fields, the reactive scalar equations and the non-adiabatic flamelet cost is the same between 48–2160 cores. The performance chart shows that the combustion modelling framework is inexpensive, as the cost remains below 15 % across the range of cores used. The cost of solving the flow and mixing fields increases when the number of cores is beyond 2160 cores, which affects the scaling of the solver. It is deemed that 1080 cores is an optimum value for this case by considering both the computational speed and from a post-processing point of view; the number of files written at each writing interval increases with the number of cores used.

3.7 Summary

In this chapter, an overview has been provided of the different approaches of CFD with a focus on using the LES methodology. The necessary filtered balance equations required for modelling turbulent reacting flows are shown and an overview of the state-of-the-art combustion models for LES is presented. The unstrained flamelet model for premixed and partially premixed flames has been shown, along with the proposed extension for non-adiabatic effects and a brief description of the CFD solvers tested in this work is

provided. The remainder of this work will use the premixed and partially premixed flamelet models for flames that are stabilised behind a bluff body or with swirling flow.

Chapter 4

Isothermal Flow Validation Cases

Three burner configurations are presented in this chapter, where validations are undertaken of the numerical set-up and the computational grid using isothermal flow statistics. Two of these cases consist of a bluff body flame holder, where a recirculation zone is formed behind the bluff body, and the notable difference is the presence of walls for one configuration. The third configuration is a swirling flow case, which represents a case that is comparable to a practical combustion chamber. These three cases all exhibit complex fluid mechanics that are different from one case to another. The flow fields must be inherently resolved in the simulations by the chosen LES modelling framework, numerical set-up and computational grid. It is imperative that the flow fields are accurately captured before undertaking simulations of turbulent reacting flows.

4.1 Criteria for isothermal flow validations

The computational grids for this work are created using ANSYS ICEM CFD, which is used to create structured and unstructured hexahedral or tetrahedral grids. The distribution of the turbulent kinetic energy field and the resolution of the near-wall boundary layers are used to assess the quality of the grid. For the former, a general rule of thumb proposed by Pope (2000) is used, whereby a computational grid is deemed to be suitable provided at least 80 % of the turbulent kinetic energy is resolved within the LES. This is expressed as

$$\text{Pope's criterion} = \frac{\langle \widetilde{k}_{\text{res}} \rangle}{\langle \widetilde{k}_{\text{res}} \rangle + \langle \widetilde{k}_{\text{sgs}} \rangle} \geq 0.8\,. \tag{4.1}$$

The resolved turbulent kinetic energy is approximated by summing the total resolved isotropic variances of the velocity field $\langle \widetilde{k}_{\text{res}} \rangle = (\langle \sigma^2_{U,\text{res}} \rangle + \langle \sigma^2_{V,\text{res}} \rangle + \langle \sigma^2_{W,\text{res}} \rangle)/2$, where the resolved variance for the velocity field is determined as $\langle \sigma^2_{\boldsymbol{U},\text{res}} \rangle = \langle \widetilde{\boldsymbol{U}}^2 - \langle \widetilde{\boldsymbol{U}} \rangle^2 \rangle$. The SGS contribution is typically absorbed into the filtered pressure term and therefore, it has to be approximated through a model. The instantaneous SGS turbulent kinetic energy is typically approximated as $\widetilde{k}_{\text{sgs}} \approx 3\, u'^2_\Delta/2$. The sub-grid velocity scale can be estimated using an eddy viscosity model $u'_\Delta \approx C_q \nu_T/\Delta$, where C_q is a modelling constant (Pope, 2000). The eddy viscosity is assigned using one of the models described in § 3.3.3.

The quality of the grid is also monitored by ensuring that the boundary layers are resolved in the near-wall regions, especially for the cases that contain a bluff body. This is important because it ensures that the flow separation at the trailing edge is accurately captured, since this affects the shear layer that leads to the formation of the recirculation zone. In addition, the recirculation zone that forms behind bluff bodies, along with the recirculation zone in the swirling flow case, contains combustion products of high temperatures and this zone acts as a constant ignition source. The dimensionless wall distance y^+ can be used to assess the wall refinement of a grid for the viscous sublayer in the boundary layer (Hanjalić & Launder, 2011). Wall functions are not used in this work and therefore, the viscous sublayer is resolved if the condition of $y^+ \leq 5$ is met. The grids that are generated in this work have at least two computational cells present within the viscous sublayer, which has been determined *a priori* using experimental data, if available, or *a posteriori* with the LES results.

The grid is then validated through comparisons with experimental measurements of the time-averaged pointwise data obtained through non-intrusive laser techniques with high frequencies. These techniques include Laser Doppler Velocimetry (LDV), also known as Laser Doppler Anemometry (LDA), Planar Laser-Induced Fluorescence (PLIF), Particle Image Velocimetry (PIV), Coherent Anti-stokes Raman Spectroscopy (CARS), and spontaneous Raman scattering and Rayleigh techniques. For the isothermal flow grid validations, the time-averaged velocity fields are compared with the ensemble averaged filtered velocity fields $\langle \widetilde{\boldsymbol{U}} \rangle$ and their time-averaged r.m.s. fields.

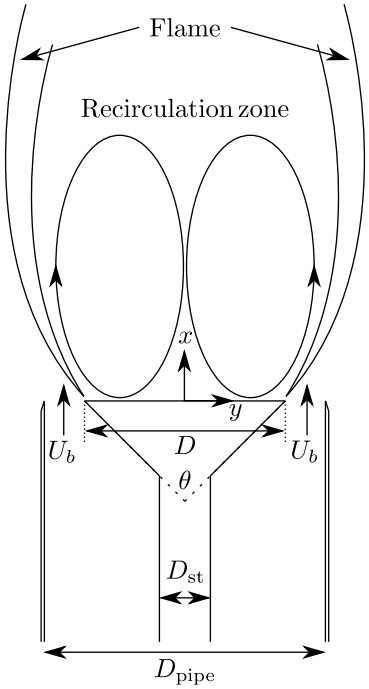

Fig. 4.1 Schematic of the open bluff body burner studied by Kariuki *et al.* (2012).

Parameter	Value	Description
D	25 mm	Bluff body diameter
D_{pipe}	35 mm	Pipe diameter
D_{st}	6.35 mm	Stem diameter
T_u	298 K	Inlet temperature for air
U_{air}	0.1 m/s	Coflow velocity (see Fig. 4.2)
U_b	21.6 m/s	Reference bulk velocity at the bluff body base
θ	90°	Bluff body apex angle

Table 4.1 Physical parameters of the open bluff body burner studied by Kariuki *et al.* (2012).

4.2 Open bluff body burner

4.2.1 Experiment

The open bluff body burner used for this study was developed by Balachandran *et al.* (2005) and experimental measurements have been obtained by Dawson *et al.* (2011), Kariuki (2013) and Kariuki *et al.* (2012, 2015). The schematic of this burner is shown in Fig. 4.1 and the geometrical parameters of the burner are listed in Table 4.1. This burner consisted of an inlet pipe of length 300 mm with an inner diameter of $D_{\text{pipe}} = 35$ mm

that was mounted to a plenum with a flow straightener. A conical bluff body with an apex angle of $\theta = 90°$ and a base diameter of $D = 25\,\text{mm}$ was mounted on to a rod of diameter $D_{\text{st}} = 6.35\,\text{mm}$ and concentrically fitted within the inlet pipe. The base of the bluff body was exposed to air at atmospheric conditions, where there was no external flow present. Atmospheric air with a temperature of $T_u = 298\,\text{K}$ was fed through the pipe with a constant mass flow rate to give the measured bulk-mean velocity of $U_b = 21.6\,\text{m/s}$ at the base of the bluff body, which is used as the reference velocity for this study. There was not a turbulence generating device present upstream of the bluff body base and therefore, only the turbulence produced through shear is present, which originates from the trailing edge of the bluff body.

4.2.2 Computational set-up

The computational model of the open bluff body burner is shown in Fig. 4.2. A block structured computational grid is used to discretise the computational volume with a total cell count of approximately 3.6 million hexahedral cells. There is refinement near the bluff body walls and base and in the regions where the shear layers and filtered flames are expected to be present. The minimum cell size in these regions is approximately 0.2 mm and the wall boundary layers are resolved by placing two cells within the viscous sublayer. The dynamic Smagorinsky model is used as closure for the residual stress.

The computational grid starts at 70 mm upstream of the bluff body base, which is twice the pipe diameter, since this was a sufficient length for turbulence to naturally evolve before the bluff body. A cylindrical region of length $30D$ and diameter $10D$ is added downstream from the bluff body base, as illustrated in Fig. 4.2, to represent the boundary entraining the atmospheric air. A top-hat velocity profile is prescribed at the inlet boundary with a value that gives the reference bulk-mean velocity of $U_b = 21.6\,m/s$ at the bluff body base. A constant velocity of $U_{\text{air}} = 0.1\,\text{m/s}$ is specified at the boundary marked as 'Coflow' in Fig. 4.2 to mimic the ambient air entrainment around the bluff body. Adiabatic no-slip wall conditions are imposed on the pipe walls and bluff body. The cylindrical boundary is specified to be a slip wall and streamwise gradients of all the variables are set to zero at the outlet boundary.

The simulations for this case are undertaken using PRECISE–MB, which has been described in § 3.6.1. The CFL number is ensured to be consistently less than 0.3 across the entire domain by specifying a constant time step of 5 µs. The isothermal flow simulation is run using 96 cores, which requires 24 hrs of wall clock time for a simulation over a period of 12 flow through times. Half of this period is deemed as a long enough period

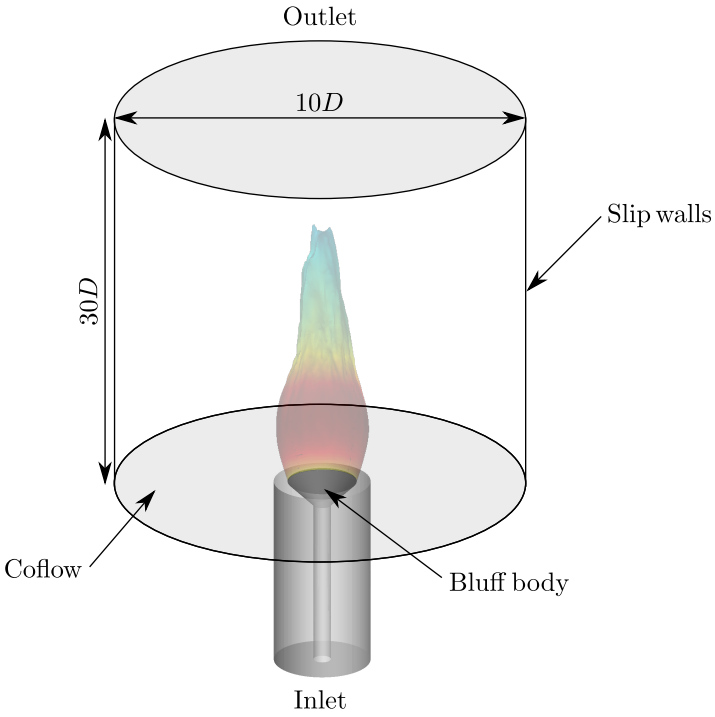

Fig. 4.2 Computational model of the open bluff body burner studied by Kariuki *et al.* (2012).

to ensure that the numerical transients have passed out of the domain for this case. The flow through time is defined as $t_f = l_f/U_b$, where l_f is reference length that is taken as $l_f = 150\,\text{mm}$. The time-averaged statistics are obtained after the transient period of $6\,t_f$ for a further $6\,t_f$. This is deemed as a long enough period, since no changes are seen in time-averaged velocity statistics when the simulation is run for more flow through times.

4.2.3 Isothermal flow results

The computed and measured variations of the streamwise velocity along the centreline are shown in Fig. 4.3. The time-averaged value is normalised using the reference velocity and the axial distance is normalised using the bluff body diameter. The velocity measurements were made using PIV (Kariuki *et al.*, 2012) and the recirculation zone lengths are compared, since this measurement poses as the simplest way of validating the recirculation zone length L_R. As shown in this figure, the comparison between the measured and computed values for L_R/D is good. The negative values of the velocity imply reverse flow within the recirculation zone and thus, the length of the recirculation zone is given by the x distance of the zero crossing of the normalised velocity. The

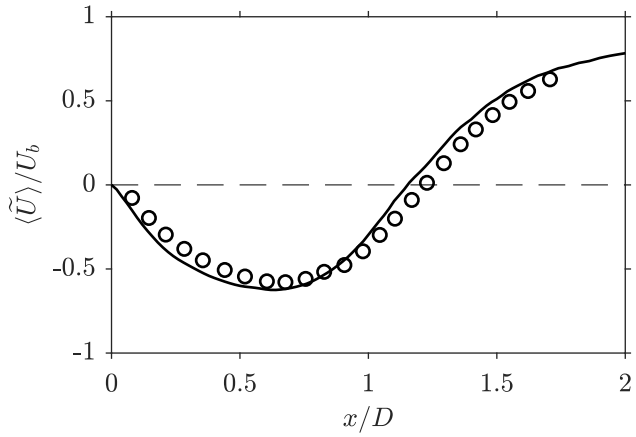

Fig. 4.3 Comparisons of the centreline axial velocity from the bluff body base between the LES [—] and the experiment [○] (Kariuki *et al.*, 2012) for the isothermal case.

computed value of L_R/D is approximately $1.15D$, which agrees well with the measured value of approximately $1.22D$.

The computed radial variations of the time-averaged axial velocity, which is normalised using U_b, are compared to the measurements in Fig. 4.4 for three streamwise locations. The results are averaged azimuthally in the radial direction, due to the axisymmetric nature of the averaged flow features. These results are directly compared against the velocity on the y plane, since no measurements are available for the z component. The comparison seen here is good and suggests that the salient features, such as shear layers and peak velocity values of the flow, are satisfactorily captured in the computations. The broad peak seen for the location $x/D = 0.2$ corresponds to the annular jet region, implying there are two shear layers; these are the inner shear layer and the outer shear layer. The width of the recirculation zone changes from approximately $0.5D$ at $x/D = 0.2$ to approximately $0.4D$ at $x/D = 0.8$. The change in the radial variation with the streamwise distance shows that the width of the shear layers are increasing with x. These variations are captured well in the computations, as seen in Fig. 4.4. Specifically, the recirculation zone size is directly influenced by the turbulence level near the bluff body base because this zone is established by the momentum diffusion caused by the turbulence diffusivity. It is essential to accurately capture the averaged velocity and turbulence statistics variations near the bluff body base, as they control the recirculation zone attributes that aids the stabilisation of the flame.

As noted in § 4.2.1, the turbulence is shear driven and it is expected that the r.m.s. value of axial velocity fluctuations u' is larger in the regions with large gradients $\partial\langle\widetilde{U}\rangle/\partial r$, which can be clearly seen in Figs. 4.4 and 4.5. Comparisons of the radial variations

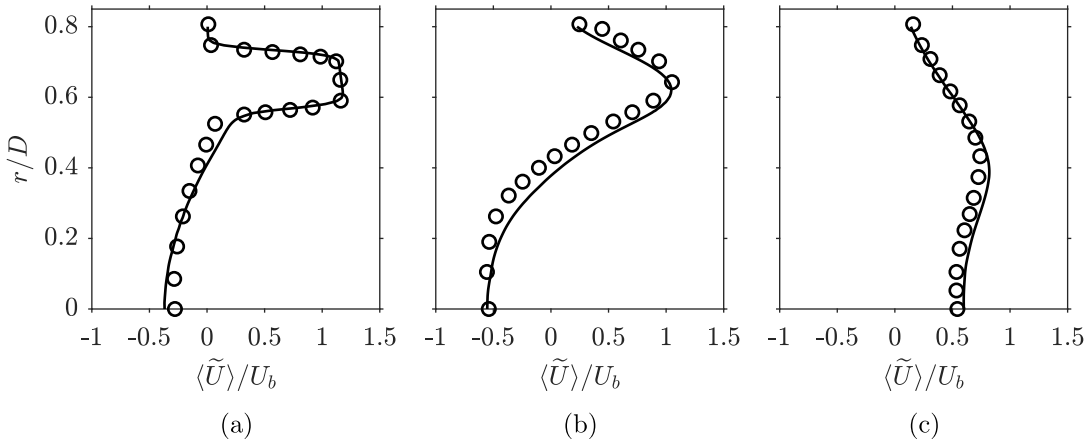

Fig. 4.4 Comparisons of the LES [——] and measured [○] (Kariuki *et al.*, 2012) averaged axial velocity at (a) $x/D = 0.2$, (b) 0.8 and (c) 1.6 for the isothermal case.

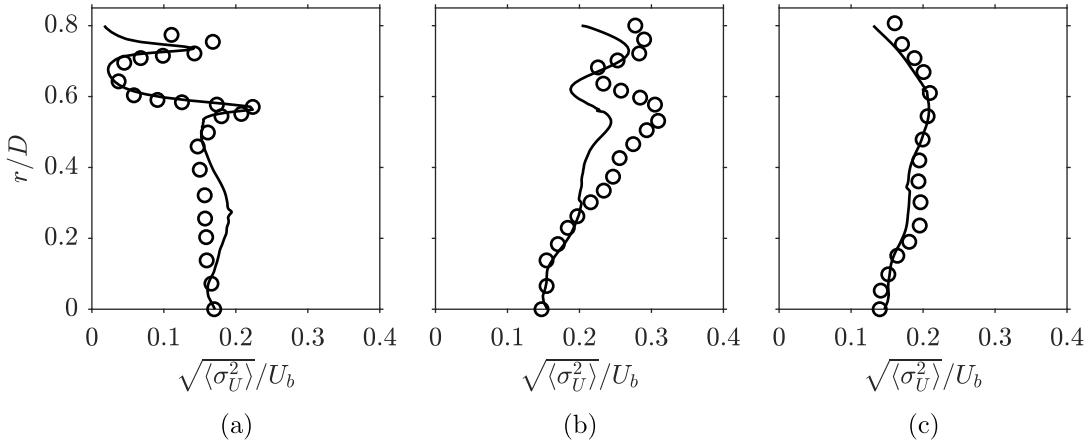

Fig. 4.5 Comparison of the LES [——] and measured [○] (Kariuki *et al.*, 2012) r.m.s. axial velocity at (a) $x/D = 0.2$, (b) 0.8 and (c) 1.6 for the isothermal case.

of the computed r.m.s. axial velocity $\langle u'' \rangle \simeq \sqrt{\langle \sigma_U^2 \rangle}/U_b$ with measurements at three axial locations are shown in Fig. 4.4. The SGS contribution is not included, since it was observed that over 90 % of the turbulent kinetic energy field in the shear layers was resolved by the LES. The positions and magnitudes of the two local peaks at the location $x/D = 0.2$ are captured well in the computations. There is an overall increase in the r.m.s. axial velocity further downstream, as seen in Fig. 4.5b, which is due to the increase in the shear driven turbulence level, but there is some small under prediction in the simulation for this location. The local peaks are less defined as the shear layers become thicker with axial distance because of turbulent diffusion. The measured values for the location $x/D = 1.6$ are well captured in the computation, as seen in Fig. 4.5c, and this location is outside of the recirculation zone (beyond the downstream stagnation point).

The comparisons between the computed and measured statistics for the isothermal flow case suggest that the numerical grid and the computational set-up is good and this set-up is used for reacting flow.

4.3 Confined bluff body burner

4.3.1 Experiment

The schematic of the confined bluff body burner investigated here is shown in Fig. 4.6a and the geometrical parameters are presented in Table 4.2. The velocity measurements were obtained using LDA by Pan *et al.* (1992*b*). Atmospheric air at a temperature $T_u = 294\,\mathrm{K}$ entered the combustion chamber, which consisted of a square duct with a constant area of $W^2 = 79 \times 79\,\mathrm{mm}^2$ and had a length of $L = 284\,\mathrm{mm}$. The conical bluff body at the base of the combustor had a cylindrical stem of diameter $D_{\mathrm{st}} = 12.7\,\mathrm{mm}$, a base diameter of $D = 44.45\,\mathrm{mm}$ and an apex angle of $\theta = 45°$. Air entered the combustor section with a bulk-mean velocity of $U_b = 15\,\mathrm{m/s}$ at the bluff body base, as shown in Fig. 4.6a. A turbulence generator grid with holes of diameter 3.46 mm was positioned 58 mm upstream of the bluff body base in the experiment. Different turbulence grids were used in the experiment to supply a different Turbulence Intensity (TI) at the bluff body base. The different turbulence intensities supplied are $\mathrm{TI} = u'/U_b = 2\,\%$, 17 % and 22 %. These values were measured at a radial location of $r/D = 0.55$ at the bluff body base and were used as reference values for the respective experiments. The cases with 2 % and 22 % TI are considered for the LES cases, since an extensive set of experimental data is available for these two cases for a thorough model validation.

4.3.2 Computational set-up

The computational domain for the experimental burner is shown in Fig. 4.6b, which is discretised using a structured multi-block mesh with a total of approximately 2.2 million cells. The development of this grid was previously undertaken by Langella (2016), which contains a grid sensitivity study and an investigation of the use of wall functions, where it was concluded that wall functions were not required. The LDA measurements that were obtained by Pan *et al.* (1992*b*) were used to estimate the wall distance to guide the numerical grid refinement to satisfy the criterion $y^+ \leq 5$. Approximately two cells are placed within the viscous sublayer in the grid used for this study. The lengths of the turbulent flames in the experiments exceeded the length of the combustion chamber

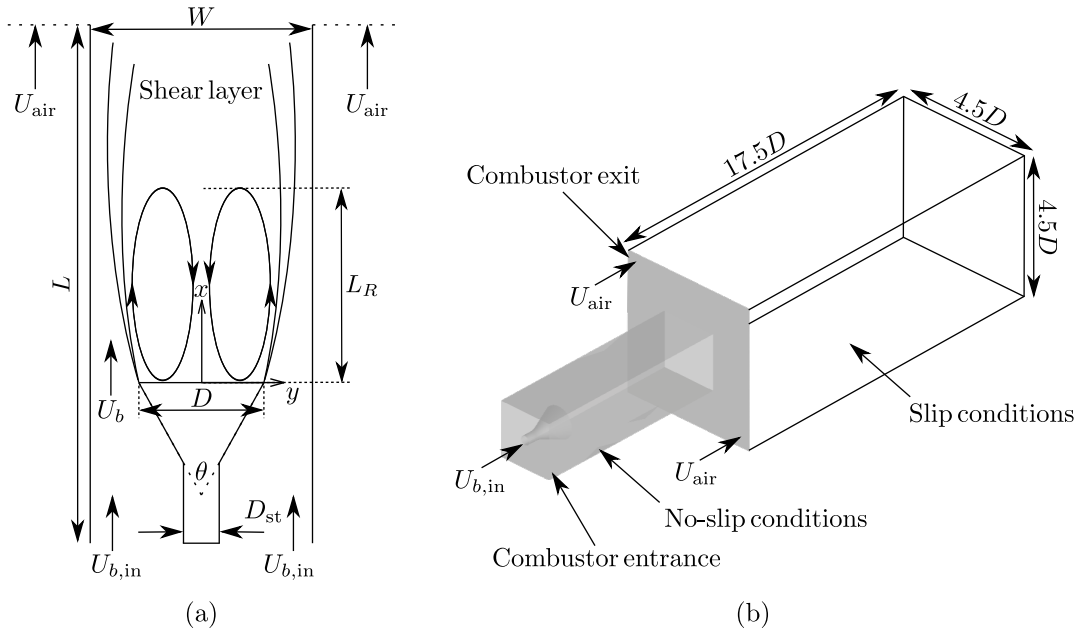

Fig. 4.6 Schematic of the (a) confined bluff body burner (not to scale) and (b) its computational model (Nandula, 2003; Pan *et al.*, 1992*b*).

Parameter	Value	Description
D	44.45 mm	Bluff body diameter
D_{st}	12.7 mm	Stem diameter
L	284 mm	Length of the combustion chamber
T_u	294 K	Inlet temperature for air
U_{air}	0.2 m/s	Coflow velocity (see Fig. 4.6)
U_b	15 m/s	Reference bulk velocity at the bluff body base
W	79 mm	Width of the combustion chamber
θ	45°	Bluff body apex angle

Table 4.2 Physical parameters of the confined bluff body burner studied by Pan *et al.* (1992*b*) and Nandula (2003).

and hence, difficulties arise with specifying meaningful and numerically stable boundary conditions for the combustor exit. This is overcome by including an additional domain of size $4.5D \times 4.5D \times 17.5D$ downstream of the combustor exit, as shown in Fig. 4.6b. This additional domain allows for the effect of entrained air on the flow exiting the combustor to be captured and also helps to specify clear exit boundary conditions for the computational domain.

A top-hat velocity profile of $U_{b,\text{in}} = 11.5\,\text{m/s}$ is prescribed at the inlet, based on the measured mass flow rate to give the required reference bulk-mean velocity of $U_b = 15\,\text{m/s}$

at the bluff body base, as marked in Fig. 4.6a. A small velocity of $U_{\text{air}} = 0.2\,\text{m/s}$ is specified at the boundary in line with the combustor exit, as shown in Fig. 4.6, in order to mimic the ambient air entrainment. Langella *et al.* (2016*a*) showed that the velocity close to the bluff body base could be affected by the heat losses from the recirculation zone to the bluff body base and this loss was reported to be roughly 5–8 % by Pan *et al.* (1991*b*). However, it was also shown that the computed recirculation zone length agreed well with the measurements, although the heat loss was excluded in the LES (Langella *et al.*, 2016*a*). Hence, this study follows that approach by imposing adiabatic no-slip conditions for the bluff body and walls of the combustion chamber. The lateral walls of the additional domain are specified with slip conditions, while the outlet boundary is specified to have zero streamwise gradients for all variables. The TI at the inlet is specified using the synthetic turbulence obtained using the digital filter technique (Klein *et al.*, 2003) instead of including the turbulence generator used in the experiment. No synthetic turbulence is supplied at the inlet boundary for the low TI case and a TI of 24 % is supplied at the inlet boundary of the domain for the high TI case.

The simulations for this case are undertaken using PRECISE–MB, which has been described in § 3.6.1. A constant time step of 7.5 µs is chosen to ensure that the CFL number does not exceed 0.3. The simulations for $12\,t_f$ requires 18 hrs of wall clock time on 80 cores, where the flow through time is $t_f = L/U_b$. The time-averaged statistics are obtained for $6\,t_f$ after allowing the transients to escape the computational domain.

4.3.3 Isothermal flow results

There is a limited amount of LDA measurements available for validating the isothermal flow cases. The time-averaged centreline velocities behind the bluff body are compared against LDA measurements for low and high turbulence intensities of 2 % and 22 % respectively. The results obtained from the isothermal flow simulation of the two cases are shown in Fig. 4.7, where the axial velocity and the streamwise distance are normalised by U_b and D respectively. The length of the recirculation zone for the low TI case is $1.45D$, which is approximately 3 % smaller than the length obtained in experiment of approximately $1.5D$. The high TI case gave a length of $1.27D$, which is an over prediction of approximately 6 % in comparison to the length obtained in the experiment of approximately $1.2D$. For both cases, the variation of the reverse flow is well captured by the simulations. It is demonstrated in the simulations that the length of the recirculation zone decreases when the TI is increased, as observed in the experiment (Pan *et al.*, 1992*b*). This is described in further detail in § 6.3.2.

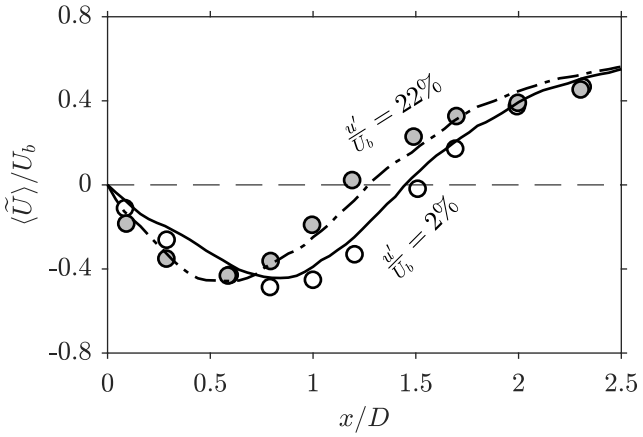

Fig. 4.7 Comparison of the centreline axial velocity from the bluff body base between the simulations [lines] and the experiment [symbols] (Pan *et al.*, 1992*b*) for isothermal flow.

4.4 Gas turbine model combustor

4.4.1 Experiment

The gas turbine model combustor developed by the German Aerospace Centre (DLR) is a swirling flow system and is shown in Fig. 4.8 (Duan *et al.*, 2004; Meier *et al.*, 2005, 2006; Weigand *et al.*, 2006). Dry air at atmospheric pressure and room temperature entered a single plenum and the flow was split through two radial swirlers. The two co-swirling flows entered the combustion chamber through a central nozzle of diameter 15 mm and an annular nozzle with inner and outer diameters of 17 mm and 25 mm respectively. Methane was fed through a non-swirling nozzle ring that contains 72 channels ($0.5 \times 0.5\,\mathrm{mm}^2$) that were located between the two air nozzles, although air is used for the isothermal flow case. The air mass flow rates through the nozzle and plenum are denoted using $\dot{m}_{\mathrm{air,n}}$ and $\dot{m}_{\mathrm{air,p}}$ respectively. The exit planes of the central air and fuel nozzle ring are 4.5 mm below the exit of the annular air nozzle and the entrance to the combustion chamber. This location corresponds to $x = 0$, as shown in Fig. 4.8 with the co-ordinate axes. The combustion chamber had a square cross-section with an internal area of $85 \times 85\,\mathrm{mm}^2$ and a length of 114 mm. The time-averaged statistics for the three components of velocity and their r.m.s. values at various axial positions across the combustor were obtained using LDV.

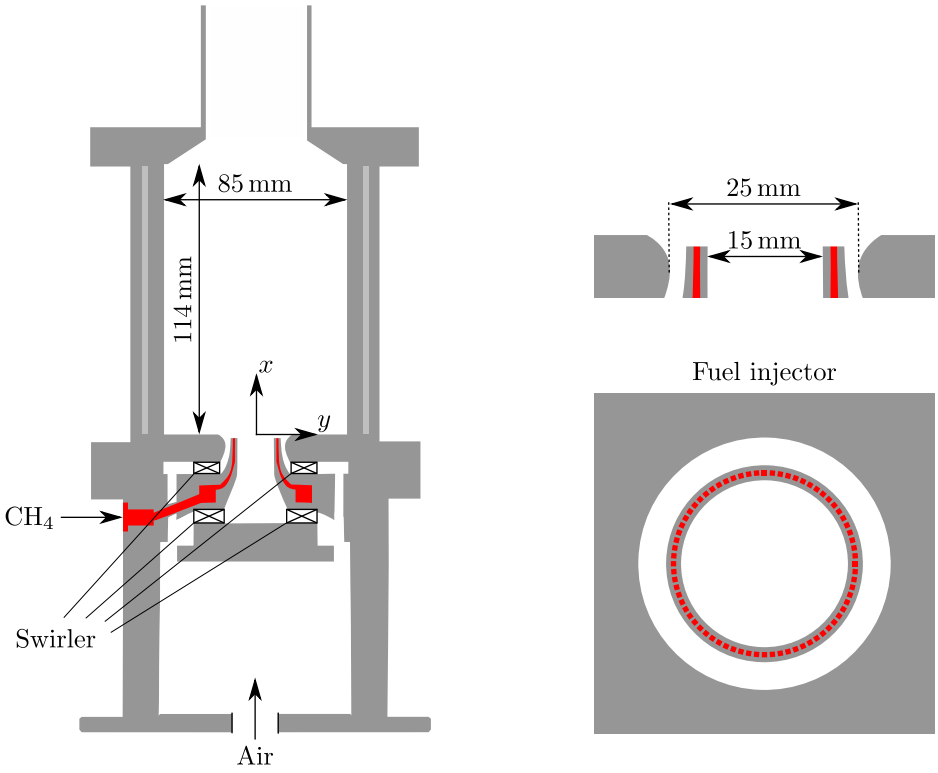

Fig. 4.8 Schematic drawing of the gas turbine model combustor (Meier *et al.*, 2006; Weigand *et al.*, 2006).

Parameter	Value	Description
$\dot{m}_{\text{air,n}}$	1.256 g/s	Air flow rate through the nozzle
$\dot{m}_{\text{air,p}}$	19.74 g/s	Air flow rate through the plenum
S	0.9	Swirl number
T	295 K	Air temperature

Table 4.3 Isothermal flow operating conditions for the gas turbine model combustor (Widenhorn *et al.*, 2009).

4.4.2 Computational set-up

The computational domain, shown in Fig. 4.9, includes an air feed pipe, the plenum, both swirlers and the combustion chamber. A large cylindrical atmospheric far-field, which is 350 mm in length and has a diameter of 400 mm, is included downstream of the combustion chamber exit to prevent acoustic wave reflection. Adiabatic no-slip conditions are imposted on to all walls, apart from the walls in the streamwise direction of the extended far-field domain, which have slip conditions imposed. The outlet is specified to have zero streamwise gradients for all the variables. The air feed pipe and fuel injector

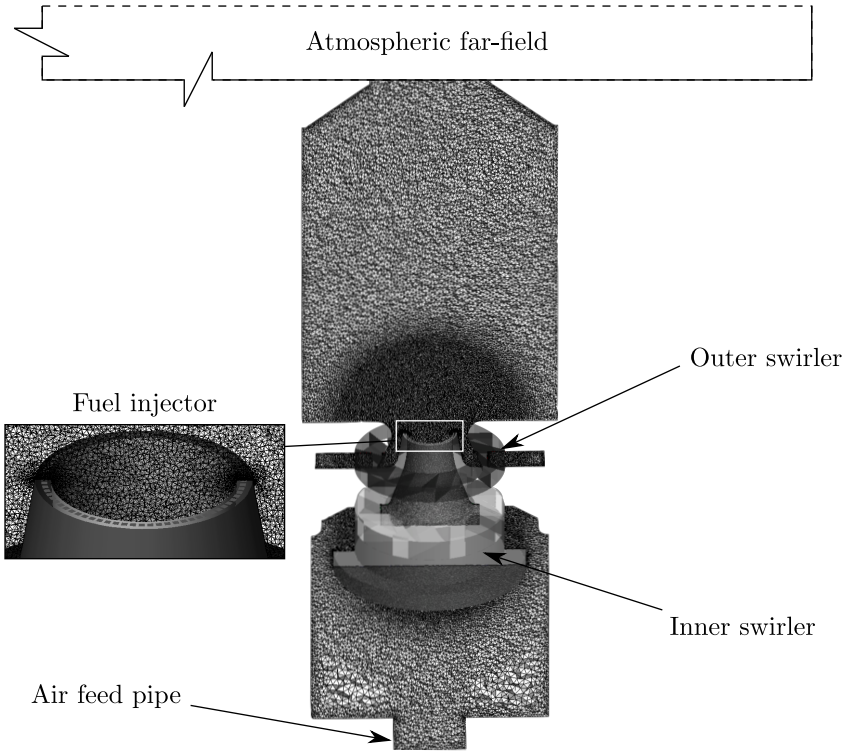

Fig. 4.9 Compuational grid for the gas turbine model combustor (Meier *et al.*, 2006; Weigand *et al.*, 2006).

have constant mass flow rate boundary conditions imposed using the values shown in Table 4.3 and have a top-hat velocity profile. The swirl number S was calculated from the velocity profile measured just above the nozzle exit with a radius R; the pressure term is also neglected. This is written as (Gupta *et al.*, 1984)

$$S = \frac{\int_0^R 2\,\pi U U_\theta \rho r \,\mathrm{d}r}{\int_0^R 2\,\pi U^2 \rho r \,\mathrm{d}r}\,. \tag{4.2}$$

All 72 fuel injectors are included in the mesh to provide improved accuracy for the fuel–air mixing. The computational grid consists of 20 million unstructured tetrahedral cells; Chen *et al.* (2019*b*) conducted a grid sensitivity study and demonstrated that the grid presented here suitably resolved the turbulence and mixing fields. At least two cells adjacent to the wall are within $y^+ \leq 5$, in order to ensure that the velocity field in those regions is insensitive to the use of a wall model. A small time step of $\Delta t = 0.1\,\mu\mathrm{s}$ is used to ensure suitable accuracy for the time derivatives and to ensure the CFL number remains below 0.4 across the whole domain. This low CFL number is required, since there are very small grid cells near the fuel nozzle (these are of the order $10^{-4}\,\mathrm{m}$) and to

ensure numerical stability for the second-order velocity spatial discretisation schemes, since no blending factors are used, as outlined in § 3.6.2. The simulation uses 1080 cores for 40 hrs of wall clock time to give 90 ms of statistics for the PISO scheme, whereas using the PIMPLE scheme increased the wall clock time to 90 hrs. The time-averaged samples are collected over 30 ms and are compared with the LDV measurements next.

4.4.3 Isothermal flow results

Typical time-averaged velocity and their r.m.s. fields are shown for the axial, radial and azimuthal components of velocity respectively in Figs. 4.10, 4.11 and 4.12. The time-averaged statistics are used to assess the performance of the residual stress closure models for the computational grid. The closure models tested are the constant Smagorinsky, k-equation and WALE models. The first set of comparisons investigates the sensitivity of using PISO and PIMPLE schemes with the constant Smagorinsky model. Using the PIMPLE scheme increased the computational cost by approximately 150 % in comparison to the PISO scheme. However, the results produced are insensitive to the change in the algorithms, as shown in Figs. 4.10, 4.11 and 4.12, and the PISO scheme is used to test the other two residual stress closure models. It should be noted that the PIMPLE scheme should be used for reacting flow simulations, due to the density variation across the flame and it is difficult to achieve suitable convergence with the PISO scheme.

The time-averaged statistics for the three velocity components are analysed first. The axial velocity results are shown in Fig. 4.10a, where it is demonstrated in the near-field at $x = 2.5$ mm and 5 mm that the k-equation model over predicts the peak values. This trend is also seen further downstream and at $x = 20$ mm, the zero crossing of the axial velocity is located approximately 5 mm closer to the centreline ($y = 0$), which suggests that the width of the recirculation region is 10 mm smaller. The time-averaged radial velocity profiles in Fig. 4.11a also indicate that the width of the recirculation zone is smaller, as the peak radial velocity values in the near-field of the nozzle exit at $x = 2.5$ mm, 5 mm and 10 mm are all under predicted and are closer to the centreline. This behaviour is also seen in r.m.s. axial and radial velocities in Figs. 4.10b and 4.11b respectively. The azimuthal velocity in Fig. 4.12a shows some intriguing behaviour at $x = 2.5$ mm and 5 mm, since two distinct peaks are seen on either side of the centreline. This suggests that the k-equation model does not capture the merging of the two air streams that is observed in the LDV measurements. The axial velocity at $x = 2.5$ mm shows a velocity gradient at $|y| \approx 15$ mm, whereas this is located closer to $|y| \approx 20$ mm in the LDV measurements. This is also shown by all of the near-field r.m.s. components

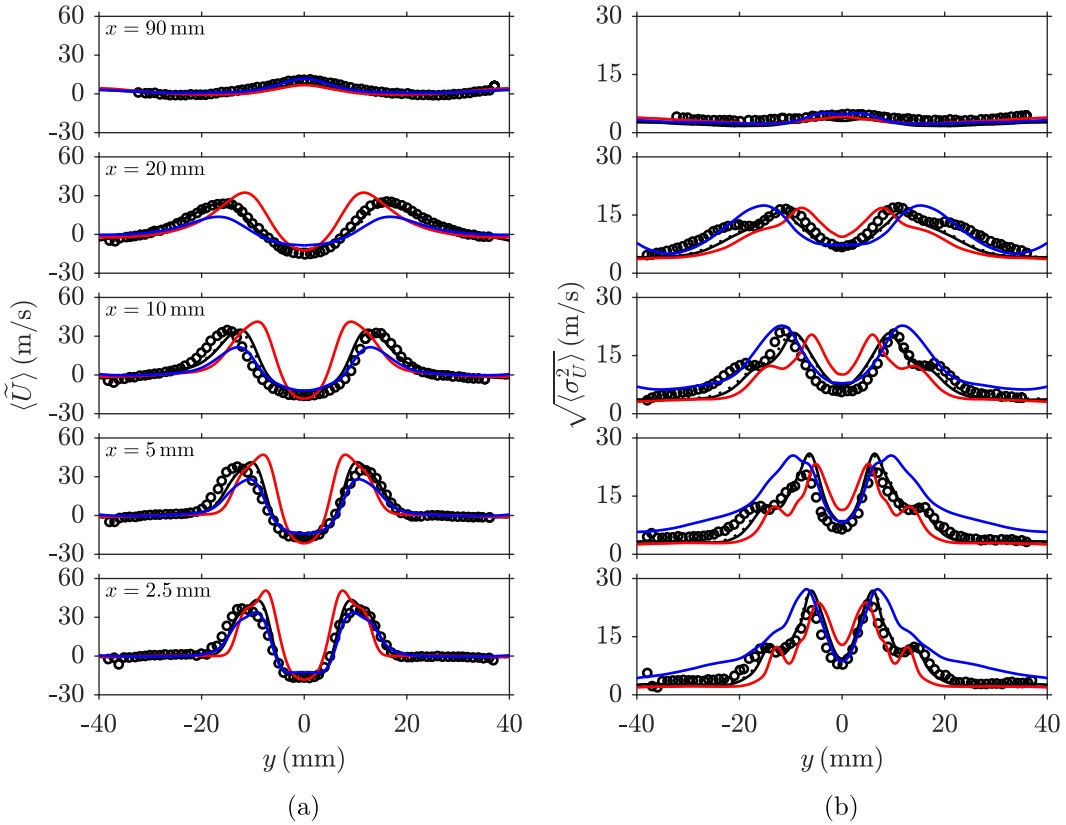

Fig. 4.10 Isothermal flow comparisons of the time-averaged (a) axial velocity and (b) the r.m.s. axial velocity resolved fluctuations. The LES results using the constant Smagorinsky model with PISO [——] and PIMPLE [· · ·] schemes, k-equation model [——] and the WALE model [——] are compared against the LDV measurements [○] (Widenhorn *et al.*, 2009).

in Figs. 4.10b, 4.11b and 4.12b. This suggests that the flow separates along the outer contoured wall further upstream in the flow exiting the outer swirler.

On the other hand, the WALE model under predicts the peak values of the axial velocity at $x = 20\,\text{mm}$ by roughly 25 % in comparison to the LDV measurements, as seen in Fig. 4.10a. The radial velocity is also under predicted in the near-field locations of $x = 2.5\,\text{mm}$, 5 mm and 10 mm, as shown in Fig. 4.11a. The locations of the peaks are well captured by the LES, although the magnitude of the radial velocity is severely over predicted when approaching the wall for the locations $x = 2.5\,\text{mm}$ and 5 mm. This suggests that the outer air flow is distributed over a wider area, which implies there is a delayed boundary separation on the outer contoured wall. This behaviour is reflected in the corresponding r.m.s. fields in Fig. 4.11b, as there are significant over predictions for $|y| > 20\,\text{mm}$ at $x = 2.5\,\text{mm}$ and 5 mm; this is also seen in the r.m.s. azimuthal velocity values in Fig. 4.12b. The azimuthal velocity profiles in Fig. 4.12a do not show

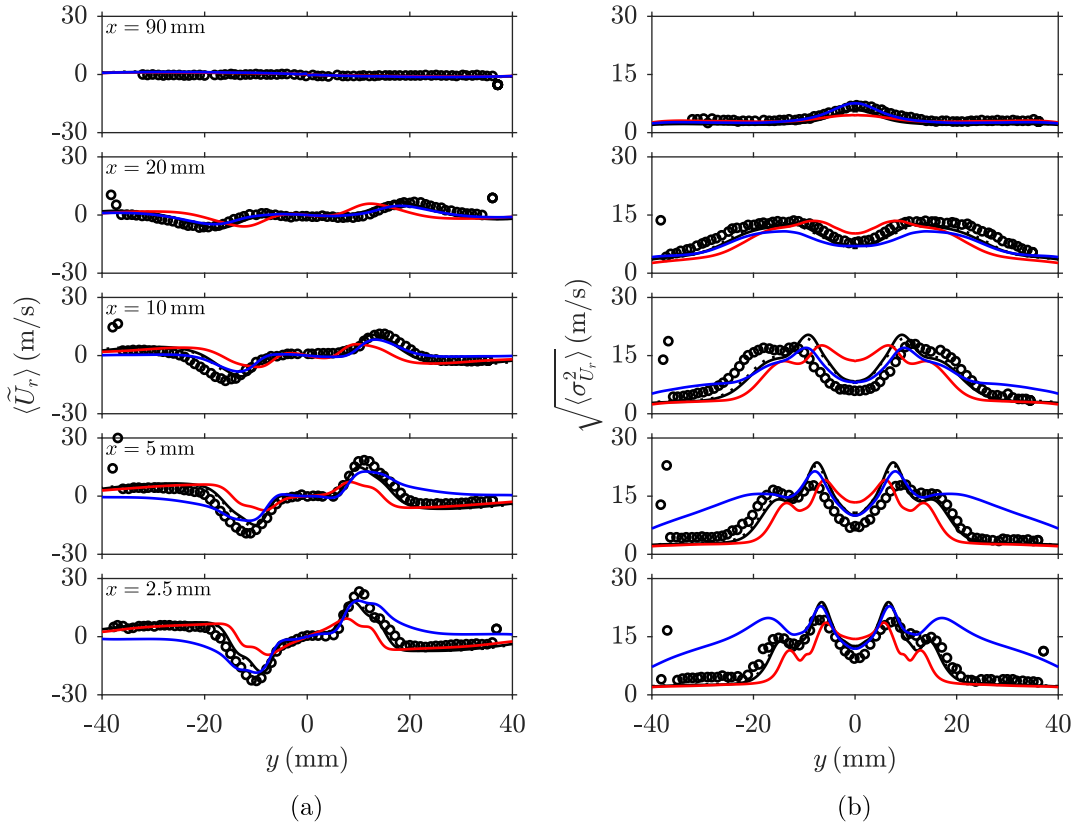

Fig. 4.11 Isothermal flow comparisons of the time-averaged (a) radial velocity and (b) the r.m.s. radial velocity resolved fluctuations. The LES results using the constant Smagorinsky model with PISO [——] and PIMPLE [· · ·] schemes, k-equation model [——] and the WALE model [——] are compared against the LDV measurements [○] (Widenhorn *et al.*, 2009).

two distinct peaks as observed for the statistics from the k-equation model, indicating that the two air streams merge and this suggests that the WALE model is less diffusive.

The Smagorinsky model gave improvements in the time-averaged statistics in comparison to the other closure models. As shown in Fig. 4.10a, the peak values are close to the maximum values in the LDV measurements. The width of the recirculation zone (the radial positions of $\langle\widetilde{U}\rangle = 0$) at $x = 10\,\text{mm}$ is under predicted by approximately 4 mm, as suggested by the LDV measurements. These observations are also seen in Fig. 4.11a for the radial velocity fields. However, both the axial and radial velocity fields are in good agreement with the LDV measurements at the downstream locations of $x = 20\,\text{mm}$ and 90 mm. The azimuthal velocity is well captured at all streamwise locations, as seen in Fig. 4.12a. The peak r.m.s. values for all velocity components at $x = 10\,\text{mm}$ are located approximately 2 mm closer to the centreline than the LDV measurements. However at the downstream locations of $x = 20\,\text{mm}$ and 90 mm, the r.m.s. values for all velocity

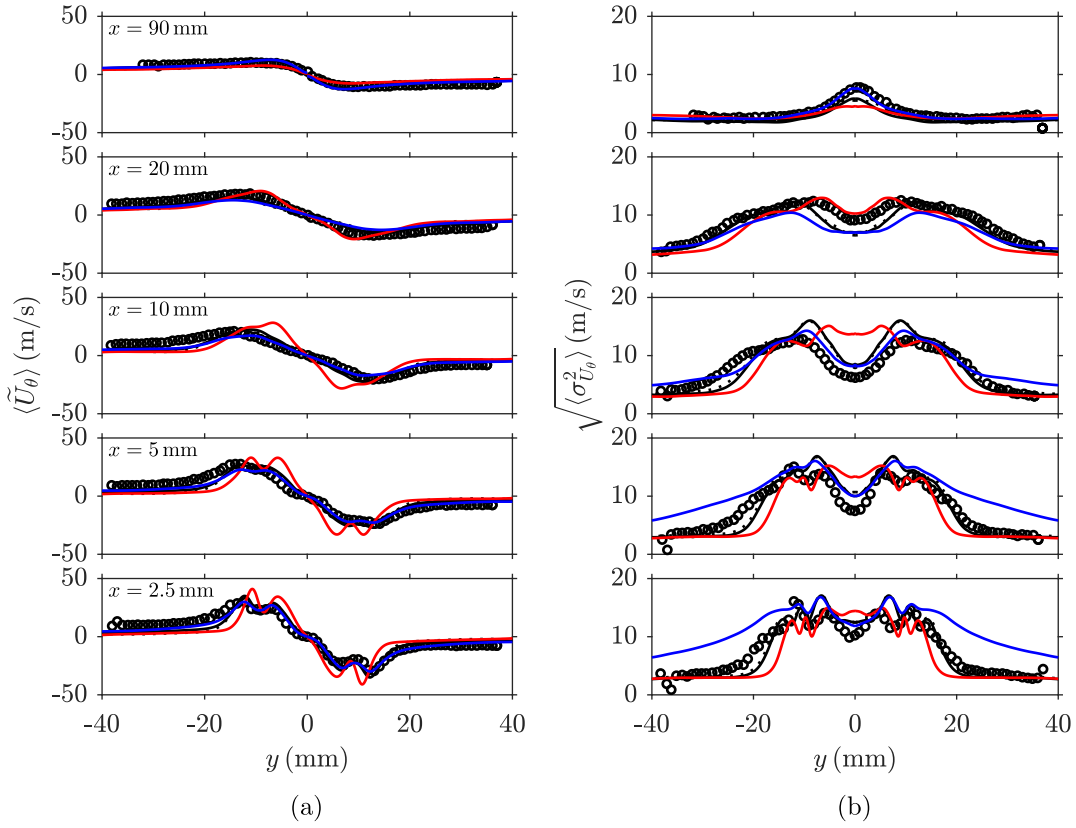

Fig. 4.12 Isothermal flow comparisons of the time-averaged (a) azimuthal velocity and (b) the r.m.s. azimuthal velocity resolved fluctuations. The LES results using the constant Smagorinsky model with PISO [——] and PIMPLE [· · ·] schemes, k-equation model [——] and the WALE model [——] are compared against the LDV measurements [○] (Widenhorn *et al.*, 2009).

components are in good agreement with the LDV measurements, albeit for some under prediction near the centreline in the r.m.s. azimuthal velocity field.

4.4.4 Swirling flow structure

On the whole, the constant Smagorinsky model has produced the best comparisons with the LDV measurements and the flow field structure is analysed in further detail. The filtered axial velocity field for an arbitrarily chosen time on the x–y mid-plane is shown in Fig. 4.13a with the corresponding velocity streamlines. It is seen that an Inner Recirculation Zone (IRZ) is formed, due to the swirling flow within the central nozzle. An inner shear layer is formed from the trailing edge of the burner nozzle and the circular patterns that are seen in Fig. 4.13a represent large-scale coherant structures. These regions have a very high vorticity, as shown in the vorticity magnitude contour in Fig. 4.14b. The vortex structures are convected further downstream with the incoming

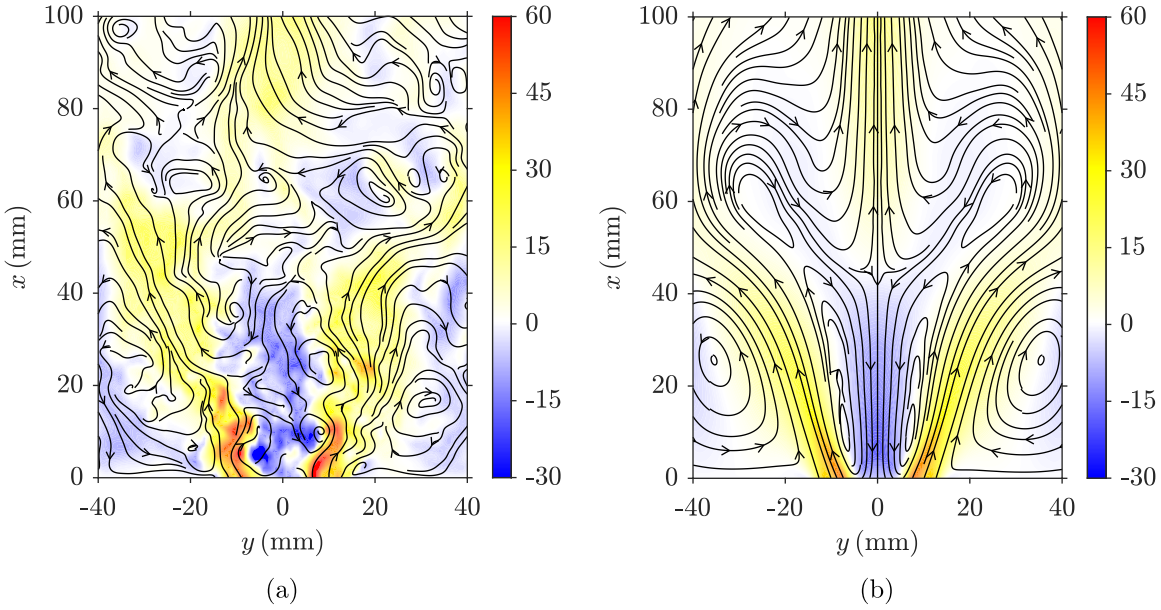

Fig. 4.13 Filtered (a) and time-averaged (b) axial velocity contours with the corresponding streamlines for the isothermal flow case.

jet stream until vortex breakdown occurs, which leads to the formation of the IRZ. The time-averaged axial velocity field is shown in Fig. 4.13b and it is seen that the IRZ has a 'Y' shape, which is formed by the converging geometry at the burner exit. An Outer Recirculation Zone (ORZ) is also formed because flow separation occurs on the outer contoured wall of the annular nozzle and then re-attaches further downstream on to the wall of the combustion chamber.

The other important feature of the swirling flow in this case is the formation of a Precessing Vortex Core (PVC). This is illustrated in Fig. 4.14 by using an iso-surface of the pressure, which is marked with a dynamic pressure of $-2000\,\mathrm{Pa}$. It is shown in Fig. 4.13a that there is a zig-zag arrangement of the large vortices around the inner shear layer, which suggests there is a helical PVC and it rotates with the swirling flow; the PVC is also close to the inner shear layer, as shown by Fig. 4.13a. The PVC is a form of hydrodynamic instability that swirling flow is susceptible to (Candel *et al.*, 2014; Syred, 2006). The PVC is highly sensitive to boundary conditions, such as the swirl number and the air velocity (Widenhorn *et al.*, 2009). The equivalence ratio for reacting flow also affects the structure of the PVC, since the PVC plays a prominent role in the stabilisation of the flame, which has been shown experimentally (Stöhr *et al.*, 2011*b*) and numerically (Chen *et al.*, 2019*a*) for this configuration.

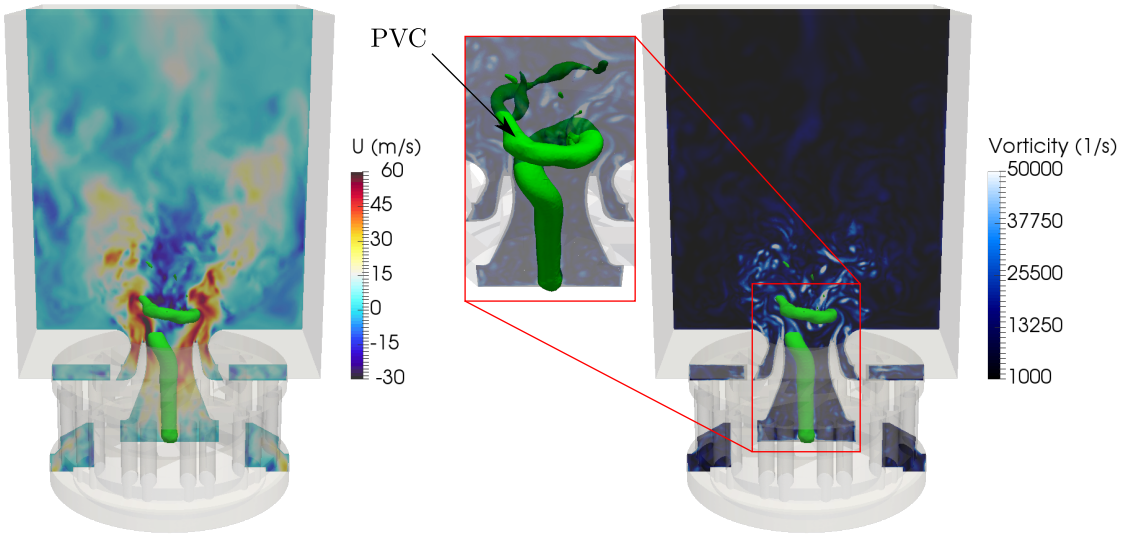

Fig. 4.14 Snapshots of the filtered velocity (a) and vorticity magnitude (b) of the isothermal flow case. The PVC is marked with a dynamic pressure of −2000 Pa.

4.5 Summary

Three isothermal flow studies have been undertaken in this chapter, where the computational grids for each case have been assessed through comparisons with time-averaged measurements. Good comparisons have been obtained for all three cases with their respective numerical set-up and the chosen residual stress model. An investigation with the residual stress closure model is undertaken for isothermal swirling flow conditions in a gas turbine model combustor, where it was seen for this case that the constant Smagorinsky model produced the best comparisons with the LDV measurements. The reacting flow simulations are undertaken using these three grids and are presented over the next four chapters. Chapter 5 shows the reacting flow results for the open bluff body flame, which is followed by the results for the confined bluff body burner in Chapter 6. The reacting flow simulations for the gas turbine model combustor are presented and analysed in Chapters 7 and 8.

Chapter 5

Open Bluff Body Flame

This chapter presents the results for a simulation of an unconfined turbulent premixed flame that is stabilised behind a bluff body. The simulation statistics are compared to measurements and the relative positioning of the shear layers and flame brush are analysed to understand the radial variations of the turbulent kinetic energy at various streamwise locations. These results are also compared to confined bluff body stabilised flames to gain insights into the relative role of incoming and shear driven turbulence on the behaviour of flame brush and the turbulent kinetic energy variation across it.

5.1 Motivation

Bluff body burners are often used in practical combustion systems, such as stationary gas turbines, industrial burners and afterburners. The hot recirculation zone behind the bluff body offers a simple mechanism for flame stabilisation by providing a continuous supply of heat to ignite the incoming fuel–air mixture. However, the size and shape of the recirculation zone influences the performance of these combustion systems and these attributes depend on the incoming flow rate, equivalence ratio and bluff body geometry. Such configurations make it feasible to investigate flame blow-off conditions as a function of incoming flow rates and equivalence ratio for a given bluff body geometry through well controlled experiments, as done in the study by Kariuki *et al.* (2012). This fundamental information is required at the design stage of combustors with the purpose of operating under lean-burn conditions, since efficiency and environmental benefits can be achieved. It is well known that lean flames are susceptible to extinction and combustion instabilities. These phenomena can lead to the occurrence of flame blow-off, which is typically treated as the complete extinction of the flame (Brewster *et al.*, 1999; Driscoll, 2008; Huang &

Yang, 2009). The physical processes and their interactions governing these phenomena are highly unsteady, where it has been mainly hypothesised in previous studies that the competing effects of convection and chemical reaction (combustion) lead to flame blow-off. These competing effects are influenced by a number of physical processes, such as large-scale entrainment of reactants into the recirculation zone among other phenomena. It has also been noted by Shanbhogue *et al.* (2009) that the process of flame blow-off and a general physical mechanism for its occurrence is not fully understood.

A long-term objective is to predict flame blow-off using the flamelet approach. However, the specific focus of this study is to demonstrate, as a first step, that an unstrained flamelet based model can accurately capture the stabilisation of flames far from blow-off conditions, along with the various flame and flow attributes of the bluff body stabilised open flame. This is achieved by simulating the bluff body stabilised methane–air flame investigated experimentally by Kariuki *et al.* (2012), which differs substantially from the flames considered in the study by Langella *et al.* (2016*a*). The experimental flames investigated by Langella *et al.* (2016*a*) were confined within a rectangular duct that contained a turbulence generator upstream of the bluff body base. Thus, the turbulence experienced by those flames came from both incoming and shear generated turbulence, whereas the flames investigated by Kariuki *et al.* (2012) experienced no additional incoming turbulence, since a turbulence generator was absent in the burner configuration. An additional complexity exists due to the entrainment of surrounding air because the flames are exposed to atmospheric conditions from the bluff body base. The entrainment effects are expected to be small for flames far from blow-off but could play an important role for flames close to blow-off because of the potential dilution of an already weaker mixture of flames close to blow-off, as the equivalence ratios are lower. However, the flame features could be quite different between the open and confined flames, specifically near the bluff body because there is no incoming turbulence in the open flames considered for this study.

The aims of this study are:

- To test the applicability of the unstrained premixed flamelet as SGS combustion closure for modelling the open bluff body stabilised flame that is furthest from blow-off (the most stable flame) in the study by Kariuki *et al.* (2012).
- To highlight the differences in the spatial evolution of the shear layers and the flame brush between flames that are exposed to ambient conditions and flames that are enclosed in a combustion chamber.

Parameter	Value	Description
T_u	298 K	Inlet temperature for the methane–air mixture
U_{air}	0.1 m/s	Coflow velocity (see Fig. 4.2)
U_b	21.6 m/s	Reference bulk velocity at the bluff body base
ϕ	0.75	Methane–air equivalence ratio

Table 5.1 Parameters for flame A1 (Kariuki *et al.*, 2012).

5.2 Flame conditions and numerical detail

The open bluff body burner that is studied here has been previously described in § 4.2, which was investigated experimentally by Kariuki *et al.* (2012, 2015) and Kariuki (2013). Measurements of four flames that approached blow-off conditions were taken in the experiments. These were obtained using PIV for velocities, and OH^* chemilluminescence and OH-PLIF techniques to identify the flame location and shape. A premixed methane–air mixture at ambient conditions with an equivalence ratio of $\phi = 0.75$ entered through the annular gap, shown in Fig. 4.1. The mass flow rate is chosen to give the same bulk velocity of $U_b = 21.6\,\text{m/s}$ as the isothermal case at the base of the bluff body. Blow-off conditions were approached by gradually decreasing the equivalence ratio from $\phi = 0.75$ (flame A1) to a value just prior to blow-off (flame A4), whilst maintaining the same value for U_b. As mentioned in § 5.1, flame A1 is of interest for this study, which is furthest from blow-off conditions. This flame has been simulated in previous studies using combustion models that include CMC (Farrace *et al.*, 2018, 2017), the Eulerian stochastic field method (Hodzic *et al.*, 2017*b*, 2019), a finite rate chemistry approach (Hodzic *et al.*, 2017*a*), and Partially Stirred Reactor (PaSR) and Implicit LES (ILES) approaches (Hodzic *et al.*, 2019).

The relevant parameters for flame A1 are listed in Table 5.1 and the computational grid is the same as shown in Fig. 4.2. The variables $\widetilde{c}$ and $\sigma^2_{c,\text{sgs}}$ are set to be zero for both the inlet and coflow boundaries and the enthalpies for these boundaries are set to be consistent with their temperature and composition. The dilution of the methane–air mixture is captured by transporting a passive fluid marker $\widetilde{Z}$, which is set to be unity in the methane–air stream and zero in the ambient air. The simulations are run using 96 cores, which required 36 hrs of wall clock time for a simulation over a period of 16 flow through times. The flow through time is defined as $t_f = l_f/U_b$, where l_f is a reference length that is taken as $l_f = 150\,\text{mm}$. The time-averaged statistics are obtained over a sample of $8\,t_f$.

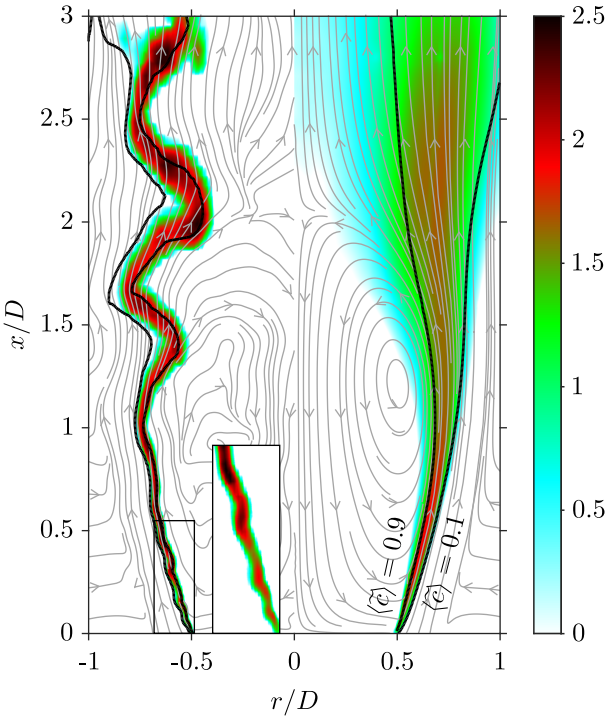

Fig. 5.1 Contours of instantaneous $\log(1000\widehat{\mathrm{Da}}_\Delta)$ and the velocity streamlines are shown in the left half. The right half shows the contours of time-averaged quantities $\log(1000\langle\widehat{\mathrm{Da}}_\Delta\rangle)$ and the corresponding streamlines.

5.3 Results

5.3.1 General flame features

The qualitative features of the computed flame are shown in Figs. 5.1, 5.2, 5.3 and 5.4; the quantitative comparisons are presented in § 5.3.2. The local SGS Damköhler number, defined as the ratio of the SGS flow time scale τ_{sgs} to the chemical time scale τ_c, is used to provide insights into the combustion regimes, as the Karlovitz number is not available from the LES. This dimensionless quantity is given by $\widehat{\mathrm{Da}}_\Delta = \tau_{\mathrm{sgs}}/\tau_c = \bar{\dot{\omega}}\Delta/(\rho_u u'_\Delta)$. The spatial variation of $\widehat{\mathrm{Da}}_\Delta$ is shown in Fig. 5.1, along with the velocity streamlines. The left half of this figure shows the local values of $\log(1000\widehat{\mathrm{Da}}_\Delta)$ from an arbitrarily chosen snapshot of the data, along with the corresponding streamlines. The right half shows the log of the averaged values, i.e., $\log(1000\langle\widehat{\mathrm{Da}}_\Delta\rangle)$, along with the streamlines of the averaged flow field. In addition, the isolines of the instantaneous and averaged progress variable, having values of $\tilde{c} = 0.1$ and 0.9, are also shown to mark the filtered flame and the flame brush.

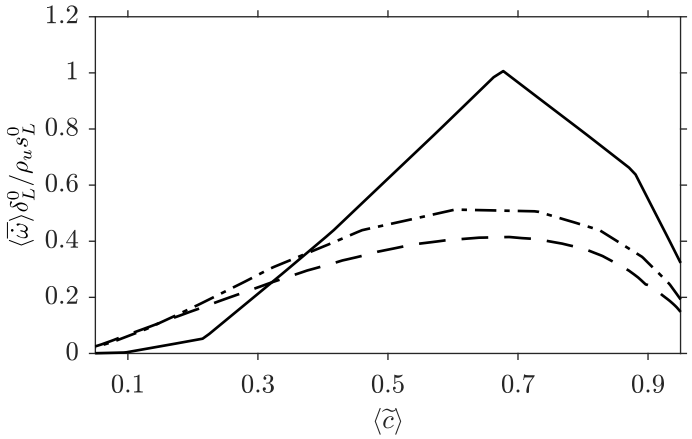

Fig. 5.2 Time-averaged reaction rate across the flame brush at the streamwise locations $x/D = 0.2$ [——], 0.8 [– · –] and 1.6 [– –].

The variation of $\widehat{\mathrm{Da}}_\Delta$ is strong within the instantaneous and averaged reacting regions, as shown in Fig. 5.1. Larger values are near the bluff body base in the averaged image, while the instantaneous field shows that large values also occur at downstream locations. These results suggest that the combustion is in the corrugated flamelet regime for the region immediately downstream of the bluff body base, as seen in the inset of Fig. 5.1. The flame becomes thicker for $0.5 \leq x/D \leq 1.5$, due to the influence of shear layer roll-up because of the Kelvin–Helmholtz instability on the filtered flame. The values of $\langle\widehat{\mathrm{Da}}_\Delta\rangle$, shown on the right-hand side of Fig. 5.1, suggest that the combustion is in the thin reaction zones regime. For $x/D > 2$, the combustion is observed to be in the distributed reaction zones regime, as the flame brush width significantly increases downstream of this location. In addition, the left half of Fig. 5.1 shows a larger proportion of the flame $(0.1 < \widetilde{c} < 0.9)$ has $\log(1000\widehat{\mathrm{Da}}_\Delta) < 1$ downstream of $x/D > 2$, indicating that the local burning rates are weaker as the chemical time scales are larger. Therefore, it is clear that multi-regime combustion occurs within this bluff body stabilised flame.

The radial variation of the time-averaged filtered reaction rate is shown in Fig. 5.2 as a function of the time-averaged progress variable. Thus, this figure shows the variation of the averaged reaction rate across the flame brush. The reaction rates are normalised using ρ_u, s_L^0 and δ_L^0 and the results are shown for three axial locations. If the peak normalised reaction rate is close to unity, this suggests the reaction zone is not affected by turbulence and the reaction zone is laminar. The peak value of this normalised reaction rate is of order unity for the location $x/D = 0.2$, suggesting that the combustion is occurring in the flamelet regime, as the peak reaction rate is close to its laminar value. Moving downstream from this point, the peak value decreases gradually from unity,

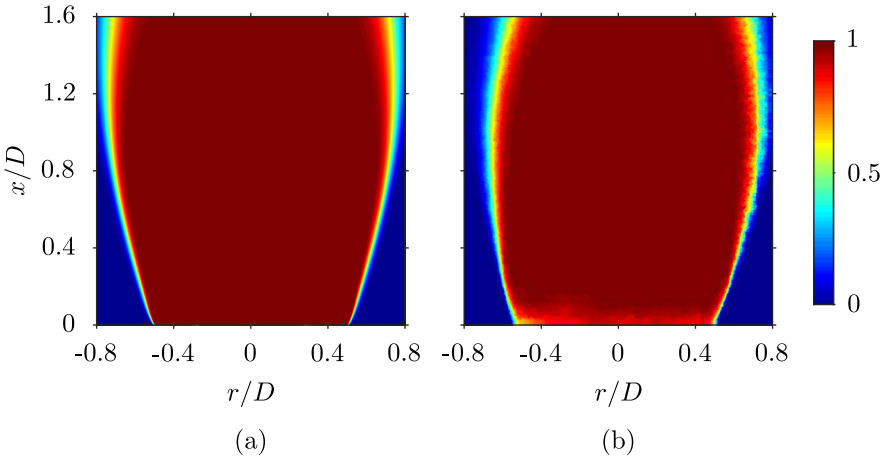

Fig. 5.3 Comparison of (a) the averaged progress variable contours from the LES against (b) the OH-PLIF field (Kariuki *et al.*, 2012).

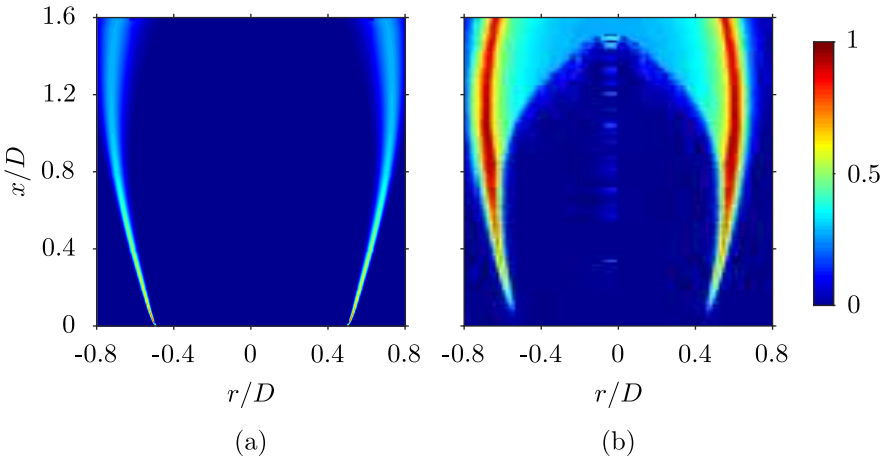

Fig. 5.4 Comparison of (a) the averaged reaction rate contours from the LES against (b) the Abel transformed OH^* (Kariuki *et al.*, 2012).

suggesting a broadening of the flame. This broadening implies that the combustion regime is changing gradually further downstream from the bluff body base. These results support the observations made in Fig. 5.1 regarding the combustion regime. The change in the combustion regime is due to the chemical time scales becoming larger as the shear generated turbulence affects the flame more significantly when moving downstream.

Figures 5.3 and 5.4 compare the computed spatial variations of averaged reaction progress variable and reaction rate with appropriate measurements. All quantities are normalised so that they vary from zero to unity. The progress variable fields in the experiment are obtained from the OH-PLIF measurements, whereas the progress variable in the computations is based on CO and CO_2 mass fractions. The progress variable fields, shown in Figs. 5.3a and 5.3b, suggest that the flame length and width are slightly

overestimated in the computations. However, the LES results show a flame shape that is very similar to that observed in the experiment. This is also supported by the results in Figs. 5.4a and 5.4b, showing the computed averaged reaction rate and the measured OH^* chemiluminescence image respectively, where the latter is used to monitor the heat release regions of the flame. Thus, the reaction rate is used for this comparison, which is readily available in the computations. The heat release can be obtained by taking the product of lower heating value of the fuel and the reaction rate. It can be seen in Fig. 5.4a that the peak reaction rate is in the vicinity of the bluff body base within the thin layer, as noted in the analysis of Fig. 5.1, and this thin layer consist of roughly five to six numerical cells in the radial direction. The peak reaction rate value decreases further downstream because of the broadening of the filtered flame, which is consistent with the SGS Damköhler number variation and filtered reaction rates, shown in Figs. 5.1 and 5.2 respectively. It is shown in the left half of Fig. 5.1 that the flame thickness increases downstream of $x/D < 1$, but the high reaction rate regions are confined to a thin layer. These qualitative comparisons suggest that the general features of the bluff body stabilised open flame are captured satisfactorily by the unstrained flamelet combustion closure used for this study. However, quantitative assessments are to be made, which are presented next.

5.3.2 Comparisons with measurements

The experimental investigation by Kariuki *et al.* (2012) used PIV and planar imaging of OH using laser induced fluorescence techniques and OH^* chemiluminescence. The quantitative comparisons are therefore limited to only velocity statistics, since there are no detailed pointwise temperature or species measurements available for this burner. However, it is said that the flow fields are strongly influenced by combustion and the entrainment effects. Therefore in order to get good comparisons between the measurements and computational results, the combustion model and its interaction with the flow and entrainment effects must be well captured. This is further to the numerical grid requirements, which was validated using the isothermal flow results in § 4.4.3.

The measured and computed time-averaged streamwise velocity variations along the centreline of the burner are shown in Fig. 5.5, where the velocity is again normalised using U_b. The measurements do not span the entire recirculation zone length, but the comparisons shown with the available data are good. As expected, the presence of combustion influences the recirculation zone length, which is seen to increase from a length of $1.15D$ for isothermal flow to a length of $2.02D$ for flame A1. This length is close

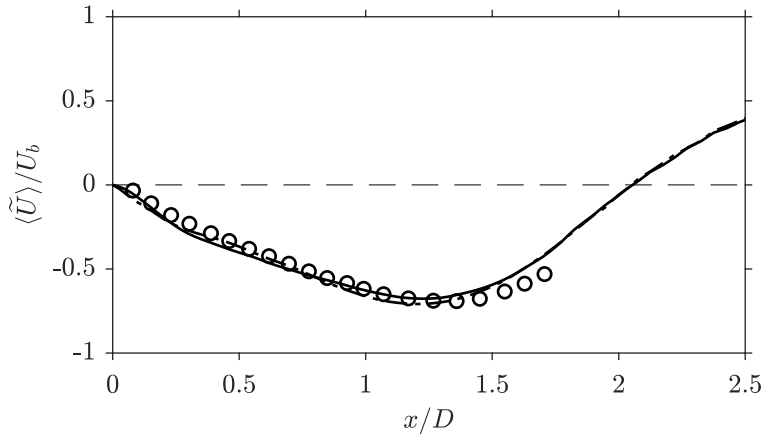

Fig. 5.5 Comparison of the computed [lines] and measured [○] (Kariuki *et al.*, 2012) time-averaged axial velocities for flame A1. The results are obtained using dynamic [——] and static [– · –] approaches for β_c in Eq. (3.35).

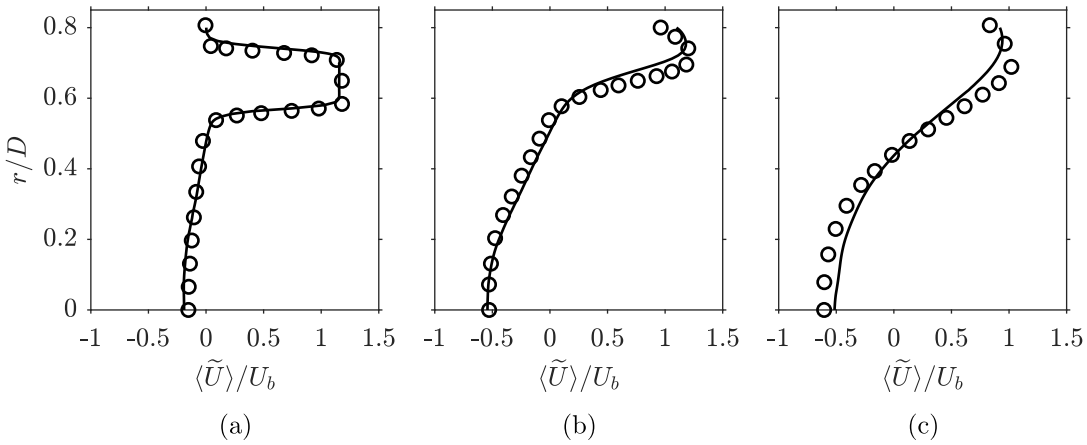

Fig. 5.6 Computed [——] and measured [○] (Kariuki *et al.*, 2012) radial variations of the time-averaged axial velocity at (a) $x/D = 0.2$, (b) 0.8 and (c) 1.6 for flame A1.

to the value reported in the experiment, which was approximately $2D$ (Kariuki *et al.*, 2012). As mentioned in § 3.5, the model parameter β_c in Eq. (3.35) can be evaluated dynamically or prescribed with a static value. For the sake of comparison, the axial variation of normalised averaged streamwise velocity is obtained using the dynamic and static approaches; these are shown in Fig. 5.5. A static value of $\beta_c = 0.4$ was chosen *a posteriori* using the results from the dynamic procedure for β_c (Gao *et al.*, 2015; Langella *et al.*, 2015). It is seen that the results are almost identical, which is due to the careful selection of the value for β_c. The results shown from this point use the dynamic procedure for β_c. The radial variations of computed and measured axial velocity are compared in Fig. 5.6 for the same three streamwise locations that were considered for the isothermal case in Fig. 4.4. The LES results at all three locations show a good agreement with

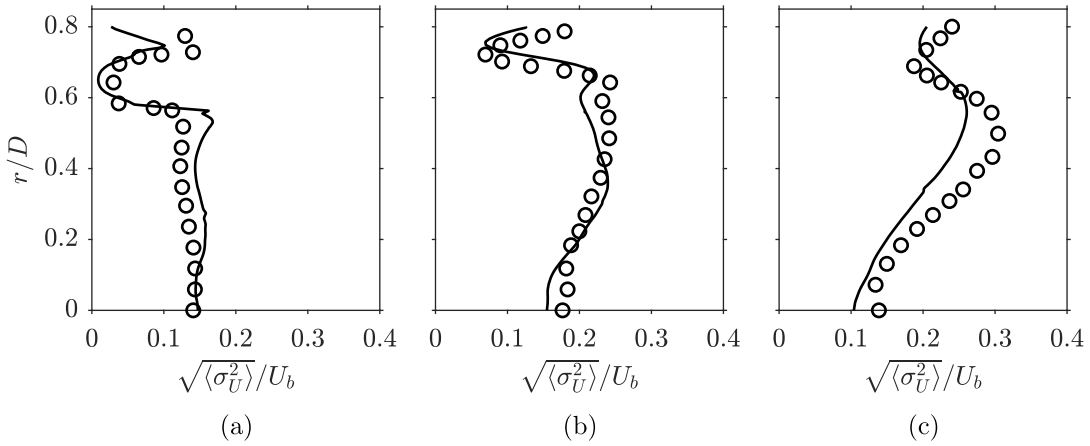

Fig. 5.7 Computed [——] and measured [○] (Kariuki *et al.*, 2012) radial variations of the r.m.s. axial velocity at (a) $x/D = 0.2$, (b) 0.8 and (c) 1.6 for flame A1.

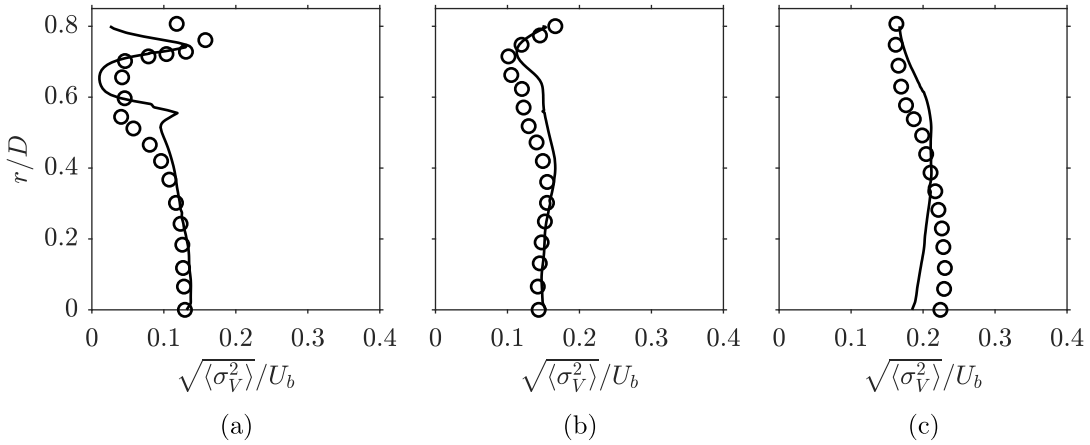

Fig. 5.8 Computed [——] and measured [○] (Kariuki *et al.*, 2012) radial variations of the r.m.s. radial velocity at (a) $x/D = 0.2$, (b) 0.8 and (c) 1.6 for flame A1.

the measurements (Kariuki *et al.*, 2012). These variations are similar to those observed for non-reacting flow, except the maximum velocity is larger for reacting flow, due to the heat release in the flame near the inner shear layer. The good comparisons shown in Fig. 5.6 suggest that the locations of both the inner and outer shear layers are well captured in the LES.

The r.m.s. of axial and radial velocities are shown in Figs. 5.7 and 5.8 respectively, which are estimated using the resolved variance $\langle \boldsymbol{u}'' \rangle \simeq \sqrt{\langle \sigma_{\boldsymbol{U}}^2 \rangle}/U_b$. The r.m.s. radial velocity is directly compared against the r.m.s. y component of the velocity, due to no measurements being available for the z plane, as mentioned in § 4.2.3. Since the turbulence is shear driven in this burner, it is expected to see peak values of the r.m.s. velocities in the regions of strong shear, which is observed in the computations, as shown

in Figs. 5.7 and 5.8. However, the inner peak for the r.m.s. axial velocity is somewhat lower than the outer peak for the location $x/D = 0.2$. This may be due to the additional shear generated by the entraining flow in the outer shear layer. In addition, the reason for the decrease in the r.m.s. radial velocity within $0.4 \leq r/D \leq 0.6$ at the location $x/D = 0.2$ is not clear. It is indeed expected to see a peak for the r.m.s. axial velocity variation in the region close to the bluff body base, as shown by the computational result and shows a similar trend to the isothermal case. The radial variations of both r.m.s. velocities are well captured, except for some over predictions within the inner shear layer. The variations are well captured at the second location in Figs. 5.7b and 5.8b, but the r.m.s. velocities within the recirculation zone at $x/D = 1.6$ are under predicted in the computation, as shown in Figs. 5.7c and 5.8c. Nonetheless, the overall agreement of these quantities with the experimental data is good.

5.4 Further discussion

5.4.1 Multi-regime combustion

It has been shown that the flame and flow features are well captured by the LES, showing good comparisons with the measurements to a similar standard reported in previous numerical studies using different combustion models (Farrace *et al.*, 2018, 2017; Hodzic *et al.*, 2017*a*,*b*, 2019). In general, the magnitudes of the r.m.s. axial and radial velocities increase with axial distance from the bluff body base, suggesting that the turbulent kinetic energy production increases with axial distance. The turbulent kinetic energy at the axial locations $x/D = 0.2$, 0.8 and 1.6 that have been analysed thus far is computed using both the experimental data and LES results. Since w' is not available from the measurements (Kariuki *et al.*, 2012), the turbulent kinetic energy is estimated as $\langle k_{\text{exp}} \rangle = 0.5(u'^2 + 2\,v'^2)$ by assuming that $w' \simeq v'$. This is compared to the turbulent kinetic energy from the LES results, which is computed as $\langle \widetilde{k}_{\text{res}} \rangle = 0.5(u''^2 + v''^2 + w''^2)$ using only the resolved velocities, and also the total kinetic energy $\langle \widetilde{k}_{\text{tot}} \rangle = \langle \widetilde{k}_{\text{res}} \rangle + \langle \widetilde{k}_{\text{sgs}} \rangle$ by including the SGS kinetic energy $\widetilde{k}_{\text{sgs}} = 3u'^2_{\Delta}/2$, where u'_{Δ} is estimated using a model (Langella *et al.*, 2018*b*). These variations are shown in Fig. 5.9, where the symbols represent the measurements $\langle k_{\text{exp}} \rangle$, the black line represents $\langle \widetilde{k}_{\text{tot}} \rangle$ and the dash-dotted black line is for $\langle \widetilde{k}_{\text{res}} \rangle$. The edges of the shear layer originating from the trailing edge of the bluff body are drawn using the contours at 10 % of the local peaks of $\partial \langle \widetilde{U} \rangle / \partial r$ and shown with grey lines. Red lines denote the flame brush, which is marked using $\langle \widetilde{c} \rangle = 0.1$ and 0.9.

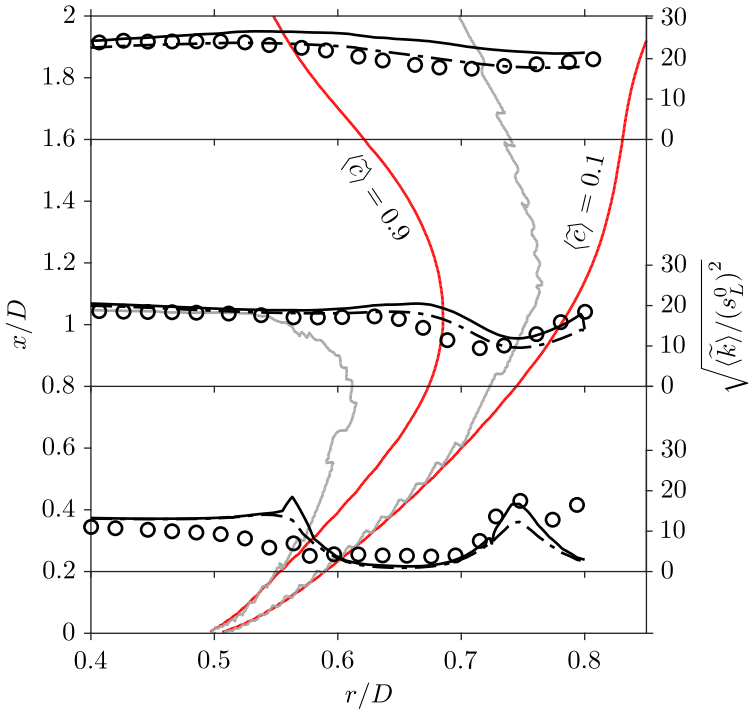

Fig. 5.9 Radial variations of computed and measured turbulent kinetic energy in flame A1. The edges of the inner shear layer are shown with [——] and those of the flame brush marked using $\langle\widetilde{c}\rangle = 0.1$ and 0.9 are shown with [——]. The turbulent kinetic energy with [——] and without [-··-] the modelled SGS contribution are also shown.

It is seen that the sharp peak of $\langle\widetilde{k}_{\text{tot}}\rangle$ at $x/D = 0.2$ is located within the inner shear layer, where the flame brush is also located. It should be noted that the other sharp peak is within the outer shear layer and is not considered for the analysis here, as it is outside the flame brush. Since the peak seen within the inner shear layer for $\langle\widetilde{k}_{\text{tot}}\rangle$ is not present for $\langle\widetilde{k}_{\text{res}}\rangle$, this means that there are some flame-generated velocity fluctuations in this region. These fluctuations can come from two sources; one is flame-generated turbulence and the other is due to intermittent effects from the flame. The current framework for the analysis makes it challenging to ascertain these two mechanisms and to identify a dominant one; this will be explored in a future work. Since the numerical grid used resolves more than 80 % of the turbulence, the SGS turbulence is expected to be small and the flame induced effects would be strong. Nevertheless, the trends are the same for both $\langle\widetilde{k}_{\text{res}}\rangle$ and $\langle\widetilde{k}_{\text{tot}}\rangle$. Furthermore, it should be noted that $w' \simeq v'$ is assumed for the experimental data and the validity of this approximation is an open question. At $x/D = 0.8$ and 1.6, it is observed that the peak value of $\langle\widetilde{k}_{\text{res}}\rangle$ is within the shear layer and decays from the product side to the reactant side of the flame for the burner configuration used here. There is a slight increase close to the reactant side for

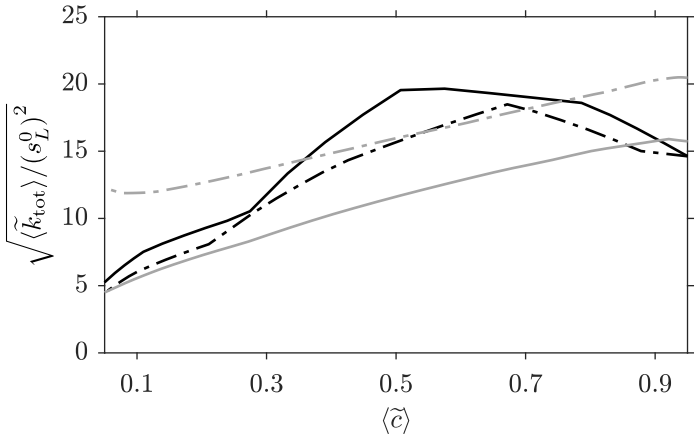

Fig. 5.10 Turbulent kinetic energy variation across the flame brush at four streamwise locations $x/D =$ 0.1 [——], 0.2 [– · –], 0.4 [——] and 0.8 [– · –].

these two locations, which is caused by the outer shear layer resulting from ambient air entrainment. In addition, it is observed that there is some interaction between the flame and the shear layer, which is illustrated in Fig. 5.9 when the flame and the shear layer are no longer aligned downstream of $x/D = 0.6$. Although all of the shear layer is within the flame brush near the flame stabilisation region, this layer gradually moves out of the flame when moving downstream. The contour of $\langle\widetilde{c}\rangle = 0.9$ moves from the inner to outer side of the shear layer starting from the bluff body base to $x/D = 1$, as shown in Fig. 5.9. This contour then moves back into the inner shear layer in a similar manner to the outer part of the shear layer. On the other hand, the $\langle\widetilde{c}\rangle = 0.1$ contour continuously moves further away from the shear layer from $x/D = 0.6$ because the reactant stream is unconfined. This relative movement of the shear layer and the flame brush will lead to an unexpected behaviour of the turbulent kinetic energy distribution across the flame brush for various downstream positions.

A previous DNS study by Chakraborty *et al.* (2011) reported that the turbulent kinetic energy has a peak value for flames within the corrugated flamelet regime, due to generation of turbulent kinetic energy within the flame brush. However for flames within the thin reaction zones regime, it was found that the turbulent kinetic energy decays monotonically across the flame brush. This is due to the effects of the mean pressure gradient and pressure dilatation being relatively weaker than those of viscous dissipation for flames within the thin reaction zones regime. This is not the case for flames within the corrugated flamelets regime as the effects of viscous dissipation are much weaker compared to the effects of the mean pressure gradient and pressure dilatation and hence, this leads to flame-generated turbulence. These behaviours are seen in the

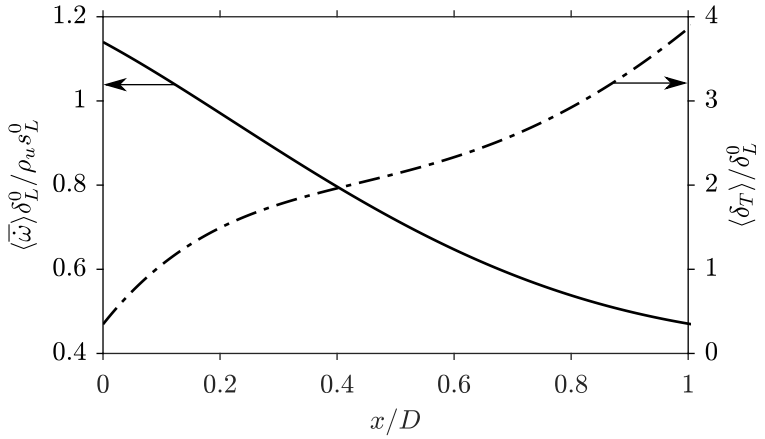

Fig. 5.11 Variations of the peak time-averaged normalised filtered reaction rate [——] and normalised flame thickness [– · –] with axial distance.

variations of $\langle\widetilde{k}_{\text{tot}}\rangle$ with $\langle\widetilde{c}\rangle$ and are depicted in Fig. 5.10. It is seen that the peak turbulent kinetic energy is at the centre of the flame for $x/D = 0.1$ and then shifts towards the product side for $x/D = 0.2$ and $x/D = 0.4$. However, there is no peak for the location $x/D = 0.8$, which suggests that there is a transition in the combustion regimes in the region $0.2 < x/D < 0.8$. The flame is burning within the corrugated flamelet regime close to the bluff body, which is shown by the flame wrinkling caused by large-scale eddies resulting from Kelvin–Helmholtz instability, and this thin layer structure is seen in Fig. 5.1. Hence, it could be said that the flame near the stabilisation region is quasi-steady and quasi-laminar. This claim is also supported by the high values of the parameter $\widehat{\text{Da}}_\Delta$ (indicating stronger reaction rates) in those regions, as observed in Fig. 5.1.

To further investigate this quasi-laminar flame observation, the variation of peak averaged reaction rate $\langle\dot{\overline{\omega}}\rangle$ and the flame brush thickness $\delta_T = 1/|\partial\langle\widetilde{c}\rangle/\partial r|_{\text{max}}$ are studied. If the flame is truly laminar, then the peak reaction rate should scale as $\rho_u s_L^0/\delta_L^0$ as laminar flame theory suggests. Therefore, normalising the peak averaged reaction rate with this scaling should yield the normalised reaction rates of order unity if the flame is quasi-laminar and δ_T/δ_L^0 must also be of order unity. These two normalised quantities are plotted in Fig. 5.11 as a function of x/D. It is shown that for $x/D < 0.15$, the normalised reaction rate is slightly greater than unity. The strain thinning of the filtered flame caused by large-scale eddies near the flame base causes the normalised reaction rate to be larger than unity. For $x/D > 0.2$, the normalised reaction rate decreases monotonically from unity. For $x/D > 0.8$, the normalised quantities are in the ranges $\langle\dot{\overline{\omega}}\rangle\delta_L^0/\rho_u s_L^0 < 0.6$ and $\delta_T/\delta_L^0 > 3$, which suggests that turbulence has significantly altered

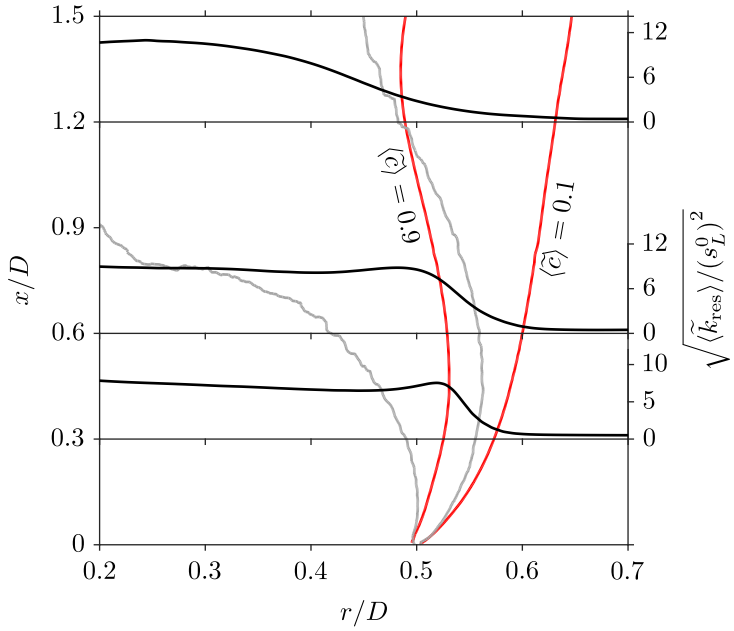

Fig. 5.12 Radial variations of turbulent kinetic energy in a confined bluff body stabilised flame with 2 % incoming turbulence. The edges of the inner shear layer are shown with [——] and those of the flame brush, marked using $\langle\widetilde{c}\rangle = 0.1$ and 0.9, are shown with [——].

the flame structure. Furthermore, it is shown that $\delta_T/\delta_L^0 < 1$ for $x/D \leq 0.2$, which supports the quasi-laminar flame observation.

5.4.2 Comparison with a confined flame

Figures 5.12 and 5.13 show the radial variation of $\langle\widetilde{k}_{\mathrm{res}}\rangle$, which is normalised by $(s_L^0)^2$, for three axial locations inside the recirculation zones of confined bluff body stabilised flames. These are similar to the flames studied by Langella *et al.* (2016*a*), but use a higher equivalence ratio of $\phi = 0.8$, since these conditions are closer to the equivalence ratio of $\phi = 0.75$ for flame A1. These two flames have turbulence levels of approximately $u'/U_b = 2\,\%$ and 22 % at the bluff body base. The lengths of the recirculation zones are $1.37D$ and $0.76D$ for the low and high turbulence intensity confined flames respectively. Therefore, both of these recirculation zones are significantly shorter than the observed length of $2.02D$ for flame A1. As noted in § 5.1, the aim of the following analysis is to distinguish the behaviour between flame A1 and the two confined flames. Flame A1 has only shear driven turbulence, but the other two flames have both shear driven and incoming turbulence.

It is clear that the relative locations of the shear layers and flame brush are very similar near the bluff body for these three flames, as seen when comparing Figs. 5.9, 5.12

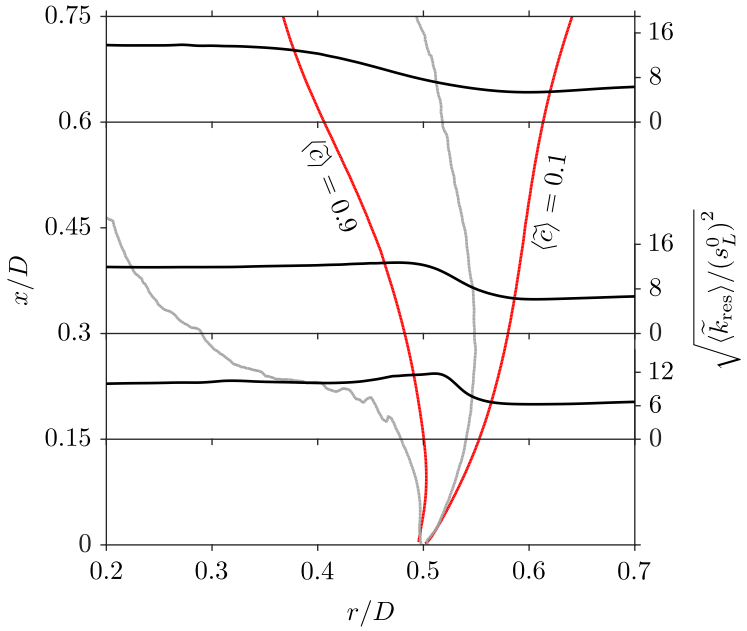

Fig. 5.13 Radial variations of turbulent kinetic energy in a confined bluff body stabilised flame with 22 % incoming turbulence. The edges of the inner shear layer are shown with [——] and those of the flame brush, marked using $\langle\tilde{c}\rangle = 0.1$ and 0.9, are shown with [——].

and 5.13. In the low turbulence level case in Fig. 5.12, the initial evolution of the shear layer is similar to that observed for flame A1 in Fig. 5.9. However as seen in Fig. 5.12, the $\langle\tilde{c}\rangle = 0.9$ contour moves completely out of the shear layer at approximately $x/D = 1.18$, which is around 86 % of the recirculation zone length. It can be suggested that beyond this point, the flame does not experience any shear generated turbulence. This is not the case with flame A1, as the absence of walls allows the flame to remain within the shear layer, whereas the shear layer is pushed further inwards for this confined flame. The turbulent kinetic energy decays from the product side to the reactant side of the flame at all three locations for the low turbulence intensity confined case in Fig. 5.12. In the near-field of flame A1 in Fig. 5.9, the peak turbulent kinetic energy at $x/D = 0.2$ was located within the flame brush, which is not the case for the near-field location of $x/D = 0.3$ in Fig. 5.12. This is due to the presence of walls for the confined case in Fig. 5.12, which causes the shear layer to be shifted further inwards away from the flame and suppresses the flame-generated turbulence.

When the incoming turbulence intensity is increased to 22 %, it is shown that part of the shear layer always remains within the flame for the entire recirculation zone length, as illustrated in Fig. 5.13, which is also the case for flame A1. However, the high TI confined flame experiences more shear generated turbulence than the low TI confined

flame, as the flame brush and shear layer are thicker and hence, a larger part of the flame is encompassed within the shear layer. The increasing trend of the turbulent kinetic energy from the contour $\langle\widetilde{c}\rangle = 0.1$ into the ambient air region for flame A1 is due to the presence of the outer shear layer that results from the air entrainment. The relative positions of the shear layer and the flame brush in the vicinity of the bluff body base are similar for both confined flames, suggesting the flame stabilisation processes are similar. This is seen in Figs. 5.12 and 5.13 as the shear layers are pushed inwards by the pressure forces exerted by the wall in the regions close to the bluff body base from approximately $x/D = 0.1$ and $x/D = 0.05$ respectively. This is not the case for flame A1, as both the product and reactant sides of the flame are well aligned with the shear layer until $x/D = 0.2$. The reactant side of the flame remains aligned with the outer part of the shear layer from this point until $x/D = 0.6$, as seen in Fig. 5.9. Thus, the presence of the walls close to the bluff body does affect the relative positions of the flame and shear layer.

5.5 Summary

A lean turbulent premixed bluff body stabilised flame far from blow-off conditions is computed and compared against the corresponding experimental data. The statistics from the LES show that the recirculation zone and inner shear layers are accurately captured. In addition, the overall shape of the flame in the LES is slightly longer and wider than the flame in the experiment. Further analysis of the distribution of the turbulent kinetic energy across the flame and inner shear layer shows that the turbulent kinetic energy has a peak value within the flame in the vicinity of the bluff body base. However, the turbulent kinetic energy decays monotonically from the product to reactant side of the flame further downstream. This suggests a shift from the corrugated flamelets regime to the thin reaction zones regime of turbulent premixed combustion. The behaviour of the open bluff body stabilised flame is compared to confined bluff body stabilised flames, which experienced additional incoming turbulence. The main difference between the open and confined flames is observed to be the relative positioning of the shear layer and flame brush, and their spatial evolution. It is also observed that the change in turbulence intensity causes significant changes to the evolution of the flame and the shear layer for the confined flames. This is caused by the increased turbulence intensity supplied to the bluff body base that increases the width of the shear layer due to turbulent diffusion, which causes the recirculation zone length to decrease. This suggests that these physical

attributes are highly sensitive to the inlet conditions, such as the turbulence intensity and the equivalence ratio, when the flame is stabilised within an enclosed chamber. However, the recirculation zone length for the flames studied by Kariuki *et al.* (2012) showed no significant changes when the equivalence ratio was varied. Therefore, it is of interest to elucidate the behaviour of the recirculation zone for bluff body stabilised flames in confined flows by varying the fuel–air equivalence ratio and the turbulence intensity. This is investigated next in Chapter 6.

Chapter 6

A Scaling Relation for the Recirculation Zone Length

This chapter presents the analysis of a set of isothermal and reacting flow simulations with premixed reactants within a combustion chamber that contains a conical bluff body. The turbulence intensity and the fuel–air equivalence ratio are varied, in order to observe their influences on the recirculation zone. These observations are used to undertake a force balance on a control volume behind the bluff body and determine which forces influence the change in the recirculation zone structure. A scaling relation is then deduced for recirculation zone length as a function of the inlet boundary conditions. The application of this scaling to flames in an open environment and behind a backward facing step is also explored.

6.1 Motivation

The recirculation zone that is formed directly behind the bluff body aids the stabilisation process for a flame, as there is a continuous turbulent exchange of mass, momentum and energy with its surroundings (Winterfeld, 1965). As mentioned in Chapter 5, this zone contains hot combustion products and therefore, it acts as a constant source of heat, radicals and intermediate species to sustain combustion. This also helps the flame stabilisation processes over a wide range of fuel–air mixture equivalence ratios and velocities (Davies & Beér, 1971). However, these physical processes that govern the recirculation zone structure for isothermal and reacting flow are not well understood.

Early work on flow around bluff bodies and obstacles has been studied in detail for several decades. These investigations vary from small-scale configurations, such as

the flow around a small bluff body (Britter *et al.*, 1979; Hunt, 1973), to large-scale atmospheric flows, which focus on the dispersion of dense gases and pollutants around buildings (Britter, 1989; Fackrell, 1984). Studies of these atmospheric flow problems have aimed to predict the build up of pollutants in the near-field wake, including their residence time and concentrations. In addition, these studies have investigated the size of the near-field wakes behind the building and the re-attachment length at ground level (Vincent, 1977, 1978). Scaling relations have also been proposed in these studies, which include predicting the near-field wake length as a function of the height and width of the building (Fackrell, 1984) and as a function of the free stream velocity (Britter & Griffiths, 1982).

For small-scale configurations, there have been numerous studies of isothermal flows with bluff bodies, which have provided additional insights into these recirculation zones, their flow patterns and various factors influencing the attributes of these zones (Calvert, 1967; Carmody, 1964; Chigier & Beer, 1964). These flows were also used to develop and investigate measurement techniques for velocity and turbulence, since there are strong velocity gradients present in these flows (Bradbury, 1976; Castro & Robins, 1977; Davies & Beér, 1971; Durao & Whitelaw, 1978; Fuchs *et al.*, 1979; Roberts, 1973; Taylor & Whitelaw, 1984; Uberoi & Freymuth, 1970). The recirculation zone length L_R is commonly used to evaluate the influences of inlet flow conditions. This length is sensitive to the incoming turbulence level and decreases towards an asymptote when the inlet turbulence level is increased (Castro & Robins, 1977; Durao & Whitelaw, 1978; Humphries & Vincent, 1976*a*,*b*). Moreover, an increase in the blockage ratio in unconfined flows decreases L_R when it is normalised by the bluff body diameter D (Davies & Beér, 1971; Durao & Whitelaw, 1978). However, the walls in confined bluff body flames cause L_R to increase with blockage ratio, since large streamline curvature at the rear stagnation point is prevented (Taylor & Whitelaw, 1984). Taylor (1982) has provided a comprehensive review of the various experimental studies on this topic.

It has also been demonstrated that the heat release from combustion significantly influences L_R. Bill & Tarabanis (1986) claimed that the effects of combustion are to (i) increase this length, (ii) dampen the velocity fluctuations and (iii) increase the magnitude of the velocities, due to the decrease in the gas density within the recirculation zone. For premixed systems, it was observed that the value of L_R was at its minimum for flames around stoichiometric conditions (Winterfeld, 1965; Wright, 1959). Furthermore, Pan *et al.* (1992*b*) demonstrated that increasing the incoming Turbulence Intensity (TI) for a given equivalence ratio ϕ led to a decrease in L_R, which was consistent with

the earlier studies on isothermal bluff body flows. The flame was observed to reside within the shear layer originating from the trailing edge of the bluff body, where strong turbulence–combustion interactions are present. Experimental studies have shown that increasing the TI thickened the preheat zone and hence, the flame brush was observed to thicken (Chowdhury & Cetegen, 2017; Nandula, 2003). These configurations involve combustion conditions ranging from the flamelets regime to the distributed reaction zones regime of turbulent combustion (Peters, 2000) and thus, such configurations serve as suitable candidates for robust validation of turbulent combustion models. A number of previous studies have used this configuration for this purpose (Bai & Fuchs, 1994; Fureby & Möller, 1995; Langella *et al.*, 2016*a*; Rydén *et al.*, 1993; Spalding, 1971).

Backward facing step configurations with reacting flow have also been previously used to study the effects of combustion on the recirculation zone and to gather experimental data for combustion model validation. In this configuration, the flame is stabilised in the shear layer that is formed between the incoming free stream at a velocity of U_∞ and the recirculation zone behind the step. The influences of thermochemical parameters, such as ϕ and fuel composition, on the values of L_R have been studied by Ghoniem and his co-workers using backward facing step configurations for a wide range of thermochemical conditions (Chakroun *et al.*, 2017; Hong *et al.*, 2015; Michaels *et al.*, 2017; Shanbhogue *et al.*, 2016; Speth & Ghoniem, 2009). The TI at the combustor entry in these studies was approximately 6 % (Hong *et al.*, 2015). Both reacting and isothermal conditions were investigated and the results showed that L_R decreased with increasing ϕ for the various fuel–air mixtures studied. These investigations concluded that the consumption speed s_c of a strained laminar flame could be used to scale the recirculation zone length as $L_R/L_{R,\mathrm{ref}} \sim U_\infty/s_c$, where $L_{R,\mathrm{ref}}$ is the recirculation zone length for the corresponding isothermal flow case (Hong *et al.*, 2015). The strain rate at the streamwise location where the flame exited the recirculation zone was suggested to be the characteristic strain rate used to obtain s_c in the study by Michaels *et al.* (2017). The aforementioned scaling expression was also revised as $L_R/L_{R,\mathrm{ref}} \sim (\rho_b U_\infty/\rho_u s_c)$ to include the density change arising from thermal expansion. The densities of unburnt and burnt mixtures are denoted using ρ_u and ρ_b respectively. However, the study by Shanbhogue *et al.* (2016) concluded that using a characteristic strain rate alone is insufficient to quantify the influence of combustion on the recirculation zone and the effects of turbulence on the flow field must also be considered. It is worth noting here that the recirculation zone behind a backward facing step is constrained by the wall and the associated boundary layer at the bottom

wall, yielding a secondary recirculation zone near the bottom corner. These features are absent for the flow configuration considered for this study.

The influences of TI and ϕ on the recirculation zone length behind a bluff body have not been investigated thoroughly, although some trends have been reported by Pan *et al.* (1992*b*, 1991*a*,*b*). It was suggested that the influences of combustion on the recirculation zone may come through the pressure dilatation influencing the turbulent kinetic energy. However, a careful consideration of the problem shows that the recirculation zone behind a bluff body is a near-field wake phenomenon, which is governed by pressure and the momentum exchange between the body and the flow; more specifically, the momentum transfers into and out of the near-field wake region. This suggests that a force balance analysis is appropriate. Furthermore, the momentum exchanges will be influenced by turbulence, combustion and their interactions. Hence, the balance among the various forces acting in the radial and axial directions is likely to dictate the behaviour of the recirculation zone length. These forces are influenced by the incoming TI, the amount of heat release and the turbulence–combustion interactions. The amount of heat release is related to ϕ, as well as the fuel composition.

Thus, the objectives of this study are:

- To understand these influences using the LES results of bluff body stabilised turbulent premixed flames.
- To propose a scaling relation for L_R relating the TI at the bluff body base and the temperature rise across the flame front. The heat release parameter τ is used to represent the temperature rise and this is directly related to ϕ. This objective is achieved by employing a control volume analysis for the various forces acting on the recirculation zone in isothermal and reacting flows.

6.2 Flame conditions and numerical detail

The burner that is studied in this chapter is the same as described in § 4.3.1 and is illustrated in Fig. 4.6. The flames that are simulated here were first studied experimentally by Pan *et al.* (1992*a*,*b*, 1991*a*,*b*) using LDA and CARS techniques. Spontaneous Raman scattering and Rayleigh techniques were later used by Nandula *et al.* (1996) and Nandula (2003) for this burner to obtain detailed temperature and chemical species measurements. Premixed methane–air mixtures with equivalence ratios of $\phi = 0.59$, 0.80 and 0.90 at temperatures of $T_u = 294\,\mathrm{K}$ entered the combustion chamber at a constant mass flow rate

ϕ	τ	s_L^0 (m/s)
0.59	4.558	0.122
0.80	5.703	0.299
0.90	6.171	0.366

Table 6.1 Laminar flame parameters.

to give the same bulk velocity at the bluff body base $U_b = 15\,\mathrm{m/s}$ as the isothermal flow case. The scalar measurements obtained by Nandula *et al.* (1996) and Nandula (2003) were obtained only for the equivalence ratio of $\phi = 0.59$. These were used as validation for the previous numerical study of this burner (Langella *et al.*, 2016*a*), along with the LDA measurements for the recirculation zone (Pan *et al.*, 1992*b*). The TI at the bluff body base for low TI conditions was 2 %, whereas the high TI condition was 22 %.

The inlet and coflow velocity boundary conditions described in § 4.3.2 are used for all isothermal and methane–air simulations shown in this chapter; these values are shown in Table 4.2. The laminar flame properties for the flames studied here are given in Table 6.1. The TI at the inlet is varied using the digital filter technique (Klein *et al.*, 2003) for isothermal flow conditions and the leanest flames with $\phi = 0.59$. The variables $\widetilde{c}$ and $\sigma^2_{c,\mathrm{sgs}}$ are set to be zero for both the inlet and coflow boundaries and the enthalpies for these boundaries are set to be consistent with their temperature and composition. The passive fluid marker is set to be unity in the methane–air stream and zero for the ambient air coflow stream. The same time step of 7.5 µs that was used for the isothermal flow validation case is used here to ensure the CFL number did not exceed 0.3. The simulations for $16\,t_f$ required 24 hrs of wall clock time on 80 cores and the time-averaged statistics are obtained over the second $8\,t_f$ period.

6.3 Results

6.3.1 Case validations

Before addressing the objectives of this study, the modelling framework and the combustion models are validated first using the time-averaged statistics. Experimental measurements are only available for 6 cases of the 20 simulations used for this study, which are listed in Table 6.2. These 20 simulations include both isothermal and reacting flows. The isothermal cases and flames with $\phi = 0.59$ are labelled respectively using 'I'

Case	ϕ	u'_b/U_b	L_R/D	Ka	Exp. Validation?
I1	0	0.009	1.45	-	Y
I2	0	0.092	1.27	-	Y
I3	0	0.078	1.24	-	-
I4	0	0.090	1.19	-	-
I5	0	0.093	1.23	-	-
L1	0.59	0.009	1.98	0.12	Y
L2	0.59	0.097	1.25	4.46	Y
L3	0.59	0.118	1.22	5.88	-
L4	0.59	0.115	1.31	5.69	-
L5	0.59	0.116	1.21	5.82	-
L6	0.59	0.117	1.34	5.85	-
L7	0.59	0.072	1.38	2.85	-
L8	0.59	0.063	1.40	2.32	-
L9	0.59	0.037	1.53	1.06	-
L10	0.59	0.066	1.42	2.49	-
L11	0.59	0.059	1.45	2.08	-
R1	0.80	0.010	1.37	0.03	Y
R2	0.80	0.086	0.76	0.66	-
S1	0.90	0.011	1.30	0.02	Y
S2	0.90	0.079	0.70	0.39	-

Table 6.2 Database of simulations and their attributes used for analysis in this study. The bulk-mean turbulence level u'_b is the surface-averaged value at the bluff body base.

and 'L', which are taken from the study by Langella (2016). The relatively richer flames with $\phi = 0.8$ and 0.9 are labelled using 'R' and 'S' respectively and are simulated in this study. In addition, simulations of cases I1, I2, L1 and L2 are undertaken in this study, in order to ensure the numerical set-up and inlet turbulence boundary conditions are consistent for all cases labelled with 'R' and 'S'. Cases labelled with '1' and '2' after the letter correspond to turbulence intensities of 2 % and 22 % respectively, which were used in the experiment. The methane–air flames have a Lewis number close to unity.

The values of u'_b/U_b at the bluff body base for these cases are also listed in Table 6.2, which scale approximately as $u'/U_b \sim 2.3\, u'_b/U_b$. These values are obtained by varying the axial r.m.s. velocity value at the computational inlet boundary and assigning lateral and longitudinal length scales, as required for the digital filter technique used in the LES (Klein *et al.*, 2003). The Karlovitz number, defined as the ratio of the chemical time

scale to the Kolmogorov time scale, is given as (Swaminathan & Bray, 2005)

$$\mathrm{Ka} = \frac{\tau_c}{\tau_\eta} = \left\{ \left[2\big(1+\tau\big)^{0.7} \right]^{-1} \left(\frac{u_b'}{s_L^0} \right)^3 \left(\frac{\delta_L^0}{\Lambda} \right) \right\}^{0.5}, \tag{6.1}$$

where Λ is the integral length scale at the bluff body base, which is estimated using 70 % of the flow passage width of $(W - D)/2$ and is approximately 12.1 mm (Turns, 2011). The values of Ka listed in Table 6.2, which are based on the turbulence characteristics at the bluff body base, suggest that the combustion conditions in the various cases range from the wrinkled flamelets regime to the thin reaction zones regimes in the turbulent premixed combustion regime diagram shown in Fig. 2.3. However, the local turbulent time scale, rather than one based on the incoming turbulence level, is more appropriate for understanding the local combustion condition, which can change with the downstream distance from the bluff body base. Indeed, Langella *et al.* (2016*a*) showed that there is multi-regime combustion behind the bluff body in cases L1 and L2, where the regimes ranged from the flamelets regime to the distributed flamelets regime. Similar behaviour is observed for the other reacting flow cases listed in Table 6.2. Cases I1, I2, L1 and L2 were validated thoroughly by Langella *et al.* (2016*a*) using velocity measurements (Nandula, 2003; Pan *et al.*, 1992*b*) and scalar fields (Nandula, 2003; Nandula *et al.*, 1996), where it was demonstrated that the modelling framework has successfully captured the flame behaviour in the multi-regime combustion. For these reasons and for further validation, cases I1, I2, L1, L2, S1 and S2 are used for analysis in this section, in order to highlight how the equivalence ratio and the TI at the inlet affect the values of L_R. These validation cases are marked in Table 6.2 and the additional cases will be used to gain further insights that are required to identify a semi-empirical scaling relation for L_R, which will be presented in § 6.3.3.

Figure 6.1 compares the measured (Pan *et al.*, 1992*b*) and computed time-averaged axial velocity along the centreline for five cases; the computational results for case S2 are shown for comparison purposes. It should be noted that Fig. 6.1a is the same as Fig. 4.7, but is included here for comparison purposes. For the following analysis, the time-averaged statistics, denoted using the angle brackets, are obtained using the samples collected over $8\,t_f$ and the averaging is done both in time and in the azimuthal direction. The simulations require $8\,t_f$ for the transients to pass out of the computational domain and the averaging period of $8\,t_f$ is required for recirculation zone length to remain unchanged when collecting the statistics over a longer period. The negative values for the axial velocity imply reverse flow within the recirculation zone and hence, the values

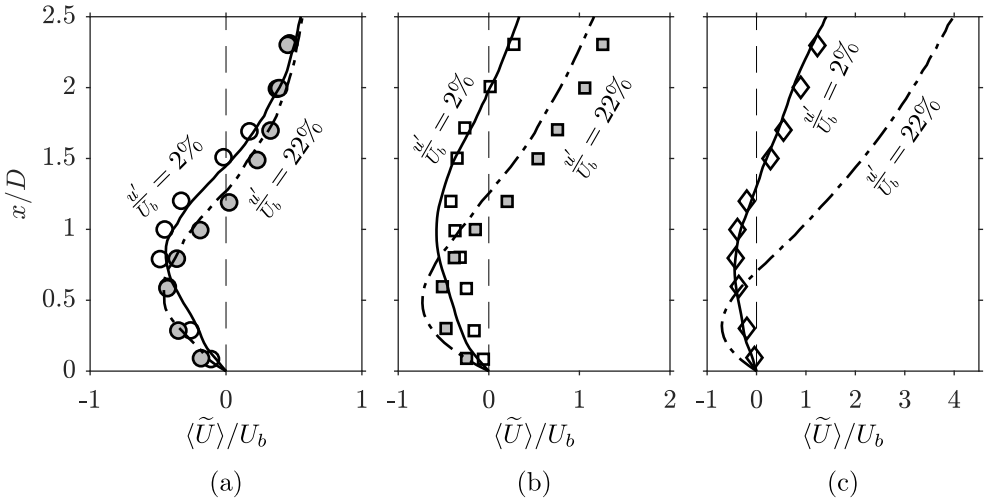

Fig. 6.1 Time-averaged centreline axial velocity comparison between the LES results (lines) and experimental data (symbols) for (a) isothermal flow (I1 & I2), and reacting flows with (b) $\phi = 0.59$ (L1 & L2) and (c) 0.90 (S1). There is no experimental data for case S2 (22 %) shown in (c).

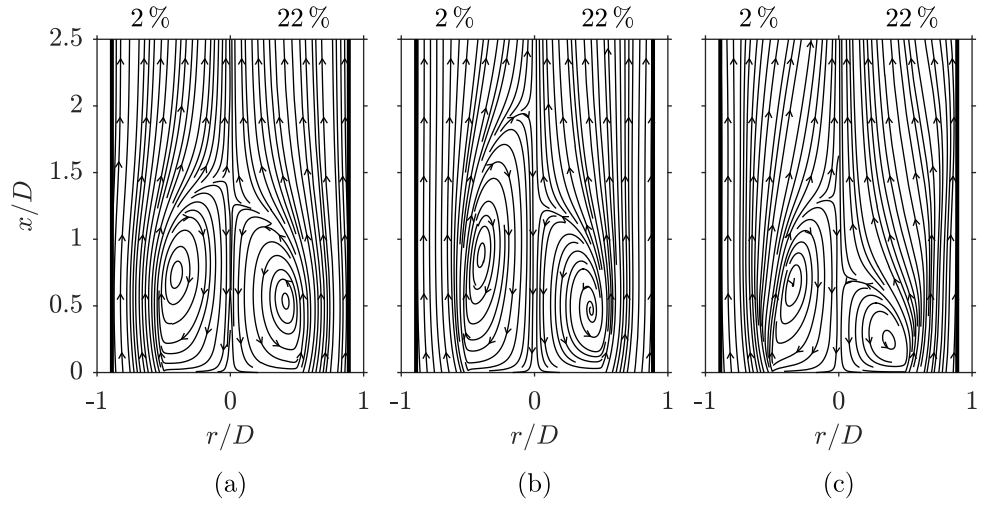

Fig. 6.2 Computed streamlines of the time-averaged velocity in the low and high TI cases of (a) isothermal flows (I1 & I2), and reacting flows with (b) $\phi = 0.59$ (L1 & L2) and (c) $\phi = 0.90$ (S1 & S2).

of L_R are given by the axial distance of the zero crossing of the normalised axial velocity; this location corresponds to the rear stagnation point of the recirculation zone. The results in Fig. 6.1 show that the measured streamwise variation of the axial velocity is captured well in the computations and hence, the values for L_R are close to the values seen in the experiment. There are no scalar or temperature measurements available for cases L1 and S1 shown respectively in Figs. 6.1b and 6.1c.

The streamlines of the time-averaged velocity for the six cases are presented in Fig. 6.2. The two isothermal cases are shown in Fig. 6.2a and the streamline patterns are similar

for both low and high TI cases, although there is a decrease in L_R from $1.45D$ to $1.27D$ when the TI is increased from 2 % to 22 %. There is a non-monotonic variation of L_R with ϕ, or τ, for low TI, as shown in Fig. 6.2. The value of L_R increases to $1.98D$ in case L1 from its isothermal value of $1.45D$. When the equivalence ratio is increased to $\phi = 0.9$, the value of L_R decreases to $1.3D$ for case S1 with TI = 2 %, as shown in Fig. 6.2c. However, this behaviour is different when the TI is increased to 22 %. The value of L_R for case L2 is $1.25D$, which is very similar to the length of $1.27D$ for the isothermal case I2. The general flow patterns for these cases are also very similar, as shown in Figs. 6.2a and 6.2b. This is consistent with the experimental observation by Pan *et al.* (1992*b*), where it was suggested that L_R in reacting flows approached its isothermal value when the TI at the bluff body base was increased. However for case S2, the value for L_R is $0.7D$, which is significantly lower than for the isothermal case I2 for TI = 22 %, as seen when comparing Fig. 6.2a and 6.2c.

These variations presented in Fig. 6.2 show that L_R generally decreases when the TI increases, but it is highly sensitive to changes in the TI for a given ϕ in reacting flow. In addition, the study by Bill & Tarabanis (1986) concluded that the effect of combustion is to increase L_R, which does not seem to hold according to the measurements obtained in the study by Pan *et al.* (1992*b*) and the current LES results. The measured values of L_R in reacting flows behind a backward facing step were observed to decrease with an increase in ϕ (Hong *et al.*, 2015), which also contradicts the observation of Bill & Tarabanis (1986). However, the value of L_R is larger than the isothermal counterpart for the low TI cases with moderate heat release. When the heat release is stronger, the value of L_R is smaller than the length for the isothermal case at a given TI. This intriguing behaviour is shown in Fig. 6.3a, which is to be described in § 6.3.2. The physical reasoning for this non-monotonic behaviour is unclear and this study attempts to provide insights into this behaviour. As noted in § 6.1, the recirculation zone is in the near-field wake behind the bluff body, which is governed by the momentum transfer and the pressure field. It should be noted that the far-field is also affected by momentum transfer, since the evolution of turbulence and the flame is different when the TI and ϕ are varied. This translates into the forces acting on the recirculation zone. Hence, the value of L_R is dictated by the various forces acting on the recirculation zone and these forces are not only influenced by turbulence but also by combustion and its nonlinear interaction with turbulence. Therefore, it is imperative to investigate the balance of these forces acting on the recirculation zone in reacting flows.

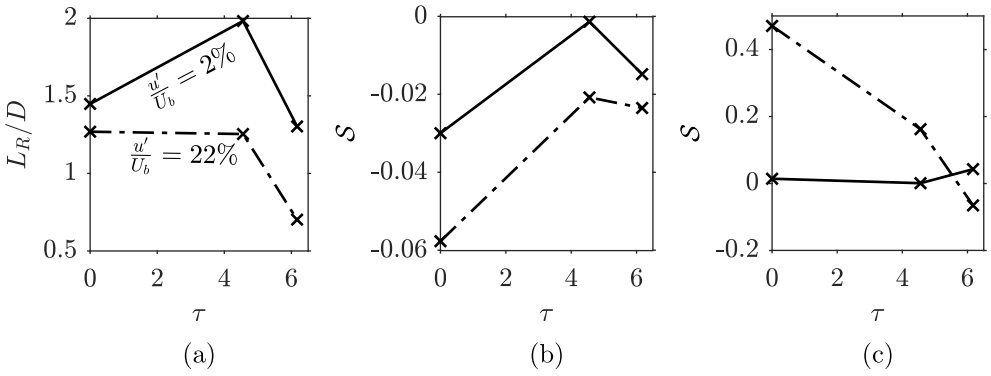

Fig. 6.3 Variation of (a) the recirculation zone length, and the time-averaged normalised source $\mathcal{S} = -\langle(\widetilde{\boldsymbol{U}} - \langle\widetilde{\boldsymbol{U}}\rangle)\rangle \cdot \langle\boldsymbol{\nabla}\overline{p}\rangle/(\rho_u U_b^3/D)$ at (b) $x = L_R$ and (c) the maximum width of the recirculation zone, for the six LES cases shown in Fig. 6.2 with τ.

6.3.2 Force balance on the recirculation zone

The previous analysis suggests that L_R is influenced by the TI at the bluff body base and the methane–air equivalence ratio, or τ, but the physical mechanisms for this are unclear. However, Pan *et al.* (1992*b*) speculated that the turbulence production through the interaction of the velocity fluctuations with the pressure gradients could play an important role. This production is given by $-\langle\boldsymbol{u}''\rangle \cdot \langle\boldsymbol{\nabla}\overline{p}\rangle$, where $\boldsymbol{u}''$ denotes the Favre fluctuation of velocity (Heitor *et al.*, 1987). It was also suggested that this quantity could be of high importance at the maximum width and at the rear stagnation point of the recirculation zone, since $\boldsymbol{u}''$ and $\boldsymbol{\nabla}\overline{p}$ are large at these locations. The maximum width of the recirculation zone is taken as twice the distance between the centreline to the furthest radial position on the zero axial velocity contour.

This source can be extracted from the LES results for the two locations in the six cases shown in Fig. 6.2 and its variation with τ is shown in Fig. 6.3. The source term is normalised using ρ_u, U_b and D, and is written as $\mathcal{S} = -\langle(\widetilde{\boldsymbol{U}} - \langle\widetilde{\boldsymbol{U}}\rangle)\rangle \cdot \langle\boldsymbol{\nabla}\overline{p}\rangle/(\rho_u U_b^3/D)$. This source term is normalised using these quantities because they are readily available as inlet conditions. The variation of L_R/D with τ is also shown in Fig. 6.3a. If this source term is responsible for the variation of L_R/D with τ, a similar behaviour of $\mathcal{S}$ with τ must be seen, but it is apparent that no such trend is seen in Fig. 6.3. This source term directly contributes to the turbulent stress and hence the turbulent shear force, which is one among many forces acting on the recirculation zone. Thus, it is worthwhile to conduct a force balance on the stationary (time-averaged) recirculation zone. The control volume considered for this analysis is shown in Fig. 6.4, which spans the entire

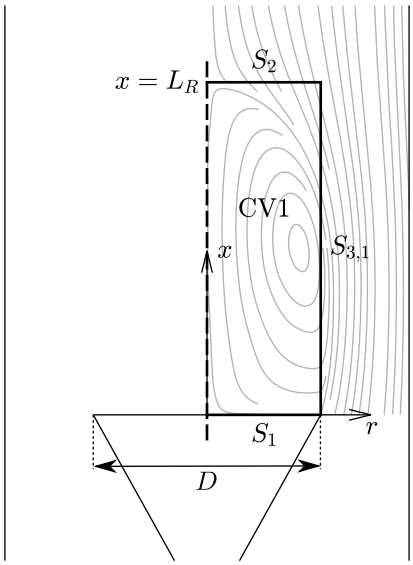

Fig. 6.4 Control volume for the force balance of the recirculation zone.

length of the recirculation zone and covers the bluff body base in the radial direction. Since the mean structure is axisymmetric, only one half is considered.

Using Eq. (3.8), the stationary form of the mean momentum equation is

$$\left\langle \boldsymbol{\nabla} \cdot \overline{\rho}\widetilde{\boldsymbol{U}}\widetilde{\boldsymbol{U}} \right\rangle + \left\langle \boldsymbol{\nabla}\overline{p} \right\rangle \approx \left\langle \boldsymbol{\nabla} \cdot \overline{\boldsymbol{\tau}}_{\text{eff}} \right\rangle, \tag{6.2}$$

where $\overline{\boldsymbol{\tau}}_{\text{eff}}$ is an effective stress tensor, which includes the molecular and anisotropic turbulent stresses. The averaged molecular stresses are smaller than the turbulent stresses, except on the surface S_1 marked in Fig. 6.4, and this is verified using the LES results.

By applying Gauss's theorem to Eq. (6.2) over the control volume CV1, the force balance is written as

$$\underbrace{\int_S \left\langle \overline{\rho}\widetilde{\boldsymbol{U}}\widetilde{\boldsymbol{U}} \right\rangle \cdot \hat{\mathbf{n}} \, \mathrm{d}S}_{\boldsymbol{F}_i} + \underbrace{\int_S \left\langle \overline{p} \right\rangle \hat{\mathbf{n}} \, \mathrm{d}S}_{\boldsymbol{F}_p} = \underbrace{\int_S \left\langle \overline{\boldsymbol{\tau}}_{\text{eff}} \right\rangle \cdot \hat{\mathbf{n}} \, \mathrm{d}S}_{\boldsymbol{F}_T}, \tag{6.3}$$

where S denotes boundaries of the control volume and $\hat{\mathbf{n}}$ is the unit normal vector that points outwards from each of the boundaries. The subscripts i, p and T for the force vector $\boldsymbol{F}$ denote the force due to momentum flux, the pressure force and the turbulent shear force respectively. These forces can be extracted from the LES results and since the inertial and pressure forces can influence the turbulent velocity fluctuations, and hence the turbulent shear forces, the values of inertial and pressure forces are investigated here. Furthermore, the turbulent shear force can be extracted from these two forces using

Case	L_R/D	$F_{i,x}$ (N)	$F_{p,x}$ (N)	$F_{i,r}$ (N)	$F_{p,r}$ (N)
I1	1.45	−0.0379	0.239	0.0118	0.914
L1	1.98	−0.0080	0.307	0.0019	1.299
S1	1.30	−0.0086	0.303	0.0004	0.839
I2	1.27	−0.0319	0.237	0.0175	0.851
L2	1.25	−0.0095	0.298	0.0051	0.868
S2	0.70	−0.0084	0.286	0.0010	0.495

Table 6.3 Net inertial and pressure forces acting on the control volume CV1 in the axial and radial directions.

Eq. (6.3). The net inertial and pressure forces acting in the axial and radial directions are listed in Table 6.3 for the six cases analysed previously in Figs. 6.2 and 6.3. The signs for these forces are according to the co-ordinate system shown in Fig. 6.4. The values listed in Table 6.3 show that the pressure forces are significantly larger than the inertial forces in both radial and axial directions. In addition, the radial pressure forces are significantly larger than the axial pressure forces. When the TI is increased for the isothermal cases, I1 and I2, the axial pressure force remains relatively the same, but the radial pressure force decreases by approximately 7 % and this leads to the decrease in the recirculation zone length. It is seen that there is a substantial increase in $F_{p,r}$ in case L1 compared to the isothermal case I1, which corresponds to the increase in the value for L_R/D. The radial pressure force for case S1 is roughly 35 % lower in comparison to the radial pressure force for case L1 and leads to an approximate 34 % decrease in the value for L_R/D, as shown in Table 6.3. All of these trends and the interplay between the radial pressure force and L_R/D are shown in Fig. 6.5c, along with the corresponding variation of the axial pressure force, shown in Fig. 6.5b. The axial pressure force is marginally affected when increasing the TI for a given value of τ and this force increases with τ before decreasing slightly for the flames close to stoichiometric conditions (S1 and S2). There is a direct correspondence between the variations of L_R/D and $F_{p,r}$ with τ, which suggests that the changes in the recirculation length are dictated by the changes in the radial pressure force in confined bluff body stabilised flames.

The radial pressure force is influenced by the heat release from the flame and the corresponding momentum transport is influenced by turbulent stresses produced through mean shear. In addition, the predominant balance for the radial momentum equation is by these two forces, as shown in Eq. (6.3). This is investigated by plotting the shear

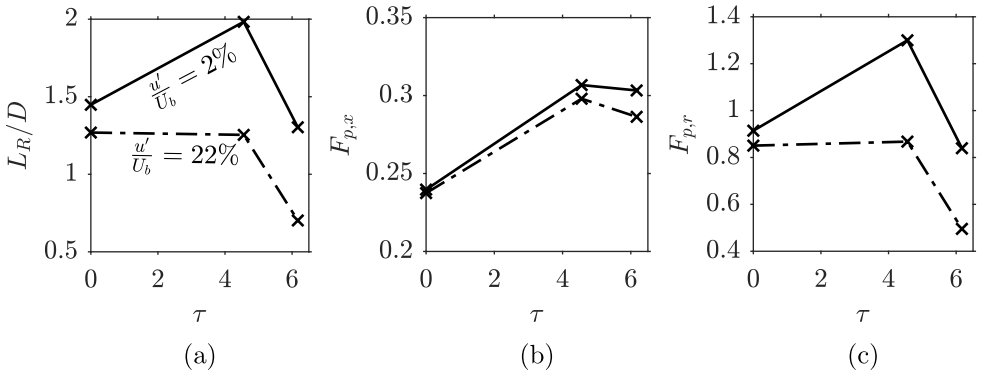

Fig. 6.5 Variations of (a) L_R/D and the pressure force in (b) axial and (c) radial directions with τ. These are deduced from LES results.

layers and the flame brush for these cases; these are displayed in Fig. 6.6. The edges of the shear layer are marked using 10 % of the maximum positive shear $\partial U/\partial r$ observed for every x/D location and the non-smoothness seen along the inner edges is caused by the limited sample size available for azimuthal averaging at positions with small r. The time-averaged progress variable values of $\langle\widetilde{c}\rangle = 0.1$ and 0.9 are used to mark the flame brush. The results are shown in the region of $r/D \leq 0.7$ for clarity and the recirculation zone length is also marked. The shear layers for isothermal flows are shown in Fig. 6.6a, where it is seen that the shear layer for case I2 is thicker in comparison to case I1, particularly in the region close to the bluff body. This is related to the increased momentum transport that results from the higher TI in case I2, which leads to the decrease in the radial pressure force (see Table 6.3). This causes the recirculation zone to be shorter in case I2, as marked in Fig. 6.6a.

This situation is more complicated for reacting flow, due to the interplay between the induced effects of turbulence and combustion. This interplay depends on the TI and heat release, which is related to the equivalence ratio of the mixture. The averaged shear layer and flame brush isolines are shown in Figs. 6.6b and 6.6c. Only the outer edge of the shear layer is influenced by the heat release when the TI is low because the major portion of the flame brush is located close to this edge, as seen in Figs. 6.6b and 6.6c. Radial forces are exerted by the combustor wall, due to thermal expansion effects and these forces push the outer edge of the shear layer inward, which is clearly visible in both Figs. 6.6b and 6.6c for cases L1 and S1 in comparison to Fig. 6.6a. Increasing the equivalence ratio causes the heat release rate to increase, which leads to the outer edge moving further inward in the near-field region ($x \leq D$). The flame brush is also thinner in case S1 in comparison to case L1 in the near-field region but widens when moving

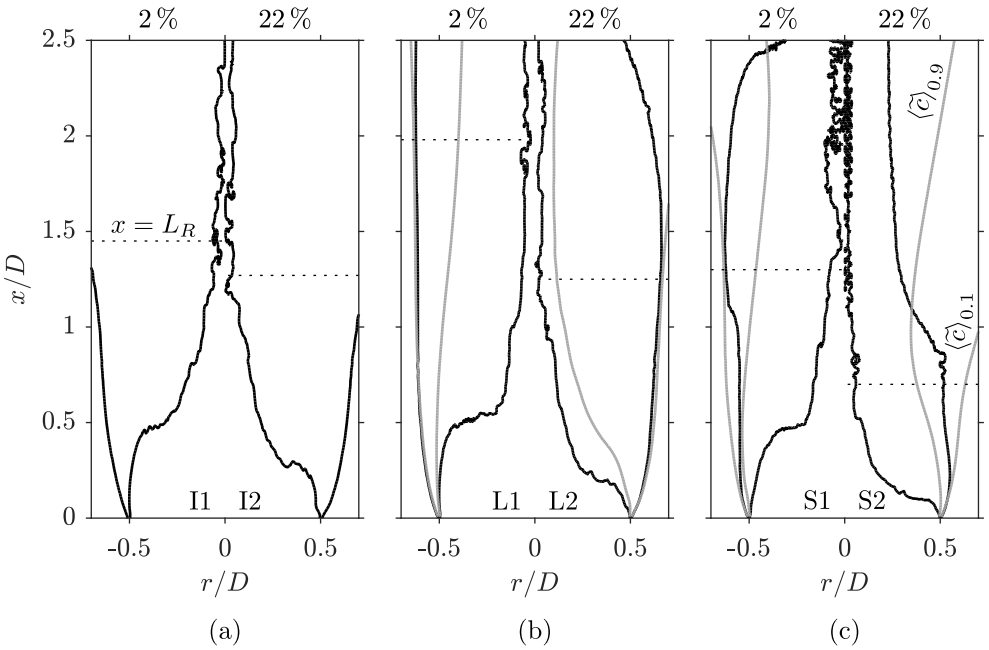

Fig. 6.6 Edges of the time-averaged shear layers (black lines) in (a) isothermal flows and reacting flows. The flame brushes are marked along $\langle\widetilde{c}\rangle = 0.1$ and 0.9 (grey lines) for (b) $\phi = 0.59$ and (c) $\phi = 0.90$ cases. These are deduced using LES results.

downstream because of turbulent (diffusive) transport. The flame brush width increases further to accommodate the burning of excess fuel in case S1 compared to case L1. This causes a further inward shift of the shear layer edge, as seen in Fig. 6.6c, which also leads to a decrease in the radial pressure force acting in the control volume CV1, as described previously. These interactions cause substantial changes in the net radial pressure forces exerted on the recirculation zone, leading to significant changes in the recirculation zone lengths. The axial pressure force is also influenced by this interplay, but the magnitudes are relatively smaller compared to the radial pressure force, as seen by their values in Table 6.3.

The interactions of the shear layer and flame brush become more complex when the turbulence intensity is increased to 22 % for cases L2 and S2, as seen in Figs. 6.6b and 6.6c respectively. The increased turbulent transport widens the flame brush substantially and the majority of the flame brush is inside the shear layer in the near-field of case L2, whereas the flame brush is still located in the vicinity of the outer shear layer edge for case S2 (with larger heat release). The flame brush is relatively thinner in case S2 when compared to case L2, as the flame in case S2 is closer to stoichiometric conditions. For all of these reasons, the outer shear layer edge is shifted further inward in the near-field region for case S2. Moving further downstream, the heat release effects become stronger

in case S2, where it is clearly seen that the flame brush is located outside the shear layer in Fig. 6.6c. These strong nonlinear interactions between the flow and thermochemical effects yield further changes to the radial pressure force, which leads to significant changes in the recirculation zone length.

It has become clear that the changes in the values of L_R are predominantly caused by the radial forces exerted on the recirculation zone rather than the turbulence production through the source term $-\langle \boldsymbol{u}'' \rangle \cdot \langle \boldsymbol{\nabla} p \rangle$, as speculated in the earlier study (Pan *et al.*, 1992*b*). Further understanding and support of the role of radial pressure force can be obtained if a scaling relation for L_R could be obtained using the insights gained in this analysis.

6.3.3 Recirculation zone length scaling relation

Based on the analysis presented in § 6.3.2 and for the reasons outlined in § 6.1, it is necessary to consider all of the forces, including those exerted by the confinement of heat release. Hence, the appropriate control volume to deduce a scaling relation for L_R is shown in Fig. 6.7. This modified control volume now spans the whole width of the combustion chamber. It should be noted that the control volume CV2 is not cylindrical, since the outer walls of the combustion chamber form a square duct. The various surfaces of this control volume are marked in Fig. 6.7. The surface-averaged radial velocity on S_1 is observed to be significantly (more than an order of magnitude) smaller than the corresponding axial velocity and hence, the inertial forces acting in the radial direction at S_1 are neglected. This is also suggested by the streamlines shown in Fig. 6.7, since the curvature at S_1 is small. In addition, the turbulent shear force $\int_S \langle \overline{\mu}_T \rangle \left(\partial \langle \widetilde{U} \rangle / \partial r \right) \mathrm{d}S$ on surface S_1 is assumed to be smaller compared to its value on surface S_2. This is verified using the LES results, which showed that the magnitude of this force on S_2 is nearly two orders of magnitude larger. Therefore, the force balance includes only the radial forces acting on surfaces S_2 and $S_{3,2}$ of the control volume CV2. Applying conservation of mass in the axial direction across CV2 gives

$$\rho_u U_b \left(W^2 - \frac{\pi D^2}{4} \right) = \rho_2 U_2 W^2 \,, \tag{6.4}$$

where the subscript '2' denotes the condition on surface S_2 and $\rho_2 U_2 = \int_{S_2} \rho U \, \mathrm{d}S \, / W^2$. The angle brackets used to denote the time-averaged quantities are omitted in this and the following expressions for simplicity. Rearranging the mass conservation equation

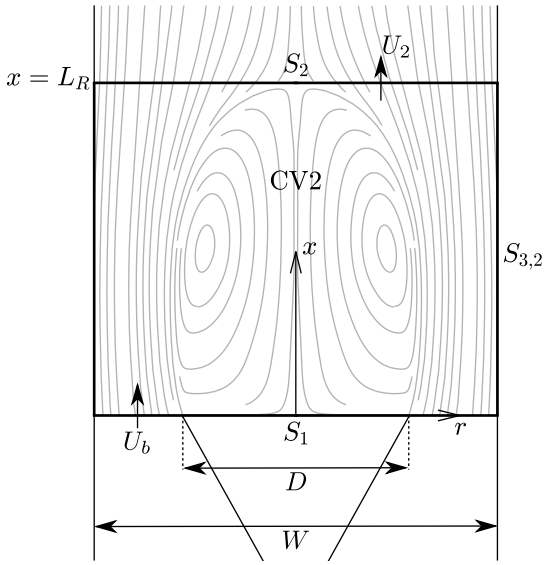

Fig. 6.7 Control volume used to deduce a scaling expression for L_R.

gives

$$U_2 = U_b \frac{\rho_u}{\rho_2}\left(1 - \frac{\pi D^2}{4\,W^2}\right) = U_b G \frac{\rho_u}{\rho_2}\,, \tag{6.5}$$

where G is a geometrical parameter. The radial force balance is now written as

$$\int_{S_2} \rho U U_r \,\mathrm{d}S \;+\; \int_{S_{3,2}} p \,\mathrm{d}S \;\approx\; \int_{S_2} \mu_T \frac{\partial U}{\partial r} \,\mathrm{d}S\,, \tag{6.6}$$

where U_r represents the radial velocity. The velocity gradient $\partial U/\partial r$ is approximated as $\Delta U/\Delta r \approx \mathcal{A}\,U_2/W$, where $\mathcal{A} \approx 8$ because U varies from zero to a maximum over a length of approximately $W/4$ and the maximum velocity is roughly twice the value of U_2. Furthermore, the gradient $\partial U_r/\partial x \ll \partial U/\partial r$ on surface S_2 for this flame configuration. Integrating Eq. (6.6) and rearranging gives

$$4\,p_w W L_R \;\approx\; 8\,\mu_{T,2} U_2 W \;-\; \rho_2 U_2 U_{r,2} W^2\,. \tag{6.7}$$

The pressure on surface $S_{3,2}$ is integrated along the walls of the combustion chamber to give a surface-averaged value of $p_w = \int_{S_{3,2}} p \,\mathrm{d}S\,/(4\,L_R W)$. The dynamic viscosity $\mu_{T,2}$ is the average over surface S_2. Substituting the expression for U_2 from Eq. (6.5) into the radial force balance in Eq. (6.7) and rearranging the resulting expression gives

$$\frac{L_R}{W} \simeq \frac{U_b G}{4\,p_w}\left(\frac{8\,\mu_{T,2}}{W}\frac{\rho_u}{\rho_2} - \rho_u U_{r,2}\right). \tag{6.8}$$

The mixture on surface S_2 will consist of unburnt, partially burnt and fully burnt mixtures, as suggested by the flame brush contours in Fig. 6.6 and therefore, the mixture density ρ_2 must be in the range $\rho_b \leq \rho_2 \leq \rho_u$. Hence, the density ρ_2 can be expressed as a fraction of the burnt mixture density ρ_b using $\rho_2 = f\rho_b$, with f bounded as $1 \leq f \leq \tau+1$; this yields $\rho_u/\rho_2 = (\tau+1)/f$. Using this expression and noting the flow symmetry on the surface S_2, Eq. (6.8) is written as

$$\frac{L_R}{D} \simeq \left(\frac{2\,GU_b\mu_{T,2}}{Dp_w}\right)\left(\frac{\tau+1}{f}\right). \tag{6.9}$$

For isothermal flow, where $\tau = 0$ and $f = 1$, it is observed that L_R/D is influenced by the bulk strain U_b/D, the eddy viscosity and the wall pressure. Although the TI does not appear explicitly in (6.9), the latter two terms, $\mu_{T,2}$ and p_w, will vary with the TI at the combustor entry for a given geometry and U_b. Hence, the decrease in L_R for increasing TI suggests that the rise in the wall pressure is larger than the increase in $\mu_{T,2}$. Furthermore, it is known that $\mu_{T,2} \sim \rho_2 k_2^2/\varepsilon_2$, where k_2 and ε_2 are the surface-averaged turbulent kinetic energy and its dissipation rate on surface S_2 respectively. The values of k_2 and ε_2 would depend on the incoming turbulence level and this dependence may be represented using a power law. The pressure distribution on $S_{3,2}$ will also be influenced by the incoming turbulence level and this distribution determines p_w.

For reacting flows, there is an additional factor τ (related to heat release) that influences the values of L_R. The expression (6.9) shows that the recirculation zone length increases linearly with τ for a given turbulence level, which is superficial since the heat release will also influence p_w and $\mu_{T,2}$. The experimental results presented in § 6.3.2 show that L_R increases with τ for low turbulence level and moderate values of τ. This is because the thermochemical effects due to the heat release from combustion are stronger compared to turbulence effects at low TI values. This behaviour also suggests that the increase in p_w due to thermal expansion is smaller in comparison to the influences of heat release on L_R through $\mu_{T,2}$ and τ. The increase in $\mu_{T,2}$ is consistent with the known behaviour of the increase in the turbulence level and its integral length scale across premixed flames with low turbulence intensity (high Damköhler number flames). However, this increase in L_R is observed only for a moderate value of τ and the recirculation zone length becomes smaller for higher values of τ, as seen in Fig. 6.5. This is because the combustion effects coming through the eddy viscosity and τ are offset by the rise in p_w, as suggested by Eq. (6.9), due to larger thermal expansion effects. For higher turbulence levels, the observed variation of the recirculation zone length with τ is different. The

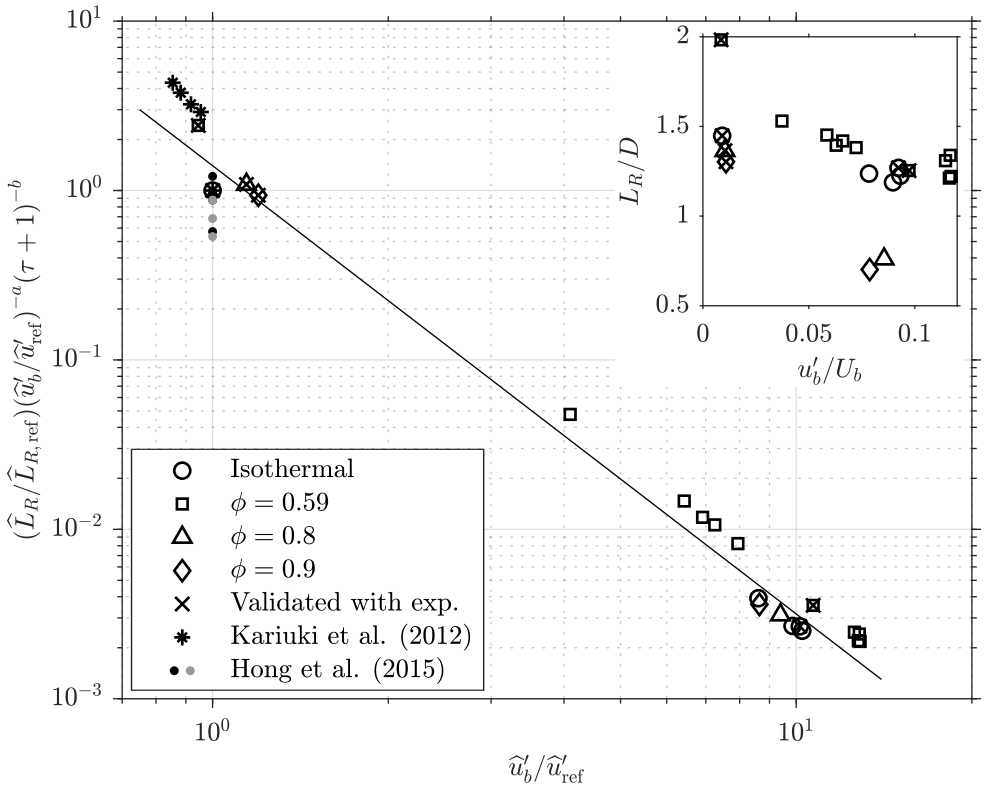

Fig. 6.8 Variation of the normalised L_R with the normalised TI at the bluff body base for the 20 cases listed in Table 6.2. The result of the scaling relation in Eq. (6.10) is shown for $a = 2.5$ and $b = -0.25$. The open flame data points shown are from the study by Kariuki *et al.* (2012). The recirculation zone lengths for a backward facing step configuration measured by Hong *et al.* (2015) for reacting flows of propane–air mixtures with 0 % (black dots) and 50 % hydrogen (grey dots) by volume are also shown. The unscaled recirculation zone lengths are shown in the inset.

influences of combustion, on average, are overwhelmed by the effects of turbulence at higher TI and moderate τ values, which yield almost no variation of L_R with τ. It is apparent that these behaviours are contained implicitly in Eq. (6.9). The wall pressure and the eddy viscosity are influenced not only by turbulence, but also by dilatation and turbulence–chemistry interactions, as described previously. The influences of the latter two thermochemical effects on the spatial evolution and distribution of k and ε are nonlinear. If the change in the wall pressure is relatively large compared to the change in $\mu_{T,2}$ for a given value of τ and TI, then L_R will decrease. Hence, a relatively larger thermal expansion coming from near-stoichiometric flames will lead to shorter recirculation zones, irrespective of the TI values, which is also observed in the values listed in Tables 6.2 and 6.3.

Deducing an explicit expression for L_R as a function of u' and τ is not quite straightforward, since the effects of combustion on turbulence and related quantities are nonlinear.

These nonlinear effects may be represented using a power law for the reasoning presented previously and hence, the scaling expression may be generalised by writing a functional form of the expression as $f(p_w, \mu_{T,2}, \tau) \approx f(u'/U_b, \tau) = (u'_b/U_b)^{a+1}(\tau+1)^b$, where the exponents a and b are constants, and u'_b is the surface-averaged turbulence level at the bluff body base; these values are listed in Table 6.2. Therefore, the generalised form of the scaling expression is written as

$$\frac{L_R}{D} = \widehat{L}_R \simeq \mathcal{C}(\widehat{u}'_b)^{a+1}(\tau+1)^b\,, \tag{6.10}$$

where $\mathcal{C}$ is a constant accounting for a given bulk-mean velocity and the combustion chamber geometry, and $\widehat{u}'_b = u'_b/U_b$. Figure 6.8 shows the results for all of the simulations listed in Table 6.2 that are collapsed using the scaling equation in (6.10). It should be noted that $\widehat{L}_R/\widehat{L}_{R,\mathrm{ref}}$ is plotted instead of $\widehat{L}_R$, so that the constant $\mathcal{C}$ can be eliminated. The subscript 'ref' represents the isothermal case I1, which is used as the reference case. The exponents $a = 2.5$ and $b = -0.25$ are used for the scaling equation in (6.10) and a line of best fit is shown in Fig. 6.8, where it is seen that the proposed expression collapses the data well. The results show that the same behaviour may be seen for higher equivalence ratios, since these results collapse together well, as seen in Fig. 6.8. The variation of the unscaled L_R/D with u'_b/U_b is shown in the inset of this figure.

The values of $\widehat{L}_R/\widehat{L}_{R,\mathrm{ref}}$ deduced using the results in Fig. 8 in the study by Hong *et al.* (2015) for reacting flows over a backward facing step are also scaled as per Eq. (6.10) and the results are shown in Fig. 6.8. Hong *et al.* (2015) considered propane mixed with 0 %, 30 % and 50 % hydrogen by volume and air mixtures for their experiments; all cases had a TI of approximately 6 %. The scaled recirculation zone lengths shown here are for the two extreme cases with 0 % and 50 % hydrogen. The values for ϕ considered in the experiments with the pure propane–air mixture are 0.65, 0.72, 0.79, and 0.88, while the values of ϕ for the 50 % hydrogen case are 0.63, 0.67 and 0.72. The scaled values shown in Fig. 6.8 range from 1.2 to 0.57 for the pure propane–air mixture and from 0.88 to 0.53 for the 50 % hydrogen cases. These mixtures have Lewis numbers of approximately 1.9 (pure propane) and 1.6 (mixtures with 50 % hydrogen). The turbulence–chemistry interactions in these non-unity Lewis number flames are substantially different from those in unity Lewis number flames. Furthermore, the recirculation zone behind a backward facing step is constrained by the bottom and side walls and thus, the corresponding shear forces cannot be ignored. These additional effects in the flames considered by Hong *et al.* (2015) may need a different exponent and, perhaps, a Lewis number scaling also. However, the

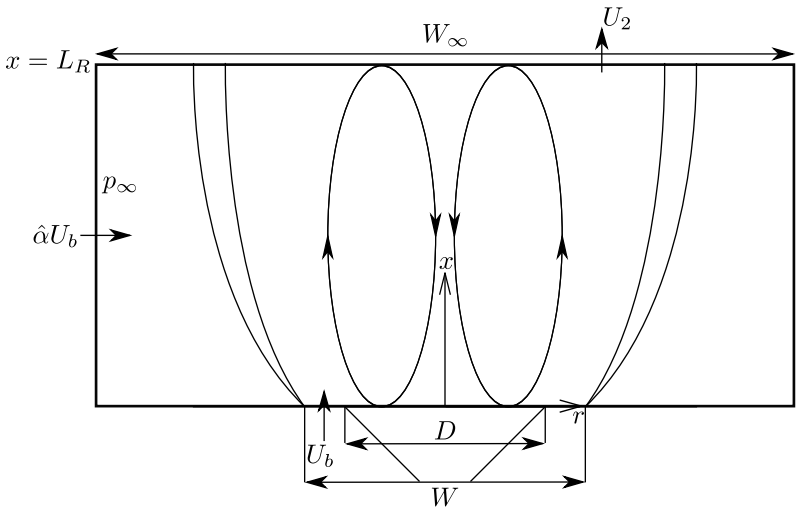

Fig. 6.9 Control volume for an open bluff body burner configuration.

scaled values for these flames shown in Fig. 6.8 are of the same order as that given by the scaling relation, which is quite remarkable given the complexity involved in this problem.

6.3.4 Application of the scaling to open flames

An illustration of a bluff body stabilised flame without confinement is shown in Fig. 6.9, where it is seen that an outer shear layer will form at the top edges of the walls. The appropriate cylindrical control volume is extended beyond this outer shear layer into the air entrainment region with zero streamwise velocity. If the observations from § 6.3.3 regarding the role of radial forces acting on the recirculation zone are extended, then the radial force balance in Eq. (6.6) for this control volume is now written as

$$4\,p_\infty W_\infty L_R \;\approx\; 8\,\mu_{T,2} U_2 W_\infty \;-\; \rho_2 U_2 U_{r,2} W_\infty^2\,. \tag{6.11}$$

Applying the mass balance across the cylindrical control volume gives

$$\rho_u U_b \left(\frac{W^2 - D^2}{4}\right) + \rho_{\text{air}} \hat{\alpha} U_b W_\infty L_R = \rho_2 U_2 \frac{W_\infty^2}{4}\,, \tag{6.12}$$

where the entrained mass flow rate is taken to be $\pi W_\infty L_R \rho_{\text{air}} \hat{\alpha} U_b$, with $\hat{\alpha}$ representing an entrainment coefficient for air that accounts for scaling the velocity to U_b and the area change to include the entrainment at the surface of the control volume in line with the bluff body base. After taking $\rho_{\text{air}} \approx \rho_u$ and then using $\rho_u/\rho_2 = (\tau + 1)/f$, Eq. (6.12)

is rearranged for U_2 and is written as

$$U_2 = U_b \frac{\tau + 1}{f} \left(G + \frac{4 L_R}{W_\infty} \hat{\alpha} \right) , \tag{6.13}$$

where the geometrical parameter is expressed as $G = (W^2 - D^2)/W_\infty^2$. Substituting the expression for U_2 into Eq. (6.11) and rearranging for $\widehat{L}_R = L_R/D$ gives

$$\widehat{L}_R \simeq \frac{U_b^2 G^*}{4\, p_\infty} \left(\frac{8}{W_\infty} \frac{\mu_{T,2}}{U_b} \frac{\tau + 1}{f} + \rho_u \frac{|U_{r,2}|}{U_b} \right) \mathcal{E} , \tag{6.14}$$

where $\mathcal{E}$ is a correction term accounting for the air entrainment, which can lead to some cross-stream velocities and hence, the velocity $U_{r,2}$ is retained in Eq. (6.14).

The scaling relation in Eq. (6.14) is similar to Eq. (6.8) besides the change in variables for the geometrical parameter, defined for the open flame as $G^* = G(W_\infty/D)$, the pressure p_∞ and the width W_∞. The influence of heat release and the TI on the entrained air is signified by the factors $(\tau + 1)/f$ and $\mu_{T,2}$ appearing in the first part. Thus, the justifications given earlier can be used to introduce a functional dependence on the TI and τ and hence, the scaling relation in Eq. (6.14) can be written in a form similar to Eq. (6.10) but perhaps with different values for the exponents a and b. This suggests that the values for L_R/D for open flames are also likely to follow the scaling shown in Fig. 6.8. This is demonstrated in Fig. 6.8 by including the values of L_R/D for four open flames, which are also normalised using corresponding isothermal case in that experimental study. The values for the recirculation zone lengths are taken using the centreline PIV measurements made in the study by Kariuki *et al.* (2012). These results suggest that the scaling given by Eq. (6.10) works well for both confined and open flames.

6.4 Summary

The LES results from 5 isothermal and 15 reacting flows, which include a conical bluff body within a square duct, are analysed to determine a scaling law relating the recirculation zone length, heat release parameter and TI at the bluff body base. It is observed that the recirculation zone length is influenced by the TI, heat release and turbulence–combustion interactions. The values of L_R decrease monotonically with increasing TI in isothermal and reacting flows, but its variation is found to be non-monotonic with τ in reacting flows. The recirculation zone length increases from its isothermal value as ϕ increases and then decreases when approaching stoichiometric conditions for low TI (2 %). On the other

hand, the values of L_R are found to be insensitive to τ (or ϕ) before decreasing when approaching near-stoichiometric conditions for a higher TI (22 %). This non-monotonic behaviour is observed to emerge from the competing effects of dilatation and turbulence that influence the radial pressure forces acting on the recirculation zone. This force influences the relative positions of the shear layer and flame, thereby leading to the variation in the levels of turbulence–combustion interactions and their effects on the radial force balance. This demonstrates that the nonlinear influences of the TI, heat release and their interactions controlling the radial forces govern the behaviour of the recirculation zone length. This is because the near-field wake containing the recirculation zone is governed by the momentum transfer to and from the zone, which is related to the forces acting on this zone. The surface-averaged wall pressure and the eddy viscosity on a plane located at the rear stagnation point emerge as two key quantities, which are influenced by the TI, heat release and turbulence–chemistry interactions. Careful considerations of these effects permits the derivation of a scaling relation, which is found to be in the form $L_R/D \sim (u'/U_b)^{(a+1)}(\tau+1)^b$. This relation is found to work well for premixed flames that are stabilised behind a bluff body with and without confinement and also for flames that are stabilised behind a backward facing step.

Chapter 7

Flame Root Dynamics in a Gas Turbine Model Combustor

It has been demonstrated in Chapters 5 and 6 that the combustion closure is robust and accurate for bluff body stabilised premixed flames. Such flames are present in afterburners, where the geometries and fluid mechanics are simplified in comparison to the main burner of gas turbine systems. Gas turbine combustors employ swirling flows for flame stabilisation. Hence, it is of interest to model a swirl-stabilised flame in a more complex geometry that resembles a gas turbine combustion system. Previous studies using the same combustion closure have been undertaken for flames under acoustically stable and unstable conditions (Chen *et al.*, 2019*a*,*b*; Langella *et al.*, 2018*a*). This chapter presents the results of a lean swirl-stabilised flame close to lean blow-off in a gas turbine model combustor and provides physical insights into the stabilisation of the flame.

7.1 Motivation

Modern gas turbine engines have to comply with stringent environmental regulations for pollutant emissions. Lean combustion can provide improved efficiency, while lowering flame temperatures and thereby a reduction in pollutant emissions (Driscoll, 2011). However, operating under lean conditions make such combustion systems prone to risks that may hinder successful ignition and flame stability (Gicquel *et al.*, 2012). Feikema *et al.* (1991) demonstrated that the effect of swirl can provide increased stability for gas turbines operating under lean combustion and extend the lean flammability limit. In addition, swirling flows allow gas turbine combustors to be more compact, since swirling flow causes intense mixing and hence, the reactant mixture is either premixed or partially

premixed prior to ignition (Syred, 2006). Partially premixed combustion is present for swirling flows where the flames are lifted, which is due to the fuel and air entering the combustion chamber through separate inlet streams (Masri, 2015). The potential for flame blow-off is also inevitable in lean combustion and thus, the physical mechanisms behind this phenomenon should be investigated thoroughly.

Flames that are close to blow-off conditions are highly unstable and local extinction typically occurs. This has been observed in experimental studies of the Sandia D–F jet flames with homogeneous (Barlow & Frank, 1998) and inhomogeneous mixing (Barlow *et al.*, 2015; Meares & Masri, 2014), and the Sydney Swirl Burner (Dally *et al.*, 1998). These experimental observations have also been captured in LES studies with transported PDF (Jones & Prasad, 2010; Xu & Pope, 2000), FPV (Ihme & Pitsch, 2008*b*; Wu & Ihme, 2016), CMC (Garmory & Mastorakos, 2011; Kronenburg & Kostka, 2005) and MMC (Galindo *et al.*, 2017; Wandel & Lindstedt, 2013) models. Computational studies on flame blow-off are very limited, where CMC (Zhang *et al.*, 2015; Zhang & Mastorakos, 2016), FPV and thickened flame models (Ma *et al.*, 2019) have been used to predict flame blow-off in the Cambridge Swirl Burner (Cavaliere *et al.*, 2013). However, the geometries of these burners are simple in comparison to more complex configurations employed for gas turbine combustors.

The gas turbine model combustor developed by the German Aerospace Centre (DLR) is a good example of a complex configuration, which is a partially premixed system containing two swirl generators (Meier *et al.*, 2005, 2006; Weigand *et al.*, 2006). Extensive measurements using laser diagnostics for three operating conditions were obtained, which were for thermo-acoustically stable and unstable conditions, and for a flame close to blow-off (Meier *et al.*, 2006; Weigand *et al.*, 2006). The thermo-acoustically stable flame was investigated by See & Ihme (2015), Benim *et al.* (2017) and Donini *et al.* (2017) using LES, and Chen *et al.* (2019*a*,*b*) have investigated the thermo-acoustically stable and unstable flames. The third case is of interest for this study, which has recently been investigated using CMC (Zhang & Mastorakos, 2019). This flame showed sudden lift-off with partial extinction and re-ignition, leading to re-anchoring of the flame to the stabilisation point (Stöhr *et al.*, 2011*a*). Understanding the mechanisms leading to blow-off is challenging, owing to the complex interactions between turbulence, the heat release from combustion and molecular transport (Shanbhogue *et al.*, 2009). These phenomena are challenging for computational modelling and provides the motivation for this investigation. Therefore, the aims for this work are:

- To simulate the flame close to blow-off in the DLR gas turbine model combustor and validate the simulation with detailed pointwise time-averaged velocity and scalar measurements obtained in the experiment.
- To investigate the various physical processes involved in the stabilisation of the flame leading to its blow-off and provide physical insights into the unstable flame behaviour.

7.2 Flame conditions and numerical detail

The flame that is simulated in the gas turbine model combustor developed by DLR is shown in Fig. 4.8 and the geometry is previously described in § 4.4.1. Methane was fed through the nozzle ring with no swirlers and the fuel nozzle is located between the two air nozzles with co-swirlers. The time-averaged statistics for the three components of velocity at various axial positions across the combustor were measured using LDV and laser Raman spectroscopy was used to measure the chemical species mass and mole fractions, the mixture fraction and temperature. In addition, stereoscopic PIV was used to capture the instantaneous flow field in a chosen mid-plane, along with the OH-PLIF technique to capture the radical species OH (Stöhr *et al.*, 2011*a*). These PLIF images span the width of the combustion chamber up to an axial position of $x = 45\,\mathrm{mm}$, whereas the PIV measurements were limited to a $30 \times 30\,\mathrm{mm}^2$ region from the exit of the annular air nozzle. The full description of the measurement techniques are outlined in the experimental studies by Meier *et al.* (2006), Weigand *et al.* (2006) and Stöhr *et al.* (2011*a*).

The various important parameters for the flame close to blow-off, referred to as flame C, are listed in Table 7.1 (Meier *et al.*, 2006; Weigand *et al.*, 2006). This flame was also seen to be the most thermo-acoustically stable flame, as the pressure oscillation amplitude was weakest out of the three flames investigated experimentally (Steinberg *et al.*, 2012). The flow rates, thermal power and global equivalence ratio that were used in the experiment are listed in Table 7.1. Under these operating conditions, the flame root was positioned at an average height of approximately 6 mm above the fuel nozzle exit. The average lift-off height that is reported in the experimental study by Weigand *et al.* (2006) is based on the average flame position using the OH-PLIF and CH-PLIF images. In addition, the flame experienced random lift-off events where the flame root was extinguished and then re-stabilised at $x \approx 1.5\,\mathrm{mm}$. These lift-off events occurred 1–2 times per second. This lift-off event was observed to reach a height of 30–40 mm and

Parameter	Value	Description
$\dot{m}_{\text{air}}$	4.68 g/s	Air flow rate through the plenum
$\dot{m}_{\text{CH}_4}$	0.15 g/s	Methane flow rate through the nozzle
P_{th}	7.6 kW	Overall thermal power
S	0.55	Swirl number
ϕ_{glob}	0.55	Global equivalence ratio

Table 7.1 Operating conditions for flame C (Meier *et al.*, 2006; Weigand *et al.*, 2006).

lasted approximately 0.1–0.15 s in the experimental study (Weigand *et al.*, 2006). The stabilised flame and its lift-off events were shown by Stöhr *et al.* (2011*a*) using the time sequences of the combined high-speed (5 kHz) PIV and OH-PLIF images.

The computational domain is the same as described in § 4.4.2 and uses the same wall boundary conditions; the mesh is shown in Fig. 4.9. A small time step of $\Delta t = 0.15\,\mu$s is used to ensure suitable accuracy for the time derivatives and that the CFL number remains below 0.4 across the whole domain. The PIMPLE algorithm is used and iterated for a maximum of five times within each time step, in order to ensure close coupling between pressure and velocity. The simulation for flame C uses 1080 cores and a simulation for 1 ms of physical time requires approximately 1 hr of wall clock time. This case requires around 80 ms of physical time to allow initial transients to pass out of the domain and for the flame to stabilise. The time-averaged statistics are computed using samples collected over 24 ms after the initial 80 ms transient period. This 24 ms sample corresponds to roughly 6 flow through times.

Figure 7.1 shows three histograms of the normalised filter width $\Delta^+ = \Delta/(\delta_L^0)_{\text{st}}$ for the reacting regions ($\overline{\dot{\omega}^*} > 0$) in the computational domain. The histograms constructed for the cells above and below $x = 20$ mm are coloured using red and green respectively, and blue is used to mark the histogram for cells with $\overline{\dot{\omega}^*} > 0$ over the entire combustion chamber. In general, it is seen that the grid does not resolve the flame front and hence, combustion is entirely modelled within the SGS region. It should be noted that the SGS reaction rate closure used for this study is flamelets based, which typically assumes that the chemical time scale is shorter than the relevant turbulent time scales. In the context of RANS modelling, it is permissible to question whether this combustion model can be used to study flame blow-off mechanisms. However, the situation is different for LES modelling, since many of the fluid dynamic time scales, along with their interactions and mutual influences on the scalar fields, are resolved explicitly and captured by the LES equations. In addition, a flame will physically exist if the local mixture is flammable

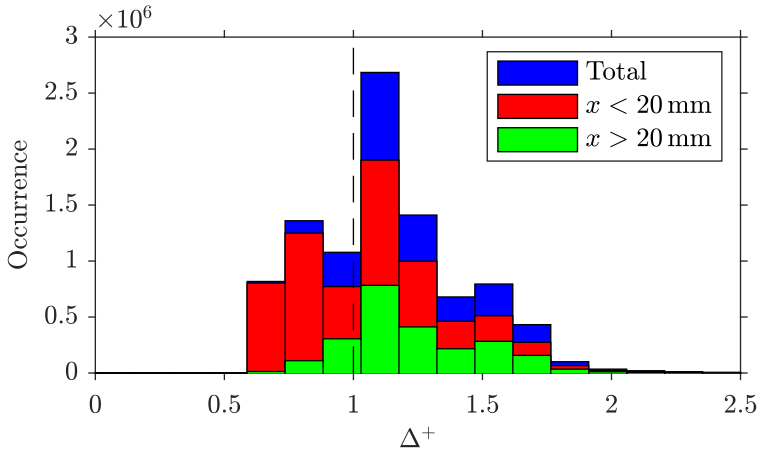

Fig. 7.1 Histograms of the normalised filter width distribution, where the cell samples are collected within the reaction region and is marked using $\overline{\dot{\omega}^*} > 0$.

with a right reactedness value. The local mixture value is denoted by the filtered mixture fraction and its SGS variance, whereas the reactedness value is represented by the filtered progress variable and its SGS variance. The influences of strain due to the resolved fluid motion on the evolution of these fields are captured inherently by the LES equations. However, it may be queried as to whether the influence of SGS straining on the flame should be included. The multi-scale analysis of Doan *et al.* (2017) and Ahmed *et al.* (2018) demonstrated that turbulent eddies smaller than $2\delta_L^0$ to $3\delta_L^0$ contribute weakly to the overall straining of the flame. Hence, the unstrained flamelets based models can be used (provided that the numerical grid satisfies the aforementioned condition) as SGS closure to investigate mechanisms leading to flame blow-off, which are related to the dynamic interaction between the flame and the large-scales of motion. These points will become evident from the results analysed next.

7.3 Results

7.3.1 Reacting flow structures

The axial velocity with streamlines and temperature distributions in the x–y mid-plane are shown in Figs. 7.2a and 7.2b respectively. The left-hand side of each figure shows a snapshot of the LES results and the right-hand side shows the time-averaged fields, which are also azimuthally averaged. The Reynolds number based on the cold inflow bulk-mean velocity and minimum diameter of the outer annulus (25 mm) is approximately 15000. An Inner Recirculation Zone (IRZ), which is typical in swirling flows, is seen in Fig. 7.2a

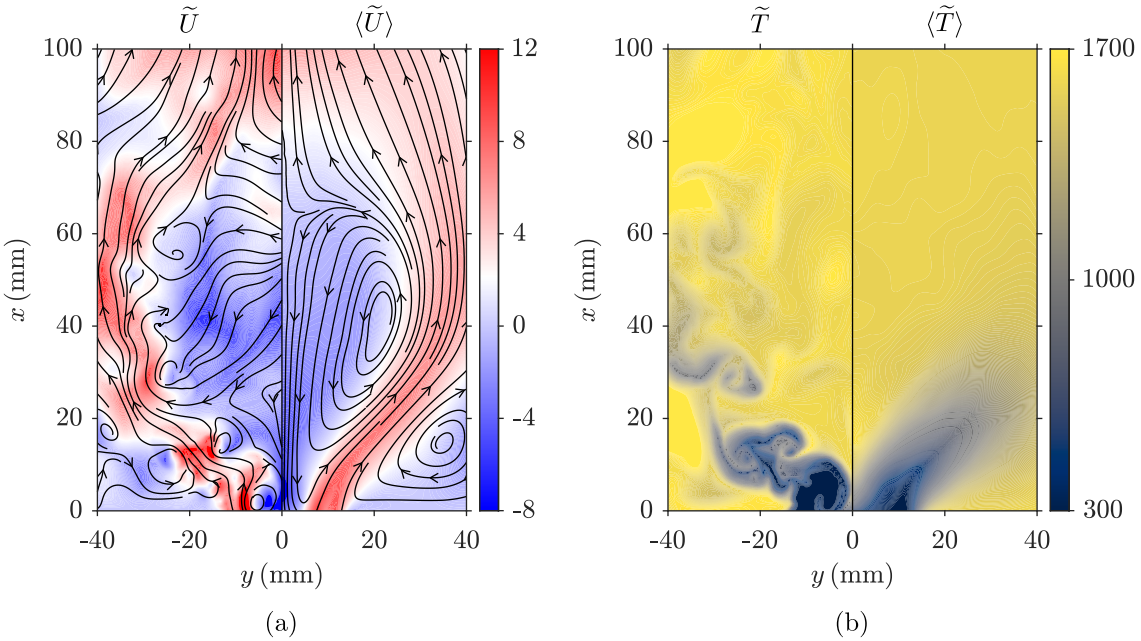

Fig. 7.2 Distributions of the (a) axial velocity and (b) temperature fields for flame C. The filtered and averaged, in both time and the azimuthal direction, variations are shown on the left- and right-hand sides respectively. The corresponding streamlines are also shown.

with a length of approximately 63 mm in the axial direction. This computed value is in excellent agreement with the measured value of 65 mm (Weigand *et al.*, 2006). The high negative axial velocities near $x = 0$ at the centreline indicate that the recirculation flow is strong. An Outer Recirculation Zone (ORZ) is also formed at the bottom of the combustion chamber near the walls, since the chamber is confined. It is seen in the left-hand side of Fig. 7.2a that there are some instantaneous circular patterns along the inner shear layer (white coloured region) between the IRZ and the inflow stream. These regions of high vorticity magnitude (not shown) correspond to the large-scale coherent structures in the flow.

A strong axial temperature gradient at the centreline near the bottom of the combustion chamber is seen in Fig. 7.2b. This represents the leading edge of the flame and the continuous supply of hot products within the IRZ to this region ensures that the flame stabilises here and is lifted. Strong temperature gradients are also observed within the large vortex structures, indicating that combustion is also favoured within these regions. It should be noted that the large temperature gradient seen within the ORZ near the bottom of the combustion chamber is caused by the hot products attempting to perturb the incoming air stream and hence, there is no flame at this region.

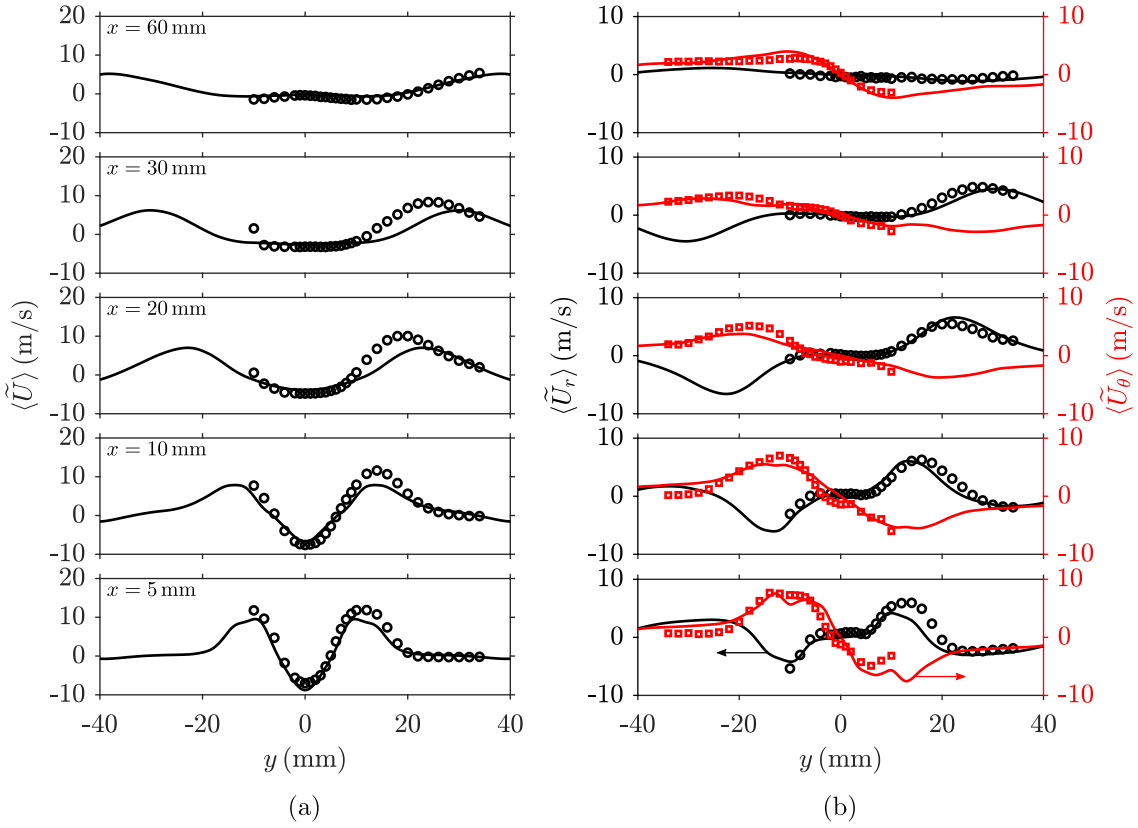

Fig. 7.3 Comparisons of the time-averaged (a) axial and (b) radial and azimuthal velocities between the measurements (Meier *et al.*, 2006; Weigand *et al.*, 2006) (symbols) and the computations (lines), where the latter results are azimuthally averaged.

Figure 7.3 shows typical comparisons of the time-averaged statistics from the simulation and measurements for the three components of the Favre-filtered velocity. The results are shown for different heights from the exit of the annular nozzle. The axial velocity profiles are shown in Fig. 7.3a, and the radial and azimuthal velocity profiles are shown in Fig. 7.3b. Some under prediction in the axial and radial velocities is seen in the near-field profiles at $x = 5\,\text{mm}$, but the reverse flow at the centreline is captured well. Moving further downstream, it is shown that the under prediction in the peak axial velocity continues, as seen in Fig. 7.3a, and the locations of the local peaks are further away from the centreline for $x = 20\,\text{mm}$ and $30\,\text{mm}$. There is a small over prediction in the peak radial velocity at $x = 20\,\text{mm}$ and its radial position is also slightly over predicted. All of these differences suggest that the width of the IRZ at this location is over predicted in the LES. This is caused by the difficulty in capturing the flow separation along the contoured outer-wall of the annular air nozzle (see Fig. 4.8). At the furthest downstream location, the three velocity components are captured well. The corresponding r.m.s.

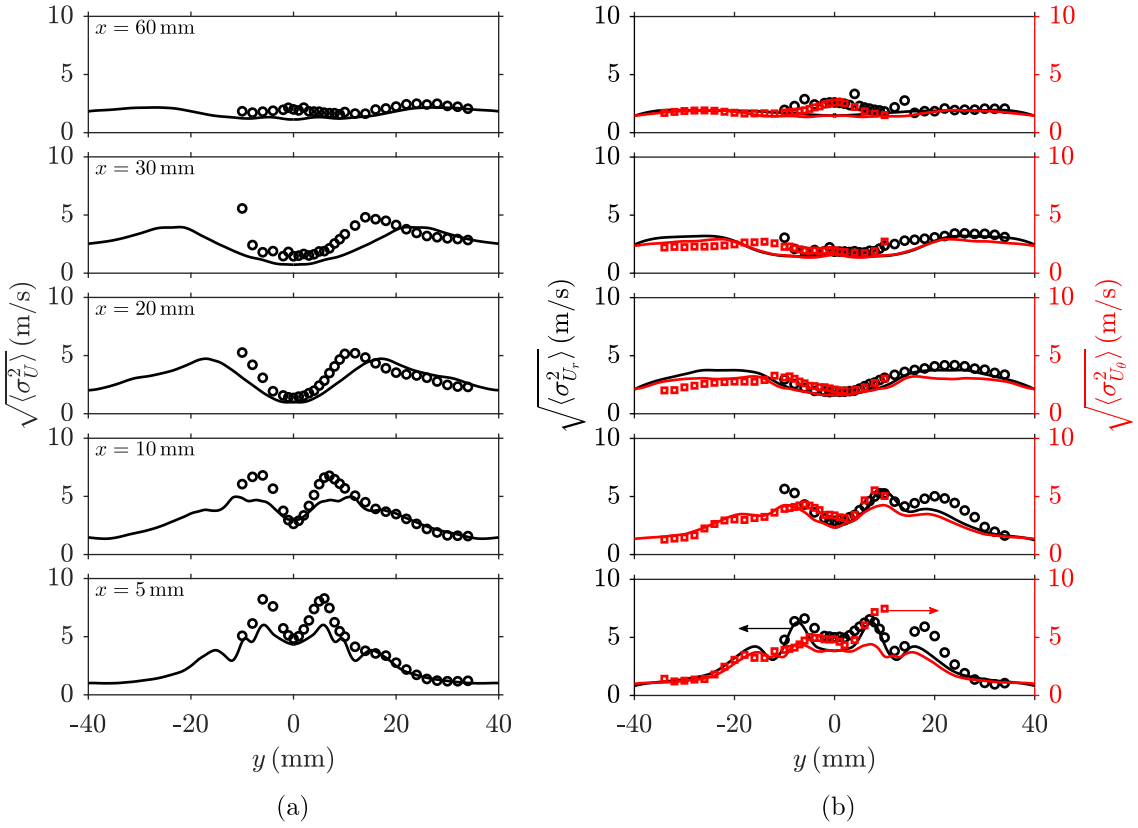

Fig. 7.4 Comparisons of the time-averaged (a) axial and (b) radial and azimuthal r.m.s. velocities between the measurements (Meier *et al.*, 2006; Weigand *et al.*, 2006) (symbols) and the computations (lines), where the latter results are azimuthally averaged.

values of the three velocity components are shown in Fig. 7.4, where the r.m.s. is obtained using only the resolved variance as $\langle \sigma^2_{\widetilde{U}} \rangle = \langle \widetilde{\boldsymbol{U}}^2 - \langle \widetilde{\boldsymbol{U}} \rangle^2 \rangle$. The position of the local peaks corresponds to the shear layers, where the fluctuations of the velocity are highest. These peak r.m.s. positions are sufficiently captured in the LES for all velocity components, except a radial shift in the axial velocity is shown at $x = 20\,\text{mm}$ and $30\,\text{mm}$, as seen in Fig. 7.3a for the mean velocities. Furthermore, the discrepancies seen between the measured data and simulation are partly attributed to including only the resolved fields. The r.m.s. axial velocity at $x = 5\,\text{mm}$ is captured well and the maximum resolved r.m.s. value is 70 % of the maximum peak in the measured data, suggesting that the flow field is resolved satisfactorily.

The time-averaged Favre-filtered mixture fraction and temperature profiles are shown in Figs. 7.5a and 7.5b respectively. As with the velocity statistics, the agreement between the measured and computed values at the near-field is good, especially for the averaged mixture fraction. The temperature at $x = 5\,\text{mm}$ and $10\,\text{mm}$ along the centreline is under

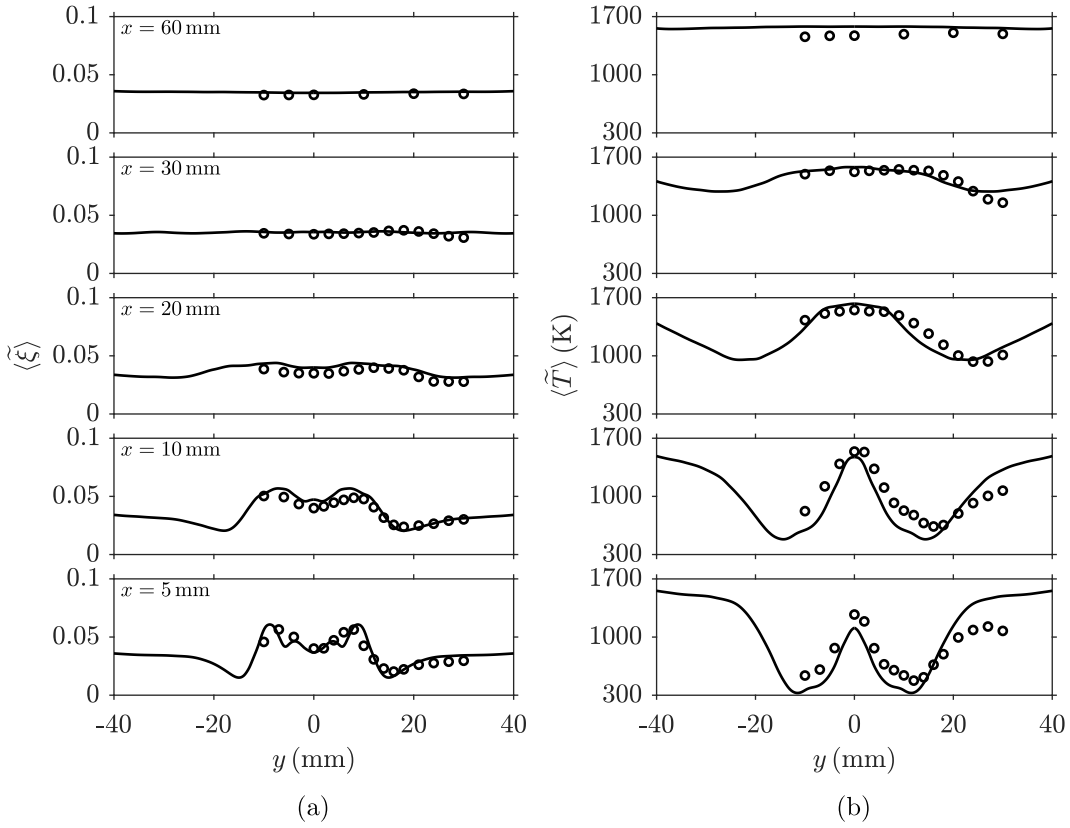

Fig. 7.5 Comparisons of the time-averaged (a) mixture fraction and (b) temperature profiles between the measurements (Meier *et al.*, 2006; Weigand *et al.*, 2006) (symbols) and the computations (lines), where the latter results are azimuthally averaged.

predicted by 13 % and 4 % respectively. This would suggest that the lift-off height for the flame root is overestimated by approximately 10 % in the simulation; this will be discussed in further detail in the next section. Furthermore, the temperature in the region $|y| > 20\,\mathrm{mm}$ is overestimated in the simulation. However, it is demonstrated in Fig. 7.5a that the mixing in the near-field regions is captured well by the simulation. Thus, the over prediction in temperature in the large radial positions is due to the adiabatic wall treatment in the LES. Moving further downstream, it is shown that the agreement between the measurements and the simulation is good, but the temperature in the regions close to the wall ($|y| \geq 30\,\mathrm{mm}$), is again over predicted by the simulation at $x = 30\,\mathrm{mm}$. The over predictions of the near-wall temperature are also seen in the r.m.s. temperature profiles in Fig. 7.6b. The effect of non-adiabatic wall treatment on this flame will be investigated in a future study. There are also some over predictions in the peak mixture fraction r.m.s. values in the near-field within the jet regions, despite the good agreement for the mean values. This is mainly due to the averaging effects coming

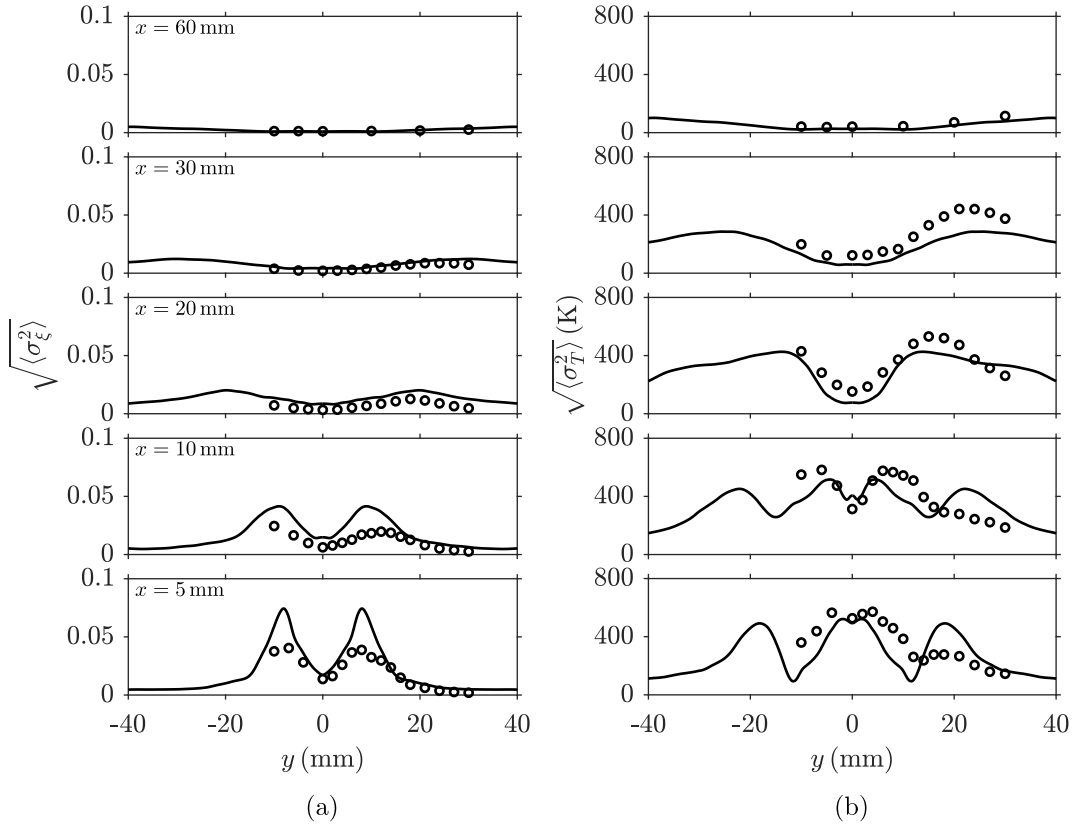

Fig. 7.6 Comparisons of the time-averaged (a) r.m.s. mixture fraction and (b) r.m.s. temperature profiles between the measurements (Meier *et al.*, 2006; Weigand *et al.*, 2006) (symbols) and the computations (lines), where the latter results are azimuthally averaged.

from the significantly larger sized Raman measurement probe used (0.6 mm) compared to the LES grid size (0.3 mm) for the near-field at $x = 5$ mm and 10 mm. It can be seen in Fig. 7.6a that this effect becomes less influential as the agreement for the r.m.s. mixture fraction improves when moving downstream. Nonetheless, the comparisons show that the overall flow and flame structures are well predicted in the LES for this flame, which is close to the lean blow-off limit. This permits further analysis of the LES data, in order to gain physical insights into the unsteady behaviours of this lean swirl flame in the following sections.

7.3.2 Flame dynamics

It was observed in the experimental study that this flame experienced random lift-off events and therefore, the flame location and its structure changes significantly, along with the distribution of the heat release rate; these experimental observations are investigated in this subsection. The distributions of the filtered (at an arbitrarily chosen time

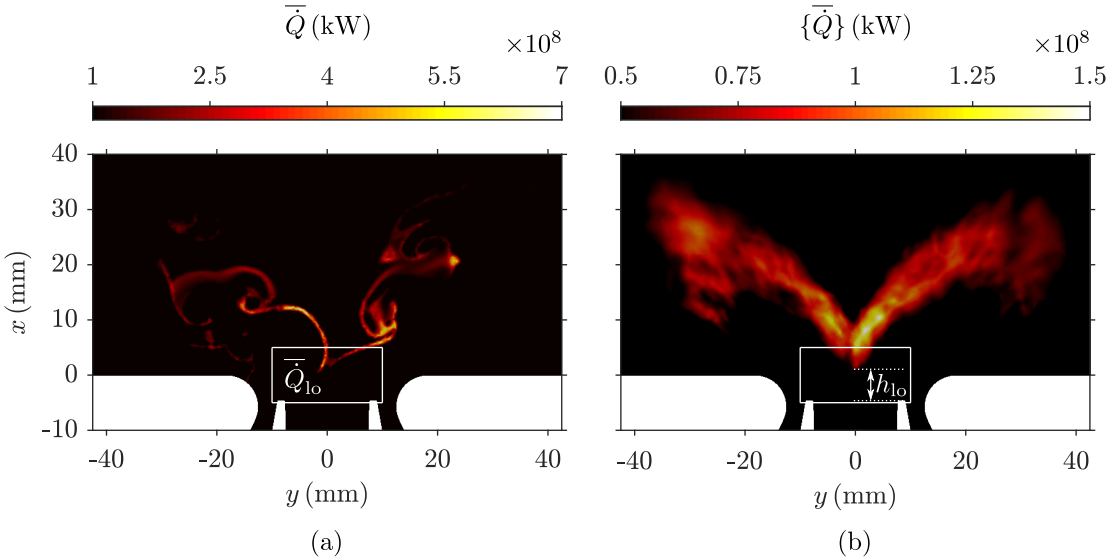

Fig. 7.7 Distributions of the (a) filtered and (b) time-averaged heat release rate fields in the x–y mid-plane.

$t = 104.525\,\mathrm{ms}$) and time-averaged heat release rate, denoted by the braces, in the x–y mid-plane are shown in Figs. 7.7a and 7.7b. The time-averaged field in Fig. 7.7b is fairly noisy, suggesting that heat release regions vary significantly in space over the sample taken and indicate that the flame is highly unstable. It is shown that the flame has regions of high heat release at a root in the regions close to the bottom of the combustion chamber and within the vortices along the inner shear layer. The time-averaged field in Fig. 7.7b shows that the flame brush has a 'V' shape and the highest heat release is around the flame root region, where the fresh reactants mix rapidly with the recirculating hot products. This flame root then acts as an ignition source to reactant mixtures within the flammability limits that are convected downstream along the inner shear layer within vortical structures, as seen in Fig. 7.7a. This results with an elongated reaction zone along the inner shear layer, as observed in Fig. 7.7b. It is shown that the average position of the root is at $x = 2\mathrm{mm}$, which corresponds to a lift-off height of $h_{\mathrm{lo}} = 6.5\mathrm{mm}$ (above the fuel nozzle), as marked in Fig. 7.7. This is close to the lift-off height observed in the experiment, which was around 6mm above the fuel nozzle (Weigand *et al.*, 2006), suggesting that the complex interactions between the flame root and the swirling flow are captured well in the LES.

It was also reported by Stöhr *et al.* (2011*a*) that during an unstable event, the flame root was extinguished, leading to flame lift-off. The flame then moved back upstream and returned to the location of $h_{\mathrm{lo}} \approx 6\mathrm{mm}$. Different flame shapes were seen during the lift-off event and therefore, the distribution of the heat release rate will have changed

significantly with time. These phenomena captured in the LES are depicted in Fig. 7.8. The dash-dotted line in Fig. 7.8a shows the temporal variation of the heat release rate integrated over the entire combustion chamber, denoted as $\overline{\dot{Q}}_{\mathrm{glob}}$, for 45 ms, which is an arbitrarily chosen interval that included a lift-off event in the simulation. The volume integrated heat release rate varies with time, but it is close to the thermal power of $P_{\mathrm{th}} = 7.6\,\mathrm{kW}$ for the experiment. However, it is difficult to identify the lift-off event from this quantity. Therefore, it is decided to monitor the temporal variation of the heat release rate integrated over a small volume centred at $x = 0\,\mathrm{mm}$ of size $10 \times 20 \times 20\,\mathrm{mm}^3$, as shown in Fig. 7.7. This heat release rate, denoted as $\overline{\dot{Q}}_{\mathrm{lo}}$, is also shown in Fig. 7.8a, using the solid line, but multiplied by 100 to show on the same scale as the global heat release values. It is evident that the heat release rate in this region changes significantly over the time interval shown. The fluctuation observed for the first 4 ms is due to some initial transients and this heat release rate is large when the flame root comes into the smaller monitoring region. A large drop in $\overline{\dot{Q}}_{\mathrm{lo}}$ is observed until $t = 109\,\mathrm{ms}$, but since the global heat release rate is large at this time, this suggests that the flame root is moving out of the smaller monitoring region. Some fluctuations in $\overline{\dot{Q}}_{\mathrm{lo}}$ are observed for the time interval $109 < t < 124\,\mathrm{ms}$, suggesting that the flame root is coming into the monitoring region periodically. These fluctuations weaken for the interval $124 < t < 141\,\mathrm{ms}$, which suggests that the flame is outside of the monitoring region. The last part of the sequence $t > 141\,\mathrm{ms}$ shows that $\overline{\dot{Q}}_{\mathrm{lo}}$ now steadily increases up to the values seen when the flame has an established flame root in the monitoring region and hence, it is suggested that the flame has re-stabilised.

The lift-off height, denoted using h_{lo} and illustrated in Fig. 7.7b, is tracked and is based on the minimum height from the fuel injector exit where $\widetilde{T} = 1500\,\mathrm{K}$ within a radius of $r < 10\mathrm{mm}$. This variation is shown in Fig. 7.8b, where the lift-off height is also averaged over every 4.5 ms and the averaged values are shown using horizontal thick lines. On the whole, the trend seen for the lift-off height is directly linked to $\overline{\dot{Q}}_{\mathrm{lo}}$. After the first window of 4.5 ms, the lift-off height fluctuates up to $t = 131\,\mathrm{ms}$, since the unstable behaviour and fluctuating heat release rate is caused by the flame root trying to establish itself. However, the averaged lift-off heights are 3–6 mm larger than the height in the first interval of approximately 6 mm. Beyond this time, the averaged lift-off height significantly increases, suggesting that the flame recedes downstream and does not stabilise at the root, which is shown by the low heat release rate seen in this region. The last window of 4.5 ms shows that the average height is very similar to the first window

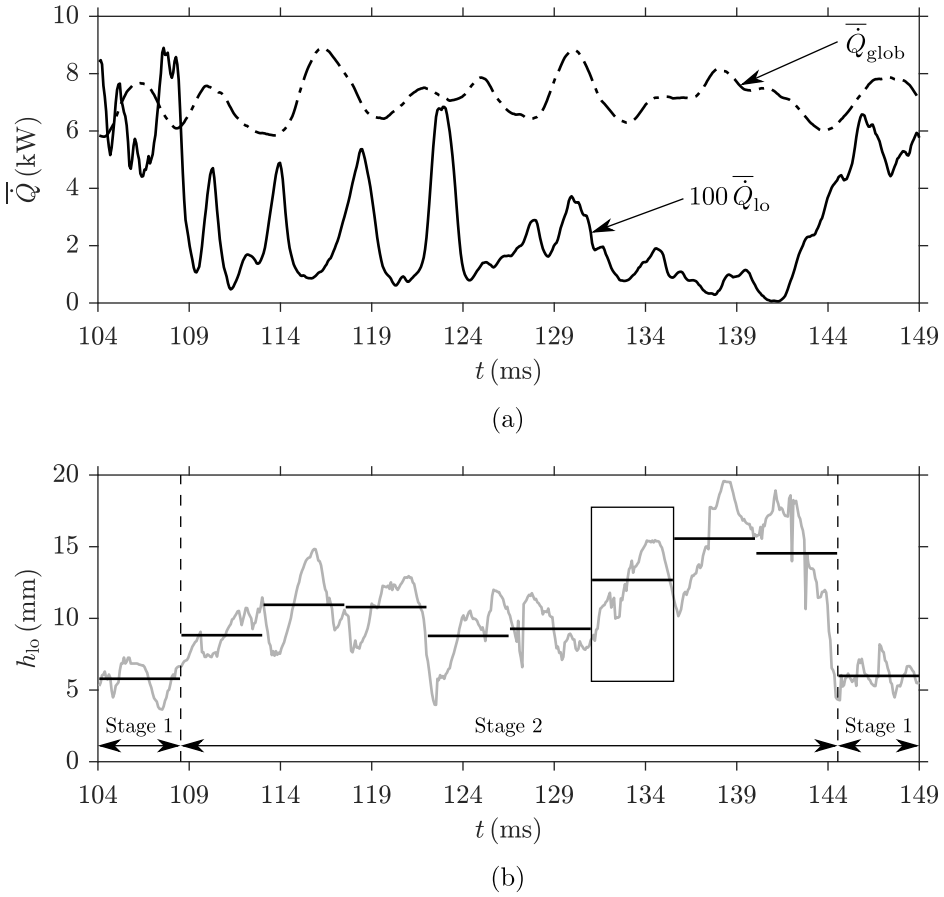

Fig. 7.8 Time series of (a) the volume integrated heat release rate in the combustion chamber and in the marked volume in Fig. 7.7 and (b) the flame lift-off height above the fuel nozzle.

and hence, the flame leading edge is established again at its typical location to give a more stable flame in its typical 'V' shape.

The results shown in Fig. 7.8 suggest that there could be some frequency of the transient lift-off event and the flame root returning to its typical location. The duration of the LES is insufficient to estimate this frequency, which will be explored in a future study. However, it is possible to identify two different stages of the flame, as marked in Fig. 7.8b. Stage 1 denotes a stabilised flame with an established flame root and Stage 2 is the transient lift-off event when the flame root is lost or receding downstream. These two stages of the flame base dynamics are described next.

Stage 1: stabilised flame

This stage corresponds to the situation of having the flame base within the monitoring volume and $h_{\mathrm{lo}} \approx 6\,\mathrm{mm}$, as marked in Fig. 7.8. A comparison of the time series showing

the stabilised flame behaviour, arbitrarily chosen from the measurements and the LES, is presented in Fig. 7.9. The filtered reaction rate contours and velocity vectors from the LES are shown in Fig. 7.9a. The blue and red vectors show the smallest and largest velocity magnitude respectively, where the values are shown in the legend in Fig. 7.9 and the experimental measurements use the same scale. Figure 7.9b shows the combined PIV and OH-PLIF measurements, where the former is taken across a square region as marked in the top of Fig. 7.9a. The filtered reaction rate is compared with the OH-PLIF measurements, since the reaction rate is readily available from the LES and clearly marks the flame. The time interval between each simulation frame is 0.375 ms, where the first frame is at $t = 104.525$ ms (see Fig. 7.8). The total duration of the LES sequence is 1.875 ms, which is similar to the 2 ms duration used for the experimental images, as marked in Fig. 7.9b.

The high reaction rates typically occur in two favoured regions, as shown in Fig. 7.9. The first is within small pockets inside the large coherent structures, which can be seen by the velocity vectors and their circular patterns that are present along the 'V' shape of the flame. The second region is near the bottom of the combustion chamber, which is the flame root. On the left-hand side of the sequences, it is shown that the flammable mixture is ignited near the bottom at the flame root and the reaction then continues when the structure is convected downstream with time, but ends at around $y = -20$ mm in the fourth frame of Fig. 7.9a. Ignition at the flame root then occurs on the right-hand side in the fifth and sixth frames of Fig. 7.9a. The repetition rate is controlled by the rotation of the PVC, as described by Stöhr *et al.* (2011*a*). The frequency for this from the Fourier analysis undertaken by Stöhr *et al.* (2011*a*) is 510 Hz. It is estimated that the frequency in the simulation by using the sequence shown in Fig. 7.9a is approximately 520 Hz. The flame root acts as a source of heat and radicals close the exit of the nozzles and is responsible for the ignition of fresh reactants in the helical zone. It is important that this root remains established, robust and does not recede downstream to ensure that a stable flame exists. This is not guaranteed for flames close to the blow-off limit, which is the case for flame C. Hence, the flame experiences another stage of evolution, which is described next.

Stage 2: lift-off event

It was suggested in the experimental study by Stöhr *et al.* (2011*a*) that the lean blow-off event is triggered when the flame root extinguishes and re-ignition does not occur after more than 2 ms, which corresponded to one rotation of the PVC. Following this extinction

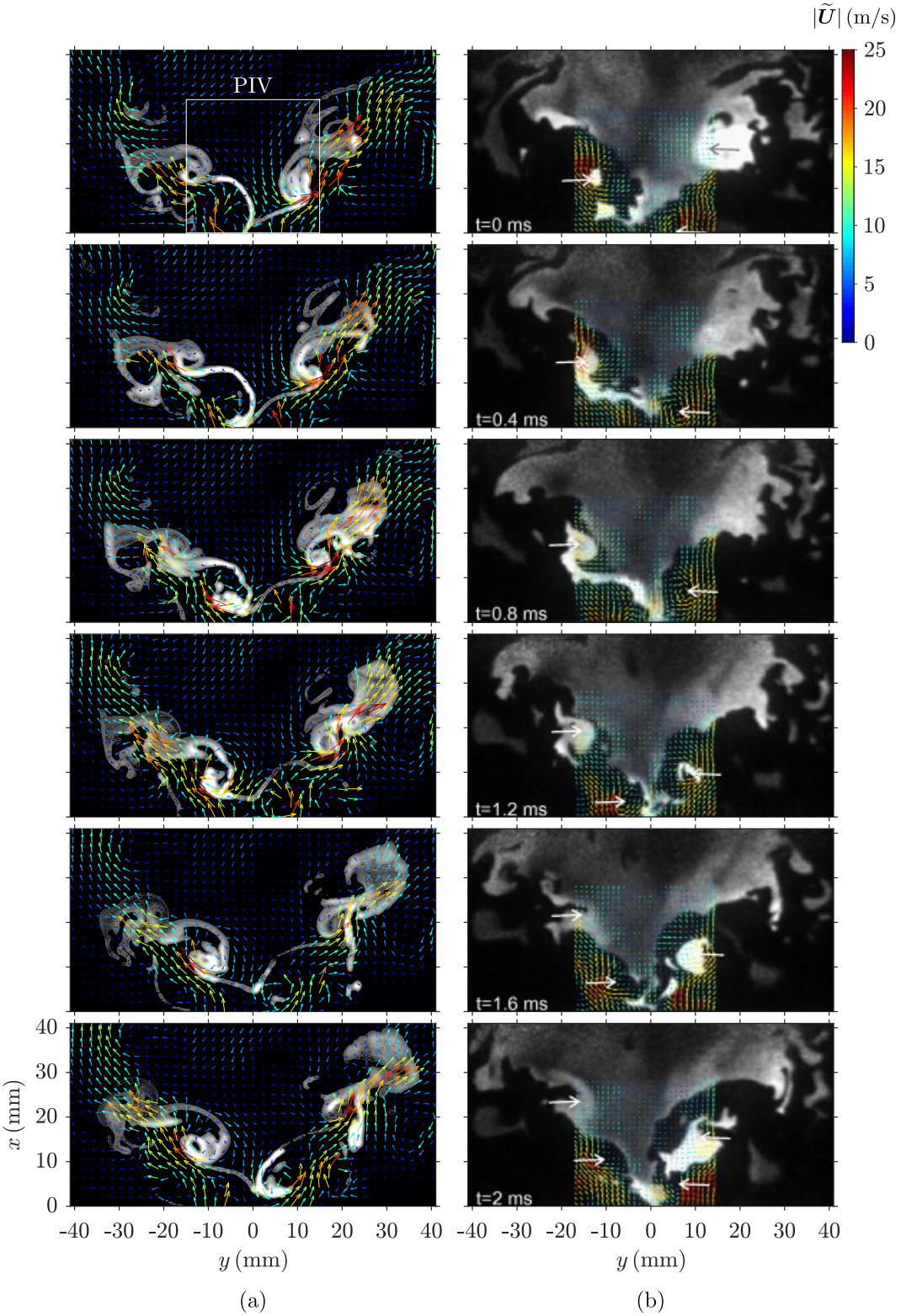

Fig. 7.9 Time series of the simultaneous (a) filtered reaction rate and velocity vectors (coloured by magnitude) and (b) the PIV and OH-PLIF measurements for the flame in Stage 1. The time interval between each simulation frame is 0.375 ms.

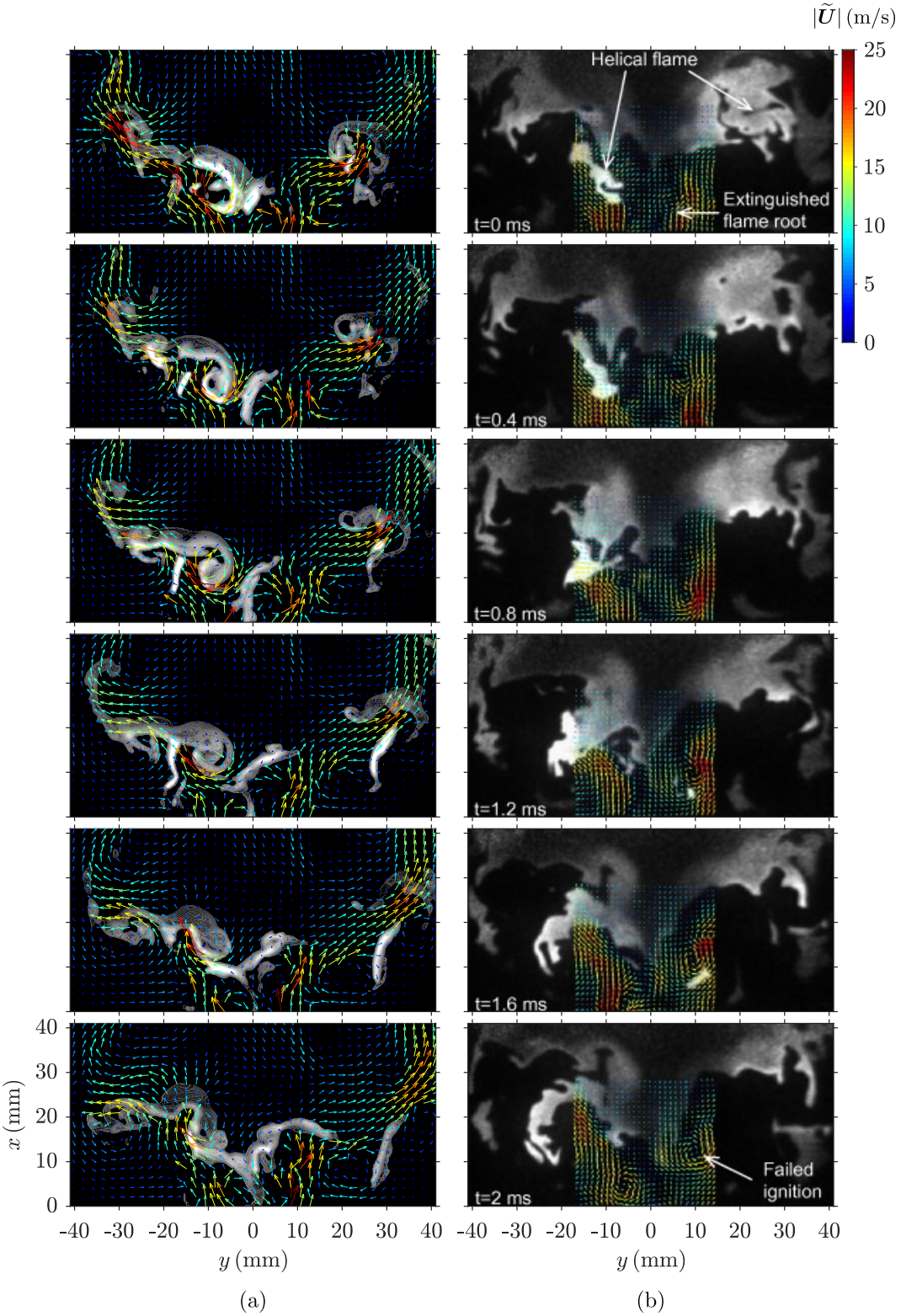

Fig. 7.10 Time series of the simultaneous (a) filtered reaction rate and velocity vectors (coloured by magnitude) and (b) the PIV and OH-PLIF measurements for the event showing the loss of the flame root and local extinction. The time interval between each simulation frame is 0.375 ms.

of the flame root, if there is failed ignition at the vortex centres, then the flame will blow-off. This was observed to be due to the insufficient supply of heat and radicals by the flame root. Furthermore, the entrainment of cold unburnt reactants into the IRZ and intermittent variations in the mixture fraction can trigger extinction.

Figure 7.10 compares the time sequence of these events from the LES and the experiment. The time interval for the simulation between each frame is the same as that used for Fig. 7.9, but the first frame is at $t = 111.05\,\text{ms}$ (see Fig. 7.8). It is observed that the reaction has been instigated within the vortex in the LES, but the reaction stops before a radial position of 20 mm from the centreline. This is not the case for Stage 1 of the flame, as seen in Fig. 7.9a, as it is seen that the reaction continues after this radial position. Furthermore, the right-hand side of Fig. 7.10a shows that the reaction is very weak and some difficulty of re-ignition is seen around $x = 20\,\text{mm}$. This is not the case for the experiment, as failed ignition is highlighted in the last frame of Fig. 7.10b. On the other hand, the reaction at the flame root is very weak in Fig. 7.10a and it is seen in the last two frames that the flame root is approximately 4 mm higher in comparison to its position in Fig. 7.9a. After the final frame of Fig. 7.10a, the lift-off height increases significantly, as shown in Fig. 7.8. Therefore, the sequence shown in Fig. 7.10a is important and it is suggested that the weak reaction within the vortices and the change in position of the flame root causes the lift-off event to occur. Therefore, an additional investigation into the precursors that lead to the described lift-off event is presented next using the simulation data, since further information can be extrapolated from the LES that is not available in the experiment.

7.3.3 Further insights into flame stabilisation

The purpose of this section is to investigate the various physical processes involved in the stabilisation of the flame and the lift-off event seen in Fig. 7.10. The mechanisms involved at the flame root region for Stage 1 of the flame are studied first. The distributions of the filtered mixture fraction and reaction rate in the x–y mid-plane are shown in Figs. 7.11a and 7.11b respectively. The isolines denote the stoichiometric mixture fraction and the lean and rich flammability limits are approximately 0.028 and 0.08 respectively; the dark regions in Fig. 7.11a indicate that these mixtures consist of air. Figure 7.11b shows the filtered reaction rate $\overline{\dot{\omega}^*}$ and indicates that the reaction rates are highest along the contour for ξ_{st}, specifically near the centreline. This typical behaviour is seen during a continuous sequence of the flame in Stage 1. Although the local mixture is stoichiometric, a high reaction rate is not seen in the locations further downstream. This implies that

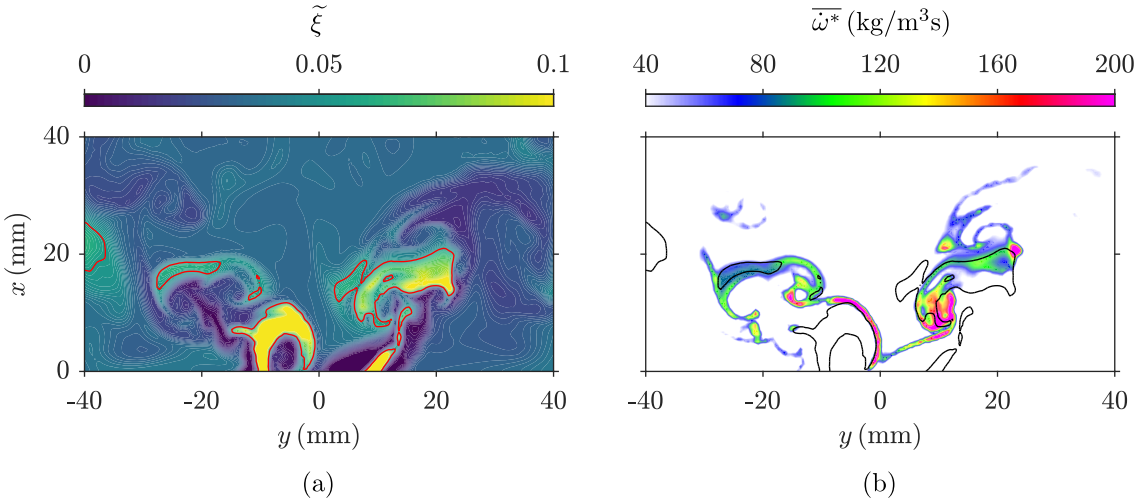

Fig. 7.11 Distributions of (a) the filtered mixture fraction and (b) the reaction rate for the flame in Stage 1 at $t = 104.525$ ms. The isolines denote the stoichiometric mixture fraction value of $\xi_{st} = 0.055$.

the stronger flame located at the base provides the heat and radicals required for flame stabilisation.

Figure 7.12 shows the filtered mixture fraction and reaction rate distributions for two instances ($t = 108.05$ ms and 111.05 ms), which are early into Stage 2, as shown in Fig. 7.8. As seen in Fig. 7.8b, the lift-off height increases and the heat release rate in the flame root region decreases after both of these instances. The mixture fraction and reaction rate fields for $t = 108.05$ ms are shown in Figs. 7.12a and 7.12b respectively. In the right half of Fig. 7.12b, there is no reaction along the stoichiometric mixture fraction line and the reaction rate is very weak in comparison to the reaction rate field in Fig. 7.11b. This is caused by the air entrainment between the stoichiometric reactant mixture and hot products and prevents ignition at the flame root region. This causes the flame to move away in the radial direction in the right half of the domain and leads to the sudden drop of $\overline{\dot{Q}}_{lo}$ that is seen in Fig. 7.8a. Consequently, the flame root recedes downstream, leading to an increase in the flame lift-off height around $t = 108$ ms, as shown in Fig. 7.8b.

The mixture fraction and reaction rate fields at $t = 111.05$ ms are shown in Fig. 7.12c and 7.12d respectively. It is seen that a pocket of rich mixture is present along the centreline near the bottom of the combustion chamber in the region where the flame root typically stabilises. This causes the flame to move to a downstream position and therefore, the flame root is shifted from its typical location and this initiates the lift-off event.

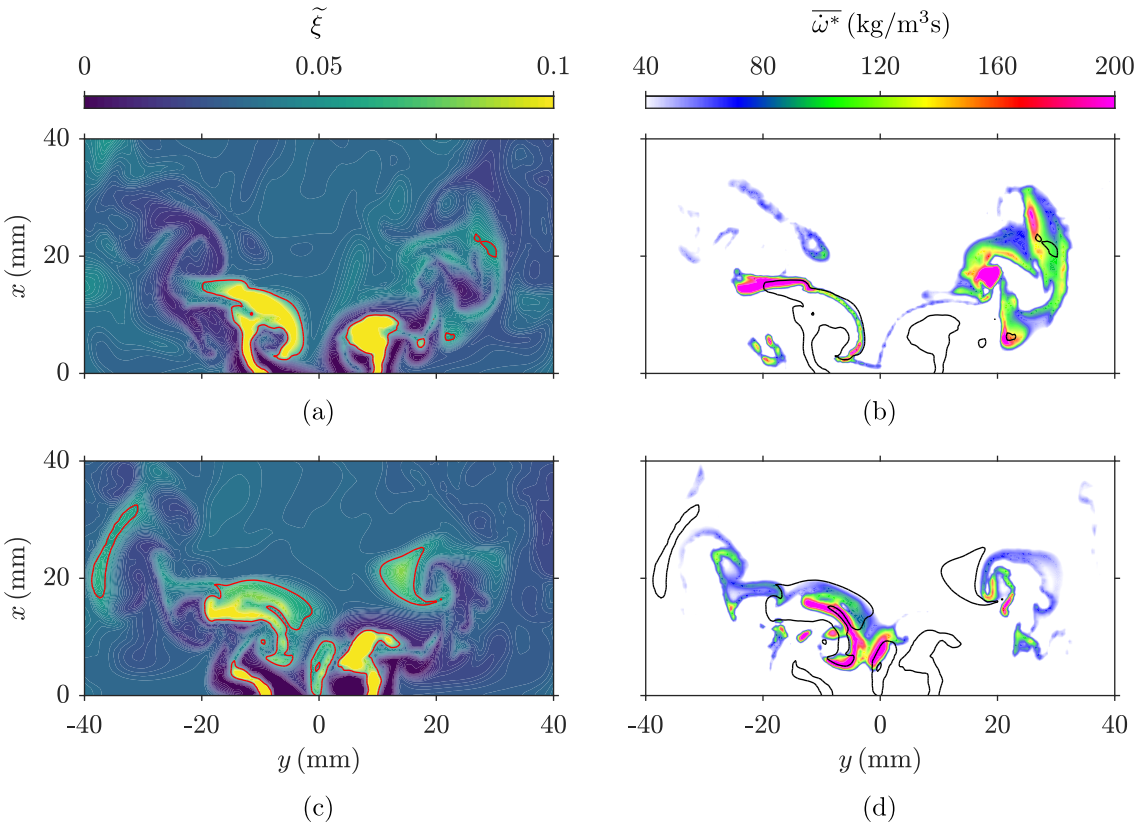

Fig. 7.12 Distributions of (a) the filtered mixture fraction and (b) the reaction rate prior to the lift-off event at $t = 108.05$ ms. The frames (c) and (d) respectively show the filtered mixture fraction and the reaction rate at $t = 111.05$ ms. The isolines denote the stoichiometric mixture fraction value of $\xi_{st} = 0.055$.

Figure 7.13 shows the filtered mixture fraction and reaction rate at $t = 138.5$ ms, which corresponds to the maximum lift-off height, as seen in Fig. 7.8b. It is seen here that there is a large island of rich mixture above the fuel nozzle and the flame root is not present. The reaction rate is distributed across a large region and with weaker burning, which is dissimilar to the higher reaction rates that are concentrated in smaller regions, as seen in Fig. 7.11. The reaction is weaker in the monitoring region and causes lower values of $\overline{\dot{Q}}_{lo}$, as seen in Fig. 7.8a. The mixture fraction distribution in Fig. 7.13a shows that the local mixture in this region is typically below the lean flammability limit and therefore, the flame leading edge cannot move upstream towards its location observed in Stage 1. Hence, these results show that the large-scale events controlling the fuel–air mixing and the proximity of flammable mixture and hot products control the flame lift-off events.

Statistics are obtained across an additional 255 ms, in order to gain a further understanding of the stabilisation of the flame. The volume integrated heat release rate and

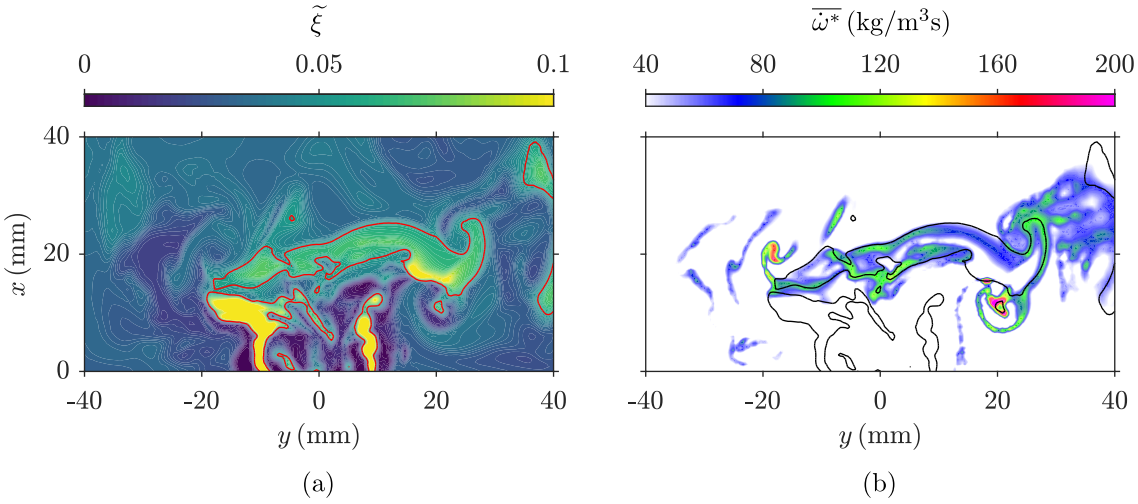

Fig. 7.13 Distributions of (a) the filtered mixture fraction and (b) the reaction rate for the flame at the maximum lift-off height ($t = 138.5$ ms). The isolines denote the stoichiometric mixture fraction value of $\xi_{st} = 0.055$.

lift-off height are shown in Figs. 7.14a and 7.14b respectively for the total sample of 300 ms. It is shown that both quantities vary significantly across the whole sample, suggesting that the flame is highly unstable and the position of the flame root varies considerably. The lift-off height does approach values that are similar to the maximum value seen in Fig. 7.8a at $t = 138.5$ ms; the large lift-off height values occur at $t = 189.125$ ms, 263 ms, 315.5 ms, 343.475 ms and 355.925 ms, as seen in Fig. 7.14b. However, no correlation is seen when comparing the heat release rate in Fig. 7.14a at these instances; the heat release rate varies between approximately 6–8 kW.

The mixture fraction and its dissipation rate at the flame root are shown in Figs. 7.15a and 7.15b over the same time sample as Fig. 7.14. The blue and red regions of Fig. 7.15a represent regions beyond the lean and rich flammability limits respectively. The mixture fraction dissipation rate is normalised as $\widetilde{\chi}_\xi^+ = \widetilde{\chi}_\xi / \chi_q$, where the quenching dissipation rate for methane–air is taken as $\chi_q = 5\,\mathrm{s}^{-1}$ (Peters, 2000). The yellow region denotes partial quenching of the flame ($0.5 \leq \widetilde{\chi}_\xi^+ \leq 1$), whereas the red region represents the events when the scalar dissipation rate exceeds the quenching value ($\widetilde{\chi}_\xi^+ > 1$). At $t = 189.125$ ms, it is shown that the mixture fraction at the flame root is within the flammability range and the dissipation rate is small and within the white region, which suggests the flame root is not quenched. However, the mixture fraction and the scalar dissipation rate are within the red regions approximately 2 ms earlier, which is similar for $t = 315.5$ ms and 355.925 ms. Hence, it is suggested that the flame lift-off height is high, due to the combination of these two processes. At $t = 343.475$ ms and for an

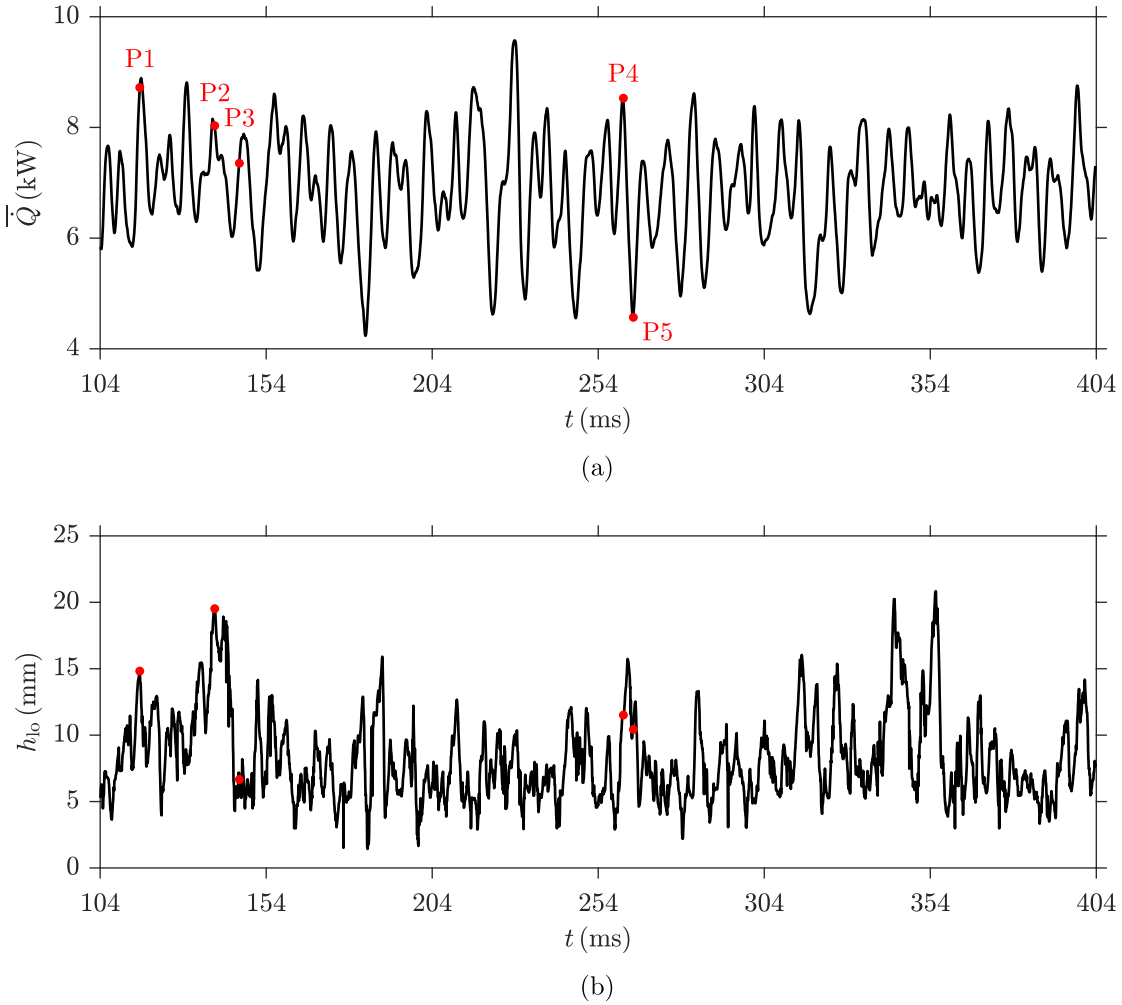

Fig. 7.14 Extended time sample of (a) the volume integrated heat release rate in the combustion chamber and (b) the lift-off height above the fuel nozzle.

earlier period of approximately 20 ms, the dissipation rate is very small and far from the quenching regions. The mixture fraction is beyond the rich flammability limit just prior to $t = 343.475$ ms. Therefore, it is suggested that the lift-off height increases because rich mixtures are present near the flame root, which is due to the entrainment of fuel–rich mixtures into the flame root region. For $t = 263$ ms, the observations are different because the heat release rate shown in Fig. 7.14a at this time is $\overline{\dot{Q}} = 4.6$ kW, which is approximately 4 kW lower than at $t = 260$ ms. Over this 3 ms period, the scalar dissipation rate is small and the mixture fraction at the flame root is beyond the rich flammability limit for 1 ms. However, the lift-off height remains at a similar value and hence, it is suggested that the flame is weaker as the heat release rate is reduced but the flame root is still present. This behaviour is to be explored in further detail.

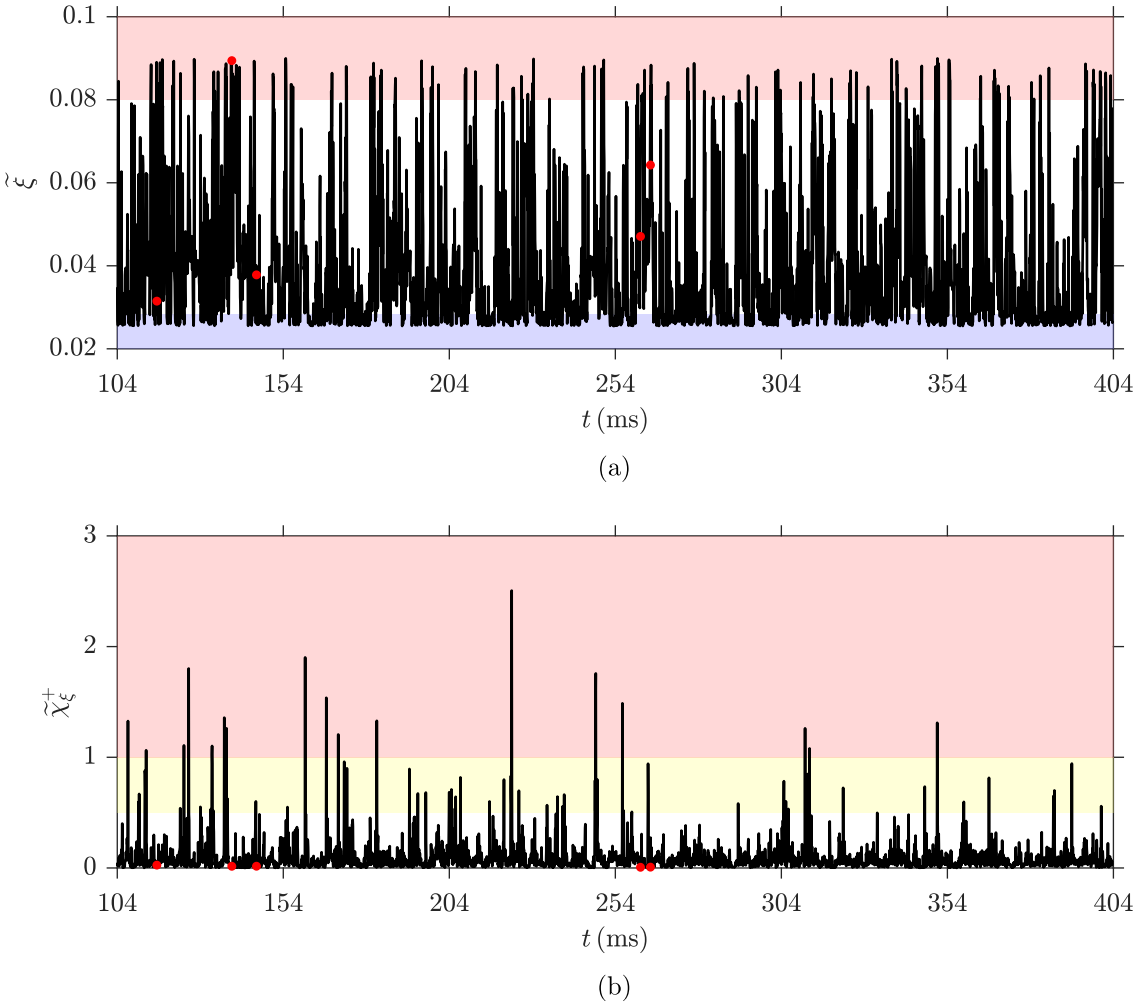

Fig. 7.15 Extended time sample of (a) the filtered mixture fraction and (b) the mixture fraction scalar dissipation rate at the flame root.

The histograms of the volume integrated heat release rate, the lift-off height, the mixture fraction and the mixture fraction dissipation rate are shown in Fig. 7.16. It is shown that the flame is highly unstable, since it is most likely that h_{lo} is within the range $5 \leq h_{\mathrm{lo}} \leq 10\,\mathrm{mm}$, as seen in Fig. 7.16b. The occurrence of $6 \leq \overline{\dot{Q}} \leq 8\,\mathrm{kW}$ is also high, as seen in Fig. 7.16a. The normalised mixture fraction dissipation rate at the flame root in Fig. 7.16d is $\widetilde{\chi}_{\xi}^{+} > 0.5$ for approximately 2 % of the sample shown in Fig. 7.15b. However, the mixture fraction in Fig. 7.16c is outside of the flammability range for approximately 32 % of the sample in Fig. 7.15b, which suggests that the unstable flame behaviour is related to the entrainment of mixtures within the flame root region that are outside of the flammability limits.

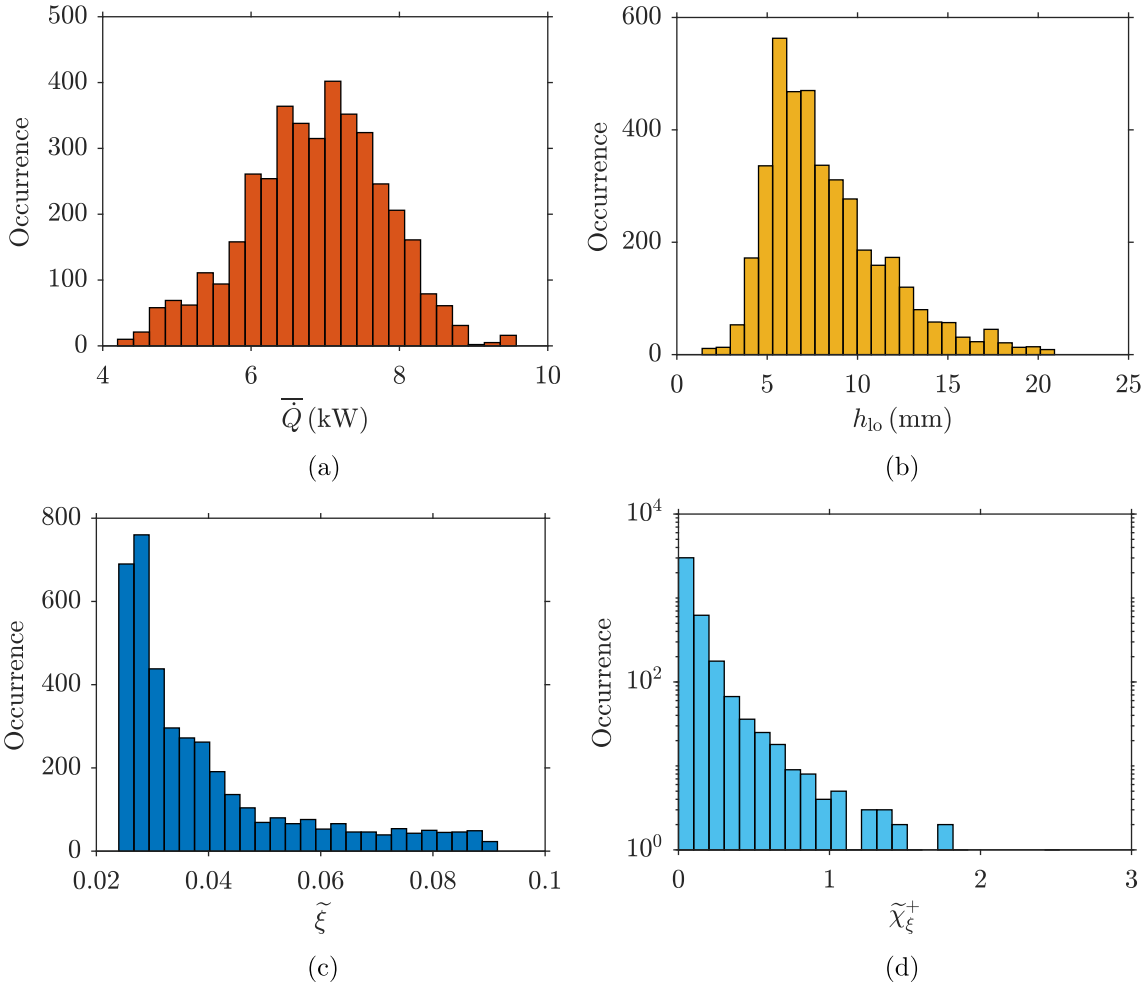

Fig. 7.16 Histograms of (a) the volume integrated heat release rate, (b) the lift-off height, and (c) the filtered mixture fraction and (d) the mixture fraction scalar dissipation rate at the flame root.

The histograms for the filtered mixture fraction and its dissipation rate are shown in Figs. 7.17 and 7.18 respectively for three time intervals, which are marked in Fig. 7.14a. Points P1 and P2 represent the interval $115.925 \leq t \leq 138.5$ ms and points P2 and P3 represent the interval $138.5 \leq t \leq 145.925$ ms. These two intervals are significant because the heat release rate decreases by only 8 % between P1 and P2 and then by a further 8.4 % between P2 and P3. However, the lift-off height increases between P1 and P2 by 32 % and then decreases between P2 and P3 by 66 %. The histograms for the mixture fraction and its scalar dissipation rate between P1 and P2 are shown in Figs. 7.17a and 7.18a. The dissipation rate exceeds $\widetilde{\chi}_{\xi}^{+} > 0.5$ for 2 % of the interval between P1 and P2, which is the same as the full sample in Fig. 7.16d, and the mixture fraction falls outside the flammability limit for approximately 20 % of the counts shown in Fig. 7.17a. For P2 and P3, no values within $\widetilde{\chi}_{\xi}^{+} > 0.5$ are seen in the respective histogram in Fig. 7.18b and the

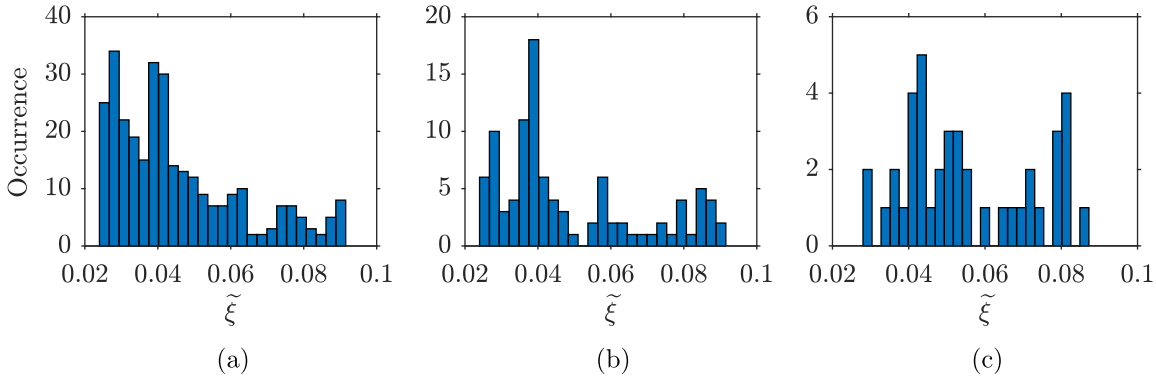

Fig. 7.17 Histograms of the filtered mixture fraction at the flame root between (a) P1 and P2, (b) P2 and P3 and (c) P4 and P5. The points are labelled in Fig. 7.14a.

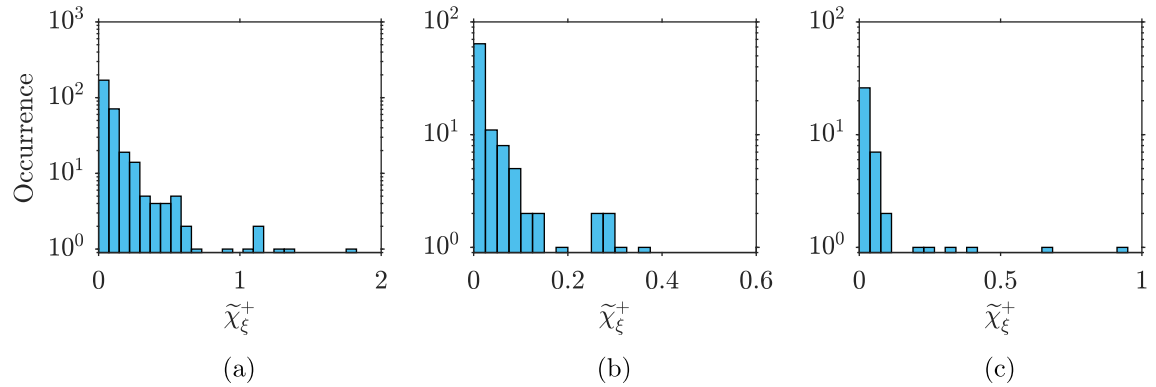

Fig. 7.18 Histograms of the filtered mixture fraction dissipation rate at the flame root between (a) P1 and P2, (b) P2 and P3 and (c) P4 and P5. The points are labelled in Fig. 7.14a.

mixture fraction is outside the flammability limit for approximately 15 % of the counts shown in Fig. 7.17b. Based on these observations, it is suggested that the lift-off height decreases between P2 and P3 because the mixture fraction dissipation rate is smaller. For P4 and P5, the mixture fraction histogram in Fig. 7.17c shows that the mixture fraction is in the rich region for 43 % of the counts, whereas the mixture fraction dissipation rate is only within the range $\widetilde{\chi}_{\xi}^{+} > 0.5$ for 5 % of the total counts in Fig. 7.18c. Therefore, the increased occurrence of rich mixtures in the flame root region may lead to the reduction of the volume integrated heat release rate between P4 and P5. No significant changes in lift-off height are seen in this interval and hence, this period represents a weaker burning mode of the flame, since a flame root is still present.

7.4 Summary

A flame close to the lean blow-off limit in a gas turbine model combustor is simulated using LES. The statistics for the velocity, mixture fraction and temperature obtained from the simulation compare well with measured values. Good comparisons are also observed for the r.m.s. statistics. These validations permit investigation of the numerical data in further detail to gather insights into the behaviour of the flame stabilisation location inside the combustor. This analysis identified two distinct stages for the evolution of flame root. In the first stage, the flame is anchored by its stable and robust root located near the centreline in the near-field of the burner and this led to a 'V' shaped flame brush (time-averaged flame) as observed in the experiment. This is verified by comparing stereo-PIV and OH-PLIF sequences with LES results. It is observed in the LES that the entrainment of mixtures outside of the flammability limits into the flame region leads to the loss of the flame root and initiated the lift-off events in the second stage. The duration of the lift-off event is observed to be approximately 30 ms and the flame is found to be positioned downstream during this event. This flame then moves upstream towards its location observed in Stage 1 of the flame. These two stages are observed to switch from one to the other, as observed in the experiment. This switching is caused by the entrainment of air and weaker mixtures into the flame region created by the unsteady fuel–air mixing phenomena, which are governed by both large-scale eddy motions and small-scale mixing processes. The combining effect of rich mixtures being present in the flame root region and dissipation rates that exceed the quenching value cause the lift-off height to increase. If the mixture fraction dissipation rate is low but rich mixtures are present, then the integrated heat release may decrease. Further analysis is required to distinguish the role of these processes when the flame is experiencing complete blow-off.

Chapter 8

Influences of Heat Loss

The previous chapter provides physical insights into the dynamics of the flame root in a lean swirl-stabilised flame. However, fully adiabatic conditions are used for the simulation. Hence, it is of interest to determine whether non-adiabatic modelling would affect the stabilisation and behaviour of the flame root. This chapter investigates the sensitivity of including heat loss effects at different levels within the combustion modelling for the flame studied in Chapter 7. These non-adiabatic effects are introduced through modifying the wall boundary conditions and using the non-adiabatic flamelet approach outlined in § 3.5.3.

8.1 Motivation

It is well known that lean combustion is highly unstable and such flames are susceptible to local extinction and flame blow-off. The mechanisms leading to blow-off are not well understood and under such conditions, the flame heat release becomes weaker and heat loss effects can play a more influential role. There have been a number of recent modelling studies on flame blow-off, e.g., in the studies by Zhang & Mastorakos (2016) and Ma *et al.* (2019), but heat loss effects are seldom considered for such studies. Thus, it is of interest from a modelling perspective to observe how heat loss effects can influence the flame behaviour close to lean blow-off conditions.

Modelling heat loss effects has been successfully achieved in previous LES studies of turbulent flames. One approach for including heat loss effects is to account for heat transfer from the walls of the combustion chamber, which can lead to achieving improved accuracy. A simple approach is by imposing wall temperature boundary conditions (Benard *et al.*, 2019; Mercier *et al.*, 2014; Palies *et al.*, 2011; Tay Wo Chong *et al.*, 2010),

where such boundary conditions are imposed by following experimental measurements obtained on the combustion chamber surfaces (Brübach *et al.*, 2013). Alternative methods include a conjugate heat transfer approach (Bauerheim *et al.*, 2015), or using a fully coupled LES/heat conduction approach, where an additional solver is used to compute the temperature distribution for the solid structure of the combustion chamber (Ghani *et al.*, 2016; Kraus *et al.*, 2018; Miguel-Brebion *et al.*, 2016; Shahi *et al.*, 2015). Alternatively, heat loss effects can be modelled by considering non-adiabatic flamelets. Previous non-adiabatic flamelet approaches include an enthalpy defect approach (Bray & Peters, 1994; Hossain *et al.*, 2002; Marracino & Lentini, 1997), a burner-stabilised flame method (Fiorina *et al.*, 2003; van Oijen & de Goey, 2000) and the heat release damping approach (Proch & Kempf, 2015; Wollny *et al.*, 2018). These non-adiabatic approaches have been reviewed by Fiorina *et al.* (2015) and an overview is previously included in § 3.5.3.

Understanding the mechanisms leading to blow-off is challenging, owing to the complex interactions between turbulence, the heat release from combustion and molecular transport (Shanbhogue *et al.*, 2009). In addition, the study by Palies *et al.* (2011) suggested the use of adiabatic walls can cause significant changes to the shape of the flame and hence, the flame to be studied here may be sensitive to changes when including heat loss effects in the modelling approach. Furthermore, the role of heat loss on the blow-off behaviour of the flame is not clear. Therefore, the aim of this study is to investigate the influences of heat loss on the stabilisation of a flame close to blow-off in the gas turbine model combustor studied in Chapter 7. The objectives are:

- To run two simulations using non-adiabatic wall conditions, and with and without non-adiabatic flamelets, and compare the statistics with the adiabatic case and the experimental data.
- To gain insights into the stabilisation of the flame when including non-adiabatic flamelets.

8.2 Flame conditions and numerical detail

The computational set-up that is used for the simulation presented in Chapter 7 is retained here for three simulations that are listed in Table 8.1. Case AD is the adiabatic case that is analysed in Chapter 7 and cases NAW and NAF are the two additional simulations undertaken in this chapter. Case NAW uses non-adiabatic wall conditions

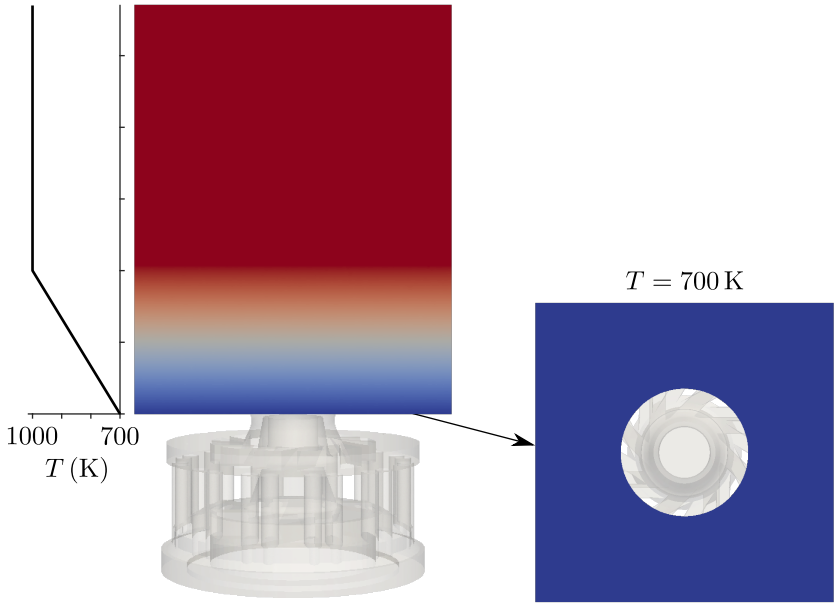

Fig. 8.1 Temperature boundary conditions for the non-adiabatic simulations (NAW and NAF).

Case	AD	NAW	NAF
Wall temperature specified	No	Yes	Yes
Non-adiabatic flamelets	No	No	Yes

Table 8.1 Details of the heat loss effects considered in the simulated cases.

and adiabatic flamelets. Case NAF also uses non-adiabatic wall conditions and the non-adiabatic flamelet approach that is outlined in § 3.5.3 is used. The same four-dimensional look-up table that is described in § 3.5.1 is used for cases AD and NAW. For case NAW, the wall heat loss effects on the temperature field are included when solving for $\widetilde{h}$ through the wall boundary condition in the LES. In addition to this, the heat loss effects at the flamelet level are considered in case NAF, where the normalised enthalpy is included in the look-up table as an additional dimension to integrate the flamelet solutions under a range of heat loss conditions.

All of the walls have no-slip conditions imposed, apart from the walls in the streamwise direction of the extended far-field domain, which have slip conditions imposed. The bottom plane of the combustion chamber is given an isothermal boundary condition of 700 K and the side walls of the combustion chamber have a linear profile up to 40 mm that increases from 700 K to 1000 K; beyond 40 mm, an isothermal temperature of 1000 K is used. These wall boundary conditions are illustrated in Fig. 8.1. The choice of

temperature boundary conditions are guided using the experimental measurements in a previous study on the PRECCINSTA burner (Yin *et al.*, 2017), since no wall temperature measurements are available for this burner[1].

A constant time step of $\Delta t = 0.15\,\mu s$ is used to ensure suitable accuracy for the time derivatives and that the CFL number remains below 0.4 across the whole domain for all three cases. Cases AD, NAW and NAF require around 80, 100 and 60 ms respectively of physical time to allow initial transients to pass out of the domain. The time-averaged statistics are computed using samples collected over 24 ms after the initial transient periods.

8.3 Results

8.3.1 General comparisons

Figure 8.2 shows typical time-averaged statistics comparisons between the three simulations and measurements for the Favre-filtered axial velocity at different heights from the exit of the annular nozzle. The axial velocity and mixture fraction profiles are shown in Figs. 8.2a and 8.2b respectively. It is seen in Fig. 8.2a that all three simulations show the same variation in the near-field, with some under prediction in the peak axial velocity at $x = 5$ mm and 10 mm. Further downstream, cases AD and NAW show the same trend, whereas there is a small shift of the peaks away from the centreline for case NAF. This suggests that when the heat loss effects are included in the canonical model, i.e., premixed flamelets, the opening angle of the swirl flame becomes slightly larger due to weakened reaction rates in the inner shear layer, which is shown later in this section. The results at $x = 20$ mm and 30 mm suggest that the width of the IRZ at this location is over predicted for all three cases. However, the velocity variation is captured well at $x = 60$ mm in the LES showing very good agreement with the measurements. For the mixture fraction fields, by contrast, all three simulations give similar predictions at all axial positions in Fig. 8.2b, suggesting that the overall mixing field is captured well in the LES regardless of the heat loss modelling. All three cases marginally over predict the mixture fraction at all streamwise locations. On the whole, the change in conditions for the three cases does not affect the axial velocity and mixture fraction fields.

The computed and measured temperature profiles are compared in Figs. 8.3a and 8.3b for the mean and resolved r.m.s. values respectively. For the near-field positions

[1]Personal communication with M. Stöhr of DLR Stuttgart.

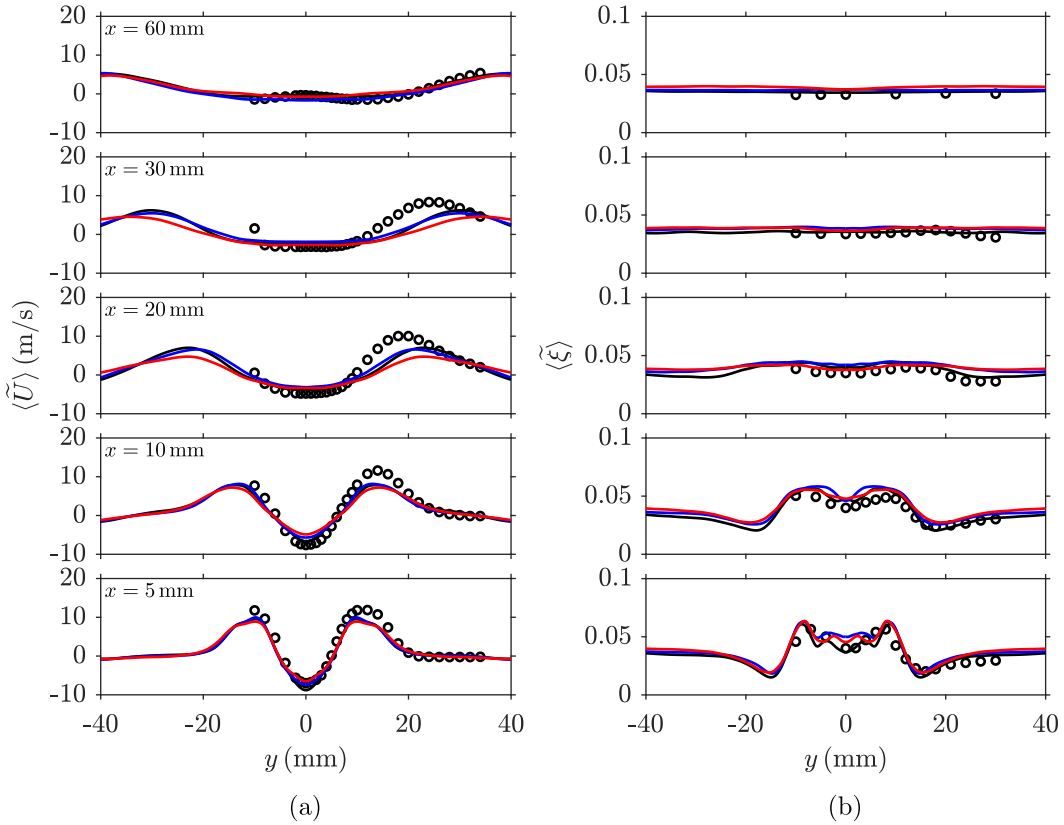

Fig. 8.2 Comparisons of the time-averaged (a) axial velocity and (b) mixture fraction between the measurements (Meier *et al.*, 2006; Weigand *et al.*, 2006) (symbols) and the computations (lines), where the latter results are azimuthally averaged. The computations are cases AD (——), NAW (——) and NAF (——).

$x = 5\,\text{mm}$ and $10\,\text{mm}$ in Fig. 8.3a, the mean temperature is over predicted by 20 % to 30 % in case AD for large radial positions ($|y| > 20$ mm) when approaching the wall, as adiabatic wall boundary conditions are imposed. The over predictions of the near-wall temperature for case AD are also seen in the r.m.s. temperature profiles in Fig. 8.3b. By contrast, the predictions given by NAW and NAF improve significantly in this region showing good agreement with the experimental data. This suggests that the temperature profiles specified on the combustion chamber dump plane and side wall are satisfactory. The temperature at $x = 5\,\text{mm}$ and $10\,\text{mm}$ along the centreline is under predicted by 13 % and 4 % respectively for case AD. However, significant decreases are seen in the centreline temperature at these two locations for cases NAW and NAF, due to the presence of non-adiabatic effects. This can also be seen in the r.m.s. profiles for cases NAW and NAF, as shown in Fig. 8.3b. This under prediction of the centreline temperature in the non-adiabatic cases NAW and NAF indicates an over predicted flame lift-off height. In addition, the temperature in the jet regions in the near-field at $x = 5\,\text{mm}$ are under

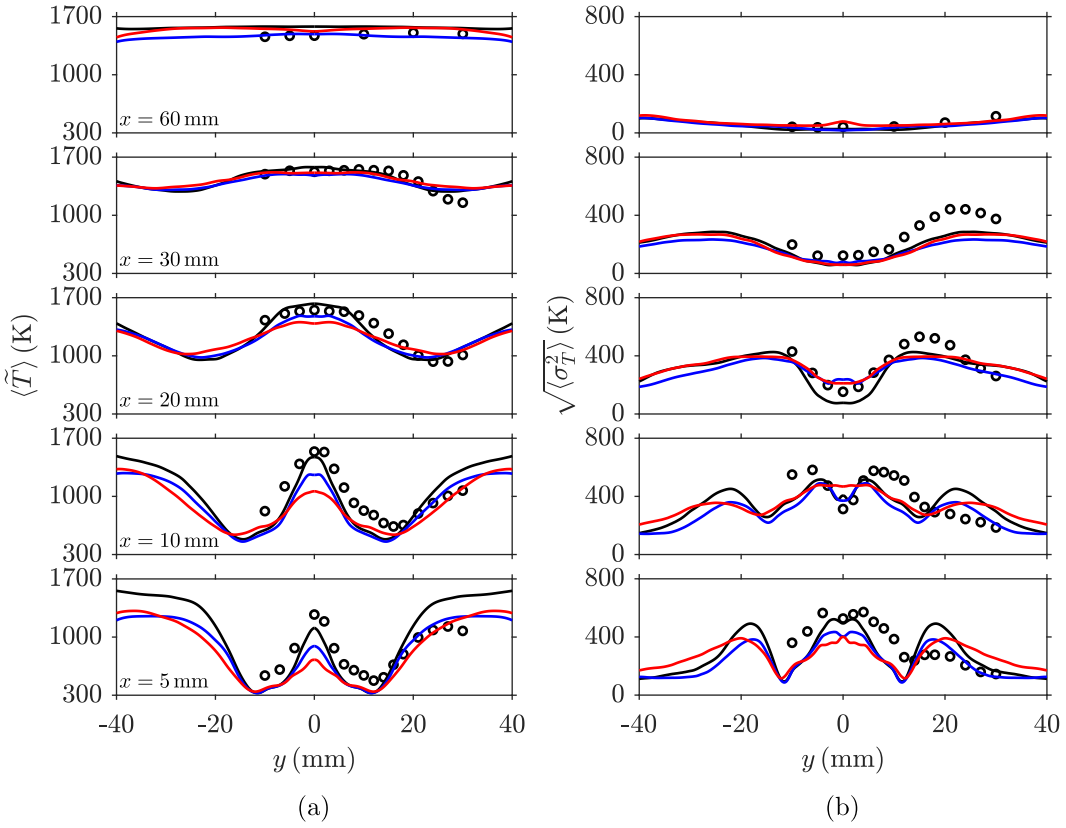

Fig. 8.3 Comparisons of the time-averaged (a) mean and (b) r.m.s. temperature between the measurements (Meier *et al.*, 2006; Weigand *et al.*, 2006) (symbols) and the computations (lines), where the latter results are azimuthally averaged. The computations are cases AD (——), NAW (——) and NAF (——).

predicted for all three cases. Therefore, the inclusion of non-adiabatic conditions severely affects the flame root and its position, which dictates the overall stability and eventual blow-off behaviours of this flame (Stöhr *et al.*, 2011*a*). In the regions further downstream from $x = 20\,\mathrm{mm}$, the profiles for all three cases are similar and hence, the non-adiabatic modelling only significantly affects the flame in the near-field around the flame root region.

Instantaneous snapshots of the filtered reaction rate of the progress variable for the three LES cases are shown in Fig. 8.4. It is shown in Fig. 8.4a that the flame appears to be thinner and more stable for case AD, whereas the reactions are distributed over a larger region for case NAW in Fig. 8.4b. In addition, the flames for these two cases have an established flame root with high values of the filtered reaction rate. Both of these observations are seen in the time-averaged fields in Fig. 8.5. The reaction rate values are higher in case NAW in comparison to case AD because the local mixture fractions for case NAW are slightly higher and closer to stoichiometry, specifically in

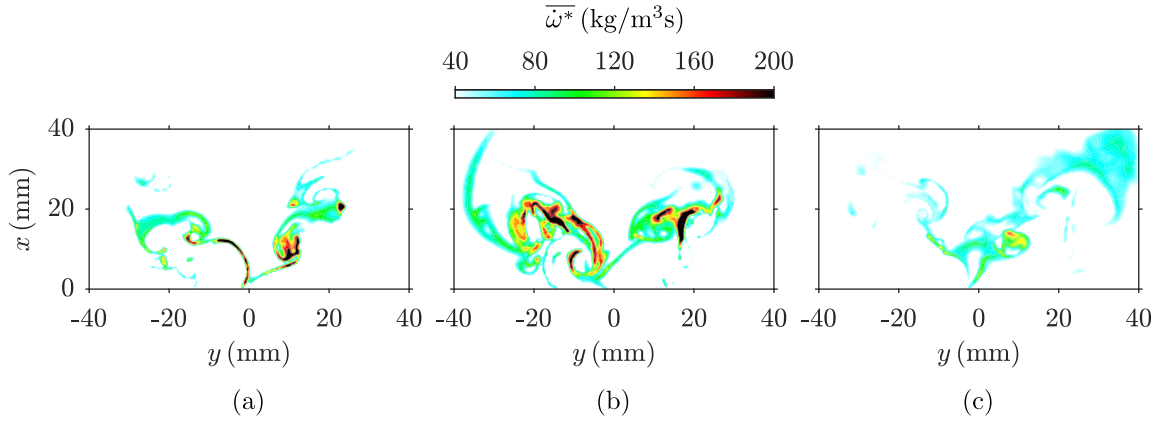

Fig. 8.4 Filtered reaction rate fields for cases AD (a), NAW (b) and NAF (c) in the x–y mid-plane.

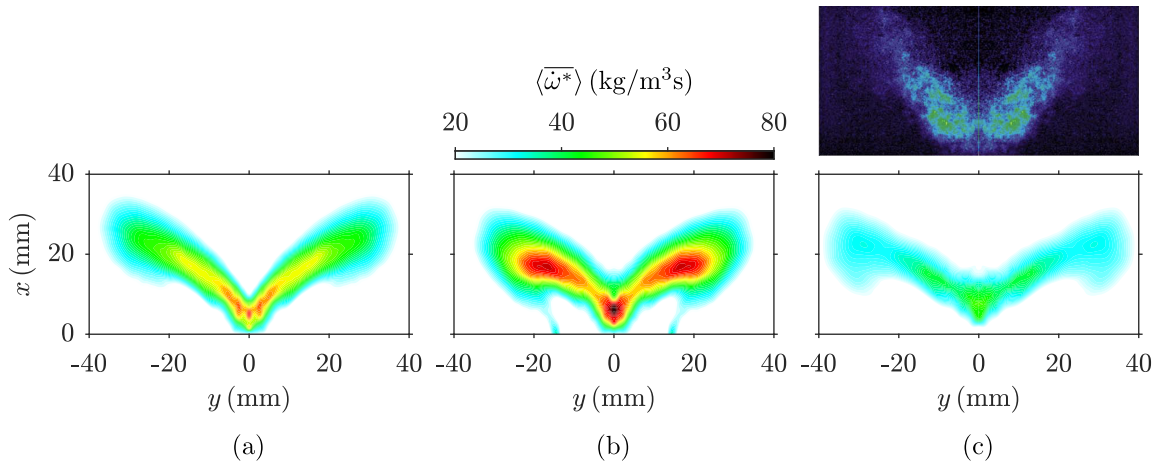

Fig. 8.5 Time- and azimuthally-averaged filtered reaction rate fields for cases AD (a), NAW (b) and NAF (c) in the x–y mid-plane. The image above is the averaged CH-PLIF image (Weigand *et al.*, 2006).

the regions further away from the centreline at $|y| \approx 20\,\text{mm}$ (see Fig.8.2b). However, the averaged field for case NAW shows that the flame stabilises on the wall of the annular air nozzle (2 mm below $x = 0$ in Fig. 8.5) and a different flame ('M' shape) is observed in comparison to the other two cases. This behaviour must be avoided because it provides an additional unphysical anchoring point for the flame, since the flame has a 'V' shape, as seen in the CH-PLIF image at the top of Fig. 8.5. Thus, the conditions used in the modelling approach for case NAW cannot be used for further investigation on flame blow-off behaviours, despite the improvements obtained for the temperature in the near-wall regions. The instantaneous and time-averaged filtered reaction rates for case NAF, as seen in Figs. 8.4c and 8.5c respectively, show that there is a significant decrease in the local values of the reaction rate. This is caused by including the heat loss effects in the flamelet reaction rate in the canonical model, as shown earlier in Figs. 3.4 and 3.5.

The average reaction rate values at the flame root for this case are approximately 50 % smaller than the values for the adiabatic flamelet cases, as well as along the inner shear layer. The time-averaged contour also shows that the flame root is in a higher position in comparison to cases AD and NAW. The flame root for case NAF is analysed in further detail next.

8.3.2 Lift-off height and heat release rate

Case NAF is analysed and compared in more detail with case AD, in order to gain insights into the role of including heat loss on the stabilisation of the flame. The lift-off height variation over a period of 45 ms is shown in Fig. 8.6 for cases AD and NAF. It is demonstrated that the lift-off height varies considerably across the sample, but only short lift-off events (< 5 ms) can be seen in Fig. 8.6 for case NAF. Therefore, a sample of case AD is directly compared with case NAF; the last 45 ms in Fig. 7.14b is included in Fig. 8.6, as the sample does not show a lift-off event nor any significant changes in the heat release rate. The average lift-off height in Fig. 8.6 is approximately 8.3 mm for case NAF, which is 2.3 mm higher than the experimentally observed value (Weigand *et al.*, 2006). The mean lift-off height is significantly higher, since it is shown in Fig. 8.6 that the lift-off height reaches larger values beyond 10 mm at least once every 5 ms. The histograms of the lift-off heights for the two cases in Fig. 8.6 are shown in Figs. 8.7a and 8.7b for cases AD and NAF respectively. It is shown that the lift-off height for case AD varies between 3–14 mm, whereas it ranges between 2.5–17 mm for case NAF. Moreover, it is seen in Fig. 8.7b that the bins in the range of 6–11 mm have a high number of counts, whereas the bins for the lift-off height in the range of 5–9 mm have a high number of counts for case AD. Therefore, the flame is more unstable when non-adiabatic effects are included, as the flame root position varies more across the time series in Fig. 8.6. This movement and frequent disappearance of the flame root is reported in the study by Stöhr *et al.* (2011*a*).

The variation of the volume integrated heat release rate is shown in Fig. 8.8 for cases AD and NAF. It is demonstrated in Fig. 8.6 that the lift-off height approaches high values between 10–15 ms and 25–30 ms for case NAF. In both of these intervals, the heat release rate decreases by approximately 4 kW. A similar decrease in case AD is not seen in Fig. 8.8, but it is seen once within the larger sample in Fig. 7.14a when the flame experiences a weaker burning mode with an established flame root, i.e., a minor change in the lift-off height is seen. As with the lift-off height time series, the heat release rate varies considerably more for case NAF. This is also seen in the histograms, which are

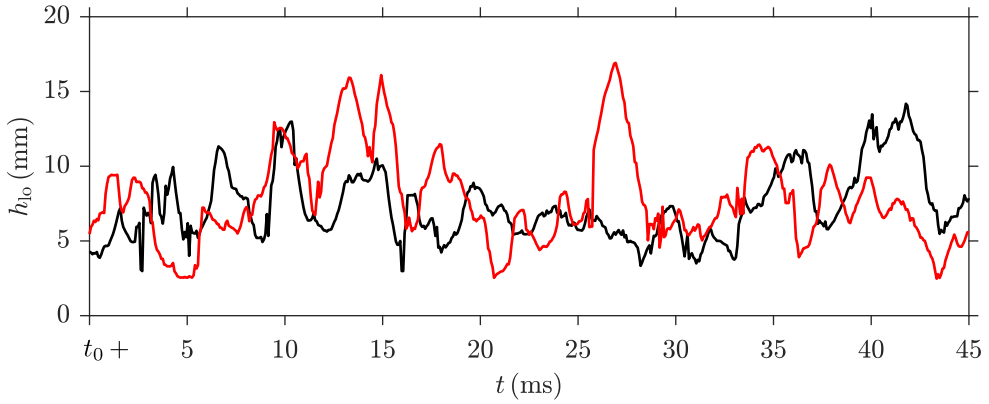

Fig. 8.6 Time series of the lift-off height for cases AD (——) and NAF (——), where $t_0 = 359$ ms and 84 ms are respectively for cases AD and NAF.

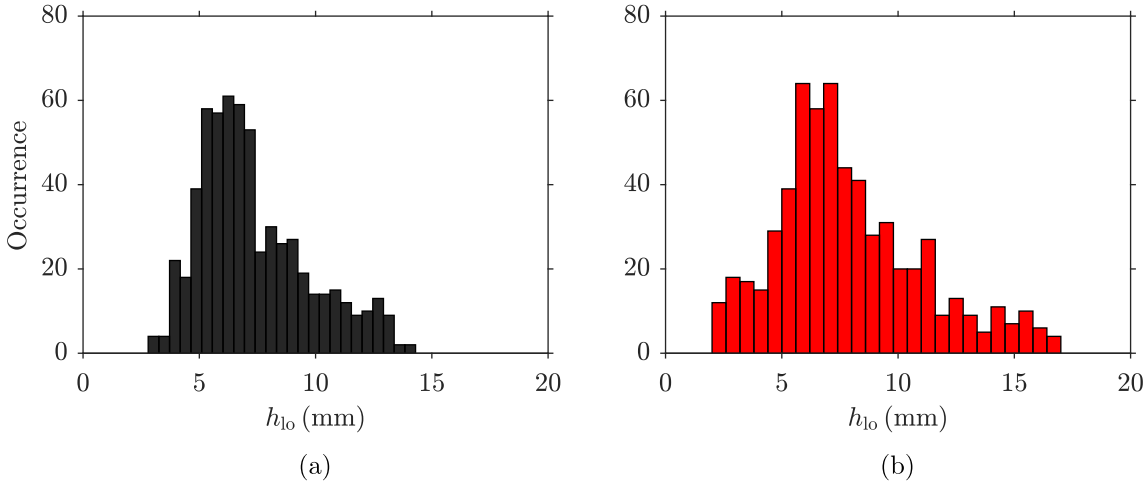

Fig. 8.7 Histograms of the lift-off height for the time series shown in Fig. 8.6 for (a) case AD and (b) case NAF.

shown in Fig. 8.9. The histogram for case NAF in Fig. 8.9b shows that the volume integrated heat release rate is between 3.1–8.4 kW, whereas the volume integrated heat release rate for case AD is between 5.4–8.8 kW, as seen in Fig. 8.9a. There are also a large number of counts between 7–7.4 kW for case AD, which is close to the thermal power of 7.6 kW that is stated by Weigand *et al.* (2006). The mean value for case NAF is approximately 5.5 kW, which is due to the reduced reaction rates that are seen in Figs. 8.4 and 8.5 that are within the flamelet table and therefore, this causes the thermal power to be reduced. It is of interest to determine how the heat loss through the enthalpy deficit in the look-up table varies when the structure of the flame changes. This is analysed next for when the flame has an established flame root and when it is as its maximum lift-off height in Fig. 8.6.

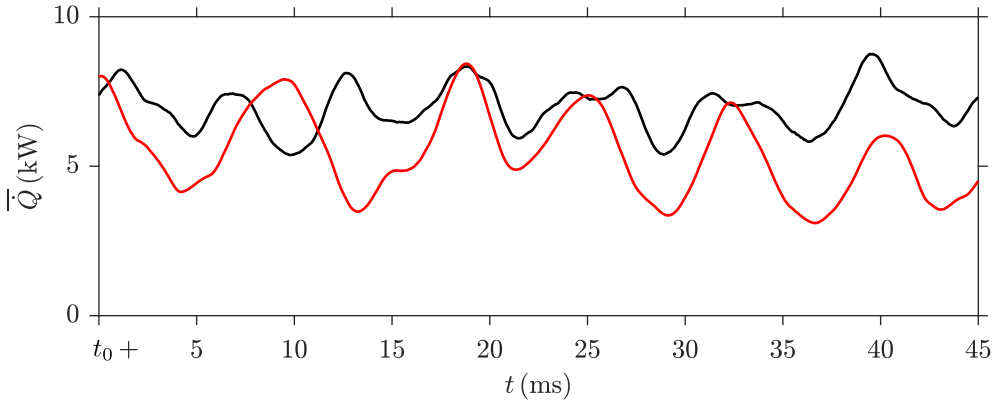

Fig. 8.8 Time series of the volume integrated heat release rate for cases AD (——) and NAF (——), where $t_0 = 359$ ms and 84 ms are respectively for cases AD and NAF.

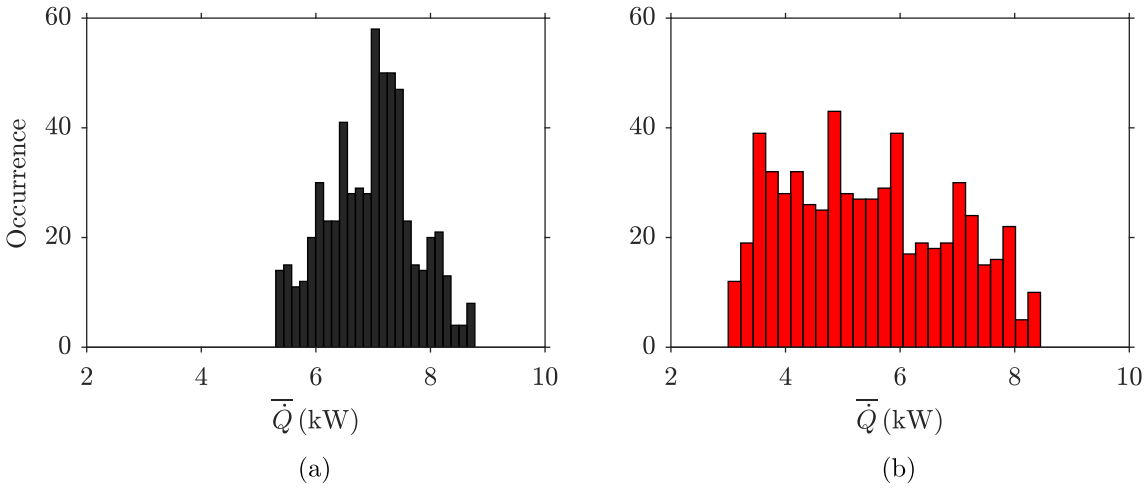

Fig. 8.9 Histograms of the volume integrated heat release rate for the time series shown in Fig. 8.8 for (a) case AD and (b) case NAF.

8.3.3 Enthalpy deficit within the flame

The instantaneous snapshot of the filtered reaction rate is shown in Fig. 8.10a, which is the same as the contour shown in Fig. 8.4c, where the flame has an established flame root. The normalised filtered enthalpy deficit $\Delta\widetilde{h}^*$ for the same instantaneous snapshot is shown in Fig. 8.10b. This is defined as

$$\Delta\widetilde{h}^* = \widetilde{h}^* - 1 = \frac{h - h_{\min}(\xi, c)}{h_{\mathrm{ad}}(\xi, c) - h_{\min}(\xi, c)} - 1\,, \tag{8.1}$$

where values of $\Delta\widetilde{h}^* = -1$ and $\Delta\widetilde{h}^* = 0$ signify maximum heat loss and adiabatic conditions respectively. It is shown that the enthalpy deficit is approximately 10 % near the flame root, which corresponds to an approximate 25 % decrease in the reaction rate

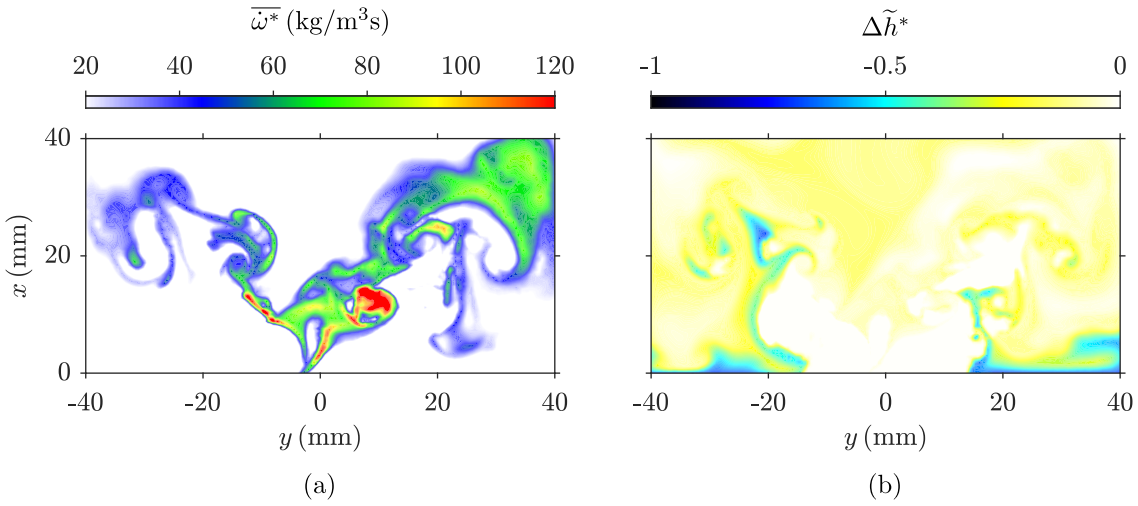

Fig. 8.10 Instantaneous snapshots of the (a) filtered reaction rate (the same as Fig. 8.4c) and (b) normalised enthalpy deficit at an arbitrarily chosen time when the flame has an established flame root.

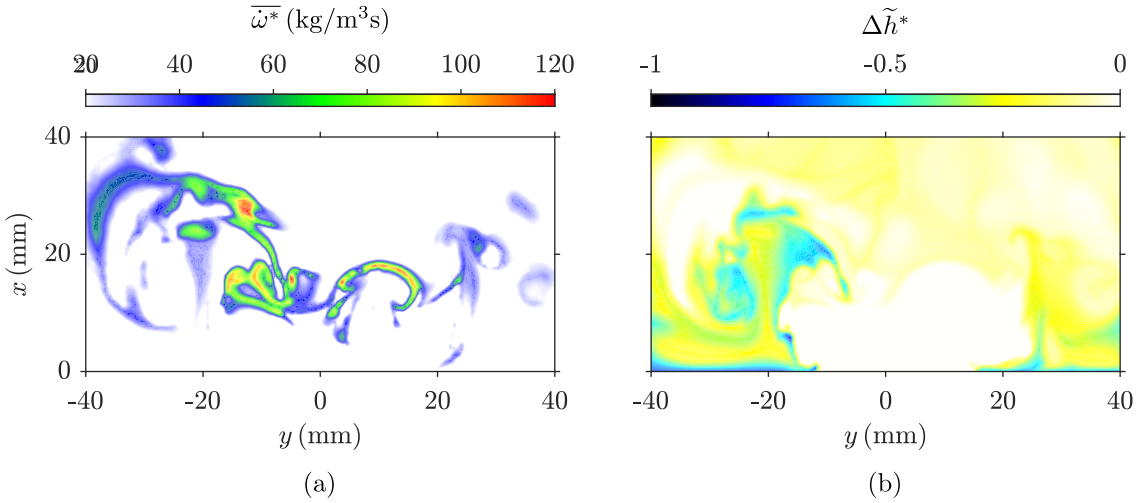

Fig. 8.11 Instantaneous snapshots of the (a) filtered reaction rate and (b) normalised enthalpy deficit when the lift-off height in Fig. 8.6 is at its maximum at $t = t_0 + 26.925\,\text{ms}$.

and is due to the reduced heat release. Further downstream in the region of $y = -15\,\text{mm}$, it is seen in Fig. 8.10a that the reaction rate is small within a large coherent structure. Within this region, the enthalpy deficit is approximately 40 %, as seen in Fig. 8.10b. This suggests that the reaction that takes place within the vortex centres that are convected downstream along the shear layer are susceptible to heat loss. These large heat loss regions are seen to be within the ORZ, due to the lower temperature boundary conditions applied to the walls. At $x > 20\,\text{mm}$ and $y > 20\,\text{mm}$, higher reaction rate regions are present with enthalpy deficits of less than 10 %, as seen in Fig. 8.10.

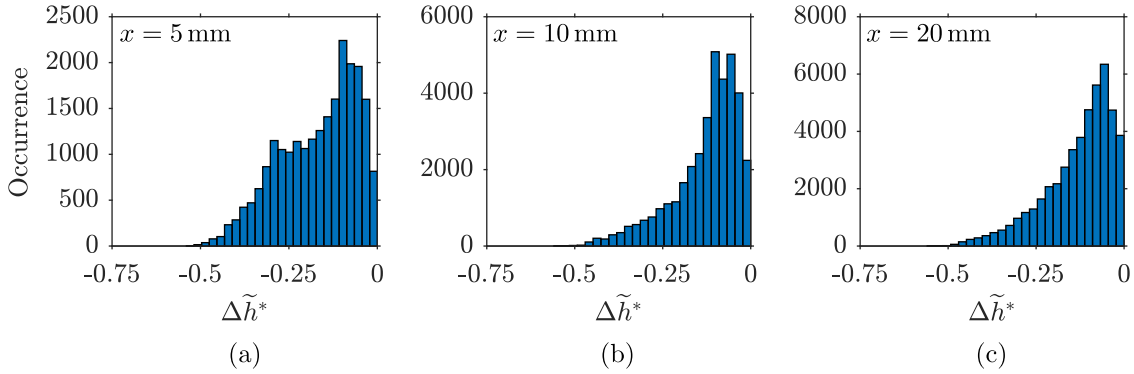

Fig. 8.12 Histograms of the normalised enthalpy deficit within the flame ($\overline{\dot{\omega}^*} > 5\,\mathrm{kg/m^3s}$) for the same time as Fig. 8.10 on planes normal to the streamwise direction at (a) $x = 5\,\mathrm{mm}$, (b) 10 mm and (c) 20 mm.

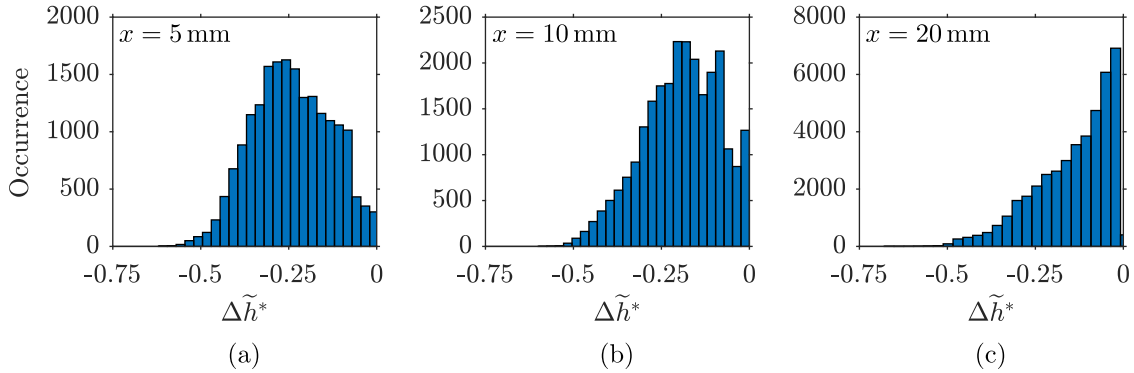

Fig. 8.13 Histograms of the normalised enthalpy deficit within the flame ($\overline{\dot{\omega}^*} > 5\,\mathrm{kg/m^3s}$) for the same time as Fig. 8.11 on planes normal to the streamwise direction at (a) $x = 5\,\mathrm{mm}$, (b) 10 mm and (c) 20 mm.

The shape of the flame with an established flame root is compared to the flame when it is as its maximum observed lift-off height in Fig. 8.6. The instantaneous snapshots for the filtered reaction rate and enthalpy deficit are shown in Figs. 8.11a and 8.11b respectively. The filtered reaction rate values are significantly smaller in Fig. 8.11a than in Fig. 8.10a. It is shown that the enthalpy deficit is higher around the flame in Fig. 8.11b, where the highest value is approximately 60 %. Furthermore, it is seen that the leading edge of the high enthalpy deficit region at $x = 10\,\mathrm{mm}$ on the left-hand side of Fig. 8.11b is within the flame. At this region, the reaction rate values in Fig. 8.11a are close to zero and therefore, the non-adiabatic flamelet model may account for some local extinction within the flame due to heat loss.

Based on the observations in Figs. 8.10 and 8.11, it is suggested that the enthalpy deficit within the flame increases when the flame does not have an established flame root and when its lift-off height increases. Only the results in the x–y mid-plane are shown

in Figs. 8.10 and 8.11 and therefore, the results are missing the full three-dimensional features of the flame. The histograms of the enthalpy deficit on planes normal to the streamwise direction are shown in Figs. 8.12 and 8.13 for the locations $x = 5\,\text{mm}$, $10\,\text{mm}$ and $20\,\text{mm}$, which correspond to Figs. 8.10 and 8.11 respectively. To ensure that the enthalpy deficit in the flame is investigated, only the enthalpy deficit in the regions with $\overline{\dot{\omega}^*} > 5\,\text{kg/m}^3\text{s}$ is used to construct the histograms. When the flame has an established flame root, it is shown that for all three locations in Fig. 8.12 that the enthalpy deficit is predominantly within $5\,\% < \Delta\widetilde{h}^* < 10\,\%$. However in the event when the lift-off height is high, the enthalpy deficit in the near-field region of $x = 5\,\text{mm}$ is within the range $15\,\% < \Delta\widetilde{h}^* < 30\,\%$, as seen in Fig. 8.13a. At $x = 10\,\text{mm}$, the enthalpy deficit decreases and is within the range $10\,\% < \Delta\widetilde{h}^* < 20\,\%$, as seen in Fig. 8.13b. This suggests that the flame is vulnerable to a high heat loss near where the flame root is expected to be when the flame experiences some lift-off. Further downstream at $x = 20\,\text{mm}$, the histogram in Fig. 8.13c is very similar to when then flame has a stable root, as seen in Fig. 8.13a, and the heat loss is smaller. Therefore, this analysis does comply with the initial observations made in Figs. 8.10 and 8.11. Further analysis needs to be undertaken with a longer time sample (similar to Fig. 7.14) and of a case where the complete blow-off of the flame is captured, in order to determine the role of heat loss with flame blow-off.

8.4 Summary

Two simulations of a swirl-stabilised flame close to blow-off are studied using fixed wall temperature boundary conditions and one simulation also uses non-adiabatic flamelets. The simulations are compared to the adiabatic simulation that is previously studied in Chapter 7, and the experimental data. The axial velocity and mixture fraction statistics are unaffected by the inclusion of heat loss, but some differences are seen in the temperature statistics comparisons. Cases NAW and NAF give improvements with the temperature in the near-wall regions, as case AD over predicts the temperature, due to the use of adiabatic walls. However, a change in flame shape is seen for case NAW, as the flame has an 'M' shape and differs from the observed 'V' shape flame in the experiment. In addition, cases NAW and NAF show under predictions in the average centreline temperature at the near-field and indicate that the flame root height is over predicted. The time series of the lift-off height and the volume integrated heat release rate shows that flame in case NAF is more dynamic in comparison to case AD. It is also suggested that the inclusion of non-adiabatic flamelets does affect the stabilisation of

the flame. It is observed that the flame in case NAF is vulnerable to a higher enthalpy deficit when the flame root is not present and experiences some lift-off.

Chapter 9

Final Remarks

This work has investigated the applicability of the combustion modelling framework to bluff body flames that are open to atmospheric conditions or enclosed within a combustion chamber. A swirl-stabilised flame close to the lean extinction limit is also investigated with and without heat loss within the modelling framework. The combustion closure is a presumed PDF closure for premixed combustion and a presumed joint PDF closure for partially premixed combustion. The simulations are undertaken within the LES framework. Comparisons with the experimental measurements for the bluff body cases are seen to be good, where no severe discrepancies between the simulations and measurements are seen. The recirculation zones in the bluff body flame simulations are accurately captured and the modelling showed a good sensitivity to changes in the inlet turbulent intensity and the equivalence ratio of the fuel–air mixture. Simulations of the lean flame in a gas turbine model combustor also show good comparisons with the experimental data, where one simulation uses a modified combustion closure with non-adiabatic flamelets. The specific conclusions for each study, along with some suggestions for further work are outlined in this chapter.

9.1 Conclusions

In Chapter 5, statistics from the LES of a stable flame are compared with measurements, where the bluff body base and flame are exposed to atmospheric conditions. The recirculation zone and inner shear layers are accurately captured in the LES and the length of the flame is slightly over predicted. The filtered reaction rate values are highest near the bluff body base within a thin flame and the turbulent kinetic energy has a peak value within the flame. The filtered reaction rate values then decrease when

moving downstream with a broadening of the flame, which suggests there is multi-regime combustion. This is ascertained by the turbulent kinetic energy distribution, as it increases from the reactant to product side of the flame, which suggests a shift from the corrugated flamelets regime to the thin reaction zones regime of turbulent premixed combustion. Additional comparisons are shown with two confined bluff body stabilised flames, where one flame experienced additional incoming turbulence. The main difference between the open and confined flames is observed to be the relative positioning and evolution of the shear layer and the flame brush.

Chapter 6 contains the analyses of confined bluff body flames with different equivalence ratios and turbulence intensities. It is observed that the recirculation zone length is influenced by the turbulence intensity, heat release and the interactions between turbulence and combustion. The recirculation zone length in isothermal flows decreases when the turbulence intensity is increased. This is also the case for reacting flows, but the variation of the recirculation zone length is found to be non-monotonic when the equivalence ratio is increased towards the near-stoichiometric region. The competing effects of dilatation and turbulence lead to changes in the radial pressure forces acting on the recirculation zone and causes the non-monotonic variation in the recirculation zone length for reacting flows. The radial forces influence the relative positioning of the shear layer and flame. This yields the variation in the levels of turbulence–combustion interactions and their influences on the radial force balance. The near-field wake containing the recirculation zone is governed by the momentum transfer to and from the zone, which is related to the forces acting on this zone. The surface-averaged wall pressure and eddy viscosity at the rear stagnation point emerge as two key quantities, which are influenced by the turbulence intensity, heat release and turbulence–chemistry interactions. The derivation of a scaling relation for the recirculation zone length is undertaken based on these observations. The scaling relation is found to work well for premixed flames that are stabilised behind a bluff body with and without confinement and also for flames stabilised behind a backward facing step.

A simulation of a flame close to the lean blow-off limit is studied in Chapter 7, where the gas turbine model combustor is the configuration developed in the studies by Duan *et al.* (2004), Meier *et al.* (2005, 2006) and Weigand *et al.* (2006) at DLR. The time-averaged statistics for the velocity, mixture fraction and temperature in the simulation show good comparisons with the experimental measurements. Further investigation of the flame stabilisation resulted in identifying two distinct stages for the evolution of the flame root. In the first stage, the flame is anchored by its stable and robust root near the

fuel nozzle and the flame has a 'V' shape. It is observed in the LES that the entrainment of reactant mixtures outside of the flammability limits into the flame region within the IRZ causes the flame root to be extinguished and initiates the lift-off event. When the flame is experiencing lift-off, this is referred to as the second stage. These two stages are observed to switch from one to the other, as observed in the experiment and with an extended time sample from the simulation. Analysis of the extended time sample showed that the lift-off events are initiated by a combination of the presence of rich mixtures at the flame root and a mixture fraction dissipation rate that exceeds the quenching value. It is also seen that a weaker burning mode of the flame exists when rich mixtures are present but the dissipation rate is small and the flame retains its stabilisation root under such conditions. The switching between stable burning and lift-off events is caused by the unsteady fuel–air mixing phenomena, which are related to the large-scale eddy motions and small-scale mixing processes at the flame root.

Two additional simulations with non-adiabatic modelling are studied in Chapter 8 with the same conditions as the flame studied in Chapter 7. Both simulations use fixed wall temperature boundary conditions and one of the simulations also includes non-adiabatic flamelets within the combustion closure. The two simulations are compared against the baseline adiabatic simulation analysed in Chapter 7 and the experimental data. The axial velocity and mixture fraction statistics are unaffected by the non-adiabatic effects, but some differences are seen for the temperature statistics. The two non-adiabatic simulations gave improvements for the temperature fields in the near-wall regions, due to the inclusion of non-adiabatic wall treatment. However, both non-adiabatic simulations under predicted the average centreline temperature in the near-field, which suggests that the flame root height is over predicted in these cases. A change in flame shape is seen for the case that uses only non-adiabatic walls, where the flame becomes anchored to the walls of the annular air exit into the combustion chamber. It is also suggested that the heat loss effects do play a role with the stabilisation of the flame by analysing the time series of the lift-off height and the volume integrated heat release rate of the non-adiabatic flamelet case. A higher enthalpy deficit is seen in the near-field regions when the flame root is not present and experiencing some lift-off, suggesting that the flame is more dynamic when including heat loss.

9.2 Suggested future work

The cases that have been analysed have proved that the combustion modelling framework is robust and accurate. The stabilisation mechanisms in both bluff body and swirl-stabilised flames have been captured for various equivalence ratios and turbulence intensities. This provides motivation to extend this work and the following recommendations are proposed:

1. It is expected that including swirl on the reactant flow may not change the proposed scaling relation for the following reason. An approximate radial pressure gradient is $\partial p/\partial r \simeq \rho U_\theta^2/r$ in a flow with a swirl velocity U_θ. Hence, the wall pressure p_w in Eq. (6.9) will increase with the swirl velocity or swirl number. This may lead to shorter recirculation zones, as observed in numerous previous studies, e.g., the works of Gupta *et al.* (1984) and Minamoto *et al.* (2015). However, the exact relationship between p_w and the swirl number in reacting flows with substantial heat release requires further investigation. Furthermore, scaling including the Lewis number may also be necessary and will also be explored.

2. The extended time sample for the lift-off height and heat release rate did not show highly transient events with the time scales that are quoted by Stöhr *et al.* (2011*a*). Indeed, multiple short lift-off events and weaker burning modes are captured in the simulations, but the duration of those are not of the size quoted in the experiments; these lasted between 100–150 ms. It is therefore of interest to run additional simulations for similar time samples using lower fuel flow rates, with the aim of capturing the complete blow-off event, and longer lift-off events and weaker burning modes, in order to gaining further physical insights into the flame stabilisation.

3. Non-premixed flame theory is applied to the flame root in the analysis shown in Chapter 7. Since the flame is partially premixed and swirl-stabilised, it is of interest to apply premixed flame theory to investigate the stabilisation of the flame. This includes investigating the flame consumption and displacement speeds, and using the progress variable gradient across the flame as a length scale. The analysis will involve observing the balance between the mass burning rate and the incoming reactant flux, and provide insights into the displacement speed of the flame during transient events.

4. The look-up library that is used for the non-adiabatic formulation of the combustion closure is bounded by using a maximum value for the heat loss factor. This means

that the minimum reaction rate across the flammability range is not the same. It is of interest to improve the construction of the flamelet look-up table by using a minimum value of the reaction rate to bound the table and improve the resolution of the table in the near-stoichiometric regions. The non-adiabatic flame case will be simulated again to obtain an improved lift-off height prediction.

5. The same form of the energy equation is used for the adiabatic and non-adiabatic flamelet closures used in this work. It is of interest to explore introducing a radiation model into the energy equation, since the filtered energy equation solved for both flamelet closures contains no heat loss terms.

6. Predicting the production of minor species, such as CO, is essential for combustion models. The combustion modelling used in this work has previously overestimated the minor species for premixed and partially premixed flames (Chen, 2017; Langella, 2016). Thus, it is of interest to develop an improved approach to capture the distribution of intermediate species. The prediction of pollutants from aero engine systems is important for the design and development of future systems.

References

Abdel-Gayed, R. G., Bradley, D., Hamid, M. N. & Lawes, M. 1984 Lewis number effects on turbulent burning velocity. *Symp. (Int.) Combust.* **20** (1), 505–512.

Abdel-Gayed, R. G., Bradley, D. & Lau, A. K. C. 1988 The straining of premixed turbulent flames. *Symp. (Int.) Combust.* **22** (1), 731–738.

Abdel-Gayed, R. G., Bradley, D. & Lung, F. K.-K. 1989 Combustion regimes and the straining of turbulent premixed flames. *Combust. Flame* **76** (2), 213–218.

Ahmed, I. & Swaminathan, N. 2013 Simulation of Spherically Expanding Turbulent Premixed Flames. *Combust. Sci. Technol.* **185** (10), 1509–1540.

Ahmed, I. & Swaminathan, N. 2014 Simulation of turbulent explosion of hydrogen-air mixtures. *Int. J. Hydrogen Energy* **39** (17), 9562–9572.

Ahmed, U., Doan, N. A. K., Lai, J., Klein, M., Chakraborty, N. & Swaminathan, N. 2018 Multiscale analysis of head-on quenching premixed turbulent flames. *Phys. Fluids* **30**, 105102.

Akselvoll, K. & Moin, P. 1996 Large-eddy simulation of turbulent confined coannular jets. *J. Fluid Mech.* **315** (387–411), 387.

Allen, R. C. 2009 *The British Industrial Revolution in Global Perspective*. Cambridge, UK: Cambridge University Press.

Amzin, S., Swaminathan, N., Rogerson, J. W. & Kent, J. H. 2012 Conditional moment closure for turbulent premixed flames. *Combust. Sci. Technol.* **184** (10–11), 1743–1767.

Anand, M. S., Zhu, J., Connor, C. & Razdan, M. K. 1999 Combustor Flow Analysis Using an Advanced Finite-Volume Design System. In *Vol. 2: Coal, Biomass and Alternative Fuels; Combustion and Fuels; Oil and Gas Applications; Cycle Innovations*. Indianapolis: ASME. Turbo Expo: Power for Land, Sea, and Air.

Anselmo-Filho, P., Hochgreb, S., Barlow, R. S. & Cant, R. S. 2009 Experimental measurements of geometric properties of turbulent stratified flames. *Proc. Combust. Inst.* **32** (2), 1763–1770.

Bai, X.-S. & Fuchs, L. 1994 Modelling of turbulent reacting flows past a bluff body: assessment of accuracy and efficiency. *Comput. Fluids* **23** (3), 507–521.

Balachandran, R., Ayoola, B. O., Kaminski, C. F., Dowling, A. P. & Mastorakos, E. 2005 Experimental investigation of the non linear response of turbulent premixed flames to imposed inlet velocity oscillations. *Combust. Flame* **143** (1–2), 37–55.

Barlow, R. S. & Frank, J. H. 1998 Effects of turbulence on specific mass fractions in methane/air jet flames. *Symp. (Int.) Combust.* **27** (1), 1087–1095.

Barlow, R. S., Meares, S., Magnotti, G., Cutcher, H. & Masri, A. R. 2015 Local extinction and near-field structure in piloted turbulent CH4/air jet flames with inhomogeneous inlets. *Combust. Flame* **162** (10), 3516–3540.

Barlow, R. S., Wang, G.-H., Anselmo-Filho, P., Sweeney, M. S. & Hochgreb, S. 2009 Application of Raman/Rayleigh/LIF diagnostics in turbulent stratified flames. *Proc. Combust. Inst.* **32** (1), 945–953.

Batchelor, G. K. 1953 *The Theory of Homogeneous Turbulence*. Cambridge, UK: Cambridge University Press.

Bauerheim, M., Staffelbach, G., Worth, N. A., Dawson, J. R., Gicquel, L. Y. M. & Poinsot, T. 2015 Sensitivity of LES-based harmonic flame response model for turbulent swirled flames and impact on the stability of azimuthal modes. *Proc. Combust. Inst.* **35** (3), 3355–3363.

Benard, P., Lartigue, G., Moureau, V. & Mercier, R. 2019 Large-Eddy Simulation of the lean-premixed PRECCINSTA burner with wall heat loss. *Proc. Combust. Inst.* **37** (4), 5233–5243.

Benim, A. C., Iqbal, S., Meier, W., Joos, F. & Wiedermann, A. 2017 Numerical investigation of turbulent swirling flames with validation in a gas turbine model combustor. *Appl. Therm. Eng.* **110**, 202–212.

Bilger, R. W. 1975 A Note on Favre Averaging in Variable Density Flows. *Combust. Sci. Technol.* **11** (5–6), 215–217.

Bilger, R. W. 1976*a* The Structure of Diffusion Flames. *Combust. Sci. Technol.* **13** (1–6), 155–170.

Bilger, R. W. 1976*b* Turbulent jet diffusion flames. *Prog. Energy Combust. Sci.* **1** (2–3), 87–109.

Bilger, R. W. 1980 Turbulent Flows with Nonpremixed Reactants. In *Turbulent Reacting Flows* (ed. P. A. Libby & F. A. Williams), chap. 3, pp. 65–114. Berlin Heidelberg, Germany: Springer-Verlag.

Bilger, R. W. 1988 The structure of turbulent nonpremixed flames. *Symp. (Int.) Combust.* **22** (1), 475–488.

Bilger, R. W. 1993 Conditional moment closure for turbulent reacting flow. *Phys. Fluids A Fluid Dyn.* **5** (2), 436–444.

Bilger, R. W. 2000 Future progress in turbulent combustion research. *Prog. Energy Combust. Sci.* **26** (4), 367–380.

Bilger, R. W. 2011 The Role of Combustion Technology in the 21st Century. In *Turbul. Combust. Model. Adv. New Trends Perspect.* (ed. T. Echekki & E. Mastorakos), chap. 1, pp. 3–18. Dordrecht, The Netherlands: Springer Netherlands.

Bilger, R. W., Pope, S. B., Bray, K. N. C. & Driscoll, J. F. 2005 Paradigms in turbulent combustion research. *Proc. Combust. Inst.* **30** (1), 21–42.

Bill, R. G. Jr & Tarabanis, K. 1986 The Effect of Premixed Combustion on the Recirculation Zone of Circular Cylinders. *Combust. Sci. Technol.* **47** (1–2), 39–53.

Birch, A. D., Brown, D. R., Dodson, M. G. & Thomas, J. R. 1979 Studies of flammability in turbulent flows using laser Raman spectroscopy. *Symp. (Int.) Combust.* **17** (1), 307–314.

Blint, R. J. 1986 The Relationship of the Laminar Flame Width to Flame Speed. *Combust. Sci. Technol.* **49** (1–2), 79–92.

Boger, M., Veynante, D., Boughanem, H. & Trouvé, A. 1998 Direct numerical simulation analysis of flame surface density concept for large eddy simulation of turbulent premixed combustion. *Symp. (Int.) Combust.* **27** (1), 917–925.

Borghi, R 1988 Turbulent combustion modelling. *Prog. Energy Combust. Sci.* **14** (4), 245–292.

Borghi, R. 1990 Turbulent Premixed Combustion: Further Discussions on the Scales of Fluctuations. *Combust. Flame* **80** (3-4), 304–312.

BP 2018 Statistical Review of World Energy (67th edition).

BP 2019 Energy Outlook (2019 edition).

Bradbury, L. J. S. 1976 Measurements with a pulsed-wire and a hot-wire anemometer in the highly turbulent wake of a normal flat plate. *J. Fluid Mech.* **77** (3), 473–497.

Bradley, D. 1992 How fast can we burn? *Symp. (Int.) Combust.* **24** (1), 247–262.

Bradley, D., Gaskell, P. H. & Gu, X. J. 1998 The mathematical modeling of liftoff and blowoff of turbulent non-premixed methane jet flames at high strain rates. *Symp. (Int.) Combust.* **27** (1), 1199–1206.

Bradley, D., Gaskell, P. H. & Lau, A. K. C. 1990 A mixedness-reactedness flamelet model for turbulent diffusion flames. *Symp. (Int.) Combust.* **23** (1), 685–692.

Bray, K., Domingo, P. & Vervisch, L. 2005 Role of the progress variable in models for partially premixed turbulent combustion. *Combust. Flame* **141** (4), 431–437.

Bray, K. N. C. 1979 The interaction between turbulence and combustion. *Symp. (Int.) Combust.* **17** (1), 223–233.

Bray, K. N. C. 1980 Turbulent Flows with Premixed Reactants. In *Turbulent Reacting Flows* (ed. P. A. Libby & F. A. Williams), chap. 4, pp. 115–184. Berlin Heidelberg, Germany: Springer-Verlag.

Bray, K. N. C. & Cant, R. S. 1991 Some applications of Kolmogorov's turbulence research in the field of combustion. *Proc. R. Soc. A* **434** (1890), 217–240.

Bray, K. N. C. & Libby, P. A. 1976 Interaction effects in turbulent premixed flames. *Phys. Fluids* **19** (11), 1687–1701.

Bray, K. N. C., Libby, P. A., Masuya, G. & Moss, J. B. 1981 Turbulence Production in Premixed Turbulent Flames. *Combust. Sci. Technol.* **25** (3–4), 127–140.

Bray, K. N. C., Libby, P. A. & Moss, J. B. 1985 Unified modeling approach for premixed turbulent combustion-Part I: General formulation. *Combust. Flame* **61** (1), 87–102.

Bray, K. N. C. & Moss, J. B. 1977 A unified statistical model of the premixed turbulent flame. *Acta Astronaut.* **4** (3–4), 291–319.

Bray, K. N. C. & Peters, N. 1994 Laminar flamelets in turbulent flames. In *Turbulent Reacting Flows* (ed. P. A. Libby & F. A. Williams), chap. 2, pp. 63–113. London, UK: Academic Press.

Brewster, B. S., Cannon, S. M., Farmer, J. R. & Meng, F. 1999 Modeling of lean premixed combustion in stationary gas turbines. *Prog. Energy Combust. Sci.* **25** (4), 353–385.

Britter, R. E. 1989 Atmospheric Dispersion of Dense Gases. *Annu. Rev. Fluid Mech.* **21** (1), 317–344.

Britter, R. E. & Griffiths, R. F. 1982 The role of dense gases in the assessment of industrial hazards. *J. Hazard. Mater.* **6** (1–2), 3–12.

Britter, R. E., Hunt, J. C. R. & Mumford, J. C. 1979 The distortion of turbulence by a circular cylinder. *J. Fluid Mech.* **92** (2), 269–301.

Brübach, J., Pflitsch, C., Dreizler, A. & Atakan, B. 2013 On surface temperature measurements with thermographic phosphors: A review. *Prog. Energy Combust. Sci.* **39** (1), 37–60.

Buckmaster, J. 2002 Edge-flames. *Prog. Energy Combust. Sci.* **28** (5), 435–475.

Buckmaster, J. & Matalon, M. 1988 Anomalous lewis number effects in tribrachial flames. *Symp. (Int.) Combust.* **22** (1), 1527–1535.

Burke, S. P. & Schumann, T. E. W. 1928 Diffusion Flames. *Ind. Eng. Chem.* **20** (10), 998–1004.

Butler, T. D. & O'Rourke, P. J. 1977 A numerical method for two dimensional unsteady reacting flows. *Symp. (Int.) Combust.* **16** (1), 1503–1515.

Calvert, J. R. 1967 Experiments on the low-speed flow past cones. *J. Fluid Mech.* **27** (2), 273–289.

Candel, S., Durox, D., Schuller, T., Bourgouin, J.-F. & Moeck, J. P. 2014 Dynamics of Swirling Flames. *Annu. Rev. Fluid Mech.* **46** (1), 147–173.

Candel, S. M. & Poinsot, T. J. 1990 Flame Stretch and the Balance Equation for the Flame Area. *Combust. Sci. Technol.* **70** (1–3), 1–15.

Cant, R. S. 2011 RANS and LES Modelling of Premixed Turbulent Combustion. In *Turbul. Combust. Model. Adv. New Trends Perspect.* (ed. T. Echekki & E. Mastorakos), chap. 4, pp. 63–90. Dordrecht, The Netherlands: Springer Netherlands.

Cant, R. S. & Mastorakos, E. 2008 *An Introduction to Turbulent Reacting Flows.* London, UK: Imperial College Press.

Carmody, T. 1964 Establishment of the Wake Behind a Disk. *J. Basic Eng.* **86** (4), 869–880.

Castro, I. P. & Robins, A. G. 1977 The flow around a surface-mounted cube in uniform and turbulent streams. *J. Fluid Mech.* **79** (2), 307–335.

Cavaliere, D. E., Kariuki, J. & Mastorakos, E. 2013 A Comparison of the Blow-Off Behaviour of Swirl-Stabilized Premixed, Non-Premixed and Spray Flames. *Flow, Turbul. Combust.* **91** (2), 347–372.

Celis, C. & Figueira da Silva, L. F. 2015 Lagrangian mixing models for turbulent combustion: Review and prospects. *Flow, Turbul. Combust.* **94** (3), 643–689.

Chai, X. & Mahesh, K. 2012 Dynamic k-equation model for large-eddy simulation of compressible flows. *J. Fluid Mech.* **699**, 385–413.

Chakraborty, N., Katragadda, M. & Cant, R. S. 2011 Statistics and Modelling of Turbulent Kinetic Energy Transport in Different Regimes of Premixed Combustion. *Flow, Turbul. Combust.* **87** (2–3), 205–235.

Chakravarthy, V. K. & Menon, S. 2001 Large-eddy simulation of turbulent premixed flames in the flamelet regime. *Combust. Sci. Technol.* **162** (1), 175–222.

Chakroun, N. W., Shanbhogue, S. J., Kewlani, G., Taamallah, S., Michaels, D. & Ghoniem, A. F. 2017 On the Role of Chemical Kinetics Modeling in the LES of Premixed Bluff Body and Backward-Facing Step Combustors. In *55th AIAA Aerospace Sciences Meeting*. Grapevine, TX, USA: AIAA 2017-1572.

Charlette, F., Meneveau, C. & Veynante, D. 2002*a* A power-law wrinkling model for LES of premixed turbulent combustion: Part I - non-dynamic formulation and initial tests. *Combust. Flame* **131** (1–2), 159–180.

Charlette, F., Veynante, D. & Meneveau, C. 2002*b* A power-law wrinkling model for LES of premixed turbulent combustion: Part II - Dynamic Formulation. *Combust. Flame* **131** (1–2), 181–197.

Chen, J. H., Choudhary, A., de Supinski, B, DeVries, M, Hawkes, E. R., Klasky, S., Liao, W. K., Ma, K. L., Mellor-Crummey, J., Podhorszki, N., Sankaran, R., Shende, S. & Yoo, C. S. 2009 Terascale direct numerical simulations of turbulent combustion using S3D. *Comput. Sci. Discov.* **2** (1), 015001.

Chen, M., Herrmann, M. & Peters, N. 2007 Flamelet modeling of lifted turbulent methane/air and propane/air jet diffusion flames. *Proc. Combust. Inst.* **28** (1), 167–174.

Chen, Z. 2017 Simulation of partially premixed turbulent flames. PhD thesis, University of Cambridge.

Chen, Z., Ruan, S. & Swaminathan, N. 2017 Large Eddy Simulation of flame edge evolution in a spark-ignited methane-air jet. *Proc. Combust. Inst.* **36** (2), 1645–1652.

Chen, Z. X., Doan, N. A. K., Lv, X. J., Swaminathan, N., Ceriello, G., Sorrentino, G. & Cavaliere, A. 2018*a* Numerical Study of a Cyclonic Combustor under Moderate or Intense Low-Oxygen Dilution Conditions Using Non-adiabatic Tabulated Chemistry. *Energy and Fuels* **32** (10), 10256–10265.

Chen, Z. X., Doan, N. A. K., Ruan, S., Langella, I. & Swaminathan, N. 2018*b* A priori investigation of subgrid correlation of mixture fraction and progress variable in partially premixed flames. *Combust. Theory Model.* **22** (5), 862–882.

Chen, Z. X., Langella, I., Swaminathan, N., Stöhr, M., Meier, W. & Kolla, H. 2019*a* Large Eddy Simulation of a dual swirl gas turbine combustor: Flame/flow structures and stabilisation under thermoacoustically stable and unstable conditions. *Combust. Flame* **203**, 279–300.

Chen, Z. X., Swaminathan, N., Stöhr, M. & Meier, W. 2019*b* Interaction between self-excited oscillations and fuel-air mixing in a dual swirl combustor. *Proc. Combust. Inst.* **37** (2), 2325–2333.

Chigier, N. A. & Beer, J. M. 1964 Velocity and static-pressure distributions in swirling air jets issuing from annular and divergent nozzles. *J. Basic Eng.* **86** (4), 788–796.

Chowdhury, B. R. & Cetegen, B. M. 2017 Experimental study of the effects of free stream turbulence on characteristics and flame structure of bluff-body stabilized conical lean premixed flames. *Combust. Flame* **178**, 311–328.

Cleary, M. J. & Klimenko, A. Y. 2009 A generalised multiple mapping conditioning approach for turbulent combustion. *Flow, Turbul. Combust.* **82** (4), 477–491.

Colin, O., Ducros, F., Veynante, D. & Poinsot, T. 2000 A thickened flame model for large eddy simulations of turbulent premixed combustion. *Phys. Fluids* **12** (7), 1843–1863.

Cook, A. W. & Riley, J. J. 1994 A subgrid model for equilibrium chemistry in turbulent flows. *Phys. Fluids* **6** (8), 2868–2870.

Dally, B. B., Masri, A. R., Barlow, R. S. & Fiechtner, G. J. 1998 Instantaneous and Mean Compositional Structure of Bluff-Body Stabilized Nonpremixed Flames. *Combust. Flame* **114** (1–2), 119–148.

Darbyshire, O. R. & Swaminathan, N. 2012 A presumed joint pdf model for turbulent combustion with varying equivalence ratio. *Combust. Sci. Technol.* **184** (12), 2036–2067.

Davies, T. W. & Beér, J. M. 1971 Flow in the wake of bluff-body flame stabilizers. *Symp. (Int.) Combust.* **13** (1), 631–638.

Dawson, J. R., Gordon, R. L., Kariuki, J., Mastorakos, E., Masri, A. R. & Juddoo, M. 2011 Visualization of blow-off events in bluff-body stabilized turbulent premixed flames. *Proc. Combust. Inst.* **33** (1), 1559–1566.

Deane, P. M. 1980 *The First Industrial Revolution*. Cambridge, UK: Cambridge University Press.

Deardorff, J. W. 1970 A numerical study of three-dimensional turbulent channel flow at large Reynolds numbers. *J. Fluid Mech.* **41** (2), 453–480.

Dhanuka, S. K., Temme, J. E. & Driscoll, J. F. 2011 Lean-limit combustion instabilities of a lean premixed prevaporized gas turbine combustor. *Proc. Combust. Inst.* **33** (2), 2961–2966.

Dhanuka, S. K., Temme, J. E., Driscoll, J. F. & Mongia, H. C. 2009 Vortex-shedding and mixing layer effects on periodic flashback in a lean premixed prevaporized gas turbine combustor. *Proc. Combust. Inst.* **32** (2), 2901–2908.

Doan, N. A. K., Swaminathan, N. & Chakraborty, N. 2017 Multiscale analysis of turbulence-flame interaction in premixed flames. *Proc. Combust. Inst.* **36** (2), 1929–1935.

Domingo, P. & Vervisch, L. 1996 Triple flames and partially premixed combustion in autoignition of non-premixed turbulent mixtures. *Symp. (Int.) Combust.* **26** (1), 233–240.

Domingo, P., Vervisch, L. & Réveillon, J. 2005 DNS analysis of partially premixed combustion in spray and gaseous turbulent flame-bases stabilized in hot air. *Combust. Flame* **140** (3), 172–195.

Donini, A., Bastiaans, R. J. M., van Oijen, J. A. & de Goey, L. P. H. 2017 A 5-D Implementation of FGM for the Large Eddy Simulation of a Stratified Swirled Flame with Heat Loss in a Gas Turbine Combustor. *Flow, Turbul. Combust.* **98** (3), 887–922.

Dopazo, C. 1994 Recent development in pdf methods. In *Turbulent Reacting Flows* (ed. P. A. Libby & F. A. Williams), chap. 7, pp. 375–474. London, UK: Academic Press.

Dopazo, C. & O'Brien, E. E. 1974*a* An approach to the autoignition of a turbulent mixture. *Acta Astronaut.* **1** (9–10), 1239–1266.

Dopazo, C. & O'Brien, E. E. 1974*b* Functional formulation of nonfsothermal turbulent reactive flows. *Phys. Fluids* **17** (11), 1968–1975.

Dowling, A. P. & Mahmoudi, Y. 2015 Combustion noise. *Proc. Combust. Inst.* **35** (1), 65–100.

Driscoll, J. F. 2008 Turbulent premixed combustion: Flamelet structure and its effect on turbulent burning velocities. *Prog. Energy Combust. Sci.* **34** (1), 91–134.

Driscoll, J. F. 2011 Future Directions and Applications of Lean Premixed Combustion. In *Turbulent Premixed Flames* (ed. N. Swaminathan & K. N. C. Bray), chap. 5, pp. 378–396. Cambridge, UK: Cambridge University Press.

Duan, X. R., Weigand, P., Meier, W., Keck, O., Stricker, W., Aigner, M. & Lehmann, B. 2004 Experimental investigations and laser based validation measurements in a gas turbine model combustor. *Prog. Comput. Fluid Dyn.* **4** (3–5), 175–182.

Dunstan, T. D., Minamoto, Y., Chakraborty, N. & Swaminathan, N. 2013 Scalar dissipation rate modelling for large eddy simulation of turbulent premixed flames. *Proc. Combust. Inst.* **34** (1), 1193–1201.

Durao, D. F G & Whitelaw, J. H. 1978 Velocity characteristics of the flow in the near wake of a disk. *J. Fluid Mech.* **85**, 369–385.

EASA, EEA & EUROCONTROL 2019 European Aviation Environmental Report. *Tech. Rep.*.

Echekki, T. & Mastorakos, E., ed. 2011 *Turbulent Combustion Modelling: Advances, New Trends and Perspectives*. Dordrecht, The Netherlands: Springer Netherlands.

Eggenspieler, G. & Menon, S. 2004 Large-Eddy Simulation of Pollutant Emission in a DOE-HAT Combustor. *J. Propuls. Power* **20** (6), 1076–1085.

Egolfopoulos, F. N. & Law, C. K. 1990 An experimental and computational study of the burning rates of ultra-lean to moderately-rich H2/O2/N2 laminar flames with pressure variations. *Symp. (Int.) Combust.* **23** (1), 333–340.

Ertesvåg, I. S. & Magnussen, B. F. 2000 The Eddy Dissipation Turbulence Energy Cascade Model. *Combust. Sci. Technol.* **159** (1), 213–235.

Fackrell, J. E. 1984 Parameters characterising dispersion in the near wake of buildings. *J. Wind Eng. Ind. Aerodyn.* **16** (1), 97–118.

Farrace, D., Chung, K., Bolla, M., Wright, Y. M., Boulouchos, K. & Mastorakos, E. 2018 A LES-CMC formulation for premixed flames including differential diffusion. *Combust. Theory Model.* **22** (3), 411–431.

Farrace, D., Chung, K., Pandurangi, S. S., Wright, Y. M., Boulouchos, K. & Swaminathan, N. 2017 Unstructured LES-CMC modelling of turbulent premixed bluff body flames close to blow-off. *Proc. Combust. Inst.* **36** (2), 1977–1985.

Feikema, D., Chen, R.-H. & Driscoll, J. F. 1990 Enhancement of flame blowout limits by the use of swirl. *Combust. Flame* **80** (2), 183–195.

Feikema, D., Chen, R.-H. & Driscoll, J. F. 1991 Blowout of nonpremixed flames: Maximum coaxial air velocities achievable, with and without swirl. *Combust. Flame* **86** (4), 347–358.

Ferziger, J. H. & Perić, M. 2002 *Computational Methods for Fluid Dynamics*, 3rd edn. Springer-Verlag.

Fiorina, B., Baron, R., Gicquel, O., Thevenin, D., Carpentier, S. & Darabiha, N. 2003 Modelling non-adiabatic partially premixed flames using flame-prolongation of ILDM. *Combust. Theory Model.* **7** (3), 449–470.

Fiorina, B., Mercier, R., Kuenne, G., Ketelheun, A., Avdić, A., Janicka, J., Geyer, D., Dreizler, A., Alenius, E., Duwig, C., Trisjono, P., Kleinheinz, K., Kang, S., Pitsch, H., Proch, F., Cavallo Marincola, F. & Kempf, A. 2015 Challenging modeling strategies for LES of non-adiabatic turbulent stratified combustion. *Combust. Flame* **162** (11), 4264–4282.

Fiorina, B., Vicquelin, R., Auzillon, P., Darabiha, N., Gicquel, O. & Veynante, D. 2010 A filtered tabulated chemistry model for LES of premixed combustion. *Combust. Flame* **157** (3), 465–475.

Fuchs, H. V., Mercker, E. & Michel, U. 1979 Large-scale coherent structures in the wake of axisymmetric bodies. *J. Fluid Mech.* **93** (1), 185–207.

Fureby, C. & Möller, S. I. 1995 Large-Eddy Simulation of Reacting Flows Applied to Bluff-Body Stabilized Flames. *AIAA J.* **33** (12), 2339–2347.

Galindo, S., Salehi, F., Cleary, M. J. & Masri, A. R. 2017 MMC-LES simulations of turbulent piloted flames with varying levels of inlet inhomogeneity. *Proc. Combust. Inst.* **36** (2), 1759–1766.

Galley, D., Ducruix, S., Lacas, F. & Veynante, D. 2011 Mixing and stabilization study of a partially premixed swirling flame using laser induced fluorescence. *Combust. Flame* **158** (1), 155–171.

Gao, F. & O'Brien, E. E. 1993 A large-eddy simulation scheme for turbulent reacting flows. *Phys. Fluids A Fluid Dyn.* **5** (6), 1282–1284.

Gao, Y., Chakraborty, N. & Swaminathan, N. 2014 Algebraic Closure of Scalar Dissipation Rate for Large Eddy Simulations of Turbulent Premixed Combustion. *Combust. Sci. Technol.* **186** (10–11), 1309–1337.

Gao, Y., Chakraborty, N. & Swaminathan, N. 2015 Dynamic Closure of Scalar Dissipation Rate for Large Eddy Simulations of Turbulent Premixed Combustion: A Direct Numerical Simulations Analysis. *Flow, Turbul. Combust.* **95** (4), 775–802.

Garmory, A. & Mastorakos, E. 2011 Capturing localised extinction in Sandia Flame F with LES-CMC. *Proc. Combust. Inst.* **33** (1), 1673–1680.

Germano, M., Piomelli, U., Moin, P. & Cabot, W. H. 1991 A dynamic subgrid-scale eddy viscosity model. *Phys. Fluids A Fluid Dyn.* **3** (7), 1760–1765.

Ghani, A., Miguel-Brebion, M., Selle, L., Duchaine, F. & Poinsot, T. 2016 Effect of wall heat transfer on screech in a turbulent premixed combustor. *Center for Turbulence Research Proceedings of the Summer Program* pp. 133–141.

Ghosal, S., Lund, T. S., Moin, P. & Akselvoll, K. 1995 A dynamic localization model for large-eddy simulation of turbulent flows. *J. Fluid Mech.* **286**, 229–255.

Giacomazzi, E., Battaglia, V. & Bruno, C. 2004 The coupling of turbulence and chemistry in a premixed bluff-body flame as studied by LES. *Combust. Flame* **138** (4), 320–335.

Gicquel, L. Y. M., Staffelbach, G. & Poinsot, T. 2012 Large Eddy Simulations of gaseous flames in gas turbine combustion chambers. *Prog. Energy Combust. Sci.* **38** (6), 782–817.

Gicquel, O., Darabiha, N. & Thévenin, D. 2000 Laminar premixed hydrogen/air counterflow flame simulations using flame prolongation of ILDM with differential diffusion. *Proc. Combust. Inst.* **28** (2), 1901–1908.

Giusti, A. & Mastorakos, E. 2017 Detailed chemistry LES/CMC simulation of a swirling ethanol spray flame approaching blow-off. *Proc. Combust. Inst.* **36** (2), 2625–2632.

Givi, P. 1989 Model-free simulations of turbulent reactive flows. *Prog. Energy Combust. Sci.* **15** (1), 1–107.

Givi, P. 2006 Filtered Density Function for Subgrid Scale Modeling of Turbulent Combustion. *AIAA J.* **44** (1), 16–23.

Goodwin, D. G., Moffat, H. K. & Speth, R. L. 2017 Cantera: An Object-oriented Software Toolkit for Chemical Kinetics, Thermodynamics, and Transport Processes. https://www.cantera.org.

Gregor, M. A., Seffrin, F., Fuest, F., Geyer, D. & Dreizler, A. 2009 Multi-scalar measurements in a premixed swirl burner using ID Raman/Rayleigh scattering. *Proc. Combust. Inst.* **32** (2), 1739–1746.

Gupta, A. L., Lilley, D. G. & Syred, N. 1984 *Swirl Flows*. Royal Tunbridge Wells, UK: Abacus Press.

Hanjalić, K. 1994 Advanced turbulence closure models: a view of current status and future prospects. *Int. J. Heat Fluid Flow* **15** (3), 178–203.

Hanjalić, K. & Launder, B. E. 1972 A Reynolds stress model of turbulence and its application to thin shear flows. *J. Fluid Mech.* **52** (4), 609–638.

Hanjalić, K. & Launder, B. E. 2011 *Modelling Turbulence in Engineering and the Environment: Second-Moment Routes to Closure*. Cambridge, UK: Cambridge University Press.

Hauke, G. & Valiño, L. 2004 Computing reactive flows with a field Monte Carlo formulation and multi-scale methods. *Comput. Methods Appl. Mech. Eng.* **193** (15–16), 1455–1470.

Hawkes, E. R. & Cant, R. S. 2001*a* Implications of a flame surface density approach to large eddy simulation of premixed turbulent combustion. *Combust. Flame* **126** (3), 1617–1629.

Hawkes, E. R. & Cant, R. S. 2001*b* Physical and numerical realizability requirements for flame surface density approaches. *Combust. Theory Model.* **5** (4), 699–720.

Haworth, D. C. 2010 Progress in probability density function methods for turbulent reacting flows. *Prog. Energy Combust. Sci.* **36** (2), 168–259.

Haworth, D. C. & Jansen, K. 2000 Large-eddy simulation on unstructured deforming meshes: Towards reciprocating IC engines. *Comput. Fluids* **29** (5), 493–524.

Haworth, D. C. & Pope, S. B. 2011 Transported Probability Density Function Methods for Reynolds-Averaged and Large-Eddy Simulations. In *Turbul. Combust. Model. Adv. New Trends Perspect.* (ed. T. Echekki & E. Mastorakos), chap. 6, pp. 119–142. Dordrecht, The Netherlands: Springer Netherlands.

Heitor, M. V., Taylor, A. M. K. P. & Whitelaw, J. H. 1987 The interaction of turbulence and pressure gradients in a baffle-stabilized premixed flame. *J. Fluid Mech.* **181**, 387–413.

Hinze, J. O. 1959 *Turbulence*. New York, NY, USA: McGraw-Hill.

Hirschfelder, J. O., Curtiss, C. F. & Byrd, R. B. 1954 *The Molecular Theory of Gases and Liquids*. New York, NY, USA: Wiley.

HM Government, Department for Transport 2018 The Road to Zero: Next steps towards cleaner road transport and delivering our Industrial Strategy. *Tech. Rep.*.

Hodzic, E., Alenius, E., Duwig, C., Szasz, R. S. & Fuchs, L. 2017*a* A Large Eddy Simulation Study of Bluff Body Flame Dynamics Approaching Blow-Off. *Combust. Sci. Technol.* **189** (7), 1107–1137.

Hodzic, E., Jangi, M., Szasz, R. Z. & Bai, X.-S. 2017*b* Large eddy simulation of bluff body flames close to blow-off using an Eulerian stochastic field method. *Combust. Flame* **181**, 1–15.

Hodzic, E., Jangi, M., Szasz, R.-Z., Duwig, C., Geron, M., Early, J., Fuchs, L. & Bai, X.-S. 2019 Large Eddy Simulation of Bluff-Body Flame Approaching Blow-Off: A Sensitivity Study. *Combust. Sci. Technol.* **191** (10), 1815–1842.

Hong, S., Shanbhogue, S. J. & Ghoniem, A. F. 2015 Impact of fuel composition on the recirculation zone structure and its role in lean premixed flame anchoring. *Proc. Combust. Inst.* **35** (2), 1493–1500.

Hossain, M., Jones, J. C. & Malalasekera, W. 2002 Modelling of a bluff-body nonpremixed flame using a coupled radiation/flamelet combustion model. *Flow, Turbul. Combust.* **67** (3), 217–234.

Huang, Y. & Yang, V. 2009 Dynamics and stability of lean-premixed swirl-stabilized combustion. *Prog. Energy Combust. Sci.* **35** (4), 293–364.

Humphries, W. & Vincent, J. H. 1976*a* Experiments to investigate transport processes in the near wakes of disks in turbulent air flow. *J. Fluid Mech.* **75** (4), 737–749.

Humphries, W. & Vincent, J. H. 1976*b* Near wake properties of axisymmetric bluff body flows. *Appl. Sci. Res.* **32** (6), 649–669.

Hunt, J. C.R. 1973 A theory of turbulent flow round two-dimensional bluff bodies. *J. Fluid Mech.* **61** (4), 625–706.

Huo, Z., Salehi, F., Galindo-Lopez, S., Cleary, M. J. & Masri, A. R. 2019 Sparse MMC-LES of a Sydney swirl flame. *Proc. Combust. Inst.* **37** (2), 2191–2198.

Ihme, M., Cha, C. M. & Pitsch, H. 2005 Prediction of local extinction and re-ignition effects in non-premixed turbulent combustion using a flamelet/progress variable approach. *Proc. Combust. Inst.* **30** (1), 793–800.

Ihme, M. & Pitsch, H. 2008*a* Prediction of extinction and reignition in nonpremixed turbulent flames using a flamelet/progress variable model: 1. A priori study and presumed PDF closure Matthias. *Combust. Flame* **155** (1–2), 70–89.

Ihme, M. & Pitsch, H. 2008*b* Prediction of extinction and reignition in nonpremixed turbulent flames using a flamelet/progress variable model: 2. Application in LES of Sandia flames D and E. *Combust. Flame* **155** (1–2), 90–107.

Ihme, M., Shunn, L. & Zhang, J. 2012 Regularization of reaction progress variable for application to flamelet-based combustion models. *J. Comput. Phys.* **231** (23), 7715–7721.

Im, H. G., Lund, T. S. & Ferziger, J. H. 1997 Large eddy simulation of turbulent front propagation with dynamic subgrid models. *Phys. Fluids* **9** (12), 3826–3833.

Issa, R. I. 1986 Solution of the implicitly discretised fluid flow equations by operator-splitting. *J. Comput. Phys.* **62** (1), 40–65.

Janicka, J. & Sadiki, A. 2005 Large eddy simulation of turbulent combustion systems. *Proc. Combust. Inst.* **30** (1), 537–547.

Janus, B., Dreizier, A. & Janicka, J. 2007 Experiments on swirl stabilized non-premixed natural gas flames in a model gasturbine combustor. *Proc. Combust. Inst.* **31** (2), 3091–3098.

Janus, B., Dreizler, A. & Janicka, J. 2005 Experimental study on stabilization of lifted swirl flames in a model GT combustor. *Flow, Turbul. Combust.* **75** (1–4), 293–315.

Jones, B. 2011 Application of Lean Flames in Aero Gas Turbines. In *Turbulent Premixed Flames* (ed. N. Swaminathan & K. N. C. Bray), chap. 4, pp. 309–335. Cambridge, UK: Cambridge University Press.

Jones, W. P., Jurisch, M. & Marquis, A. J. 2015*a* Examination of an Oscillating Flame in the Turbulent Flow Around a Bluff Body with Large Eddy Simulation Based on the Probability Density Function Method. *Flow, Turbul. Combust.* **95** (2), 519–538.

Jones, W. P. & Launder, B. E. 1972 The prediction of laminarization with a two-equation model of turbulence. *Int. J. Heat Mass Transf.* **15** (2), 301–314.

Jones, W. P., Marquis, A. J. & Vogiatzaki, K. 2014 Large-eddy simulation of spray combustion in a gas turbine combustor. *Combust. Flame* **161** (1), 222–239.

Jones, W. P., Marquis, A. J. & Wang, F. 2015*b* Large eddy simulation of a premixed propane turbulent bluff body flame using the Eulerian stochastic field method. *Fuel* **140**, 514–525.

Jones, W. P. & Prasad, V. N. 2010 Large Eddy Simulation of the Sandia Flame Series (D–F) using the Eulerian stochastic field method. *Combust. Flame* **157** (9), 1621–1636.

Jones, W. P. & Prasad, V. N. 2011 LES-pdf simulation of a spark ignited turbulent methane jet. *Proc. Combust. Inst.* **33** (1), 1355–1363.

Jou, W.-H. & Riley, J. J. 1989 Progress in direct numerical simulations of turbulent reacting flows. *AIAA J.* **27** (11), 1543–1556.

Kalghatgi, G. T. 1984 Lift-off Heights and Visible Lengths of Vertical Turbulent Jet Diffusion Flames in Still Air. *Combust. Sci. Technol.* **41** (1–2), 17–29.

Kariuki, J. 2013 Turbulent premixed flame stabilization and blow-off. PhD thesis, University of Cambridge.

Kariuki, J., Dawson, J. R. & Mastorakos, E. 2012 Measurements in turbulent premixed bluff body flames close to blow-off. *Combust. Flame* **159** (8), 2589–2607.

Kariuki, J., Dowlut, A., Yuan, R., Balachandran, R. & Mastorakos, E. 2015 Heat release imaging in turbulent premixed methane-air flames close to blow-off. *Proc. Combust. Inst.* **35** (2), 1443–1450.

Kee, R. J., Grcar, J. F., Smooke, M. D., Miller, J. A. & Meeks, E. 1985 PREMIX: A FORTRAN Program for Modeling Steady Laminar One-Dimensional Premixed Flames.

Kerstein, A. R. 1988 A Linear-Eddy Model of Turbulent Scalar Transport and Mixing. *Combust. Sci. Technol.* **60** (4–6), 391–421.

Kim, S. H. & Pitsch, H. 2005 Conditional filtering method for large-eddy simulation of turbulent nonpremixed combustion. *Phys. Fluids* **17**, 105103.

Kim, W.-W. & Menon, S. 1995 A new dynamic one-equation subgrid-scale model for large eddy simulations. In *33rd AIAA Aerospace Sciences Meeting and Exhibit*. Reno, NV, USA: AIAA 95-0356.

Kim, W.-W. & Menon, S. 2000 Numerical Modeling of Turbulent Premixed Flames in the Thin-Reaction-Zones Regime. *Combust. Sci. Technol.* **160** (1), 119–150.

Kim, W.-W., Menon, S. & Mongia, H. C. 1999 Large-Eddy Simulation of a Gas Turbine Combustor Flow. *Combust. Sci. Technol.* **143** (1–6), 25–62.

Klein, M., Sadiki, A. & Janicka, J. 2003 A digital filter based generation of inflow data for spatially developing direct numerical or large eddy simulations. *J. Comput. Phys.* **186** (2), 652–665.

Klimenko, A. Y. 1990 Multicomponenet diffusion of various admixtures in turbulent flow. *Fluid Dyn.* **25**, 327–331.

Klimenko, A. Y. 2005 Matching conditional moments in PDF modelling of nonpremixed combustion. *Combust. Flame* **143** (4), 369–385.

Klimenko, A. Y. & Pope, S. B. 2003 The modeling of turbulent reactive flows based on multiple mapping conditioning. *Phys. Fluids* **15** (7), 1907–1925.

Kolla, H., Rogerson, J. W., Chakraborty, N. & Swaminathan, N. 2009 Scalar dissipation rate modeling and its validation. *Combust. Sci. Technol.* **181** (3), 518–535.

Kolla, H. & Swaminathan, N. 2010*a* Strained flamelets for turbulent premixed flames, I: Formulation and planar flame results. *Combust. Flame* **157** (5), 943–954.

Kolla, H. & Swaminathan, N. 2010*b* Strained flamelets for turbulent premixed flames II: Laboratory flame results. *Combust. Flame* **157** (7), 1274–1289.

Kolmogorov, A. N. 1941 The local structure of turbulence in incompressible viscous fluid for very large Reynolds numbers. *Proc. R. Soc. Lond. A* **434**, 9–13.

Kraus, C., Selle, L. & Poinsot, T. 2018 Coupling heat transfer and large eddy simulation for combustion instability prediction in a swirl burner. *Combust. Flame* **191**, 239–251.

Kronenburg, A. & Kostka, M. 2005 Modeling extinction and reignition in turbulent flames. *Combust. Flame* **143** (4), 342–356.

Kronenburg, A. & Mastorakos, E. 2011 The Conditional Moment Closure Model. In *Turbul. Combust. Model. Adv. New Trends Perspect.* (ed. T. Echekki & E. Mastorakos), chap. 5, pp. 91–117. Dordrecht, The Netherlands: Springer Netherlands.

Kuenne, G., Seffrin, F., Fuest, F., Stahler, T., Ketelheun, A., Geyer, D., Janicka, J. & Dreizler, A. 2012 Experimental and numerical analysis of a lean premixed stratified burner using 1D Raman/Rayleigh scattering and large eddy simulation. *Combust. Flame* **159** (8), 2669–2689.

Kuo, K. K. 2005 *Principles of Combustion*, 2nd edn. Wiley.

Langella, I. 2016 Large eddy simulation of premixed combustion using flamelets. PhD thesis, University of Cambridge.

Langella, I., Chen, Z. X., Swaminathan, N. & Sadasivuni, S. K. 2018*a* Large-Eddy Simulation of Reacting Flows in Industrial Gas Turbine Combustor. *J. Propuls. Power* **34** (5), 1269–1284.

Langella, I., Doan, N. A. K. & Swaminathan, N. 2018*b* Study of subgrid-scale velocity models for reacting and nonreacting flows. *Phys. Rev. Fluids* **3**, 054602.

Langella, I. & Swaminathan, N. 2016 Unstrained and strained flamelets for LES of premixed combustion. *Combust. Theory Model.* **20** (3), 410–440.

Langella, I., Swaminathan, N., Gao, Y. & Chakraborty, N. 2015 Assessment of dynamic closure for premixed combustion large eddy simulation. *Combust. Theory Model.* **19** (5), 628–656.

Langella, I., Swaminathan, N., Gao, Y. & Chakraborty, N. 2017 Large Eddy Simulation of Premixed Combustion: Sensitivity to Subgrid Scale Velocity Modeling. *Combust. Sci. Technol.* **189** (1), 43–78.

Langella, I., Swaminathan, N. & Pitz, R. W. 2016*a* Application of unstrained flamelet SGS closure for multi-regime premixed combustion. *Combust. Flame* **173**, 161–178.

Langella, I., Swaminathan, N., Williams, F. A. & Furukawa, J. 2016*b* Large-Eddy Simulation of Premixed Combustion in the Corrugated-Flamelet Regime. *Combust. Sci. Technol.* **188** (9), 1565–1591.

Launder, B. E. & Spalding, D. B. 1974 The numerical computation of turbulent flows. *Comput. Methods Appl. Mech. Eng.* **3** (2), 269–289.

Law, C. K. 2006 *Combustion Physics*. Cambridge, UK: Cambridge University Press.

Lawn, C. J. 2009 Lifted flames on fuel jets in co-flowing air. *Prog. Energy Combust. Sci.* **35** (1), 1–30.

Lecocq, G., Richard, S., Colin, O. & Vervisch, L. 2010 Gradient and Counter-Gradient Modeling in Premixed Flames: Theoretical Study and Application to the LES of a Lean Premixed Turbulent Swirl-Burner. *Combust. Sci. Technol.* **182** (4–6), 465–479.

Lefebvre, A. H. & Ballal, D. R. 2010 *Gas Turbine Combustion*. Boca Raton, FL, USA: CRC Press.

Leonard, A. 1974 Energy cascade in large-eddy simulations of turbulent fluid flows. *Adv. Geophys.* **18A**, 237–248.

Lesieur, M. & Métais, O. 1996 New Trends in Large-Eddy Simulations of Turbulence. *Annu. Rev. Fluid Mech.* **28** (1), 45–82.

Libby, P. A. 1985 Theory of normal premixed turbulent flames revisited. *Prog. Energy Combust. Sci.* **11** (1), 83–96.

Libby, P. A. & Bray, K. N. C. 1977 Variable Density Effects in Premixed Turbulent Flames. *AIAA J.* **15** (8), 1186–1193.

Libby, P. A. & Bray, K. N. C. 1980 Implications of the laminar flamelet model in premixed turbulent combustion. *Combust. Flame* **39** (1), 33–41.

Libby, P. A. & Bray, K. N. C. 1981 Countergradient Diffusion in Premixed Turbulent Flames. *AIAA J.* **19** (2), 205–213.

Libby, P. A. & Williams, F. A., ed. 1980 *Turbulent Reacting Flows*. Berlin Heidelberg, Germany: Springer-Verlag.

Lieuwen, T. C. 2012 *Unsteady Combustor Physics*. Cambridge, UK: Cambridge University Press.

Lieuwen, T. C. & Yang, V., ed. 2013 *Gas Turbine Emissions*. Cambridge, UK: Cambridge University Press.

Liew, S. K., Bray, K. N. C. & Moss, J. B. 1981 A Flamelet Model of Turbulent Non-Premixed Combustion. *Combust. Sci. Technol.* **27** (1–2), 69–73.

Lilly, D. K. 1967 The Representation of Small-Scale Tubulence in Numerical Simulation Experiments. In *Proc. IBM Sci. Comput. Symp. Environ. Sci.* (ed. H. H. Goldstine), pp. 195–210. Yorktown Heights, NY, USA.

Lilly, D. K. 1992 A proposed modification of the Germano subgrid-scale closure method. *Phys. Fluids A Fluid Dyn.* **4** (3), 633–635.

Lipatnikov, A. N. 2017 Stratified turbulent flames: Recent advances in understanding the influence of mixture inhomogeneities on premixed combustion and modeling challenges. *Prog. Energy Combust. Sci.* **62**, 87–132.

Lipatnikov, A. N. & Chomiak, J. 2002 Turbulent flame speed and thickness: Phenomenology, evaluation, and application in multi-dimensional simulations. *Prog. Energy Combust. Sci.* **28** (1), 1–74.

Lyons, K. M. 2007 Toward an understanding of the stabilization mechanisms of lifted turbulent jet flames: Experiments. *Prog. Energy Combust. Sci.* **33** (2), 211–231.

Ma, P. C., Wu, H., Ihme, M. & Hickey, J.-P. 2018 Nonadiabatic Flamelet Formulation for Predicting Wall Heat Transfer in Rocket Engines. *AIAA J.* **56** (6), 2336–2349.

Ma, P. C., Wu, H., Labahn, J. W., Jaravel, T. & Ihme, M. 2019 Analysis of transient blow-out dynamics in a swirl-stabilized combustor using large-eddy simulations. *Proc. Combust. Inst.* **37** (4), 5073–5082.

Maas, U. & Pope, S. B. 1992*a* Implementation of simplified chemical kinetics based on intrinsic low-dimensional manifolds. *Symp. (Int.) Combust.* **24** (1), 103–112.

Maas, U. & Pope, S. B. 1992*b* Simplifying chemical kinetics: Intrinsic low-dimensional manifolds in composition space. *Combust. Flame* **88** (3–4), 239–264.

Magnussen, B. F. & Hjertager, B. H. 1977 On mathematical modeling of turbulent combustion with special emphasis on soot formation and combustion. *Symp. (Int.) Combust.* **16** (1), 719–729.

Mansour, M. S. 2003 Stability characteristics of lifted turbulent partially premixed jet flames. *Combust. Flame* **133** (3), 263–274.

Mantel, T. & Bilger, R. W. 1995 Some Conditional Statistics in a Turbulent Premixed Flame Derived from Direct Numerical Simulations. *Combust. Sci. Technol.* **110–111** (1), 393–417.

Marble, F. E. & Broadwell, J. E. 1977 The Coherent Flame Model for Turbulent Chemical Reactions. In *Proj. Squid Tech. Rep. TRW-9-PU*. Purdue University, West Lafayette, IN, USA.

di Mare, F., Jones, W. P. & Menzies, K. R. 2004 Large eddy simulation of a model gas turbine combustor. *Combust. Flame* **137** (3), 278–294.

Marracino, B. & Lentini, D. 1997 Radiation modelling in non-luminous nonpremixed turbulent flames. *Combust. Sci. Technol.* **128** (1–6), 23–48.

Masri, A. R. 2015 Partial premixing and stratification in turbulent flames. *Proc. Combust. Inst.* **35** (2), 1115–1136.

Mastorakos, E. 2009 Ignition of turbulent non-premixed flames. *Prog. Energy Combust. Sci.* **35** (1), 57–97.

Matalon, M. 2009 Flame dynamics. *Proc. Combust. Inst.* **32** (1), 57–82.

McDermott, R. & Pope, S. B. 2007 A particle formulation for treating differential diffusion in filtered density function methods. *J. Comput. Phys.* **226** (1), 947–993.

McMurtry, P. A., Menon, S. & Kerstein, A. R. 1992 A linear eddy sub-grid model for turbulent reacting flows: Application to hydrogen-AIR combustion. *Symp. (Int.) Combust.* **24** (1), 271–278.

Meares, S. & Masri, A. R. 2014 A modified piloted burner for stabilizing turbulent flames of inhomogeneous mixtures. *Combust. Flame* **161** (2), 484–495.

Meier, W., Duan, X. R. & Weigand, P. 2005 Reaction zone structures and mixing characteristics of partially premixed swirling CH4/air flames in a gas turbine model combustor. *Proc. Combust. Inst.* **30** (1), 835–842.

Meier, W., Duan, X. R. & Weigand, P. 2006 Investigations of swirl flames in a gas turbine model combustor: II. Turbulence-chemistry interactions. *Combust. Flame* **144** (1–2), 225–236.

Meier, W., Weigand, P., Duan, X. & Giezendannerthobe, R. 2007 Detailed characterization of the dynamics of thermoacoustic pulsations in a lean premixed swirl flame. *Combust. Flame* **150** (1–2), 2–26.

Meneveau, C. & Katz, J. 2000 Scale-Invariance and Turbulence Models for Large-Eddy Simulation. *Annu. Rev. Fluid Mech.* **32** (1), 1–32.

Menon, S. & Kerstein, A. R. 2011 The Linear-Eddy Model. In *Turbul. Combust. Model. Adv. New Trends Perspect.* (ed. T. Echekki & E. Mastorakos), chap. 10, pp. 221–247. Dordrecht, The Netherlands: Springer Netherlands.

Menon, S. & Patel, N. 2006 Subgrid Modeling for Simulation of Spray Combustion in Large-Scale Combustors. *AIAA J.* **44** (4), 709–723.

Menter, F. R. 2009 Review of the shear-stress transport turbulence model experience from an industrial perspective. *Int. J. Comut. Fluid Dyn.* **23** (4), 305–316.

Mercier, R., Auzillon, P., Moureau, V., Darabiha, N., Gicquel, O., Veynante, D. & Fiorina, B. 2014 LES modeling of the impact of heat losses and differential diffusion on turbulent stratified flame propagation: Application to the TU Darmstadt stratified flame. *Flow, Turbul. Combust.* **93** (2), 349–381.

Michaels, D., Shanbhogue, S. J. & Ghoniem, A. F. 2017 The impact of reactants composition and temperature on the flow structure in a wake stabilized laminar lean premixed CH4/H2/air flames; mechanism and scaling. *Combust. Flame* **176**, 151–161.

Miguel-Brebion, M., Mejia, D., Xavier, P., Duchaine, F., Bedat, B., Selle, L. & Poinsot, T. 2016 Joint experimental and numerical study of the influence of flame holder temperature on the stabilization of a laminar methane flame on a cylinder. *Combust. Flame* **172**, 153–161.

Minamoto, Y., Aoki, K., Tanahashi, M. & Swaminathan, N. 2015 DNS of swirling hydrogen-air premixed flames. *Int. J. Hydrogen Energy* **40** (39), 13604–13620.

Moin, P. 1997 Progress in large eddy simulation of turbulent flows. In *35th AIAA Aerospace Sciences Meeting and Exhibit*. Reno, NV, USA: AIAA 97-0749.

Moin, P. 2002 Advances in large eddy simulation methodology for complex flows. *Int. J. Heat Fluid Flow* **23** (5), 710–720.

Moin, P. & Kim, J. 1982 Numerical investigation of turbulent channel flow. *J. Fluid Mech.* **118**, 341–377.

Moin, P. & Mahesh, K. 1998 DIRECT NUMERICAL SIMULATION: A Tool in Turbulence Research. *Annu. Rev. Fluid Mech.* **30** (1), 539–578.

Moin, P., Squires, K., Cabot, W. & Lee, S. 1991 A dynamic subgrid-scale model for compressible turbulence and scalar transport. *Phys. Fluids A Fluid Dyn.* **3** (11), 2746–2757.

Möller, S. I., Lundgren, E. & Fureby, C. 1996 Large eddy simulation of unsteady combustion. *Symp. (Int.) Combust.* **26** (1), 241–248.

Moureau, V., Domingo, P. & Vervisch, L. 2011 From Large-Eddy Simulation to Direct Numerical Simulation of a lean premixed swirl flame: Filtered laminar flame-PDF modeling. *Combust. Flame* **158** (7), 1340–1357.

Mustata, R., Valiño, L., Jiménez, C., Jones, W. P. & Bondi, S. 2006 A probability density function Eulerian Monte Carlo field method for large eddy simulations: Application to a turbulent piloted methane/air diffusion flame (Sandia D). *Combust. Flame* **145** (1–2), 88–104.

Nallasamy, M. 1987 Turbulence models and their applications to the prediction of internal flows: A review. *Comput. Fluids* **15** (2), 151–194.

Nandula, S. P. 2003 Lean premixed flame structure in intense turbulence: Rayleigh/ Raman/LIF measurements and modeling. PhD thesis, Vanderbilt University.

Nandula, S. P., Pitz, R. W., Barlow, R. S. & Fiechtner, G. J. 1996 Rayleigh/Raman/LIF measurements in a turbulent lean premixed combustor. In *34th AIAA Aerospace Sciences Meeting and Exhibit*. Reno, NV, USA: AIAA 96-0937.

Navarro-Martinez, S., Kronenburg, A. & Di Mare, F. 2005 Conditional moment closure for large eddy simulations. *Flow, Turbul. Combust.* **75** (1–4), 245–274.

Nicoud, F. & Ducros, F. 1999 Subgrid-Scale Stress Modelling Based on the Square of the Velocity Gradient Tensor. *Flow, Turbul. Combust.* **62** (3), 183–200.

van Oijen, J. A. & de Goey, L. P. H. 2000 Modelling of Premixed Laminar Flames using Flamelet-Generated Manifolds. *Combust. Sci. Technol.* **161** (1), 113–137.

Palies, P., Schuller, T., Durox, D., Gicquel, L. Y. M. & Candel, S. 2011 Acoustically perturbed turbulent premixed swirling flames. *Phys. Fluids* **23**, 037101.

Pan, J. C., Schmoll, W. J. & Ballal, D. R. 1992*a* Turbulent Combustion Properties Behind a Confined Conical Stabilizer. *J. Eng. Gas Turbines Power* **114** (1), 33–38.

Pan, J. C., Vangsness, M. D. & Ballal, D. R. 1992*b* Aerodynamics of Bluff-Body Stabilized Confined Turbulent Premixed Flames. *J. Eng. Gas Turbines Power* **114** (4), 783–789.

Pan, J. C., Vangsness, M. D., Heneghan, S. P. & Ballal, D. R. 1991*a* Laser diagnostic studies of bluff-body stabilized confined turbulent premixed flames. In *Spring Technical Meeting 1991: Combustion Fundamentals and Applications*, pp. 379–384. Combustion Institute, Central States Section.

Pan, J. C., Vangsness, M. D., Heneghan, S. P. & Ballal, D. R. 1991*b* Scalar Measurements in Bluff Body Stabilized Flames Using Cars Diagnostics. In *Vol. 3: Coal, Biomass and Alternative Fuels; Combustion and Fuels; Oil and Gas Applications; Cycle Innovations*. Orlando, FL, USA: ASME. Turbo Expo: Power for Land, Sea, and Air.

Pantangi, P., Sadiki, A., Janicka, J., Mann, M. & Dreizler, A. 2014 *LES of premixed methane flame impinging on the wall using non-adiabatic flamelet generated manifold (FGM) approach*, , vol. 92.

Patankar, S. 1980 *Numerical Heat Transfer and Fluid Flow*. Washington, D.C., USA: Taylor & Francis.

Patel, V. C., Rodi, W. & Scheuerer, G. 1984 Turbulence Models for Near-Wall and Low Reynolds Number Flows: A Review. *AIAA J.* **23** (9), 1308–1319.

Peters, N. 1984 Laminar diffusion flamelet models in non-premixed turbulent combustion. *Prog. Energy Combust. Sci.* **10** (3), 319–339.

Peters, N. 1986 Laminar flamelet concepts in turbulent combustion. *Symp. (Int.) Combust.* **21** (1), 1231–1250.

Peters, N. 1992 A spectral closure for premixed turbulent combustion in the flamelet regime. *J. Fluid Mech.* **242**, 611–629.

Peters, N. 1999 The turbulent burning velocity for large-scale and small-scale turbulence. *J. Fluid Mech.* **384**, 107–132.

Peters, N. 2000 *Turbulent Combustion*. Cambridge, UK: Cambridge University Press.

Pierce, C. D. & Moin, P. 1998 A dynamic model for subgrid-scale variance and dissipation rate of a conserved scalar. *Phys. Fluids* **10** (12), 3041–3044.

Pierce, C. D. & Moin, P. 2004 Progress-variable approach for large-eddy simulation of non-premixed turbulent combustion. *J. Fluid Mech.* **504**, 73–97.

Piomelli, U. 1999 Large-eddy simulation: achievements and challenges. *Prog. Aerosp. Sci.* **35** (4), 335–362.

Piomelli, U. & Zang, T. A. 1991 Large-eddy simulation of transitional channel flow. *Comput. Phys. Commun.* **65** (1–3), 224–230.

Pitsch, H. 2005 A consistent level set formulation for large-eddy simulation of premixed turbulent combustion. *Combust. Flame* **143** (4), 587–598.

Pitsch, H. 2006 Large-Eddy Simulation of Turbulent Combustion. *Annu. Rev. Fluid Mech.* **38** (1), 453–482.

Pitsch, H. & Ihme, M. 2005 An Unsteady/Flamelet Progress Variable Method for LES of Nonpremixed Turbulent Combustion. In *43rd AIAA Aerospace Sciences Meeting and Exhibit*. Reno, NV, USA: AIAA 2005-557.

Pitsch, H. & Steiner, H. 2000*a* Large-eddy simulation of a turbulent piloted methane/air diffusion flame (Sandia flame D). *Phys. Fluids* **12** (10), 2541–2554.

Pitsch, H. & Steiner, H. 2000*b* Scalar mixing and dissipation rate in large-eddy simulations of non-premixed turbulent combustion. *Proc. Combust. Inst.* **28** (1), 41–49.

Poinsot, T. 1996 Using direct numerical simulations to understand premixed turbulent combustion. *Symp. (Int.) Combust.* **26** (1), 219–232.

Poinsot, T., Candel, S. & Trouvé, A. 1995 Applications of direct numerical simulation to premixed turbulent combustion. *Prog. Energy Combust. Sci.* **21** (6), 531–576.

Poinsot, T. & Veynante, D. 2012 *Theoretical and Numerical Combustion*, 3rd edn. Toulouse, France: (n.p.).

Poinsot, T., Veynante, D. & Candel, S. 1991 Quenching processes and premixed turbulent combustion diagrams. *J. Fluid Mech.* **228**, 561–606.

Pope, S. B. 1985 PDF methods for turbulent reactive flows. *Prog. Energy Combust. Sci.* **11** (2), 119–192.

Pope, S. B. 1987 Turbulent Premixed Flames. *Annu. Rev. Fluid Mech.* **19** (1), 237–270.

Pope, S. B. 1988 The evolution of surfaces in turbulence. *Int. J. Eng. Sci.* **26** (5), 445–469.

Pope, S. B. 1990 Computations of turbulent combustion: Progress and challenges. *Symp. (Int.) Combust.* **23** (1), 591–612.

Pope, S. B. 1991 Mapping Closures for Turbulent Mixing and Reaction. *Theor. Comput. Fluid Dyn.* **2** (5–6), 255–270.

Pope, S. B. 1997 Computationally efficient implementation of combustion chemistry using in situ adaptive tabulation. *Combust. Theory Model.* **1** (1), 41–63.

Pope, S. B. 2000 *Turbulent Flows*. Cambridge, UK: Cambridge University Press.

Pope, S. B. 2004 Ten questions concerning the large-eddy simulation of turbulent flows. *New J. Phys.* **6**, 35.

Pope, S. B. 2013 Small scales, many species and the manifold challenges of turbulent combustion. *Proc. Combust. Inst.* **34** (1), 1–31.

Proch, F. & Kempf, A. M. 2014 Numerical analysis of the Cambridge stratified flame series using artificial thickened flame LES with tabulated premixed flame chemistry. *Combust. Flame* **161** (10), 2627–2646.

Proch, F. & Kempf, A. M. 2015 Modeling heat loss effects in the large eddy simulation of a model gas turbine combustor with premixed flamelet generated manifolds. *Proc. Combust. Inst.* **35** (3), 3337–3345.

Rembold, B. & Jenny, P. 2006 A multiblock joint PDF finite-volume hybrid algorithm for the computation of turbulent flows in complex geometries. *J. Comput. Phys.* **220** (1), 59–87.

Richardson, A. 2014 *The Evolution of the Parsons Steam Turbine*. Cambridge, UK: Cambridge University Press.

Richardson, L. F. 1922 *Weather Prediction by Numerical Process*. Cambridge, UK: Cambridge University Press.

Riley, J. J., Metcalfe, R. W. & Orszag, S. A. 1986 Direct numerical simulations of chemically reacting turbulent mixing layers. *Phys. Fluids* **29** (2), 406–422.

Roberts, J. B. 1973 Coherence Measurements in an Axisymmetric Wake. *AIAA J.* **11** (11), 1569–1571.

Rogallo, R. S. & Moin, P. 1984 Numerical Simulation of Turbulent Flows. *Annu. Rev. Fluid Mech.* **16** (1), 99–137.

Rolls-Royce 2015 *The Jet Engine*, 5th edn. Wiley.

Ruan, S. 2013 Turbulent partially premixed combustion: DNS analysis and RANS simulation. PhD thesis, University of Cambridge.

Ruan, S., Swaminathan, N., Bray, K. N. C., Mizobuchi, Y. & Takeno, T. 2012 Scalar and its dissipation in the near field of turbulent lifted jet flame. *Combust. Flame* **159** (2), 591–608.

Ruan, S., Swaminathan, N. & Darbyshire, O. 2014 Modelling of turbulent lifted jet flames using flamelets: A priori assessment and a posteriori validation. *Combust. Theory Model.* **18** (2), 295–329.

Ruan, S., Swaminathan, N., Isono, M., Saitoh, T. & Saitoh, K. 2015 Simulation of Premixed Combustion with Varying Equivalence Ratio in Gas Turbine Combustor. *J. Propuls. Power* **31** (3), 861–871.

Rutland, C. J., Ferziger, J. H. & El Tahry, S. H. 1991 Full numerical simulations and modeling of turbulent premixed flames. *Symp. (Int.) Combust.* **23** (1), 621–627.

Rydén, R., Eriksson, L.-E. & Olovsson, S. 1993 Large Eddy Simulation of Bluff Body Stabilised Turbulent Premixed Flames. In *Vol. 3A: General*. Cincinnati, OH, USA: ASME. Turbo Expo: Power for Land, Sea, and Air.

Sarghini, F., Piomelli, U. & Balaras, E. 1999 Scale-similar models for large-eddy simulations. *Phys. Fluids* **11** (6), 1596–1607.

See, Y. C. & Ihme, M. 2015 Large eddy simulation of a partially-premixed gas turbine model combustor. *Proc. Combust. Inst.* **35** (2), 1225–1234.

Seffrin, F., Fuest, F., Geyer, D. & Dreizler, A. 2010 Flow field studies of a new series of turbulent premixed stratified flames. *Combust. Flame* **157** (2), 384–396.

Selle, L., Lartigue, G., Poinsot, T., Koch, R., Schildmacher, K.-U., Krebs, W., Prade, B., Kaufmann, P. & Veynante, D. 2004 Compressible large eddy simulation of turbulent combustion in complex geometry on unstructured meshes. *Combust. Flame* **137** (4), 489–505.

Shahi, M., Kok, J. B. W., Roman Casado, J. C. & Pozarlik, A. K. 2015 Transient heat transfer between a turbulent lean partially premixed flame in limit cycle oscillation and the walls of a can type combustor. *Appl. Therm. Eng.* **81**, 128–139.

Shanbhogue, S. J., Husain, S. & Lieuwen, T. C. 2009 Lean blowoff of bluff body stabilized flames: Scaling and dynamics. *Prog. Energy Combust. Sci.* **35** (1), 98–120.

Shanbhogue, S. J., Sanusi, Y. S., Taamallah, S., Habib, M. A., Mokheimer, E. M. A. & Ghoniem, A. F. 2016 Flame macrostructures, combustion instability and extinction strain scaling in swirl-stabilized premixed CH4/H2 combustion. *Combust. Flame* **163**, 494–507.

Sheikhi, M. R. H., Drozda, T. G., Givi, P. & Pope, S. B. 2003 Velocity-scalar filtered density function for large eddy simulation of turbulent flows. *Phys. Fluids* **15** (8), 2321–2337.

Shepherd, I. G., Moss, J. B. & Bray, K. N. C. 1982 Turbulent transport in a confined premixed flame. *Symp. (Int.) Combust.* **19** (1), 423–431.

Smagorinsky, J. 1963 General Circulation Experiments with the Primitive Equations. *Mon. Weather Rev.* **91** (3), 99–164.

Smith, G. P., Golden, D. M., Frenklach, M., Moriarty, N. W., Eiteneer, B., Goldenberg, M., Bowman, C. T., Hanson, R. K., Song, S., Gardiner, Jr., W. C., Lissianski, V. V. & Qin, Z. 2000 GRI–Mech 3.0.

Sohrab, S. H., Ye, Z. Y. & Law, C. K. 1984 An experimental investigation on flame interaction and the existence of negative flame speeds. *Symp. (Int.) Combust.* **20** (1), 1957–1965.

Sommerer, Y., Galley, D., Poinsot, T., Ducruix, S., Lacas, F. & Veynante, D. 2004 Large eddy simulation and experimental study of flashback and blow-off in a lean partially premixed swirled burner. *J. Turbul.* **5**, 037.

Spalding, D. B. 1971 Mixing and chemical reaction in steady confined turbulent flames. *Symp. (Int.) Combust.* **13** (1), 649–657.

Spalding, D. B. 1979 *Combustion and Mass Transfer*. Oxford, UK: Pergamon Press.

Speth, R. L. & Ghoniem, A. F. 2009 Using a strained flame model to collapse dynamic mode data in a swirl-stabilized syngas combustor. *Proc. Combust. Inst.* **32** (2), 2993–3000.

Speziale, C. 1998 Turbulence Modeling for Time-Dependent RANS and VLES: A Review. *AIAA J.* **36** (2), 173–184.

Stahler, T., Geyer, D., Magnotti, G., Trunk, P., Dunn, M. J., Barlow, R. S. & Dreizler, A. 2017 Multiple conditioned analysis of the turbulent stratified flame A. *Proc. Combust. Inst.* **36** (2), 1947–1955.

Steinberg, A. M., Boxx, I., Stöhr, M., Meier, W. & Carter, C. D. 2012 Effects of Flow Structure Dynamics on Thermoacoustic Instabilities in Swirl-Stabilized Combustion. *AIAA J.* **50** (4), 952–967.

Stöhr, M., Boxx, I., Carter, C. & Meier, W. 2011*a* Dynamics of lean blowout of a swirl-stabilized flame in a gas turbine model combustor. *Proc. Combust. Inst.* **33** (2), 2953–2960.

Stöhr, M., Sadanandan, R. & Meier, W. 2011*b* Phase-resolved characterization of vortex-flame interaction in a turbulent swirl flame. *Exp. Fluids* **51** (4), 1153–1167.

Stopper, U., Meier, W., Sadanandan, R., Stöhr, M., Aigner, M. & Bulat, G. 2013 Experimental study of industrial gas turbine flames including quantification of pressure influence on flow field, fuel/air premixing and flame shape. *Combust. Flame* **160** (10), 2103–2118.

Straub, C., Kronenburg, A., Stein, O. T., Barlow, R. S. & Geyer, D. 2019 Modeling stratified flames with and without shear using multiple mapping conditioning. *Proc. Combust. Inst.* **37** (2), 2317–2324.

Straub, C., Kronenburg, A., Stein, O. T., Kuenne, G., Janicka, J., Barlow, R. S. & Geyer, D. 2018 Multiple mapping conditioning coupled with an artificially thickened flame model for turbulent premixed combustion. *Combust. Flame* **196**, 325–336.

Swaminathan, N. & Bray, K. N. C. 2005 Effect of dilatation on scalar dissipation in turbulent premixed flames. *Combust. Flame* **143** (4), 549–565.

Swaminathan, N. & Bray, K. N. C. 2011*a* Fundamentals and Challenges. In *Turbulent Premixed Flames* (ed. N. Swaminathan & K. N. C. Bray), chap. 1, pp. 1–40. Cambridge, UK: Cambridge University Press.

Swaminathan, N. & Bray, K. N. C., ed. 2011*b* *Turbulent Premixed Flames*. Cambridge, UK: Cambridge University Press.

Swaminathan, N., Xu, G., Dowling, A. P. & Balachandran, R. 2011 Heat release rate correlation and combustion noise in premixed flames. *J. Fluid Mech.* **681**, 80–115.

Sweeney, M. S., Hochgreb, S. & Barlow, R. S. 2011 The structure of premixed and stratified low turbulence flames. *Combust. Flame* **158** (5), 935–948.

Sweeney, M. S., Hochgreb, S., Dunn, M. J. & Barlow, R. S. 2012*a* The structure of turbulent stratified and premixed methane/air flames I: Non-swirling flows. *Combust. Flame* **159** (9), 2896–2911.

Sweeney, M. S., Hochgreb, S., Dunn, M. J. & Barlow, R. S. 2012*b* The structure of turbulent stratified and premixed methane/air flames II: Swirling flows. *Combust. Flame* **159** (9), 2912–2929.

Syred, N. 2006 A review of oscillation mechanisms and the role of the precessing vortex core (PVC) in swirl combustion systems. *Prog. Energy Combust. Sci.* **32** (2), 93–161.

Syred, N. & Beér, J. M. 1974 Combustion in Swirling Flows : A Review. *Combust. Flame* **23** (2), 143–201.

Tay Wo Chong, L., Komarek, T., Kaess, R., Föller, S. & Polifke, W. 2010 Identification of Flame Transfer Functions From LES of a Premixed Swirl Burner. In *Vol. 2: Combustion, Fuels and Emissions, Parts A and B*, pp. 623–635. Glasgow, UK: ASME. Turbo Expo: Power for Land, Sea, and Air.

Taylor, A. M. K. P. 1982 Confined isothermal and combusting flows behind axisymmetric baffles. PhD thesis, Imperial College London.

Taylor, A. M. K. P. & Whitelaw, J. H. 1984 Velocity characteristics in the turbulent near wakes of confined axisymmetric bluff bodies. *J. Fluid Mech.* **139**, 391–416.

Taylor, G. I. 1935 Statistical Theory of Turbulence. *Proc. R. Soc. Lond. A* **151** (873), 421–444.

Temme, J. E., Allison, P. M. & Driscoll, J. F. 2014 Combustion instability of a lean premixed prevaporized gas turbine combustor studied using phase-averaged PIV. *Combust. Flame* **161** (4), 958–970.

Tennekes, H. & Lumley, J. L. 1972 *A First Course in Turbulence*. MIT Press.

Turns, S. R. 2011 *An Introduction to Combustion: Concepts and Applications*, 3rd edn. Singapore: McGraw-Hill.

Uberoi, M. S. & Freymuth, P. 1970 Turbulent energy balance and spectra of the axisymmetric wake. *Phys. Fluids* **13** (9), 2205–2210.

Vagelopoulos, C. M. & Egolfopoulos, F. N. 1998 Direct experimental determination of laminar flame speeds. *Symp. (Int.) Combust.* **27** (1), 513–519.

Vagelopoulos, C. M., Egolfopoulos, F. N. & Law, C.K. 1994 Further considerations on the determination of laminar flame speeds with the counterflow twin-flame technique. *Symp. (Int.) Combust.* **25** (1), 1341–1347.

Valiño, L. 1998 A Field Monte Carlo Formulation for Calculating the Probability Density Function of a Single Scalar in a Turbulent Flow. *Flow, Turbul. Combust.* **60** (2), 157–172.

Van Doormaal, J. P. & Raithby, G. D. 1984 Enhancements of the simple method for predicting incompressible fluid flows. *Numer. Heat Transf.* **7** (2), 147–163.

Vervisch, L. 2000 Using numerics to help the understanding of non-premixed turbulent flames. *Proc. Combust. Inst.* **28** (1), 11–24.

Vervisch, L. & Poinsot, T. 1998 Direct Numerical Simulation of Non-Premixed Turbulent Flames. *Annu. Rev. Fluid Mech.* **30** (1), 655–691.

Veynante, D., Trouvé, A., Bray, K. N. C. & Mantel, T. 1997 Gradient and counter-gradient scalar transport in turbulent premixed flames. *J. Fluid Mech.* **332**, 263–293.

Veynante, D. & Vervisch, L. 2002 Turbulent combustion modeling. *Prog. Energy Combust. Sci.* **28** (3), 193–266.

Vincent, J. H. 1977 Model experiments on the nature of air pollution transport near buildings. *Atmos. Environ.* **11** (8), 765–774.

Vincent, J. H. 1978 Scalar transport in the near aerodynamic wakes of surface-mounted cubes. *Atmos. Environ.* **12** (6–7), 1319–1322.

Wandel, A. P. & Lindstedt, R. P. 2013 Hybrid multiple mapping conditioning modeling of local extinction. *Proc. Combust. Inst.* **34** (1), 1365–1372.

Wang, G., Boileau, M. & Veynante, D. 2011 Implementation of a dynamic thickened flame model for large eddy simulations of turbulent premixed combustion. *Combust. Flame* **158** (11), 2199–2213.

Weigand, P., Meier, W., Duan, X. & Aigner, M. 2007 Laser-Based Investigations of Thermoacoustic Instabilities in a Lean Premixed Gas Turbine Model Combustor. *J. Eng. Gas Turbines Power* **129** (3), 664–671.

Weigand, P., Meier, W., Duan, X. R., Stricker, W. & Aigner, M. 2006 Investigations of swirl flames in a gas turbine model combustor: I. Flow field, structures, temperature, and species distributions. *Combust. Flame* **144** (1–2), 205–224.

Weller, H. G., Tabor, G., Jasak, H. & Fureby, C. 1998 A tensorial approach to computational continuum mechanics using object-oriented techniques. *Comput. Phys.* **12** (6), 620–631.

Widenhorn, A., Noll, B. & Aigner, M. 2009 Numerical Study of a Non-Reacting Turbulent Flow in a Gas-turbine Model Combustor. In *47th AIAA Aerospace Sciences Meeting including The New Horizons Forum and Aerospace Exposition*. Orlando, FL, USA: AIAA 2009-647.

Williams, F. A. 1985*a* *Combustion Theory*, 2nd edn. Menlo Park, CA, USA: Benjamin Cummings.

Williams, F. A. 1985*b* Turbulent Combustion. In *Math. Combust.* (ed. J. D. Buckmaster), chap. 3, pp. 97–131. Philadelphia, PA, USA: SIAM.

Winterfeld, G. 1965 On processes of turbulent exchange behind flame holders. *Symp. (Int.) Combust.* **10** (1), 1265–1275.

Wollny, P., Rogg, B. & Kempf, A. 2018 Modelling heat loss effects in high temperature oxy-fuel flames with an efficient and robust non-premixed flamelet approach. *Fuel* **216**, 44–52.

Wright, F. H. 1959 Bluff-body flame stabilization: Blockage effects. *Combust. Flame* **3**, 319–337.

Wu, H. & Ihme, M. 2016 Compliance of combustion models for turbulent reacting flow simulations. *Fuel* **186**, 853–863.

Xu, J. & Pope, S. B. 2000 PDF calculations of turbulent nonpremixed flames with local extinction. *Combust. Flame* **123** (3), 281–307.

Yin, Z., Nau, P. & Meier, W. 2017 Responses of combustor surface temperature to flame shape transitions in a turbulent bi-stable swirl flame. *Exp. Therm. Fluid Sci.* **82**, 50–57.

Yoshizawa, A. 1986 Statistical theory for compressible turbulent shear flows, with the application to subgrid modeling. *Phys. Fluids* **29** (7), 2152.

Yoshizawa, A. & Horiuti, K. 1985 A Statistically-Derived Subgrid-Scale Kinetic Energy Model for the Large-Eddy Simulation of Turbulent Flows. *J. Phys. Soc. Japan* **54** (8), 2834–2839.

Zhang, H., Garmory, A., Cavaliere, D. E. & Mastorakos, E. 2015 Large Eddy Simulation/Conditional Moment Closure modeling of swirl-stabilized non-premixed flames with local extinction. *Proc. Combust. Inst.* **35** (2), 1167–1174.

Zhang, H. & Mastorakos, E. 2016 Prediction of Global Extinction Conditions and Dynamics in Swirling Non-premixed Flames Using LES/CMC Modelling. *Flow, Turbul. Combust.* **96** (4), 863–889.

Zhang, H. & Mastorakos, E. 2019 LES/CMC Modelling of a Gas Turbine Model Combustor with Quick Fuel Mixing. *Flow, Turbul. Combust.* **102** (4), 909–930.

Zhang, S. & Rutland, C. J. 1995 Premixed flame effects on turbulence and pressure-related terms. *Combust. Flame* **102** (4), 447–461.